GROWTH OF STRONTIUM TITANATE ON SILICON BY PULSED LASER DEPOSITION TECHNIQUE

Dejan Klement

Doctoral Dissertation
Jožef Stefan International Postgraduate School
Ljubljana, Slovenia

Supervisor: Dr. Matjaž Spreitzer, Jožef Stefan Institute, Ljubljana, Slovenia

Evaluation Board:
Prof. Dr. Dragan Mihailović, Chair, Jožef Stefan Institute, Ljubljana, Slovenia
Prof. Dr. Anton Meden, Member, Faculty of Chemistry and Chemical Technology, Ljubljana, Slovenia
Prof. Dr. Gerd Jan Koster, Member, University of Twente, The Netherlands

MEDNARODNA PODIPLOMSKA ŠOLA JOŽEFA STEFANA
JOŽEF STEFAN INTERNATIONAL POSTGRADUATE SCHOOL



Dejan Klement

GROWTH OF STRONTIUM TITANATE ON SILICON BY PULSED LASER DEPOSITION TECHNIQUE

Doctoral Dissertation

RAST STRONCIJEVEGA TITANATA NA SILICIJU Z METODO PULZNEGA LASERSKEGA NANAŠANJA

Doktorska disertacija

Supervisor: Dr. Matjaž Spreitzer

Ljubljana, Slovenia, October 2015

To my wonderful wife Eva.

Acknowledgments

First, I would like to thank my supervisor, Dr. Matjaž Spreitzer for his guidance, support and many useful discussions.

Thanks to Prof. Dr. Danilo Suvorov for noticing my enthusiasm and giving me an opportunity to attend XRD, PLD and several other courses. The gained knowledge helped me a lot during the PhD work.

Thanks to the members of the Commision Board, Prof. Dr. Dragan Mihailović, Prof. Dr. Anton Meden and Prof. Dr. Gerd Jan Koster for the time and effort they invested in review and evaluation of the dissertation.

Thanks to Dr. Janez Kovač for the XPS analysis and valuable discussions.

Last, but not least, very special thanks to my wife, Eva, for her encouragement, support and patience.

Abstract

Epitaxial integration of multifunctional complex oxides with advanced semiconductor technology is very important and desirable because it opens the door to a wide range of novel device applications. A convenient way of integrating functional oxides on Si(001) substrate is through the $SrTiO_3$ (STO) intermediate layer which can be fabricated on Si(001) in the epitaxial form and with high crystallinity using mainly the molecular beam epitaxy (MBE) method. However, slowness of the MBE deposition process and difficult stoichiometry control makes it an inappropriate tool from industrial point of view.
In this PhD thesis the focus is placed on the possibilities of using the pulsed-laser deposition (PLD) technique for the synthesis of an epitaxial STO layer on Si(001) as an alternative manufacturing route to MBE. Deposition performed by PLD is much faster, stoichiometric transfer more easily controllable, wherein the quality of PLD thin films can be comparable to the layers synthesized by MBE. In addition, large-area PLD systems became available recently on the market which indicate that PLD will become an industrial process over the next few years.
Initial studies were focused on cleaning, i.e. removal of organic compounds from the substrate surface and elimination of native amorphous SiO_2 layer which covers the Si surface since the epitaxial growth of STO can only be achieved on carbon free and crystalline Si surface. Thermal and Sr-induced deoxidation processes for elimination of native SiO_2 from the Si surface were investigated. It was demonstrated that by selection of proper sample holder and flashing the substrate to T>1100 °C a clean (2×1)+(1×2) reconstructed Si(001) surface can be prepared. Thermal as well as Sr-induced deoxidation processes performed at lower temperatures did not result in clean Si(001) surface due to the β-SiC precipitates which form in the reaction between Si and carbon in the temperature range from 730 °C to 1100 °C. Temperatures higher than 1100 °C cause dissociation of β-SiC and diffusion of carbon into the bulk silicon. Nevertheless, it was shown that flash-annealed Si surface becomes recontaminated with carbon after a certain period of time as disclosed by the reflection high-energy electron diffraction (RHEED) either as the c(4×4) or β-SiC transmission pattern. It was concluded that the recontamination of the Si(001) surface cannot be completely avoided, however, by improving the vacuum (decreasing the hydrocarbons partial pressure) it can be significantly delayed.
Epitaxial growth of STO directly on (2×1)+(1×2) reconstructed Si(001) surface is not possible due to the high reactivity of silicon, which readily reacts with oxygen from the background gas or deposited STO material and forms an amorphous transition layer at the interface which hinders the epitaxial growth. An effective way of controlling the reactivity of silicon surface against the oxidation is to form an appropriate buffer layer on top of the Si(001) surface. Based on a number of MBE studies from the last two decades, Si surface passivated with 1/2 ML of metallic strontium (Sr) represents the most suitable buffer layer in terms of achieved crystallinity of final STO layers. This dissertation presents an experimental procedure for Sr buffer layer preparation developed with the PLD technique. Different surface reconstructions formed due to the ordering of the Sr atoms on the Si(001) surface at elevated temperatures were studied in detail. *In-situ* RHEED characterization

showed surface structure evolution from the two-domain (2×1)+(1×2) reconstruction, exhibited by the bare Si surface, to a two-domain (2×3)+(3×2) structure at 1/6 ML, which is then replaced by a two-domain (1×2)+(2×1) structure again at 1/4 ML Sr coverage. The final (1×2)+(2×1) pattern was observed to be present up to 1/2 ML Sr coverage. The observation of (2×3)+(3×2) surface structure, characteristic for 1/6 ML Sr coverage, enabled preparation of exactly 1/2 ML Sr coverage on Si, which is a prerequisite for the subsequent epitaxial growth of $SrTiO_3$ layer. In addition, the stability of Sr buffer layer against oxidation was tested and the results revealed much higher resistance of Sr(1/2 ML)/Si(001) compared to the bare reconstructed Si surface.

The last part of investigation was devoted to the growth of STO on (1×2)+(2×1) reconstructed Sr(1/2 ML)/Si(001) surface with the aim to prepare an epitaxial layer with high crystallinity. Initial deposition proved to be the most critical part of the whole deposition process since the integrity of the Sr-buffer layer can easily be disrupted by high energetic species from the laser plume. Based on the detailed studies of initial deposition parameters in terms of background gas pressure, deposition temperature, fluence, and oxidation peculiarities it was demonstrated that the growth is fully epitaxial when the STO is deposited at room temperature and 0.05 mbar Ar pressure with intermediate oxidation periods and crystallized in vacuum (1×10^{-8} mbar) at the temperature in the range from 517 °C to 546 °C. Epitaxial layer of any thickness can be grown using this procedure. However, the slowness and complexity of the process confines its use to the first few nanometers of STO only. The subsequent deposition was performed in a much faster regime when both, high-temperature and high-oxygen partial pressure (1.3×10^{-6} mbar), were applied simultaneously. XRD examination of the final STO layer revealed only one out-of-plane (STO(001)||Si(001)) and one in-plane (STO[110]||Si[100]) orientation. On the other hand, few additional well defined spots with low intensity which emerged in the RHEED pattern during subsequent deposition at 517 °C indicate not completely single-crystalline growth and require further optimization of subsequent deposition parameters. The STO layer exhibits crystallinity of 1.68°, as derived from FWHM of (002) reflection along omega axis which is similar to some of MBE grown films. Post-deposition annealing in oxygen decreased the FWHM to 1.55°. Nevertheless, for some most demanding applications of STO/Si(001) as a pseudo-substrate, crystal quality of the STO layer needs to be further improved.

Overall, a new PLD route for the epitaxial growth of STO on Si(001) was developed which is based on the use of 1/2 ML Sr-buffer layer.

Povzetek

Integracija epitaksialnih multifunkcionalnih kompleksnih oksidov z napredno polprevodniško tehnologijo je izjemno pomembna in zaželena, ker omogoča razvoj širokega spektra novih naprav. Prikladen način integracije funkcionalnih oksidov s silicijevim substratom je preko vmesne plasti $SrTiO_3$ (STO), ki so jo raziskovalci zmožni sintetizirati v epitaksialni obliki in z visoko kristaliničnostjo z uporabo sistema za epitaksijo z molekularnim curkom (ang. molecular beam epitaxy, MBE). Vendar pa proces nanašanja z MBE ni primeren za industrijsko uporabo zaradi njegove počasnosti in težavne kontrole stehiometrije.

Doktorska disertacija obravnava možnost uporabe tehnike pulznega laserskega nanašanja (ang. pulsed laser deposition, PLD) za sintezo epitaksialne STO plasti na Si(001) kot alternativo MBE sintezni poti. PLD omogoča hitrejše nanašanje in enostavnejšo kontrolo stehiometrije pri prenosu materiala s tarče na substrat, obenem pa je kvaliteta tankih plasti, sintetiziranih s PLD, primerljiva s kvaliteto plasti, nanešenih z MBE. Poleg tega so se v zadnjem času na trgu pojavili PLD sistemi, ki omogočajo nanašanje na večje substrate, kar kaže možnost prehoda PLD med industrijske procese v naslednjih nekaj letih.

Začetne študije so temeljile na čiščenju, to je na odstranitvi organskih spojin s površine substrata in desorpciji izvorne amorfne SiO_2 plasti, ki pokriva površino silicija. Epitaksialno rast STO je namreč mogoče doseči samo na kristalinični površini silicija brez ogljika. Raziskoval sem termični in s stroncijem (Sr) kataliziran proces odstranitve izvorne SiO_2 plasti s površine Si. Pokazal sem, da lahko z ustrezno izbranim nosilcem za vzorce in hitrim dvigom temperature nad 1100 °C pripravimo čisto (2×1)+(1×2) rekonstruirano površino Si(001). Tako s termičnim kot s Sr kataliziranim procesom deoksidacije ni bilo mogoče pripraviti čiste površine Si(001), kadar sta bila procesa izvedena pri nižjih temperaturah, ker so se pri reakciji med Si in ogljikom v temperaturnem območju med 730 °C in 1100 °C na površini tvorili β-SiC otočki. Pri temperaturi, višji od 1100 °C, pride do razpada β-SiC in difuzije ogljika v notranjost silicija. Pokazal sem tudi, da se čista površina, pridobljena na podlagi hitrega dviga temperature nad 1100 °C, po določenem času ponovno kontaminira z ogljikom, kar se na difrakcijski sliki refleksijske visoko-energijske elektronske difrakcije (RHEED) pokaže kot c(4×4) ali β-SiC presevni vzorec. Zaključil sem, da se ponovni kontaminaciji površine Si(001) ni mogoče popolnoma izogniti, vendar pa lahko z izboljšanjem vakuuma ali zmanjšanjem parcialnega tlaka ogljikovodikov ta čas znatno podaljšamo.

Epitaksialna rast STO neposredno na (2×1)+(1×2) rekonstruirani površini Si(001) ni mogoča zaradi visoke reaktivnosti silicija, ki reagira bodisi s kisikom kot reakcijskim plinom iz vakuumske komore ali s kisikom iz STO in tvori amorfno vmesno plast, ki ovira epitaksialno rast. Učinkovit način kontrole reaktivnosti površine silicija proti oksidaciji je tvorba ustrezne puferske plasti na površini Si(001). Na podlagi številnih MBE študij iz zadnjih dveh desetletij predstavlja 1/2 monoplasti (MP) kovinskega stroncija na površini Si(001) najbolj primerno zaščitno plast, ker omogoča nadaljnjo pripravo STO plasti na siliciju z najvišjo kristaliničnostjo. Doktorska disertacija uvaja eksperimentalni postopek priprave stroncijeve puferske plasti na siliciju, ki sem ga razvil s PLD tehniko. Podrobno

sem raziskal različne površinske rekonstrukcije, ki se tvorijo kot posledica urejanja Sr atomov na silicijevi površini pri povišanih temperaturah. *In-situ* karakterizacija z RHEED je pokazala spreminjanje strukture površine iz dvodomenske (2×1)+(1×2) rekonstrukcije, značilne za čisto površino Si brez SiO_2 plasti, v dvodomensko (2×3)+(3×2) strukturo pri 1/6 MP pokritosti, ki se nadalje pri pokritosti 1/4 MP zamenja z (1×2)+(2×1) strukturo. (1×2)+(2×1) difrakcijski vzorec je prisoten vse do 1/2 MP pokritosti s stroncijem. Uspešnost priprave (2×3)+(3×2) površinske strukture, značilne za 1/6 MP pokritosti s stroncijem, je ključna za pripravo točno 1/2 MP pokritosti s stroncijem. Slednja je predpogoj za uspešno epitaksialno rast STO plasti. Testiranje stabilnosti stroncijeve puferske plasti v kisiku je pokazalo mnogo višjo odpornost Sr(1/2 ML)/Si(001) v primerjavi s čisto rekonstruirano površino silicija.

V zadnjem delu raziskav sem se ukvarjal z rastjo STO na (1×2)+(2×1) rekonstruirani površini Sr(1/2 ML)/Si(001) z namenom priprave epitaksialne plasti z visoko kristaliničnostjo. Začetno nanašanje se je izkazalo za najbolj kritično v celotnem sinteznem postopku, ker lahko visoko-energijski delci iz plazme poškodujejo stroncijevo pufersko plast. Na podlagi podrobnih raziskav začetnih pogojev nanašanja (tlak plina, temperatura substrata, gostota energije in oksidacija) sem pokazal, da je rast STO popolnoma epitaksialna, v kolikor poteka nanašanje materiala pri sobni temperaturi in 0,05 mbar agona, z vmesnimi oksidacijskimi stopnjami in kristalizacijo v vakuumu (~1×10^{-8} mbar) v temperaturnem območju od 517 °C do 546 °C. Ta postopek omogoča pripravo epitaksialne STO plasti poljubne debeline, vendar pa počasnost in kompleksnost procesa omejuje njegovo uporabo na prvih nekaj nanometrov STO. Nadaljnje nanašanje se je zato izvajalo na mnogo hitrejši način, kjer sta bila uporabljena hkrati tako visoka temperatura kot visok tlak kisika ($1{,}3\times10^{-6}$ mbar). XRD raziskave končne STO plasti so pokazale samo eno izvenravninsko (STO(001)||Si(001)) in eno znotraj-ravninsko (STO[110]||Si[100]) orientacijo. Po drugi strani pa je RHEED pokazal nekaj dodatnih dobro definiranih difrakcijskih točk z nizko intenziteto, ki so se pojavile tekom hitrejšega nanašanja pri 517 °C. Te dodatne difrakcijske točke so najverjetneje posledica nepopolne monokristalinične rasti, kar zahteva nadaljnjo optimizacijo parametrov hitrejšega nanašanja. STO plast izkazuje kristaliničnost FWHM(STO(002), vzdolž omega osi) = 1,68°, kar je podobno kvaliteti nekaterih plasti sintetiziranih z MBE. Žganje STO plasti v kisiku po končanem nanašanju je zmanjšalo vrednost FWHM na 1,55°. Za nekatere najbolj zahtevne aplikacije STO/Si(001) kot pseudo-substrata je potrebno kristaliničnost STO plasti še nadalje izboljšati.

Doktorska disertacija podaja novo razvito PLD sintezno pot za epitaksialno rast STO na Si(001), ki temelji na uporabi 1/2 MP debele stroncijeve puferske plasti.

Contents

List of Figures **xv**

List of Tables **xxi**

Abbreviations **xxiii**

Symbols **xxv**

1 Introduction **1**
1.1 Integration of Oxides with Silicon ... 1
1.2 Strontium Titanate on Silicon ... 2
1.3 Integration of Functional Oxides on $SrTiO_3$/Si Pseudo-Substrates ... 4
1.3.1 Ferroelectric and electro-optical films epitaxially integrated with silicon. 5
1.3.2 Photocatalytic films epitaxially integrated with silicon ... 5
1.3.3 Ferromagnetic layers epitaxially integrated with silicon ... 6
1.3.4 Piezoelectric layers epitaxially integrated with silicon ... 6
1.3.5 Multiferroic layers epitaxially integrated with silicon ... 7
1.3.6 High-k dielectric layers epitaxially integrated with silicon ... 7
1.4 Approaches to achieving epitaxial growth of $SrTiO_3$ on Si(001) ... 8

2 Aim and Hypothesis **11**
2.1 Aim ... 11
2.2 Hypothesis ... 11

3 Materials and Methods **13**
3.1 Materials ... 13
3.2 Methods ... 13
3.2.1 Synthesis method ... 13
3.2.1.1 Pulsed-laser deposition ... 13
3.2.1.2 PLD set-up ... 15
3.2.1.3 Experimental procedure ... 17
3.2.2 Methods for characterization of materials ... 17
3.2.2.1 Reflection high-energy electron diffraction ... 17
3.2.2.2 X-ray photoelectron spectroscopy ... 20
3.2.2.3 Rutherford backscattering spectroscopy ... 21
3.2.2.4 Scanning electron microscopy ... 21
3.2.2.5 Atomic force microscopy ... 22
3.2.2.6 Ellipsometry ... 22
3.2.2.7 X-ray reflectivity ... 22
3.2.2.8 X-ray diffraction ... 24
3.2.2.8.1 2Theta/Theta scan ... 24
3.2.2.8.2 Phi scan ... 25

3.2.2.8.3 Rocking curve 25
3.2.2.8.4 Reciprocal space mapping 25

4 Results and Discussion **27**
4.1 Cleaning of Silicon Surface [112] 27
4.1.1 Removal of the native SiO_2 layer 28
4.1.1.1 Thermal deoxidation 28
4.1.1.1.1 Carbon contamination behavior on Si(001) surface 33
4.1.1.2 Strontium-induced deoxidation 38
4.1.2 Summary 41
4.2 Formation of a Strontium Buffer Layer on Si(001) [112] 42
4.2.1 Clean (2×1)+(1×2) reconstructed Si(001) surface [1, 172, 173] 42
4.2.2 Deposition of strontium on Si(001) surface 48
4.2.3 Temperature effect on surface reconstruction 53
4.2.4 Resistance of Sr(1/2 ML)/Si(001) surface to oxidation 54
4.2.5 Summary 55
4.3 Growth of $SrTiO_3$ Thin Film on Sr(1/2 ML)/Si(001) Surface 56
4.3.1 Determination of initial deposition conditions 56
4.3.1.1 Optimization of background gas pressure 59
4.3.1.2 Optimization of laser fluence 65
4.3.1.3 Oxidation of strontium and titanium 67
4.3.2 Final deposition of $SrTiO_3$ 69
4.3.3 Interface structure of epitaxial $SrTiO_3$ thin film on silicon 86
4.3.4 Summary 88

5 Conclusions **89**

6 References **93**

Bibliography **111**

List of Figures

Figure 1.1: A schematic cross-section of Metal-Oxide-Semiconductor Field-Effect Transistor (MOSFET). The gate controls the electrostatic potential in the silicon below the gate oxide. Inversion channel between the source and the drain opens when the gate voltage reaches a threshold value[1].....1
Figure 1.2: Valence and conduction band offsets for oxide on Si which determine carrier injection in oxide band states. Edges of valence (VB) and conduction (CB) bands for Si and oxide are presented with bold lines.....3
Figure 1.3: (a) Schematic illustration of the epitaxial oxide heterostructure on Si and (b) a cross-sectional TEM image of abrupt STO/Si interface [19].....5
Figure 3.1: (a) Academic PLD system at the Jožef Stefan Institute (Advanced Materials Department) and (b) SolMates PLD production platform. 14
Figure 3.2: A schematic illustration of a pulsed laser deposition system. 15
Figure 3.3: (a) Photograph of the PLD system coupled with the glove-box. (b) One part of the load-lock chamber extends into the glove-box. 16
Figure 3.4: (a) Side view and (b) top view of the Ewald's sphere with radius k_0 cutting into the surface reciprocal rods, leading to a diffraction pattern [111]. 19
Figure 3.5: Simulated X-ray reflectivity curve of a STO substrate and 30 nm thick STO film grown on Si substrate. 23
Figure 4.1: Ellipsometric spectra of the silicon substrate (dots) as a function of the incident angle. The lines give the fitting data. 27
Figure 4.2: RHEED patterns in the [110] azimuth of Si taken after (a) 12-hour prebaking at 630 °C and (b) heating to 860 °C. The experiments were performed using a resistive heater. 29
Figure 4.3: RHEED patterns in the (a) [110] and (b) [100] azimuth of Si taken after heating to 900 °C using IR-laser. The sample was pasted to stainless steel sample plate using Ag-paste. The arrows in (a) indicate 1/2-order streaks and in (b) β-SiC transmission pattern. 30
Figure 4.4: Custom-build tantalum holder: (a) front side where the substrate is mounted and (b) rear side for substrate heating. 30
Figure 4.5: RHEED patterns in the [110] azimuth of Si taken after heating to (a) 750 °C, (b) 800 °C, (c) 850 °C, and (d) 900 °C. The arrows pointing up (yellow) and arrows pointing down (orange) indicate 1- and 1/2-order streaks, respectively. (e) RHEED pattern of the same sample as (a) taken at larger incident beam angle. RHEED patterns in the [100] azimuth of Si taken after heating to (f) 850 °C and (g) 900 °C. The samples were mounted to custom-build tantalum holder and heated directly by IR-laser. 32
Figure 4.6: RHEED patterns in the (a) [110] and (b) [100] azimuth of Si taken after flashing to 1200 °C, and cooling to 700 °C. The sample was mounted to custom-build tantalum holder and heated directly by IR-laser. 33
Figure 4.7: RHEED patterns in the (a) [110] and (b) [100] azimuth of Si taken after SiO_2 removal by heating up to 900 °C. The arrows indicate additional diffraction spots due to the epitaxially aligned islands of β-SiC on the Si(001) surface. 35

Figure 4.8: Simulated transmission electron diffraction patterns of β-SiC along (a) SiC[110] and (b) SiC[100] with superimposed Si streaks along (a) Si[110] and (b) Si[100]. (c) Simulated diffraction pattern along the SiC[1k0] direction, with k close to 0. 36
Figure 4.9: (a) RHEED pattern along the [100] azimuth of Si, obtained after flash annealing and keeping the surface at 600 °C for t > 15 min. The arrows pointing up (red) indicate primary silicon streaks (integer-order streaks) and the arrows pointing down (yellow) indicate quarter-order streaks due to the carbon contamination. (b) The c(4 × 4) reciprocal lattice. Larger (red) and smaller (yellow) circles indicate integer- and fractional quarter-order reciprocal lattice rods, respectively. 37
Figure 4.10: Modified ad-dimer model of the Si(001)-c(4×4) reconstructed surface. The unit cell contains one perpendicular dimer in the middle (atoms 2 and 5) and two parallel dimers (atoms 1, 3, 4 and 6). All three dimers are tilted. Carbon atom is positioned below the perpendicular dimer in the third subsurface layer [158]. 38
Figure 4.11: RHEED patterns in the [110] azimuth of Si taken after Sr-assisted deoxidation process at (a) 750 °C and (b) 800 °C. 39
Figure 4.12: Top and side view of an unreconstructed (a, b), (2×1) reconstructed (c, d) and c(4×2) reconstructed (e, f) Si(001) surface. 43
Figure 4.13: A schematic illustration of surface domains on Si(001) surface with single atomic layer steps. 44
Figure 4.14: Reciprocal lattice for (a) two-domain (2×1)+(1×2), (b) (2×1) and (c) (1×2) reconstructed Si(001) surface. Larger black and smaller red circles indicate integer- and ½-order reciprocal lattice rods, respectively. The row of reciprocal lattice rods within each of the rectangles in (c) represents single Laue zone of rods. 45
Figure 4.15: RHEED patterns of a (2×1)+(1×2) reconstructed Si(001) surface after flash annealing, in the (a, b) [110] and (b) [100] azimuths. The arrows pointing down (white) and arrows pointing up (black) in (a) indicate integer- and fractional 1/2-order streaks, respectively. (b) Incident beam in the same direction as in (a) but with higher intensity. L_0, $L_{1/2}$ and L_1 in (c) indicate zero, intermediate (due to 2× surface reconstruction) and first Laue circles. 47
Figure 4.16: (a) Experimentally obtained RHEED pattern with the beam in the [1-10] direction (perpendicular to the step edges). Arrows indicate splitting of the diffraction spots. (b) A schematic model of equally spaced surface steps with a the in-plane lattice parameter and L the terrace width. (c) The reciprocal lattice for a vicinal surface. Out-of-phase (red line) and in-phase (green line) Ewald sphere sections show the condition for diffraction. 48
Figure 4.17: Transmission diffraction pattern observed after deposition of one pulse of Sr on reconstructed Si(001) surface at 700 °C in [110] direction. Too large a spot size (2.31 mm^2) caused excessive quantity of deposited Sr. 49
Figure 4.18: RHEED patterns in the [110] azimuth of Si(001) taken at various stages of the Sr deposition. (a) (2×1)+(1×2) reconstructed Si surface at 700 °C after flash annealing. (b) (2×3)+(3×2) reconstructed surface with coverage of 1/6 ML Sr at 700 °C. (c) (1×2)+(2×1) reconstructed surface with coverage of 1/2 ML Sr at 700 °C. The arrows pointing down (yellow) and arrows pointing up (orange) indicate the streaks due to the 2× and 3× reconstructions, respectively. 49
Figure 4.19: RHEED patterns in the [100] azimuth of Si(001) taken at various stages of the Sr deposition. (a) (2×1)+(1×2) reconstructed silicon surface at 700 °C after flash annealing. (b) (2×3)+(3×2) reconstructed surface with coverage of 1/6 ML Sr at 700 °C. (c) (1×2)+(2×1) reconstructed surface with coverage of 1/2 ML Sr at 700 °C. $L_{1/6}$ and $L_{1/3}$ in (b) indicate intermediate Laue circles due to 3× surface reconstruction. 50

Figure 4.20: RHEED intensity of half- and third-order streaks during Sr deposition. The inset gives enlarged peak which corresponds to 1/6 ML coverage. Arrows pointing up in the inset indicate moments when ablation plume impinges on substrate surface. 51
Figure 4.21: Reciprocal lattice for (a) two-domain (2×3)+(3×2), (b) (2×3) and (c) (3×2) reconstructed Sr(1/6 ML)/Si(001) surface. Larger black and smaller red circles indicate integer- and fractional-order reciprocal lattice rods, respectively. The row of reciprocal lattice rods lying on each dashed line in (a) represents one Laue zone of rods.....52
Figure 4.22: Top view of silicon surface at (a) 0 ML (b) 1/6 ML and (c) 1/2 ML Sr coverage. Sr atoms are in green, top layer Si atoms are in blue and second layer Si atoms are in grey. 53
Figure 4.23: Stability of the buffer layer (red line) compared to the bare reconstructed Si surface (black line) at 50 °C, 250 °C, 300 °C and 400 °C in the background gas of oxygen. The lines indicate pressure levels at which the intensity of 1/2-order streaks begins to decrease. 54
Figure 4.24: RHEED patterns of the STO layer in the [110] azimuth of Si taken after heating to (a) ~630 °C and (b) ~890 °C. 57
Figure 4.25: (a) Si 2p XPS spectra of STO/Si samples deposited on the Sr buffer layer at room temperature in vacuum (green curve) and at 0.1 mbar Ar pressure (red curve). Black curve represents spectrum of the sample prepared at room temperature in vacuum on the bare reconstructed Si surface (without Sr buffer layer) (b) Ti 2p and (c) Sr 3d XPS spectra acquired after deposition at room temperature and 0.1 mbar Ar pressure (red curve) and after further heating to 890 °C (blue curve). 58
Figure 4.26: Comparison of X-ray reflectivity curves for samples prepared at different Ar background pressures. 60
Figure 4.27: Comparison of initial part of X-ray reflectivity curves for samples prepared at different Ar background pressures in terms of critical angle ω_c. Density increases from the left (brown curve) to the right (black curve).....61
Figure 4.28: Fourier magnitude versus thickness plot for the sample prepared in vacuum (~1×10^{-8} mbar). Peak positions give thickness information. 61
Figure 4.29: AFM images of STO thin films deposited at room temperature and (a) in vacuum, (b) at 0.01 mbar, (c) 0.05 mbar, (d) 0.1 mbar, (e) 0.15 mbar Ar pressure. The lateral scan size is 1×1 μm^2. 63
Figure 4.30: SEM images of STO thin films deposited at room temperature and (a) 0.05 mbar, (b) 0.1 mbar, (c) 0.15 mbar Ar pressure.....63
Figure 4.31: Si 2p XPS spectra from a 4.5 nm STO/Si samples prepared under experimental conditions which differ in background gas type (Ar and O_2), background gas pressure (vacuum-0.15 mbar) and substrate temperature (room T and 260 °C). (b) Si 2p XPS spectrum of the sample deposited in vacuum. The Si 2p can be well fitted by Si-$2p_{1/2}$ and $2p_{3/2}$ core levels and by silicate peak.....64
Figure 4.32: Sr/Ti atomic ratio in STO films deposited at different fluencies determined by (a) XPS and (b) RBS. 66
Figure 4.33: XPS depth profiles obtained on the sample deposited at room temperature, 0.05 mbar Ar pressure and 1.5 J/cm^2. 67
Figure 4.34: Ti 2p XPS spectra obtained at different depths during XPS depth profiling of the STO layer deposited at room temperature and 0.05 mbar Ar pressure. Left and right peaks in each of the spectrum correspond to the photoemission from the Ti $2p_{1/2}$ and Ti $2p_{3/2}$ energy levels, respectively.....68
Figure 4.35: Complete experimental procedure for the preparation of STO layers on Si(001). 70

Figure 4.36: RHEED patterns in the [110] (a-d) and [100] (e-h) azimuth of Sr-buffered Si taken before the deposition of the STO seed layer (a, e) and after the deposition of 1 ML (b, f), 2 MLs (c, g) and 3 MLs (d, h) of STO at room temperature. 72
Figure 4.37: Experiment 1 - RHEED patterns in the [100] azimuth of STO taken after (a) first (3 MLs), (b) second (6 MLs) and (c) third (9 MLs) crystallization step at 636°C. (d) RHEED pattern in the [110] azimuth of STO taken after second (6 MLs) crystallization step. White arrows indicate additional quasi-spots. RHEED patterns in the (e) [100] and (f) [110] azimuth of STO taken after subsequent deposition of 7366 pulses at 636 °C..... 73
Figure 4.38: XRD 2Theta/Theta scans of STO/Si samples prepared in Experiment 1 (red curve), Experiment 2 (blue curve) and Experiment 3 (green curve)..... 74
Figure 4.39: Experiment 2 - RHEED patterns in the [100] azimuth of STO taken after (a) first (3 MLs), (b) second (6 MLs) and (c) third (9 MLs) crystallization step at 577 °C. (d) RHEED pattern in the [110] azimuth of STO taken after second (6 MLs) crystallization step. RHEED patterns in the (e) [100] and (f) [110] azimuth of STO taken after subsequent deposition of 7366 pulses at 636 °C..... 75
Figure 4.40: Experiment 3 - RHEED patterns in the [100] azimuth of STO taken after (a) first (3 MLs), (b) second (6 MLs) and (c) third (9 MLs) crystallization step at 517 °C. (d) RHEED pattern in the [110] azimuth of STO taken after second crystallization step. RHEED patterns in the (e) [100] and (f) [110] azimuth of STO taken after subsequent deposition of 7366 pulses at 636 °C..... 76
Figure 4.41: RHEED patterns in the [100] (a, c, e, g) and [110] (b, d, f, h) azimuth of Si taken after subsequent deposition of STO in Experiment 4 (a, b), Experiment 5 (c, d), Experiment 6 (e, f) and Experiment 7 (g, h). White arrows indicate additional spots which most likely arise from small portion of crystallites with other crystallographic orientation than the majority of the STO film..... 79
Figure 4.42: XRD 2Theta/Theta scan of STO/Si sample prepared in Experiment 7. 79
Figure 4.43: (a) Family of asymmetric reciprocal lattice points for STO (filled red circles) and Si (filled blue circles), measured during the Phi-scan. (b) X-ray diffraction measurements demonstrating the epitaxial relationship between STO and Si. The ϕ positions of the 011 and 022 peaks of the thin film and substrate, respectively, indicate the rotation of the STO unit cell by 45° with respect to the bulk Si cubic cell. (c) Epitaxial matching of STO and Si (001). The numbers refer to the vertical position of Si atoms with respect to the surface (set at zero), in the units of Si lattice constant..... 80
Figure 4.44: STO reciprocal space maps around (a) symmetric (002) reflection and (b) asymmetric (-103) reflection, plotted in reciprocal lattice units. (c, d) The same two reciprocal lattice points, plotted in relative angles in degrees with zero at the center of each of the scan axes. 81
Figure 4.45: Illustration of how lattice parameters can be obtained from measurement of two reciprocal lattice spots where there is a layer tilt..... 82
Figure 4.46: Crystallinity of our STO layer (Experiment 7) compared to the layers fabricated by MBE from other research groups. 84
Figure 4.47: XRD 2Theta/Theta scan of STO/Si sample prepared in Experiment 7 with additional post-annealing performed at 650 °C and 1.3×10^{-6} mbar oxygen pressure for 30 min. In the inset 29-35° 2Theta range is plotted in logarithmic scale in order to make additional peak, corresponding to the secondary phase, visible. 85
Figure 4.48: AFM height image of STO thin film prepared in Experiment 7 (unannealed). The lateral scan size is 1×1 μm^2. 86
Figure 4.49: X-ray reflectivity curve for the sample prepared in Experiment 7 (red curve) with Fourier magnitude versus thickness plot in the inset..... 86

Figure 4.50: XPS Si 2p spectrum measured on Si substrate covered with the native SiO_2 layer (blue curve) and on a sample containing ~4.7 nm thick STO seed layer deposited at room temperature and crystallized at 517 °C (red curve).....87

List of Tables

Table 1.1: Survey of buffer layers that have been used for the growth of $SrTiO_3$ on Si(001) using the PLD technique. 9
Table 4.1: SiO_2 layer thicknesses obtained from different areas on the sample surface. ...28
Table 4.2: Experimental conditions for the removal of physisorbed hydrocarbons on Si/SiO_2 by oxygen-bake procedure. 34
Table 4.3: Densities, surface roughnesses, and layer thicknesses of STO/Si samples prepared at different argon background gas pressures. 62
Table 4.4: Summary of experiments conducted under different experimental conditions .71

Abbreviations

AFM	...	Atomic Force Microscopy
AES	...	Auger Electron Spectroscopy
ALD	...	Atomic Layer Deposition
BTO	...	barium titanate
BFO	...	bismuth ferrite
DFT	...	Density Functional Theory
EOT	...	Equivalent Oxide Thickness
EELS	...	Electron Energy Loss Spectroscopy
FWHM	...	full width at half maximum
HTS	...	high-temperature superconductors
HR-XRD	...	High-Resolution X-Ray Diffraction
ITRS	...	International Technology Roadmap for Semiconductors
IR	...	infrared
ICP-MS	...	Inductively Coupled Plasma Mass Spectrometry
KCSD	...	Kinetically Controlled Sequential Deposition
LCO	...	lanthanum cobalt oxide
LAO	...	lanthanum aluminate
MOS	...	Metal-Oxide-Semiconductor
MOSFET	...	Metal-Oxide-Semiconductor Field-Effect Transistor
MBE	...	Molecular Beam Epitaxy
MEMS	...	Microelectromechanical Systems
ML	...	monolayer
PLD	...	Pulsed Laser Deposition
PZT	...	lead zirconate titanate
PMN-PT	...	lead magnesium niobate-lead titanate
RHEED	...	Reflection High-Energy Electron Diffraction
RSM	...	Reciprocal Space Map
STO	...	strontium titanate
STEM	...	Scanning Transmission Electron Microscopy
STM	...	Scanning Tunneling Microscopy
SEM	...	Scanning Electron Microscopy
SIMS	...	Secondary Ion Mass Spectrometry
TPD	...	Temperature Programmed Desorption
UV	...	ultraviolet
UHV	...	ultra-high vacuum
XRD	...	X-Ray Diffraction
XRR	...	X-Ray Reflectivity
XPS	...	X-Ray Photoelectron Spectroscopy
YSZ	...	yittria-stabilized zirconia
2DEG	...	two-dimensional electron gas
2D	...	two-dimensional

3D . . . three-dimensional

Symbols

k	...	static dielectric constant
C	...	capacitance
ε_0	...	dielectric constant of free space
A	...	area
d	...	thickness
r_{eff}	...	Pockels coefficient
T_C	...	Curie temperature
ρ	...	density
ω_c	...	critical angle
M	...	molar mass
r_e	...	electron radius
λ	...	wavelength
N_a	...	Avogadro's number
Z	...	atomic number
$\Delta f'$	...	real dispersion (Hönl) correction

Introduction

1.1 Integration of Oxides with Silicon

Silicon (Si) is the most important element in semiconductor industry. Elemental Si is commercially prepared by reduction of SiO_2 with carbon during the heating process in a furnace. Such process results in amorphous Si in a form of brown powder which can be easily melted. However, semiconductor industry uses single crystals of Si, grown by the Czochralski process. In this method, a seed is introduced into a melt and then slowly withdrawn. As-prepared single crystalline Si is hard, dark gray, and has a metallic luster. The industry uses mainly (001)-oriented wafers cut from single crystals of 300 mm diameter. Transition to 300 mm wafers from 200 mm wafers began in 2001 and it is further expected that 300 mm wafers will be replaced by 450 mm wafers by the end of this decade. A larger wafer diameter enables producing more semiconductor devices from a single wafer, enhancing productivity and efficiency. However, moving to larger wafer sizes is not a simple process since it requires large investments into machinery needed to handle and process larger wafers. The interest in Si has its roots in the success of Metal-Oxide-Semiconductor (MOS) technology, which has enabled and still maintains the mass-scale production of ever cheaper and faster microprocessors and memories. The name MOS is related to the process which originally employed SiO_2 (oxide) layers sandwiched between metal and silicon (semiconductor). Despite the substitution of metal layer by a heavily doped polycrystalline Si layer, the name MOS has still been retained. The workhorse of MOS is a field effect transistor – MOSFET, shown in Figure 1.1.

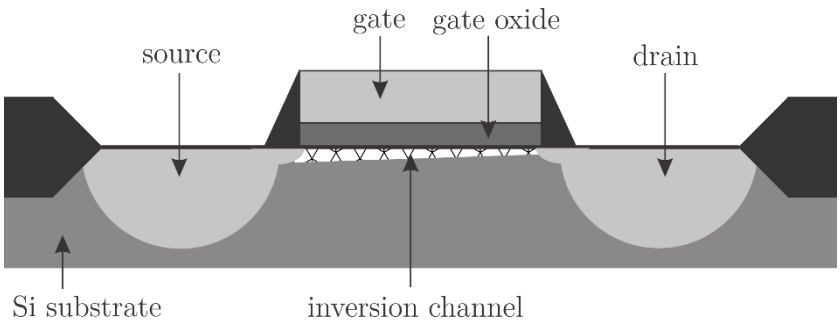


Figure 1.1: A schematic cross-section of Metal-Oxide-Semiconductor Field-Effect Transistor (MOSFET). The gate controls the electrostatic potential in the silicon below the gate oxide. Inversion channel between the source and the drain opens when the gate voltage reaches a threshold value[1].

It consists of four central parts: source, drain, gate and gate oxide. Gate potential controls the flow of electric current in a channel between the source and drain, while the gate oxide represents an insulation layer between the gate and channel. Several hundred fabrication steps must be performed in order to produce a typical integrated circuit. These steps include processes as lithography, cleaning, etching, implantation, oxidation, deposition, and polishing. It would be beneficial to use this traditional well-established silicon technology in conjunction with oxides. Integration of oxides with Si has been attracting considerable attention for more than two decades due to a wide range of potentially useful properties of oxide materials as well as reliable and well established fabrication process of Si wafers. Oxides represent an important class of materials due to their various properties, ranging from dielectric, piezoelectric, ferroelectric, ferromagnetic, optical, electro-optical, and catalytic to superconducting properties. Thus, the integration of these highly functional metal oxides with semiconductor technology is extremely important and desirable. Emphasis is placed on integration of single-crystalline oxides rather than amorphous or polycrystalline oxides with Si since the properties of epitaxial films are in many cases superior to those of the same material in amorphous or polycrystalline form. Successful heteroepitaxial growth of oxides on Si opens the door to a wide range of novel device applications with enhanced functionality and flexibility. Crystalline oxides were at first deposited on oxide substrates. However, it soon became clear that oxide substrate technology greatly limits the scope of applications due to high-cost, small size and poor quality of these substrates. Besides, many of the most advanced processing tools, such as lithography, are developed specifically for the silicon industry and oxide-substrates often cannot be processed on these tools because of the incompatibilities either with the substrate size or mechanical, electrical, and thermal properties. On the contrary, oxides on silicon could be processed on these tools.

1.2 Strontium Titanate on Silicon

The union of dissimilar materials like silicon and oxide film presents considerable challenge to heteroepitaxial growth as a consequence of very different chemical and structural nature of these two materials. Consequently, not many oxides were successfully integrated with Si(001) in the epitaxial form [2]. The most extensively studied epitaxial oxide on Si(001) both experimentally and theoretically is strontium titanate ($SrTiO_3$). It exhibits cubic perovskite crystal structure with unit cell parameter a=3.905 Å. The transition metal ion titanium (Ti) is at the B-site in the center of a cube formed by the A-site cations (Sr). Oxygen atoms are located in the center of each face forming an octahedron around the Ti.

Such an interest in the epitaxial growth of $SrTiO_3$ (STO) on Si was primarily attributed to the search for replacement of gate dielectric SiO_2 in MOSFET [3, 4]. The semiconductor industry was facing this challenge due to scaling of MOSFETs in order to continue the trend predicted by Moore's law. Intensive research efforts resulted in a steady increase of the speed and density of transistors for decades. Continuation of this process with SiO_2 as a gate oxide has become untenable because at thickness below 20 Å it suffers from high leakage current and cannot act as an effective insulator [5]. This results in increase of circuit power dissipation to unacceptable values. Therefore, alternative high-k materials to replace SiO_2 needed to be developed. STO was suggested as one of the most promising candidates for high-k dielectric gate oxide replacement due to its high bulk dielectric constant k ≈ 300 at room temperature. Approximately eighty-times larger bulk dielectric constant than that of bulk SiO_2 (k_{SiO2}=3.9) means that the equivalent gate oxide thickness can in principle be larger by the same factor for an equivalent gate capacitance, as shown by the Equation (1.1).

$$C = \frac{\varepsilon_0 k A}{d} \tag{1.1}$$

C	. . .	gate capacitance
ε_0	. . .	dielectric constant of free space
k	. . .	static dielectric constant
A	. . .	area
d	. . .	thickness

In this respect it is convenient to define the so-called »equivalent oxide thickness« (EOT) which indicates how thick the SiO_2 layer would need to be to produce the same effect as the newly developed high-k material (Eq. (1.2)).

$$EOT = \frac{k_{SiO_2}}{k_{high-k}} d_{high-k} \tag{1.2}$$

k_{SiO_2}	. . .	static dielectric constant of SiO_2
k_{high-k}	. . .	static dielectric constant of a newly developed high-k oxide
d_{high-k}	. . .	thickness of a newly developed high-k oxide

STO exhibits a high enough k that could be used for a reasonable number of years of scaling which is one of the requirements of a new gate oxide [5]. McKee et al. [6] fabricated MOS capacitor using STO as an alternative to SiO_2 and showed the extraordinary result of EOT<10 Å for 150 Å thick STO layer. This accomplishment can be primary attributed to the high dielectric constant of STO as well as atomically abrupt interface between STO and Si without amorphous silica phase. Thus, for this application it is desirable to avoid the reaction between STO and Si because the resulting low-dielectric constant SiO_2 layer would increase the overall EOT. However, another requirement for a new gate oxide is that it must act as an insulator. This requires that the potential barrier at each band must be over 1 eV in order to inhibit conduction by the Schottky emission of electrons or holes into the oxide bands (Figure 1.2).

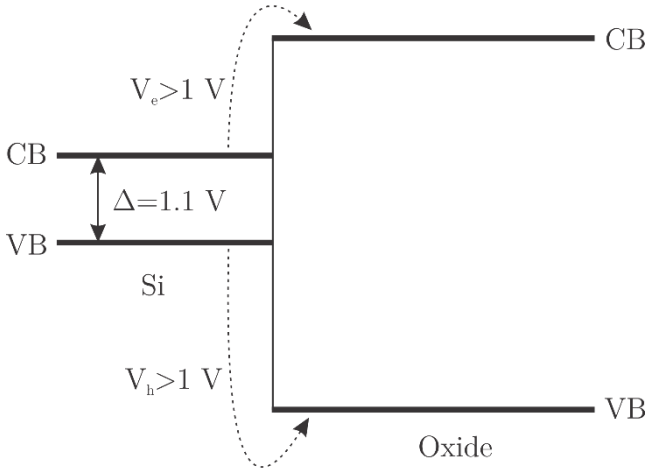


Figure 1.2: Valence and conduction band offsets for oxide on Si which determine carrier injection in oxide band states. Edges of valence (VB) and conduction (CB) bands for Si and oxide are presented with bold lines.

Si has a band gap of 1.1 eV, whereas that of STO is 3.3 eV. In order to have both barriers over 1 eV, STO bands must be aligned almost symmetrically with respect to those of Si. In fact, Chambers et al. [7] measured the band offsets of epitaxial STO/Si(001) and found valence and conduction band offsets of ~2.1 and ~0.0 eV, respectively. Nonexistent conduction band offset encountered for STO/Si(001) led this potential application to be almost abandoned until it was proposed that this problem can be overcome by carefully constructing the interface between STO and Si [8, 9]. High-k transistors were for the first time incorporated in a high volume manufacturing process in 2007 by Intel company [10]. SiO_2 was replaced by hafnium oxide compound. International technology roadmap for semiconductors (ITRS) from 2013 [11] highlights further scaling of EOT with materials which exhibit even higher dielectric constant than hafnium based compound as one of the challenges in the period from 2013 to 2020.

In addition to the possibility of STO behaving as a dielectric, also ferroelectric functionality was shown for STO on Si [12]. Although bulk STO is not ferroelectric at any temperature, the ferroelectricity of thin films can be induced by epitaxial strain which is formed as a result of ~1.7 % lattice mismatch between STO and Si. To make this possible, coherently strained STO film needs to be grown directly on Si, with no interfacial SiO_2 layer because through the interfacial layer strain can easily be released. Such a ferroelectric in combination with semiconductor Si could be used in non-volatile memories [13, 14], smart transistors that can be used as temperature or pressure sensors [15], and non-volatile ferroelectric FETs [12].

STO can exhibit also n-type semiconductor behavior when it is doped or simply deposited at too low oxygen pressure, leading to oxygen deficient $SrTiO_{3-\delta}$ [16]. When the Si substrate is p-type (B-doped), ideal diode behavior is observed, suggesting the promising potential of *p*-Si/*n*-$SrTiO_{3-\delta}$ heterostructure as a new type of ultrafast ultraviolet light detector with high sensitivity.

STO has been commonly used as a single-crystal substrate for epitaxial growth of multifunctional oxides because its unit cell constant closely matches the large number of other perovskite materials [17]. However, STO single-crystal substrates are far less perspective compared to Si substrates for the reasons outlined already in the previous section. This has led the researchers to the idea of integration of STO with large area Si wafers in the epitaxial form and use of such heterostructure as a template layer (pseudo-substrate) for the integration of other transition metal oxides with Si. Besides, there are many oxides which cannot be epitaxially grown directly on Si. And yet, their epitaxial integration with Si is possible if thin epitaxial STO layer is grown on Si first.

1.3 Integration of Functional Oxides on $SrTiO_3$/Si Pseudo-Substrates

As mentioned previously, the STO/Si pseudo-substrate represents a convenient way of integrating functional oxides on Si (Figure 1.3). A very thin STO layer (four unit cells) is already sufficient to ensure further high quality crystal growth of functional oxides. In following sections a brief review of recent developments in the epitaxial integration of multifunctional oxide thin film heterostructures on Si is given. Materials that are ferroelectric, ferromagnetic, electro-optic, photocatalytic, high-k dielectric, multiferroic and piezoelectric have already been integrated on Si. A good review of some of these applications is given in references [18] and [19].

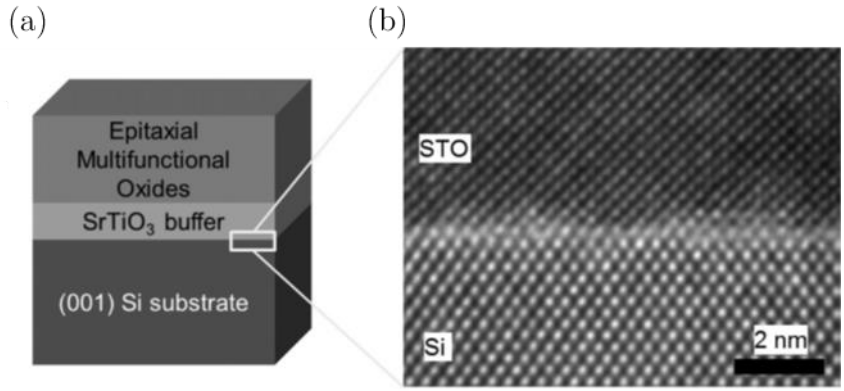


Figure 1.3: (a) Schematic illustration of the epitaxial oxide heterostructure on Si and (b) a cross-sectional TEM image of abrupt STO/Si interface [19].

1.3.1 Ferroelectric and electro-optical films epitaxially integrated with silicon

Integration of ferroelectric properties of certain perovskites with silicon can lead to realization of new kind of nonvolatile transistors that can perform both logic and memory functions. Such ferroelectric transistors have two main requirements. In addition to the epitaxial growth the ferroelectric polarization must have a component normal to the interface. $Pb_xZr_{1-x}TiO_3$ (PZT) was the first epitaxial ferroelectric grown on Si(001) through the utilization of an insulating, single-crystalline STO transition layer [20, 21]. Another material widely studied for this purpose was $BaTiO_3$ (BTO). Niu et al. [22] demonstrated the epitaxial growth of (001)-oriented BTO films on Si(001) substrate buffered by thin STO layer using both molecular beam epitaxy (MBE) and pulsed laser deposition (PLD) techniques. It was shown that due to the limited oxygen pressure during the growth, the BTO layers grown by MBE exhibit no ferroelectric properties but only typical dielectric behavior despite post deposition annealing being performed. In contrast, a ferroelectric BTO layer was obtained using the PLD method, which permits much higher oxygen pressure. Most recently, another two successful attempts at growing epitaxial BTO films with a polarization pointing perpendicular to the silicon substrate on STO-buffered silicon have been reported. Dubourdieu et al. [23] demonstrated ferroelectric switching of 8- to 40-nm-thick BTO films in metal-ferroelectric-semiconductor structure. On the other hand, Abel and coworkers [24] focused on electro-optical properties available in oxides which are not exploited yet in today's silicon photonics technology. They reported on the electro-optical properties of thin BTO films and extracted a large effective Pockels coefficient of $r_{eff} = 148$ pm V^{-1}, which is a five times larger than in the current standard material for electro-optical devices, $LiNbO_3$. The integration of electro-optical films on silicon could pave the way towards power-efficient, ultra-compact integrated devices, such as modulators, tuning elements and bistable switches.

1.3.2 Photocatalytic films epitaxially integrated with silicon

Extensive research effort has been invested in TiO_2 due to its energy and environmental applications [25-28]. TiO_2 can crystallize in one of three polymorphic crystal structures: rutile, anatase and brookite. The most abundant phase in nature is rutile. However, it has been shown that anatase exhibits significantly higher photocatalytic activity than rutile. Single-crystal anatase is typically synthesized in the form of nanoparticles [26], [29]. Chambers et al. [30] showed that it is possible to grow high-quality, single crystal anatase

films on perovskite substrates such as STO and $LaAlO_3$ (LAO). Since the main challenge for photocatalytic application is rather large band gap of anatase (approximately 3.2 eV making it ultraviolet-active), a variety of methods for band-gap engineering have been proposed to utilize solar-abundant visible light instead of ultraviolet. One of the approaches which attracted considerable attention is oxide interface engineering. Seo and coworkers [174a] grew epitaxial c-axis-oriented anatase on an STO/Si(001) pseudo-substrate using the MBE technique and they were able to elucidate the real physical and electronic structure of the interface by means of Z-contrast scanning transmission electron microscopy (STEM) and electron energy loss spectroscopy (EELS), respectively. This investigation contributes to better understanding of the interface effects on the photocatalytic activity of mixed oxide catalysts.

1.3.3 Ferromagnetic layers epitaxially integrated with silicon

Direct integration of STO on Si has opened the possibility to integrate the perovskite lanthanum-based manganites ($La_{1-x}A_xMnO_3$, where A is alkaline earth metal) on Si. Manganese oxide is a well-known carrier induced ferromagnet that shows ferromagnetism above room temperature and is therefore one of the best candidates for the realization of room temperature spin electronic devices. Kanki and coworkers [31] fabricated $La_{0.8}Ba_{0.2}MnO_3$ thin films on STO(001) single-crystal substrates using the PLD technique. Their deposition process could also be transferred to STO/Si pseudo-substrates. They investigated dependence of the magnetism on film thickness and showed room temperature ferromagnetism down to 5-nm-thick films. Integration of high-quality epitaxial $La_{0.7}Sr_{0.3}MnO_3$ films grown by PLD on STO/Si(001) by Pradhan et al. [32] is another example of integrating magnetism on Si. Tremendous potential was shown also for $LaCoO_3$ (LCO) as a result of ferromagnetic order induced by biaxial tensile strain. Fuchs et al. [33] demonstrated that the population of higher spin states is significantly enhanced in strained LCO films resulting in a ferromagnetic ground state with a Curie temperature (T_C) of ~90 K when LCO is grown on STO using PLD. Similar results were obtained also by Posadas and coworkers [34] who have grown epitaxially strained LCO on STO/Si(100) by MBE. Epitaxial growth of ferromagnetic layers on Si potentially leads to device integration where multiple types of devices (e.g., a sensor and an actuator) can be realized on a single wafer. Another proposed device is the spin field effect transistor (spin-FET) [35] which is based on efficient injection of a spin-polarized current from a ferromagnetic metal into a semiconductor such as Si. Posadas et al. [36] demonstrated the epitaxial integration of Co-substituted STO on Si by MBE. They used a thin (three unit cells) undoped STO/Si pseudo-substrate. Co-substituted STO films with a composition of 30-40 % cobalt exhibited room-temperature ferromagnetic insulating behavior with a saturation moment of ~3 μ_B/Co. It was shown by means of first-principles calculations that oxygen vacancies are crucial in stabilizing ferromagnetism in this system. That kind of multilayer structure may be useful for certain spintronic applications such as spin filters for spin-injection contacts in spin-FETs.

1.3.4 Piezoelectric layers epitaxially integrated with silicon

High performance piezoelectric microelectromechanical systems (MEMS) have been fabricated by the integration of single-crystal piezoelectric films on Si. Such multilayer structures incorporate all the advantages of large scale integration of Si substrates with on-board electronic circuits. $Pb(Mg_{1/3}Nb_{2/3})O_3$-$PbTiO_3$ (PMN-PT) single-crystal is known to have extremely large piezoelectric response compared to the conventional $Pb(Zr,Ti)_3$ (PZT) material, and is therefore used in bulk actuation and sensor devices [37, 38]. Baek et al.

[19, 39], succeeded in fabrication of high-quality PMN-PT epitaxial thin films on vicinal (001) Si wafers with the use of an epitaxial (001) STO template layer. As-prepared layers showed superior piezoelectric coefficient of $e_{31,f} = -27 \pm 3$ C m^{-2} which is the material's figure of merit for majority of the micromachined piezoelectric sensors and actuators, enabling performance comparison between systems of different geometries. Such the piezoelectric coefficient is the highest reported among any other piezoelectric thin films. Furthermore, the PMN-PT films also exhibit higher values for a figure of merit of energy-harvesting devices compared to PZT films. However, PMN-PT exhibits giant piezoelectric response only when single-crystal layer with right stoichiometry (near the morphotropic phase boundary) and $(001)_{pc}$ (pc, pseudocubic) orientation is formed. Evaporation of PbO species often leads to non-stoichiometric films which contain lead-deficient pyrochlore phase, making the synthesis rather difficult. Baek and coworkers showed that use of miscut Si substrate dramatically improves the phase purity because the high density of steps on the surface of the miscut substrates effectively incorporates volatile constituents (such as PbO) into the film. They also highlighted the importance of (001) epitaxial STO layer on Si for achieving single-crystal PMN-PT growth of the desired orientation. These thin films can provide a wide range of piezoelectric device applications such as ultrasound medical imaging, microfluidic control, piezotronics, and energy harvesting.

1.3.5 Multiferroic layers epitaxially integrated with silicon

Multiferroic materials exhibit both, ferroelectric and magnetic properties. One of the extensively investigated materials for magnetoelectric devices is perovskite $BiFeO_3$ (BFO). It exhibits ferroelectricity with a large spontaneous polarization and antiferromagnetic ordering at room temperature [40]. Wang et al. [41] demonstrated epitaxial growth of BFO layer on Si substrate with STO as a template layer and $SrRuO_3$ as bottom electrode with the PLD method. They used STO/Si(001) template layers fabricated by MBE and transferred them *ex situ* to a PLD growth chamber. It is quite likely for the PLD process to result in uncoupling of the functional properties of BFO from the Si substrate due to the SiO_2 interfacial layer which is formed as a result of high oxygen pressures used during the synthesis as well as post-deposition annealing. However, such heterostructures are still appropriate for devices where the functionality of the Si is not important [42], or for BFO membranes where the Si acts as a sacrificial substrate [43], which means that at first it serves as substrate for epitaxial growth, while later in the fabrication process it is completely removed by etching. In ref. [44] use of MBE is reported for the deposition of both, the BFO and STO thin films on Si(001) without braking vacuum for the first time. This time, formation of interfacial SiO_2 layer can be sufficiently suppressed in order to preserve coupling of the multiferroic BFO layer to Si. BFO is especially challenging in terms of domain structure engineering due to its rhombohedral symmetry. Complex domain and domain wall structures can form which results in different electrical and magnetic properties [19].

1.3.6 High-k dielectric layers epitaxially integrated with silicon

As already explained in Section 1.2, STO cannot be utilized as a gate dielectric on Si-based transistors unless the interface between STO and Si is properly constructed. However, it can still have an important role as a transition layer between Si and other high-k oxides whose direct epitaxy on Si has proven to be difficult. One of the potential candidates for use as an epitaxial gate dielectric is $LaAlO_3$ (LAO) which has a bulk dielectric constant of 24 and a band gap of 5.5 eV [45, 46]. In addition, it exhibits large potential barrier at both, valence and conduction bands. First report on successful epitaxial

integration of LAO on Si using STO was published by Mi et al [47]. Their synthesis process resulted in a small amount of interfacial layer between STO and Si. This extra interfacial layer is undesirable as it adds to the overall EOT (equivalent oxide thickness) [5]. One year later Reiner and coworkers [48] succeeded in fabricating epitaxial LAO on STO with no interfacial layer detectable at the oxide-silicon interface. In addition to MBE, the ability to obtain high crystalline quality epitaxial LAO films on Si, was shown also by ALD [49]. Moreover, atomically sharp LAO/STO heterointerfaces led researches to a remarkable new discovery of two-dimensional electron gas (2DEG) [50]. To generate 2DEG at LAO/STO interface it is crucial to control the termination of STO. The heterointerface between LAO and TiO_2-terminated STO exhibits metallic 2DEG behavior, whereas the heterointerface between LAO and SrO-terminated STO shows insulating behavior. It was demonstrated that 2DEG at LAO/STO interface can be used as optical and chemical sensors [51, 52]. In addition, these materials have been suggested as platforms for developing ultrahigh-density oxide nanoelectronic memory and logic elements. However, a prerequisite for the development of these new technologies is the integration with existing semiconductor electronic platforms. Park et al. demonstrated room-temperature conductivity switching of 2DEG nanowires formed at atomically sharp LAO/STO heterointerface grown directly on Si(001) substrates [53]. Epitaxial STO templates were grown on Si(001) substrates by MBE whereas the LAO films were grown by PLD.

1.4 Approaches to achieving epitaxial growth of $SrTiO_3$ on Si(001)

In the previous sections many potential applications of STO/Si(001) stack were described which gives this research area significant technological relevance. This section provides a brief overview of achievements obtained by two different deposition methods (MBE and PLD) in terms of epitaxial growth of STO on Si(001).

To date, MBE has been the most extensively used method for the growth of STO on Si, in particular due to its ability to control the deposition on the atomic level. First epitaxial growth of STO on Si by MBE was reported by Tambo et al. in 1998 [54]. However, growth process they developed is not considered as direct epitaxy of STO on Si due to relatively thick SrO buffer layer (10 nm) which was grown on Si(001) surface first. A significant breakthrough in the direct epitaxial growth of single crystal STO on Si(001) by MBE was achieved by McKee and co-workers [6]. They reported the use of sub-monolayer Sr on clean Si(001) surface as a buffer layer. MBE growth process has been further studied and optimized by several research groups: Schlom's group at Cornell University [55], Ahn's group at Yale University [48], IBM Zürich [56, 57], Motorola [58, 59], Saint-Giron's group at Ecole Centrale de Lyon [60, 61] and Demkov's group at the University of Texas at Austin [62]. The result of such an effort reflected in the achieved crystallinity of STO layer. STO layers with the highest crystallinity exhibit the full width at half maximum (FWHM) of 0.006° in ω direction for the 002 STO reflection [63] which is much lower than that of STO bulk single crystals (0.035°-0.108°). In addition, a MBE process for the epitaxial growth of high quality STO films on Si substrates with diameter up to 8 inch was developed [64, 65]. However, MBE technique has several disadvantages, which makes it an inappropriate tool from the industrial point of view. MBE deposition process is based on thermal evaporation of elemental sources under ultrahigh vacuum conditions where the flux of the atomic beam is controlled by the temperature of the crucible in the effusion cell. The flux is directly related to the vapor pressure of the element to be evaporated. The problem arises when materials containing metals with low vapor pressure need to be deposited. Many complex oxides can be considered as such materials because they typically

consist of at least one transition metal element. Because of the low vapor pressure of many of the transition metals, it is challenging to evaporate these with sufficient flux and flux stability. As a result of low fluxes the MBE deposition is very slow. Low growth rates severely limit practically achievable film thicknesses needed for film characterization and in device structures. This is the case for titanium for which effusion cell that can be operated at temperature close to 2000 °C needs to be used. Despite such a high temperature, the Ti flux is still relatively low [66-68]. For elements having insufficient vapor pressure one can utilize an electron beam evaporator. However, this kind of source has a poor flux stability which affects run to run reproducibility [68, 69]. Another concern is related to compatibility between the material to be evaporated and the crucible material. These two materials must not react at the temperature of evaporation. For multi-cation oxides such as the perovskite oxides, an additional difficulty is to get the two metal fluxes to match in order to obtain the correct phase with the correct stoichiometry [70]. Therefore, measurement of fluxes is a critical concern in MBE growth since a poorly calibrated metal fluxes result in the formation of secondary phases. Flux monitoring is performed by using a quartz crystal microbalance, a nude ion gauge or atomic absorption spectroscopy. The first two methods are typically accurate to about 5 %, which might not be sufficient for certain applications. Measuring flux by means of atomic absorption spectroscopy is a more accurate method (accuracy < 1 %) [71].

Thus, alternative manufacturing routes are required. In this PhD thesis focus is placed on the possibilities of using the PLD technique for the synthesis of an epitaxial STO layer on Si(001). PLD is one of the well-established physical vapor deposition techniques that in the past decade has also been directed towards the field of large-area deposition. It is anticipated that PLD will continue to mature and become an industrial process, like sputtering, over the next few years [72]. In addition, it has been shown in terms of thermal conductivity measurements that the crystalline quality of epitaxial oxide layers deposited using PLD can be analogous to layers deposited using the MBE method [73].

The epitaxial growth of STO on Si(001) is far from straightforward. Before the growth of STO is initiated, the native SiO_2 layer has to be removed from the Si surface since its amorphous structure prevents the epitaxial growth of the deposited material. The resulting reconstructed Si surface is extremely reactive and high quality epitaxial growth is not possible because STO reacts with Si in the initial stage of the film growth to form an amorphous transition layer at the interface before epitaxy occurs. Therefore, an appropriate buffer layer should be used that prevents Si from being oxidized. This buffer layer must be thermodynamically stable with Si and should also structurally match with Si as well as STO. Table 1.1 gives an overview of materials used as buffer layers when PLD was used for the STO deposition.

Table 1.1: Survey of buffer layers that have been used for the growth of $SrTiO_3$ on Si(001) using the PLD technique.

Buffer layer	Reference	Buffer layer	Reference
without buffer	[74-78]	$YSZ/Y_2O_3/YBa_2Cu_3O_7$	[75]
YSZ	[79]	$CoSi_2$	[75]
YSZ/TiN	[79]	CaF_2	[75]
TiN	[80-93]	H-terminated Si	[94]
YSZ/CeO_2	[79, 95, 96]	SrO	[75, 94, 97]
CeO_2	[75]	Sr	[98-100]
$Ce_{0.12}Zr_{0.88}O_2$	[101]		

When STO is deposited on Si(001) without any buffer layer, preferentially oriented or textured films are commonly obtained [74, 75]. Sánchez et al. [74] demonstrated that the intensity ratio between (002) and (110) STO peaks can be tuned with oxygen pressure and temperature. However, throughout the whole range of investigated pressures (10^{-5}-10^{-3} mbar) and temperatures (400-750 °C) samples exhibited more than one out-of-plane orientation. There are reports of one group from the University of Hong Kong that stand out from all other publications [76-78]. They showed epitaxial integration of STO layer on Si(100) without use of any buffer layer. The films exhibited out-of-plane relationship of STO(110)$\|$Si(100) and in-plane relationship of STO[001]$\|$Si[001]. From the generally accepted fact that the lattice mismatch between the substrate and the growing film should be lower than several percent in order to succeed in the epitaxial growth, such results appear to be controversial since the lattice mismatch along Si[001] for as-oriented STO film is very large (28 %). Despite the achieved epitaxial growth the crystallinity of their films is relatively low. The XRD rocking curve displays a full width at half maximum (FWHM) of 1.6° for the (110) peak of the STO which is not good enough for further epitaxial growth of other functional oxides.

All other PLD approaches are based on using epitaxial buffer layers which are presented in Table 1.1. The best reported properties correspond to STO films deposited on TiN buffer layer. The narrowest FWHM of ω-rocking curve measured on STO(002) reflection for STO films grown on epitaxial TiN/Si(100) was 0.8° [83]. Another relatively often used buffer layer is yittria-stabilized zirconia (YSZ)/CeO_2. YSZ has an advantage that can be deposited directly on natively oxidized Si(001) substrate because it activates the decomposition of the native SiO_2 to SiO [102]. The reducing atmosphere in the initial stage of growth promotes the reaction $Zr + 2SiO_2 \rightarrow ZrO_2 + 2SiO$. Once the amorphous SiO_2 layer is removed, YSZ grows epitaxially with the out-of-plane and in-plane epitaxial relationship of YSZ(001)||Si(001) and YSZ(100)||Si(100), respectively [103]. STO films deposited on YSZ/Si(001) are (0hh) oriented. In order to change the STO growth direction to (001), additional layer of CeO_2 needs to be deposited on YSZ. Rocking curves of the (002) peak of STO grown on YSZ/CeO_2 double buffer layer are around 1.2° wide [79].

However, based on a number of MBE studies from the last two decades, Si surface passivated with 1/2 ML of metallic Sr represents the most suitable buffer layer in terms of achieved crystallinity, which procedure has not been determined for PLD method yet. As already mentioned above, the FWHM as low as 0.006° was achieved when sub-monolayer Sr coverage was used as a buffer layer [63]. To the best of our knowledge to date only one research group used elemental Sr for the preparation of buffer layer in the PLD process of STO growth on Si(001) [85, 98, 99]. In their investigations a relatively thick Sr layer (1.2-1.9 nm) was deposited on Si(001) surface free of native SiO_2 prior to STO deposition.

Aim and Hypothesis

2.1 Aim

The main purpose of the dissertation is to establish synthesis route for the epitaxial growth of $SrTiO_3$ layer on Si using pulsed-laser deposition technique, which would serve as an excellent template layer that enables various functional oxide thin films to be integrated in the epitaxial form with silicon substrates.

The goals of the thesis are classified as follows:

- Setting up the equipment for pulsed-laser deposition needed for investigation of subjects discussed in this thesis.

- The examination of thermal and Sr-induced deoxidation processes for elimination of native SiO_2 from the Si surface with the aim to prepare surface appropriate for further deposition of buffer layer.

- The investigation of the problem related to carbon contamination on Si surface. The determination of efficient cleaning procedure which is based primarily on *in-situ* dry treatments.

- The study of different surface reconstructions formed due to the ordering of the Sr atoms on the Si(001) surface at elevated temperatures.

- The preparation of the buffer layer on clean reconstructed Si(001) surface based on 1/2 ML of Sr coverage.

- The determination of the experimental conditions for the epitaxial growth of $SrTiO_3$ on Si(001) with a focus on very critical initial parameters for $SrTiO_3$ deposition.

- The investigation of the interface between $SrTiO_3$ and Si and the detailed HR-XRD examination of the final epitaxial $SrTiO_3$ layers on Si.

2.2 Hypothesis

In this dissertation I focused on the possibilities of using the PLD technique for the synthesis of an epitaxial STO layer on silicon, enabled by a 1/2 ML strontium buffer layer. So far, there have been several reports on the successful epitaxial growth of $SrTiO_3$ on Si

substrates using the MBE technique. However, deposition process with MBE is close to thermodynamic equilibrium and therefore very slow and sensitive to deposition conditions, which makes it an inappropriate tool from the industrial point of view. On the other hand, processes with PLD technique are far from the thermodynamic equilibrium, making small changes in experimental conditions insignificant for the properties of plasma which forms as a result of interaction between ultraviolet laser pulse and target material. Deposition performed by PLD is much faster, wherein the quality of as deposited thin layers can be comparable to layers synthesized by MBE. Furthermore, our uniquely designed PLD system allows studies in ultra-high vacuum conditions, very accurate gas flow control using the needle valve, infrared laser heating of substrate up to the temperature of 1200 °C in a very short time and *in-situ* RHEED monitoring of surface structure during deposition. In addition, glove-box connected to the PLD system enables us to use reactive targets, e.g. elemental Sr, which is essential for carrying out such experiments. Based on the described advantages it is expected that PLD provides the ability to prepare Si surface passivated with 1/2 ML of metallic Sr, which represents the most suitable buffer layer based on a number of MBE studies from the last two decades. And most importantly, it is anticipated that by careful selection of deposition conditions, $SrTiO_3$ can be grown epitaxially on as-prepared silicon surface.

Materials and Methods

3.1 Materials

Silicon was used as a substrate for thin film deposition. Silicon wafers (Si-Mat, Germany) with a diameter of 200 mm were cut into substrates of 5×5 mm. The substrates were boron doped (p-type with resistivity of 1-30 Ωcm) single side polished with the thickness of 525 μm. The termination plane of the substrates was (001). The wafers were cut with an accuracy of ±0.1° along that crystal plane. For initial cleaning of substrates acetone and ethanol were used. Afterwards, the substrate was mounted on stainless steel sample plate or special tantalum sample holder. When the stainless steel sample plate was used, substrates were pasted to it with a silver paint (Leitsilber 200 Silver Paint, Ted Pella, USA). By using the silver paint a good temperature uniformity across the surface area is achieved. However, in majority of experiments substrates were clamped to a custom-build holder made out of tantalum where the silver paste was not applied. For the deoxidation and buffer layer preparation purposes target of elemental strontium with purity of 99.9 % (MaTecK, Germany) was used. Due to the high reactivity of strontium, the target was stored in the glove box when not used in the PLD chamber. As a source for $SrTiO_3$ material for thin film deposition single-crystal $SrTiO_3$ target was used (Plasmaterials, USA). The selection of single-crystal target instead of polycrystalline was based on investigation showing that a great improvement of surface quality was achieved by using the single-crystal target as a consequence of greatly reduced large particles formation [104]. Deposition of these large particles has a negative influence on the epitaxial growth and should be avoided. Targets were pasted to stainless steel target plates using base resin and hardener in an appropriate ratio, both suitable for high vacuum applications. SiC papers were used for grinding the surface of targets to prepare fresh surface for ablation.

3.2 Methods

3.2.1 Synthesis method

3.2.1.1 Pulsed-laser deposition

First demonstration of laser deposition was carried out right after the invention of high-power pulsed laser sources in the 1960s [105, 106]. Not many experiments were done in the next two decades until the discovery of the perovskite high-temperature superconductors (HTS) in 1986 [107] when the pulsed-laser deposition (PLD) technique suddenly became popularized. Relatively complex chemical composition of HTS materials (multiple cations) makes the growth especially challenging. PLD proved to be very successful in growing

stoichiometric films leading to the increased interest in this technique. Today, PLD is used in the deposition of insulators, semiconductors, metals, polymers, and even biological materials. In the past decade PLD has also been directed towards the field of large-area deposition. Recently, large-area PLD systems became available which are capable to grow thin films on wafers up to 200 mm in diameter (SolMateS and Picodeon companies). It is anticipated that PLD will continue to mature and become an industrial process, like sputtering and evaporation, over the next few years [72]. Figure 3.1 shows the comparison of research and development (R&D) system and large-scale industrial deposition system.

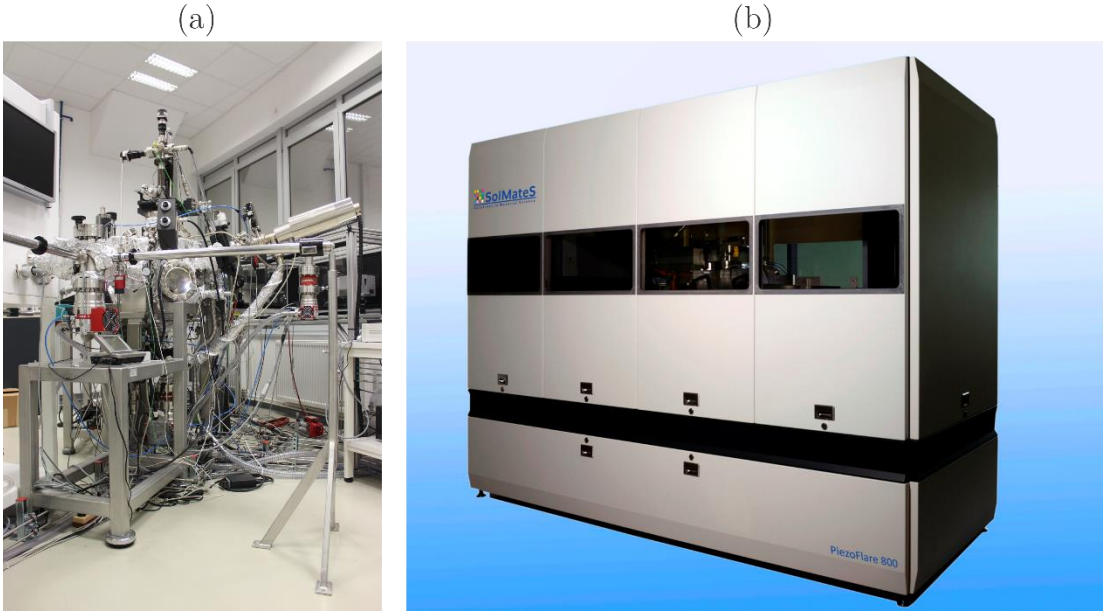


Figure 3.1: (a) Academic PLD system at the Jožef Stefan Institute (Advanced Materials Department) and (b) SolMates PLD production platform.

PLD belongs to the group of physical vapor deposition processes. The experimental setup consists of a target holder and a substrate holder housed in a vacuum chamber and a high-power laser which is decoupled from the vacuum system. As shown schematically in Figure 3.2, a pulsed laser is directed through a quartz viewport onto a target of the material to be deposited. Between the laser and the growth chamber are optical elements that are used for steering and focusing the laser beam. Interaction of high energy laser pulse with target material is a very complex physical phenomenon that causes vaporization (ablation) of a small amount of target material. Vapor which is formed in front of the target at the early stage of the laser pulse absorbs the energy of the remaining laser pulse, causing the increase of temperature and pressure of vapor. This results in partial ionization of species in the vapor and plasma is formed. Plasma then expands from the target surface towards the substrate positioned directly opposite to the target and the material is deposited onto the substrate surface. For multicomponent inorganics ablation, conditions are chosen so that the ablation plume consists primarily of atomic, diatomic, and other low-mass species, which is typically achieved by selecting an ultraviolet (UV) laser wavelength and nanosecond pulse duration. Most materials used for deposition exhibit strong absorption in UV spectral range. For the realization of stoichiometric transfer, selection of the laser energy density (fluence, J/cm^2) is the most critical. If the laser fluence is too low, the target is simply heated by the laser pulse and the composition of the ejected material from a multicomponent target is determined by the vapor pressures of the constituents. Therefore, the laser fluence should be high enough that the ablation threshold

is exceeded, resulting in vaporization that is not dependent on the vapor pressures of the constituent cations.

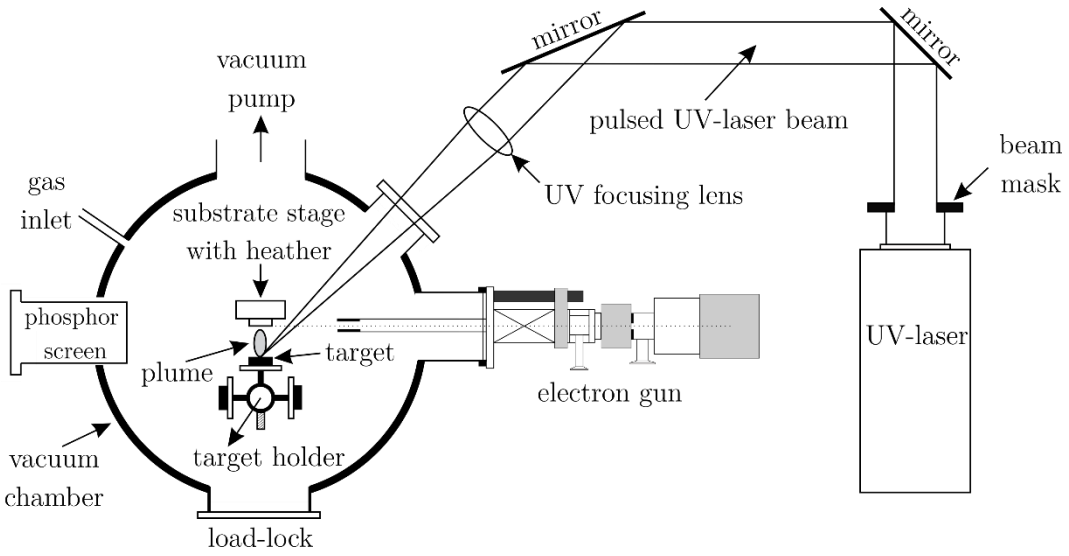


Figure 3.2: A schematic illustration of a pulsed laser deposition system.

The kinetic energy of particles in the plume can be as high as several hundred eV [108] when deposition in vacuum is performed. Since such a high-energetic species can cause implantation and sputter damage, the kinetic energy of particles is generally attenuated before they reach the substrate by using a background gas. In addition to thermalization of the ablated species, the background gas can also be used in the chemistry of the film growth. The formation of multication thin-film materials often requires a reactive species (e.g., molecular oxygen for oxides) as a component of the flux. Thus, the film growth can be carried out in an inert or reactive environment containing any kind of gas. The sample is usually heated during the deposition process in order to allow the film to crystallize. When considering the growth speed, one has to distinguish between the deposition rate per laser pulse and the average growth speed. The amount of material supplied per laser pulse depends on multiple factors, including target-substrate distance, type and pressure of the background gas, laser spot size and laser energy density. The deposition rate per laser pulse can range from 0.001 to 1 Å per pulse. The average growth speed on the other hand is given in nm/second and is additionally controlled with the laser repetition rate (frequency of pulses).

3.2.1.2 PLD set-up

In the experiments performed within the scope of this PhD thesis, a custom-made PLD system (TSST, the Netherlands) and KrF excimer laser (Coherent COMPexPro 205, USA), which is a gas laser system, were used. Such a laser produces a pulsed beam with a wavelength of 248 nm and pulse duration of 20 ns. The maximum pulse energy and repetition rate are 700 mJ and 50 Hz, respectively. Between the output port of the laser and the laser window of the deposition chamber several optical elements are placed, such as beam attenuator, mask, mirrors and lens. A reflection-type variable attenuator system was used to control the laser beam energy without changing the discharge voltage of the excimer laser. In excimer lasers, a change in the discharge voltage changes not only the output laser energy but also the beam divergence angle, thus significantly changing the

energy density on the target surface [109]. A through-chamber laser-energy measurement path allowed us to determine the exact energy on the target surface independent of the laser entrance viewport contamination or other losses in the optical path. A beam mask was used to select only the homogeneous part of the laser beam that was then focused by the lens on the target to achieve the required energy density for ablation. The targets were mounted on a multi-target carousel allowing several materials to be loaded at the same time. In-situ target exchange is possible just by rotating the target carousel. Multi-layer films of the different materials can then be easily fabricated by rotating the carousel so that the laser hits the appropriate target. The use of turbomolecular pump in combination with an ion pump and titanium sublimation pump allowed us to work in very high vacuums, reaching already into the UHV range after extensive system bake-out. Several different background gasses could be used during the growth: oxygen (purity 5.5), nitrogen (purity 5.0) and argon (purity 6.0). Another advantage of the system is the ability to use a background gas over a wide pressure range, from UHV to 1 bar. When very small pressures were required (from UHV to 10^{-3} mbar), the gas flow was regulated by a needle valve. For larger pressures, mass flow controllers were directly applied. Samples and targets were transferred in and out of the deposition chamber through the load-lock chamber that can be pumped and vented without affecting the main chamber vacuum. This results in keeping the growth chamber clean from water vapor and other contaminants, as well as increasing sample throughput. As briefly mentioned already in the Materials section, glove-box was connected to the load-lock chamber in order to be able to work with reactive targets (Figure 3.3). The glove-box served as a place from where the reactive targets were transferred into the load-lock without exposing them to the air.

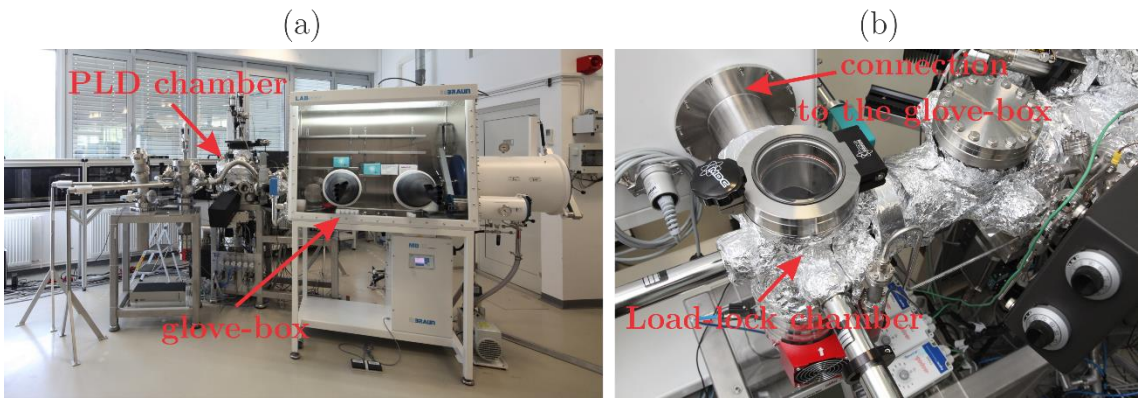


Figure 3.3: (a) Photograph of the PLD system coupled with the glove-box. (b) One part of the load-lock chamber extends into the glove-box.

The PLD system allowed us to heat the sample during the synthesis either resistively or using an infrared (IR) laser, working at the wavelength of 800-820 nm. During the resistive heating the temperature was measured by the thermocouple, while the pyrometer, operating in the spectral range of 1.45-1.8 μm, was used when the laser heating was applied. For the temperature calculation emissivity of 0.85 was used during the investigation of SiO_2 layer elimination and Sr buffer layer preparation. When the deposition of $SrTiO_3$ layer was studied, the emissivity value was changed to 0.30. Another important feature of the PLD system used in our investigation is the reflection high-energy electron diffraction (RHEED) technique (Staib Instruments, Germany), *in-situ* coupled with the deposition chamber. More information about this technique, relevant for understanding of results and discussion part of the thesis, are given in section 3.2.2.1.

3.2.1.3 Experimental procedure

Silicon substrates were ultrasonically cleaned for 10 min in acetone in order to remove organic contaminants, rinsed with absolute ethanol and pasted or clamped to the holder. As-prepared sample was inserted into the load-lock chamber which was pumped down for at least 20 min before the valve separating the deposition and load-lock chamber was opened. In the majority of experiments the substrate was prebaked at 630 °C for around 12 h. Despite the storage of Sr target in the glove-box, where both, oxygen and water vapor, were kept at the concentration level lower than 0.5 ppm, the target was resurfaced each time prior to insertion into the PLD chamber. In addition, Sr and $SrTiO_3$ targets were pre-ablated in order to ensure a completely clean surface for the final ablation. To reduce uneven target erosion during the ablation process, the target was scanning. Fine tuning of the UV laser energy was performed using the beam attenuator just before the deposition started. In all the experiments the target-substrate distance was kept constant at 55 mm.

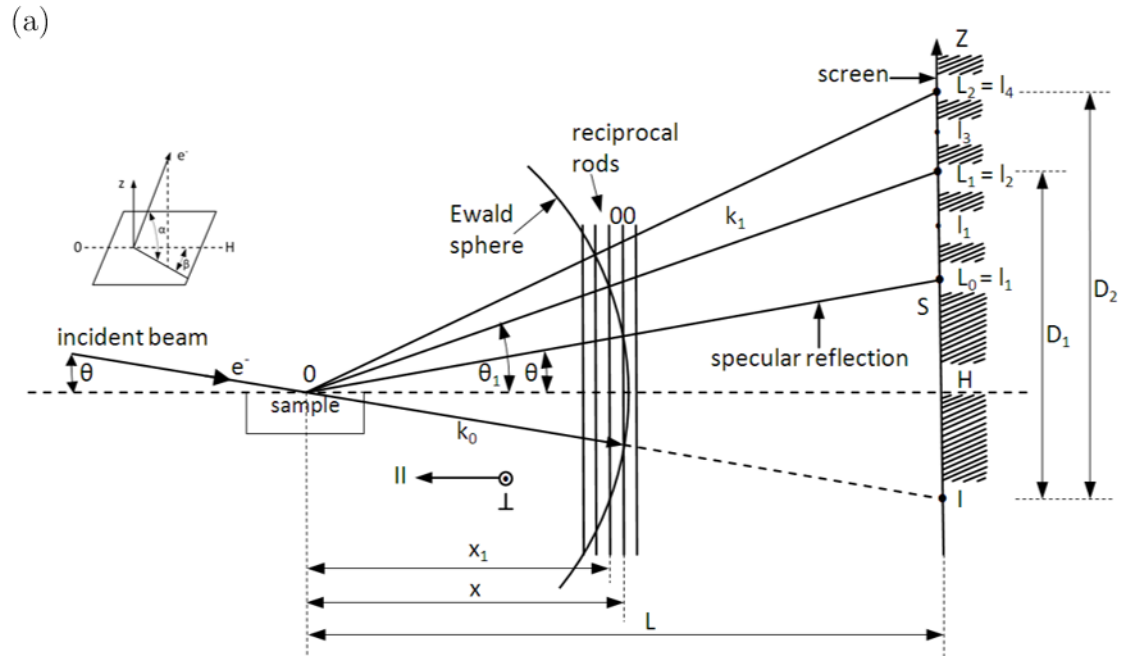
3.2.2 Methods for characterization of materials

In this section analysis techniques that are relevant for understanding the results presented in this thesis are presented. There are three techniques that were extensively used in this study and are therefore described more in detail compared to other techniques. The first technique is RHEED which relates to all the objectives of this thesis. For the investigation of different surface deoxidation processes, problems related to carbon contamination and Sr buffer layer preparation only the use of *in-situ* characterization techniques is appropriate since the sample surface changes (oxidizes) readily when it is exposed to the air. More attention is given also to X-ray reflectivity (XRR) which enabled us determination of very critical parameters for initial STO deposition and HR-XRD by which detailed structural characterization of the final single-crystal layers was performed.

3.2.2.1 Reflection high-energy electron diffraction

Reflection high-energy electron diffraction (RHEED) is an important tool in surface as well as in thin film science because it provides us comprehensive information about the surface structure and thin film growth. RHEED is ideally suited to thin film deposition techniques, like PLD or MBE, because the geometry of the setup does not interfere with the deposition which allows *in-situ* monitoring of surface structure changes during the deposition. Electrons generated by an electron gun are accelerated and directed at low angle of incidence (0.1-5°) to the surface. In our investigation energy of 30 keV was used corresponding to the wavelength of 0.069 Å (with relativistic correction). This energy is sufficient for electrons to penetrate any material for several hundreds of nanometers. However, due to a grazing angle of incidence, the electrons only interact with the topmost layer of atoms (0.5-2 nm) at the surface. The effective penetration depth varies with incident angle as well as with azimuthal angle. In the case of silicon the penetration depth is in a range from 5 to 10 Å for different azimuthal angles at 10 keV and 1.72° incidence angle [110]. There are several interaction phenomena taking place at the sample surface which contribute to the signal detected by a phosphorescent screen. Incident electron beam is partially reflected. Reflections that undergo scattering (diffuse reflections) contribute to the background signal while the unscattered reflections (specular reflections) form the specular or reflected spot in the RHEED pattern. The intensity of the specular spot is related to step density on the sample surface which enables the determination of growth rate in the case of layer-by-layer or two-dimensional (2D) growth mode. During the 2D nucleation and growth, the surface is periodically roughened and smoothened, resulting in a periodically varying density of surface steps. Electrons are easily scattered out of the

specular beam by the step edges since the layer thickness is much larger than the wavelength of the electrons. As a result, periodic intensity variations are obtained during 2D growth where every oscillation represents the growth of exactly one unit cell thick layer. If the growth mode changes to step-flow, intensity oscillations are no longer present. Another feature often observed in RHEED patterns are Kikuchi lines which are formed by electrons that have been inelastically scattered by the crystal. The advantage of these features is that they move with the crystal when it is rotated. From a very practical point of view, even changes in angle much less than one degree will noticeably move the lines, which allows one to set the crystal azimuth along a symmetry direction by adjusting for a symmetric Kikuchi pattern. However, in our investigation diffraction phenomenon was exploited mostly. In order to be able to understand and interpret RHEED diffraction patterns, concept of Fourier transformation from real to reciprocal lattice and Ewald sphere construction have to be introduced first. As already mentioned, in RHEED case, only the top few atomic layers of a crystal contribute to diffraction signal. The interacting crystal structure can therefore be described with two-dimensional real lattice, for which the periodic part extending into the z direction (normal to the surface) is neglected. The infinitive dimension in the x-y plane results in reciprocal points within the plane having zero dimension, while the small depth of the slab results in near-continuous reciprocal rods extending into the ±z direction. Figure 3.4 shows the diffraction geometry of RHEED, where the incident and diffracted electron beams are presented as wave vectors k_0 and k_1, respectively. Both wave vectors have a common origin in the center of the Ewald's sphere and the origin of the reciprocal lattice is located on the surface of the sphere at the end of k_0.



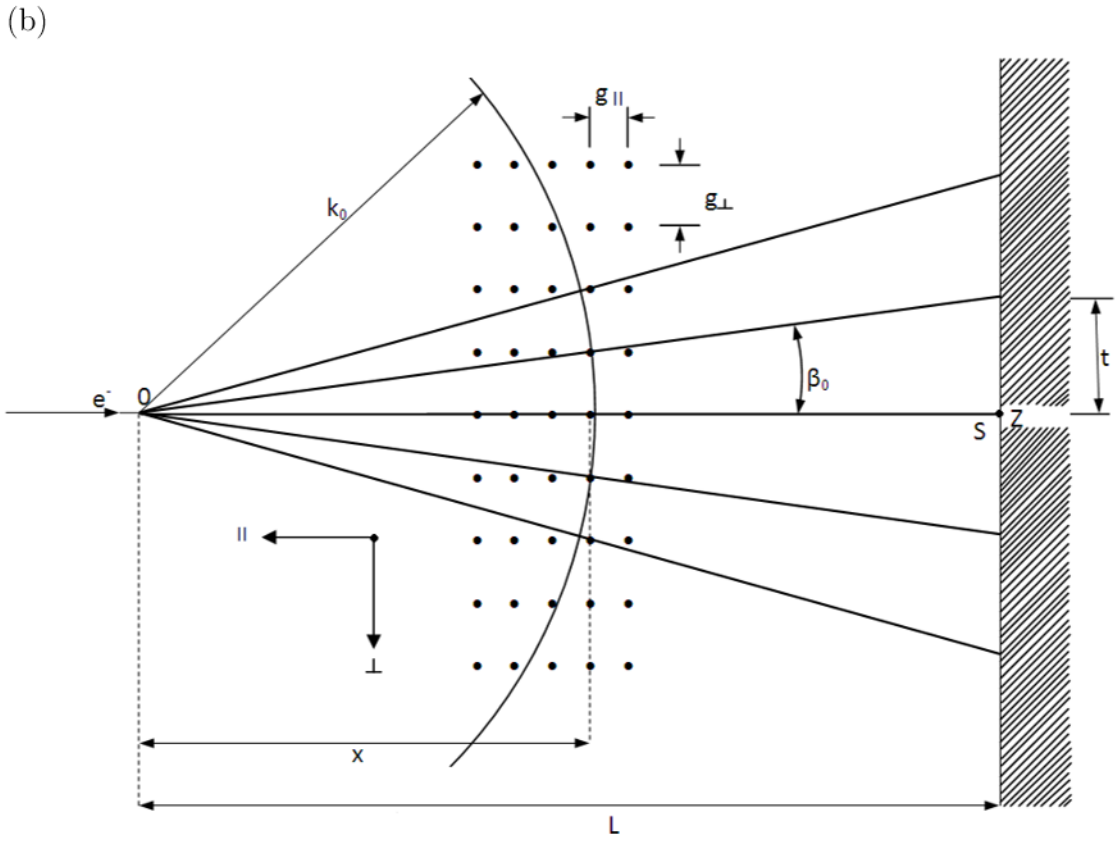


Figure 3.4: (a) Side view and (b) top view of the Ewald's sphere with radius k_0 cutting into the surface reciprocal rods, leading to a diffraction pattern [111].

Diffracted beams appear only in certain directions, pointing from the center of the Ewald's sphere through the points where the sphere intersects with reciprocal lattice rods. The Ewald's sphere intersects all the rods within the projection of the sphere onto the surface. Which diffraction spots are seen on the RHEED screen depends on the size of the screen and the distance from the screen to the point of incidence. The diffraction spots occur on the so-called Laue circles of radius L_n or l_n centered at H. Frequently, the diffraction spots seen on the screen are due to only one row of rods forming the zeroth Laue ring. The rows of rods along the direction perpendicular to the incident beam are called the Laue zones of rods. The zeroth zone includes the rod with the origin of the reciprocal lattice. Due to the high electron energy, used in RHEED, the Ewald's sphere (radius = $k_0 = 1/\lambda$) is very large compared to the reciprocal lattice spacing of oxide crystals. Therefore not only the (00) rod will touch the sphere but also a few rods at both sides of the (00) rod. From the geometrical representation in Figures 3.4a and b the separation of the reciprocal lattice rods can be obtained:

$$g_\perp = \frac{k_0}{\sqrt{(L/t)^2 + 1}} \tag{3.1}$$

$$ng_{\perp} = \frac{k_0}{\sqrt{(L/nt)^2 + 1}} \tag{3.2}$$

$$g_{\parallel} = k_0 \cdot \left(cos\theta - \frac{1}{\sqrt{\left(\frac{D_1}{L} - tan\theta\right)^2 + 1}} \right) \tag{3.3}$$

$$ng_{\parallel} = k_0 \cdot \left(cos\theta - \frac{1}{\sqrt{\left(\frac{L_n}{L}\right)^2 + 1}} \right) = k_0 \cdot \left(cos\theta - \frac{1}{\sqrt{\left(\frac{D_n}{L} - tan\theta\right)^2 + 1}} \right) \tag{3.4}$$

For small angles β (t≪L) the Equation (3.1) can be simplified into:

$$g_{\perp} = \frac{t}{L\lambda} \tag{3.5}$$

Working with a fixed energy and geometry configuration, the camera length Lλ can be calibrated with a sample whose lattice constant is well known. From the diffraction streaks/spots spacings on the screen (t) and camera length constant surface lattice parameters of unknown material can be determined using the Equation (3.5).

Diffraction spots which occur on the Laue circles represent a two-dimensional (2D) diffraction pattern. These spots are often elongated into the streaks. This is especially characteristic for zeroth Laue circle where the intersection of the Ewald's sphere with zeroth Laue zone of rods is the most pronounced. However, streaks can appear also on higher order Laue circles as a result of lower crystallinity of surface that reflects in thicker reciprocal lattice rods. By observing the fractional spots/streaks within the Laue circles or additional intermediate Laue circles (denoted with l_1 and l_3 in Figure 3.4a) we can determine the surface reconstruction. If there are islands present on the surface, 2D diffraction pattern changes into 3D pattern called also transmission pattern. In this case the diffraction pattern is a result of electron beam passing through these islands and consists of sharp spots, similar to diffraction pattern obtained by transmission electron microscope. One can easily distinguish 3D diffraction pattern from 2D pattern by changing the incident angle and observing the movement of diffraction spots. 3D spots do not move when the incident angle is changed, whereas the 2D spots do.

3.2.2.2 X-ray photoelectron spectroscopy

The chemical composition of deposited STO thin layers and the types of chemical bonds formed at the STO/Si interface were obtained ex-situ using an XPS system (Physical Electronics, Inc., USA) equipped with a monochromatic AlKα (1486.6 eV) photon source, electrostatic hemispherical energy analyzer and a multichannel electron detection system. The analyzed area was 400 μm in diameter and the take-off angle of emitted photoelectrons

was 45° with respect to the sample surface in all the experiments except for the angular dependent XPS experiment (depth profiling), where the sample was tilted.

The survey spectra were taken in the range of binding energies from 0 to 1200 eV with pass energy of 187.85 eV. The high-resolution narrow scan spectra of Si 2p, Sr 3d, Ti 2p, O 1s and C 1s were acquired with the pass energy of 29.35 eV and 23.50 eV for the composition of STO thin layers and the interface bonding investigation, respectively. Relative sensitivity factors (0.368 for Si 2p, 1.992 for Sr 3d, 2.077 for Ti 2p, 0.733 for O 1s and 0.314 for C 1s) provided by instrument manufacturer were applied to calculate surface concentrations. For the investigation of Ti oxidation state in amorphous STO layers deposited at room temperature, depth-profile analysis was performed by sequential sputtering of the sample with an ion beam. Ion sputtering was conducted with a 3 keV Ar^+ beam rastered over a 3×3 mm^2 area. The XPS analyses were performed each time after a certain number of sputter cycles with one cycle duration of 1 min. The interface bonding characteristics between epitaxial STO layer and Si substrate were obtained based on angular dependent XPS experiment, where the high-resolution spectra at 7 different angles (20°, 30°, 40°, 45°, 50°, 60° and 70°) were measured. In all the experiments where the chemical bonding at the interface was investigated, samples of thickness ~4.5 nm were specifically grown. For the purpose of qualitative and quantitative analysis of XPS spectra MultiPak software version 9.2.0.5 was used.

3.2.2.3 Rutherford backscattering spectroscopy

Stoichiometry of $SrTiO_3$ thin films was quantified using Rutherford backscattering spectroscopy. A beam of monoenergetic ions $^4He^+$ with energy of 2.5 MeV was directed at a target, and the energies of the ions which are scattered backwards were analyzed. Incident and exit (detector) angles were 0° and 10°, respectively, both measured towards the surface normal. The scattering angle θ thus amounted to 170°. Incident beam with diameter of 2 mm and sample-detector distance of 135 mm was used.

An RBS spectrum can provide us information about the composition of the surface layer. Peak areas in the spectrum are a measure of the number of particles scattered by the atoms of different elements present in sample. In addition, known composition of a layer enables us to establish a depth distribution of elements or to measure the layer thickness from the energy of the scattered particles. Since the mass of surface atoms (Sr and Ti from $SrTiO_3$ layer) is considerably higher than the mass of substrate Si atoms, the peaks from surface atoms are expected to be completely resolved and consequently, a high sensitivity is possible.

Simulations of backscattering spectra were performed using the SIMNRA software, version 6.06. Before carrying out the simulation, the model was created, which consists of proposed layers that are present in the synthesized samples. For each layer we defined the number and type of elements present in the layer, their concentrations (areal densities) and the thickness (in atoms/cm^2) of layer. The energy spectrum of the backscattered particles was calculated for the actual experimental conditions and an assumed target composition, after which the target composition was manually altered until the calculated and measured spectra were closely matched.

3.2.2.4 Scanning electron microscopy

The microstructures were examined using scanning electron microscope (SEM, Zeiss ULTRA Plus). The detection of secondary electrons, which are emitted from the top surface, was used to observe the topography of the specimen surface. Accelerating voltage small as 3 kV was applied in order to emphasize the information near the surface of the specimen and to reduce specimen damage. However, smaller accelerating voltage caused

some degradation in resolution. Due to the relatively small thickness of STO layers (< 50 nm), semiconductor nature of the substrate and small accelerating voltage used, no problems related to charging were encountered. Therefore there was no need to perform coating of samples prior to investigation.

3.2.2.5 Atomic force microscopy

In addition to SEM also the atomic force microscope (AFM, VEECO Dimension 3100) was used for topography investigations. Tapping mode was selected as an imaging mode for all the samples. Since the tapping mode is particularly suitable for soft materials, it was proved to be the only appropriate mode also for some of our samples, where the STO layer was extremely soft due to room temperature deposition. It was important to keep a minimum force between a tip and sample in order to avoid problems with image artifacts as a consequence of attached debris to the end of the tip. Silicon probes with reflective aluminum coating were used (model OTESPA, Bruker, Germany).

3.2.2.6 Ellipsometry

For the determination of a thickness of a native SiO_2 we used an auto-nulling imaging ellipsometer Nanofilm EP3SE (Accurion, Germany). The sample (Si substrate) was illuminated with a laser light at a wavelength of $\lambda = 658$ nm. The measurements were performed using a range of incidence angles, varying from 67° to 82° (multiple angle of incidence (MAI) ellipsometry). Measurements were taken at five different regions. Ellipsometry probes modifications of polarization state of the light beam reflected from the sample. From this polarization change two parameters are obtained: $\tan\Psi$, the amplitude ratio of the resolved components of the electric field vector of the reflected light parallel to and perpendicular to the plane of incidence; and Δ, the phase difference of the two components. The determination of the SiO_2 layer thickness was carried out by fitting suitable optical model (isotropic) to the measured quantities Ψ and Δ. For that purpose we used the optical modelling software EP4model (Accurion surface analysis, Germany). For Si substrate and SiO_2 layer complex refractive indices of $N_2 = 3.83 + i0.014$ and $N_1 = 1.456 + i0$ were used, respectively.

3.2.2.7 X-ray reflectivity

Grazing incidence X-ray reflectivity (GIXR) or simply reflectivity is a non-destructive X-ray technique in which the reflectivity curve of a material is measured. A reflectivity curve is a plot of the intensity of specularly reflected X-rays versus the angle of incidence (ω_0), keeping the detector and the X-ray source at the same angle with respect to the surface. The density, the thickness and the roughness of individual layers in a layer stack on a substrate can be quantitatively determined from the reflectivity curve. X-ray reflectivity (XRR) can be applied to any type of sample regardless its crystallinity, which proved to be particularly convenient in our investigations when amorphous STO layers were deposited on Si. In Figure 3.5 simulated reflectivity curves for STO substrate and 30 nm thick STO layer on Si substrate are shown.

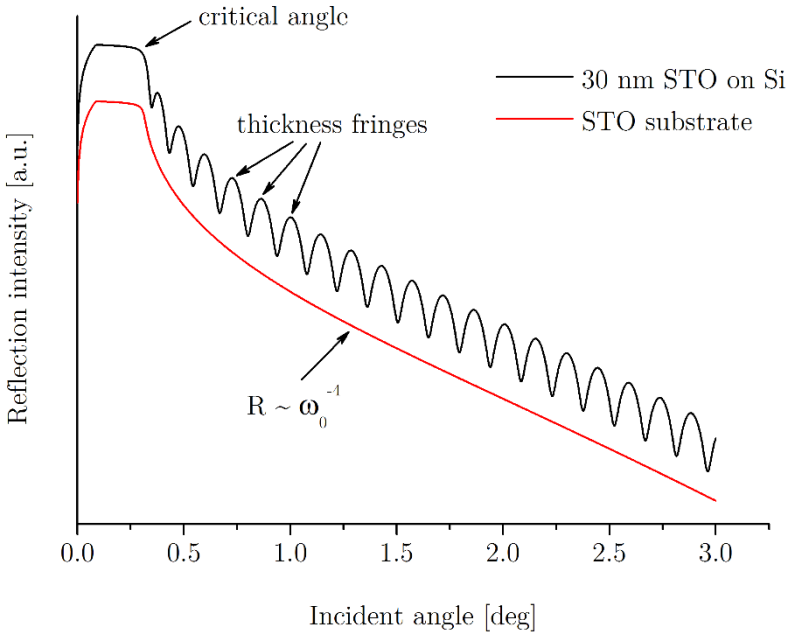


Figure 3.5: Simulated X-ray reflectivity curve of a STO substrate and 30 nm thick STO film grown on Si substrate.

From zero up to the critical angle (ω_c) there is very little intensity absorbed by the material and X-rays are almost totally reflected. The penetration depth of absorbed waves is several nanometers only. Beyond a ω_c, the X-rays penetrate into the sample and the intensity drops drastically, following ω^{-4} (red curve in Figure 3.5). The electron density (ρ_e) of the surface layer determines the position of ω_c. The relation between macroscopic material density (ρ) and ω_c is given by the Equation (3.6):

$$\rho = \frac{\omega_c^2 M \pi}{10^6 r_e \lambda^2 (Z + \Delta f') N_a} \tag{3.6}$$

where:

ρ	. . .	material density [g/cm^3]
ω_c	. . .	critical angle
M	. . .	molar mass [g/mol]
r_e	. . .	electron radius, 2.818×10^{-15} [m]
λ	. . .	wavelength of CuKα, 1.541×10^{-10} [m]
N_a	. . .	Avogadro's number, 6.022×10^{23} [mol^{-1}]
Z	. . .	atomic number
$\Delta f'$	. . .	real dispersion (or Hönl) correction

How accurately the position of critical angle can be defined depends on the nature of the material and the instrument optics. If the electron density is inhomogeneous at the surface due to the surface roughness or the materials involved have a large absorption value, the intensity drop at the critical angle may not be ideally sharp. Instrumental factors such as the wavelength spread and the divergence of the incident beam also affect the sharpness of the critical edge.

The interference of x-rays reflected at the various interfaces in the thin film structure results in the appearance of oscillations in the reflected x-ray intensity (black curve in

Figure 3.5). Angular separation of oscillations, which are called also Kiessig or thickness fringes, is inversely proportional to the thickness value. The overall course of the reflectivity curve also provides information on the surface and interface roughness of the heterostructure. The roughness causes a decrease of intensity received by the detector and contributes to the washing out of sharp fringes.

For quantitative analysis of layer parameters X'Pert Reflectivity software package version 1.3a was used. The thickness analysis was performed using three different approaches: direct method, Fourier method and fitting the measured data. In the direct method the position of the critical angle was entered first and then two neighboring fringes were identified. The method is based on path-length calculations of interference in thin films:

$$d = \frac{\lambda}{2\left[\sqrt{(cos^2\omega_c - cos^2\omega_2)} - \sqrt{(cos^2\omega_c - cos^2\omega_1)}\right]} \tag{3.7}$$

d . . . layer thickness
ω_1, ω_2 . . . angular positions of two adjacent fringes

Normally the results are more accurate if averaging over more adjacent fringes (four, six, eight and so on) is performed. If more fringes are used then the result must be multiplied by the number of fringes used.

The Fourier method presents the Fourier Magnitude versus thickness plot. The input data for this method are the start and end positions of the scan and the critical angle. The obtained results can correspond to separations of all possible pairs of interfaces in the layered samples. Therefore the number of peaks obtained in the Fourier plot can exceed the number of layers in the sample.

Even if the layer thickness can be determined by directly measuring the angular spacing between two thickness fringes (direct method) or by Fourier method, fitting the measured data is the most accurate way to determine all the parameters for each separate layer from the multilayer structure. For that purpose a model corresponding to the expected layer structure was first generated in the simulation software. Based on this model, a reflectivity curve was simulated. The simulated reflectivity curve was then compared with the measured data using a least square method. Fitting was done either manually, where the parameters were changed manually and simulation was repeated for each change, or automatically, where the fitting was performed using a segmented, genetic or combined algorithm.

The optics on the primary (incident) side consisted of Hybride monochromator with 1/32° divergence slit (does not influence the equatorial divergence but the beam height), 0.04 rad Soller slits and beam mask of 2 mm. On the secondary side parallel plate collimator with 0.04 rad Soller slits, automatic beam attenuator and Pixcel detector in open mode were used.

3.2.2.8 X-ray diffraction

3.2.2.8.1 2Theta/Theta scan Symmetric or 2Theta/Theta scan (called also specular scan) with parallel beam geometry was performed for phase analysis and determination of out-of-plane thin film orientation. In such a scan, peaks corresponding to the lattice spacings perpendicular to the sample surface are observed. On the primary side we used a Hybride monochromator with 1/16° divergence slit, beam mask of 2 mm and 0.04 rad Soller

slits. On the secondary side 0.04 rad Soller slits and Pixcel detector in scanning line mode were used. Prior the measurement the three-step alignment procedure was performed. Fist the direct beam was aligned by which the 2θ axis was placed on an absolute scale. Then the ω angle was placed on an absolute scale by performing ω and z scans. At the end we set sample surface plane exactly perpendicular to the diffraction plane on the basis of Chi scan performed at critical angle.

3.2.2.8.2 Phi scan Phi scan was used for the determination of in-plane orientation of STO layer with respect to the Si substrate. The Hybride monochromator with beam mask of 2 mm was used on the primary side, while a fixed antiscatter slit assembly with no antiscatter slit inserted and Pixcel detector were used on the secondary side. In this measurement the sample is rotated for the whole 360° range. X-ray tube is placed in exact ω angle position in which the diffraction condition for asymmetric reflection of interest is fulfilled. 2Theta position of the detector is only approximate and does not need to be set precisely since the detector is used in open mode. Two Phi scans are performed, one for the substrate and the other one for the thin layer. An epitaxial film exhibits peaks at only specific Phi angles that are symmetry related to similar asymmetric peaks from the substrate. Such a measurement requires quite a complex and time consuming alignment steps to be carried out beforehand.

3.2.2.8.3 Rocking curve A rocking curve (RC) is an omega scan or an omega/2Theta scan in both cases with an open detector. The 2θ values of peaks are not measured in this case. In a RC two peaks are usually collected, a substrate peak and a layer peak, from where the angular difference Δω is determined. Δω can consist of three contributions:

$$\Delta\omega = \Delta\theta + \Delta\alpha + \Delta\emptyset \tag{3.8}$$

$\Delta\theta$ . . . Bragg scattering angle (related to d-spacing)
$\Delta\alpha$ . . . rotation of plane due to layer tilt
$\Delta\emptyset$ . . . rotation of plane due to strain

All three effects can be calculated if a sufficient number of symmetric and asymmetric rocking curves is collected. However, for the STO layers on Si, ω RCs were measured only for reciprocal lattice points that correspond to STO layer, since there does not exist any pair of reciprocal points, one corresponding to the substrate and the other one to the layer, which would be close enough (probe size is limited) and with adequate intensity for the measurement. The results from RC measurements served us as a measure for crystal perfection or crystallinity. The Hybride monochromator with 0.04 rad Soller slits and beam mask of 2 mm was used on the primary side, while a fixed antiscatter slit assembly with 0.04 rad Soller slits and Pixcel detector were used on the secondary side.

3.2.2.8.4 Reciprocal space mapping Reciprocal space mapping was performed in order to determine d-spacings, mosaic spread and lateral correlation length. Since the crystallographic tilt is commonly present in epitaxial layers, d-spacings were determined by collecting RSM of two reflections, one symmetric and one asymmetric. RSM of an asymmetric reflection was further used for the calculation of mosaic spread and lateral correlation using Epitaxy software (PANalytical B. V., The Netherlands, Version 4.3a). The hybride monochromator with beam mask of 2 mm was used on the primary side and Pixcel detector with fixed antiscatter slit assembly (no antiscatter slit inserted) was used on the secondary side. Divergence slit size (defines the beam height) and step size, which

both determine the resolution, were chosen according to the FWHM of the peak in a way that the peak width was not affected by the instrumental resolution.

Results and Discussion

4.1 Cleaning of Silicon Surface [112]

Dimensions of novel semiconductor devices are continuously downscaling and device production becomes more and more sophisticated. When reaching the nanoscale range in thin film synthesis, quality of surface and interface regions become of central importance. High-quality epitaxial growth can only be achieved on atomically clean surfaces. Therefore, our initial studies were focused on cleaning of silicon substrates. To achieve the desired growth quality, organic compounds and the native silicon dioxide need to be removed from the surface. Carbon contamination mainly originates from ambient air and utilized chemicals while the SiO_2 layer covers the Si surface and prevents further oxidation of elemental Si. This top silica layer is amorphous and therefore has to be removed from the surface since the growth process of epitaxial layers must begin not only on carbon free but also crystalline Si surface.

First the thickness of the native SiO_2 layer was determined using the ellipsometer. Measurements of ellipsometric angles, Δ and Ψ, were taken at five different sample areas. Layer thickness was determined by fitting the measured quantities Δ and Ψ, as shown in Figure 4.1.

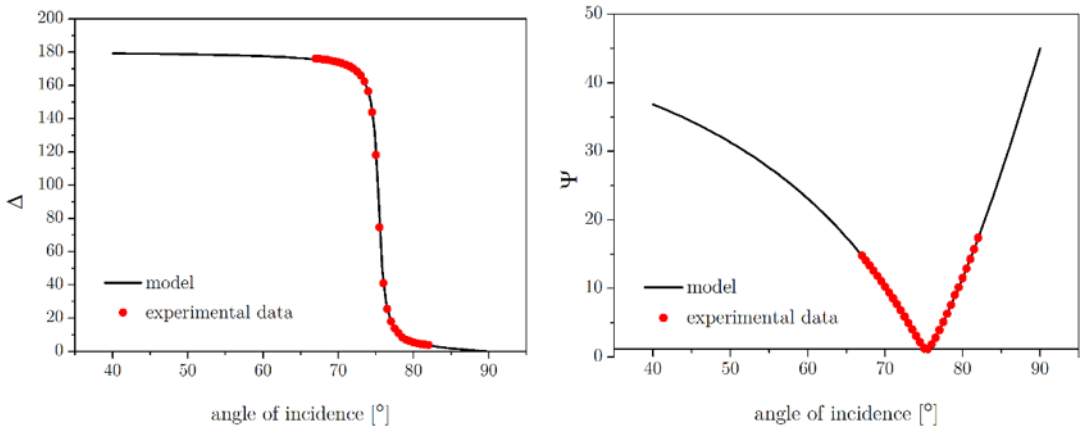


Figure 4.1: Ellipsometric spectra of the silicon substrate (dots) as a function of the incident angle. The lines give the fitting data.

For that purpose an isotropic model corresponding to the expected layer structure was first generated. Since the refractive indices (complex number) of Si and SiO_2 materials are well known, the accuracy of results is expected to be relatively high. The results of obtained

layer thicknesses from different areas on the sample are presented in Table 4.1. Average thickness was calculated to be 2.0 ± 0.2 nm which corresponds to the expected value for the native SiO_2 layer [113].

Table 4.1: SiO_2 layer thicknesses obtained from different areas on the sample surface.

Area on the sample surface	Thickness [nm]
1	2.2
2	1.9
3	1.9
4	2.0
5	2.2

4.1.1 Removal of the native SiO_2 layer

Several processes are known for the removal of oxide layer which can be categorized into two groups: physical and wet chemical processes. Physical processes commonly employed for this purpose are ion sputtering and high-temperature annealing. Sputtering, however, causes entrapment of incident Ar ions and contamination due to the simultaneous sputtering-out of impurities from the sample holder and surroundings. Undesirable radiation damage which is formed at the surface and point defects often remain even after annealing [114]. These secondary effects show that sputtering is not well suited for nanotechnology. We were investigating two oxide removal processes which are both based on high-temperature annealing: thermal and strontium-assisted deoxidation process. RHEED technique was used for the *in-situ* characterization of surface quality after SiO_2 elimination. These results are presented in the following two sections. Wet chemical processes on the other hand are based on using hazardous chemicals, i.e. NH_4OH (ingredient of RCA clean [115]) or hydrofluoric (HF) acid, for etching of the surface. Treatment with HF acid removes the SiO_2 layer and produces an H-terminated silicon surface [116, 117]. However, HF-treated Si(001) surface is microscopically rough and faceted [118] with a tendency to re-oxidize in ambient conditions [98, 119].

4.1.1.1 Thermal deoxidation

In our thermal deoxidation study the Si(001) substrate was first ultrasonically cleaned for 10 min in acetone, in order to remove organic contaminants (residues of the foil covering the substrate). Then the substrate was rinsed with ethanol and dried with a nitrogen gun. The as-prepared sample was loaded into the PLD chamber and prebaked at 630 °C for 12 hours (overnight). Senftleben et al. showed that Si surface is still heavily carbon contaminated after cleaning with organic solvents [114]. Prebaking or thermal degassing of substrates at moderate temperatures causes strong reduction of the carbon contamination due to desorption of organic molecules. Degassing is therefore often applied in UHV experiments as a first step in the growth process. However, it is important that the maximum temperature applied is below the temperature needed for thermal oxide desorption [120]. After the degassing oxide-removal process was investigated by annealing at the temperature between 750 °C and 1200 °C for the time needed for the RHEED pattern exhibiting crystalline Si surface to appear. Lander and Morrison reported that at high temperatures, SiO_2 can be removed via an interfacial reaction [121]:

$$SiO_2(s) + Si(s) = SiO(g)$$

This removal process was proposed to be conducted in four steps. First a silicon monomer has to be produced. Secondly, it has to migrate along the Si surface and, eventually, reacts with SiO_2 to volatile SiO, and finally SiO desorbs [122]. Voids are formed during this process whose size increases with annealing duration, leading to a complete desorption of the oxide [123-126]. Our first thermal deoxidation experiments were performed on silicon substrates Ag-pasted to a resistive-heating sample holder. Figures 4.2a and b show RHEED patterns before and after heating to 860 °C, respectively.

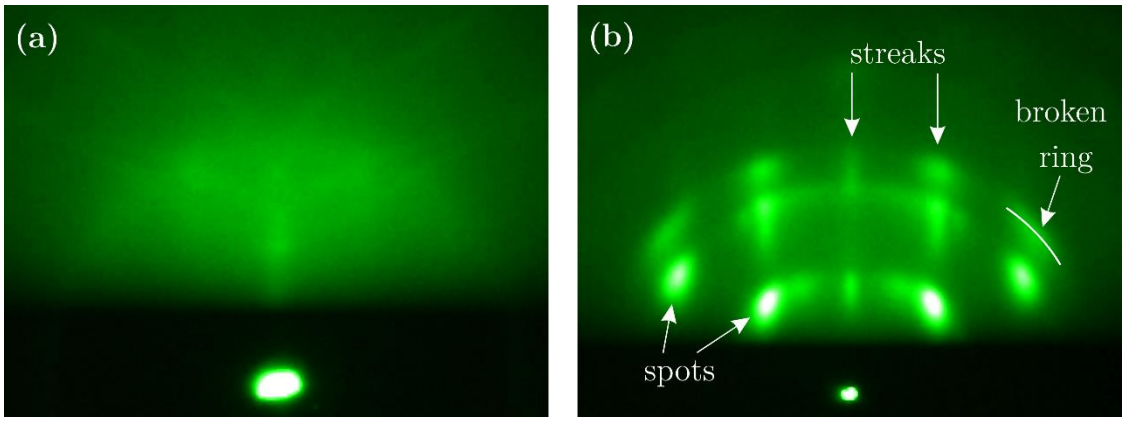


Figure 4.2: RHEED patterns in the [110] azimuth of Si taken after (a) 12-hour prebaking at 630 °C and (b) heating to 860 °C. The experiments were performed using a resistive heater.

Diffuse background in RHEED pattern after 12-hour prebaking is a clear indication that 630 °C is not a high enough temperature for the initiation of deoxidation at the interface. After heating to higher temperature diffuse background gradually evolved into diffraction pattern indicating the removal of amorphous SiO_2 layer and disclosure of crystalline Si surface. However, such a surface was of very poor quality since beside the streaks also the spots and broken rings were observed in the RHEED pattern. Spots are related to islands on the surface while the observation of broken rings is a proof of textured surface. With heating up to 860 °C we reached the temperature limit for the resistive heater. In order to be able to heat silicon substrates to slightly higher temperatures, samples were pasted to stainless steel sample plate and heated with the IR-laser from the back side. By using the maximum power of IR-laser the temperature of 920 °C was achieved. Figure 4.3 shows RHEED patterns in two high-symmetry directions, [110] and [100], after heating the Si substrate to 900 °C. Additional half-order streaks were observed in [110] azimuth direction indicating the reconstructed Si surface, as shown by arrows in Figure 4.3a. Very faint and broad streaks, however, imply only partial surface reconstruction and significant surface disorder, respectively. In [100] direction, in addition to the streaks characteristic for the Si surface, some spots can be observed. These spots are indicated by the arrows in Figure 4.3b and correspond to the β-SiC transmission pattern as a result of carbon contamination on the Si surface [127-129].

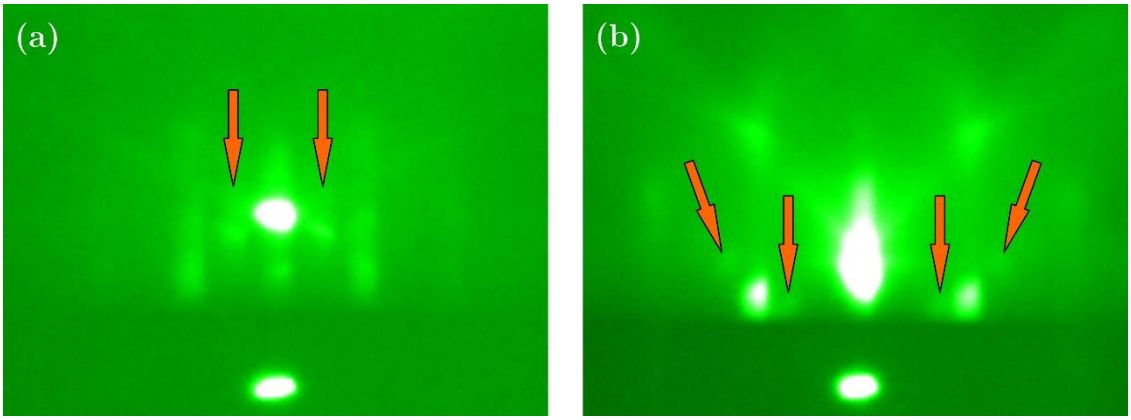


Figure 4.3: RHEED patterns in the (a) [110] and (b) [100] azimuth of Si taken after heating to 900 °C using IR-laser. The sample was pasted to stainless steel sample plate using Ag-paste. The arrows in (a) indicate 1/2-order streaks and in (b) β-SiC transmission pattern.

Using either the resistive heater or the stainless steel sample plate in combination with IR-laser heating, we were unable to prepare highly-ordered Si surface without the presence of carbon contamination. It was very likely that such a disorder on the Si surface was caused by strong outgassing of silver paint during heating, which raised the pressure in the chamber from 10^{-9} mbar into the 10^{-6} mbar range. Ukraintsev et al. studied the influence of metal impurities and stressed the importance of the material of the sample holders [130]. Hata et al. claimed that direct contact of Si substrate to stainless steel should be avoided [131]. Based on those assumptions we decided to design and fabricate a sample holder with a special clamping mechanism out of refractory metal tantalum. This way the sample was not in contact with stainless steel anymore and most importantly, we avoided the use of silver paint for fastening the substrates to the holder. Figure 4.4 shows the latest improved version of the tantalum holder. Sample is placed on the central area of the holder and heated directly from the back side using the IR-laser. Absorption properties of silicon in the spectral range of 1.45-1.8 μm enable heating the substrate to the temperature as high as 1250 °C in just a few seconds.

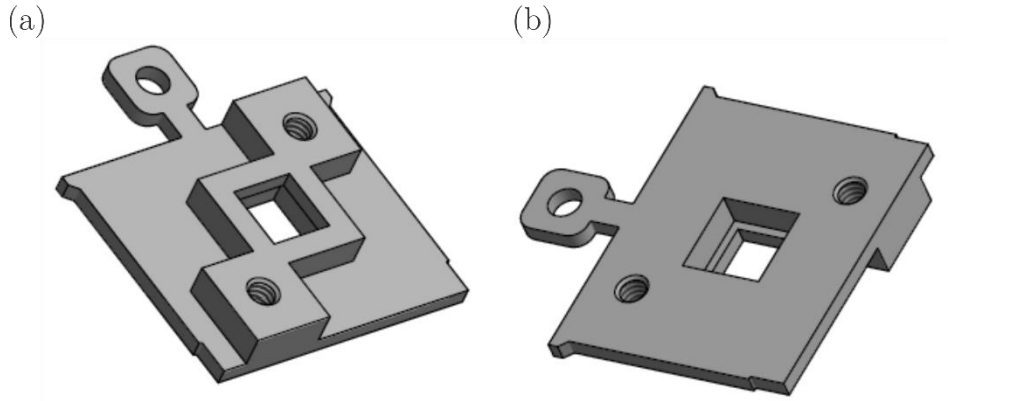


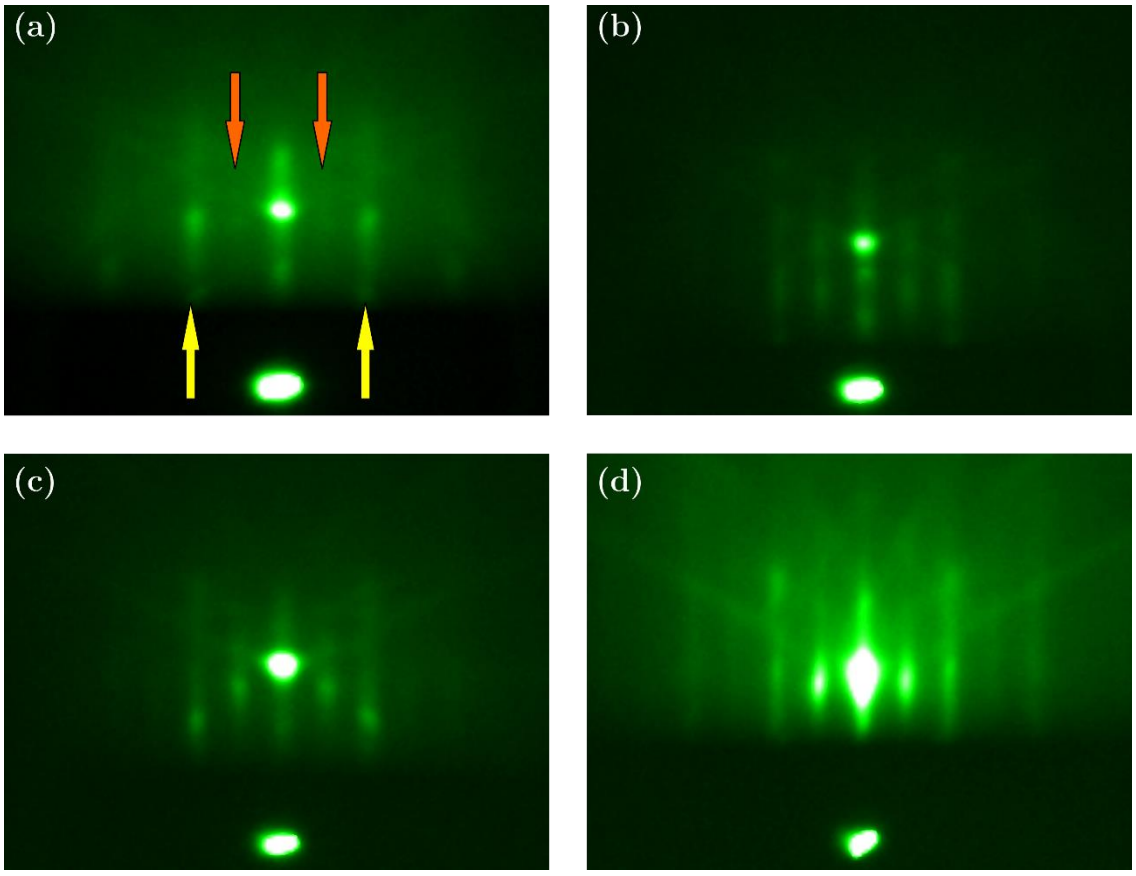
Figure 4.4: Custom-build tantalum holder: (a) front side where the substrate is mounted and (b) rear side for substrate heating.

Using the tantalum holder we investigated the oxide-removal process based on heating of Si substrate to several different temperatures (750, 800, 850, 900 and 1200 °C) after it was prebaked. Special attention was paid to the time needed for the RHEED pattern

showing a diffuse background, corresponding to the SiO_2-covered amorphous surface, to change into a (2×1) pattern, corresponding to a clean, reconstructed Si surface. The origin of each individual line/spot present in the (2×1) pattern is explained in section 4.2.1. At this point only a qualitative description is given.

When the substrate was heated to 750 °C, the RHEED pattern appeared after 45 min, showing 1-order and very faint 1/2-order streaks in the [110] high-symmetry direction (Figure 4.5a). This is a clear indication that 750 °C is a high enough temperature for the interfacial reaction between Si and SiO_2 to be initiated. However, faint 1/2-order streaks indicate an incomplete surface reconstruction under such conditions. The presence of 1/2-order streaks was additionally verified by tilting of the substrate until reaching a position where Kikuchi envelopes cross the Ewald-sphere intersection on the 1/2-order rods which resulted in an enhancement in intensity (Figure 4.5e). Furthermore, intensity modulation along the 1-order streaks indicates a rough surface (Figure 4.5a, yellow arrows).

At 800 °C, the RHEED pattern appears after 5 min, at 850 °C–after 2 min, while at 900 °C–after just 1 min. In addition to a significant influence on the kinetics of SiO_2 layer elimination, temperature also has a major influence on the surface quality. With increasing temperature of the thermal deoxidation, both, the intensity and sharpness of the 1/2-order streaks increase, indicating an improvement in the surface order (Figures 4.5a, b, c and d).



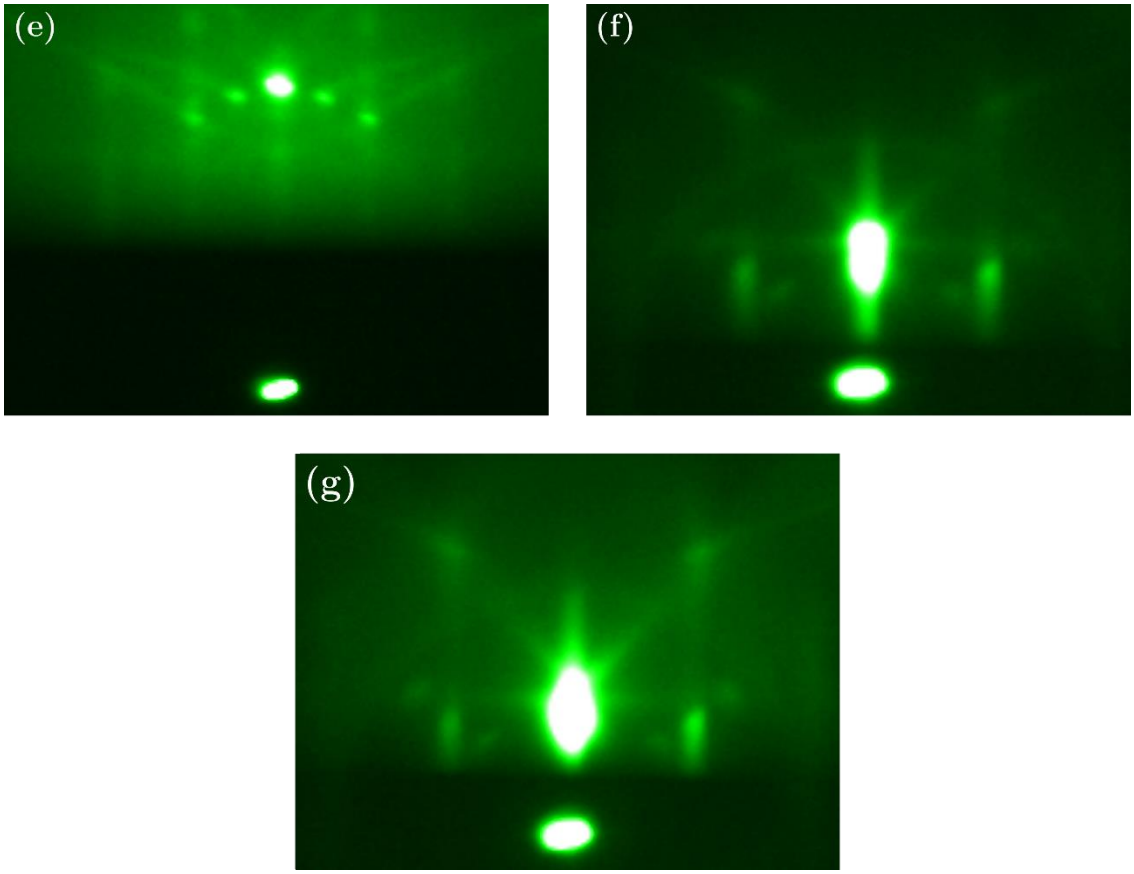


Figure 4.5: RHEED patterns in the [110] azimuth of Si taken after heating to (a) 750 °C, (b) 800 °C, (c) 850 °C, and (d) 900 °C. The arrows pointing up (yellow) and arrows pointing down (orange) indicate 1- and 1/2-order streaks, respectively. (e) RHEED pattern of the same sample as (a) taken at larger incident beam angle. RHEED patterns in the [100] azimuth of Si taken after heating to (f) 850 °C and (g) 900 °C. The samples were mounted to custom-build tantalum holder and heated directly by IR-laser.

For the samples annealed at 850 °C and 900 °C, faint and broad diffraction spots positioned to the outside of the primary silicon streaks, corresponding to the β-SiC islands, were observed in the [100] high-symmetry direction, showing that the use of tantalum holder instead of stainless steel plate did not eliminate surface carbon contamination completely. Nevertheless, a large improvement in surface quality can be noticed when RHEED patterns from the Figure 4.3 are compared to those in Figure 4.5d and g. The reason for this can be primarily ascribed to the avoidance of silver paste. Outgassing to much lower extent was noticed in the experiments where tantalum holder was used. For example, heating from 630 °C to 900 °C raised the background pressure from ~1×10^{-8} mbar to ~2×10^{-8} mbar only. Senftleben et al. showed that carbon contamination in form of β-SiC on Si surface can drastically deteriorate the crystallinity of overgrown layer, leading to the formation of polycrystalline layer instead of epitaxial [132]. Even more effort was thus needed to be invested into the cleaning procedure in order to achieve clean reconstructed Si surface without SiC precipitates on the surface. In surface science flashing (rapid increase of temperature) to the temperature higher than 1100 °C is often applied as a simple way of obtaining a clean and smooth surface. After pre-baking at 630 °C in our experiments, the sample was flashed to 1200 °C for 1.5 min. Figure 4.6 shows RHEED patterns of flash-annealed sample acquired after it was gradually cooled to 700 °C. During the flashing period spots related to β-SiC vanish from the RHEED pattern and only

streaks/spots corresponding to a clean reconstructed Si surface are left. Thus, by flashing at T>1100 °C we succeeded in fabricating clean (free of carbon) and the most ordered Si(001) surface.

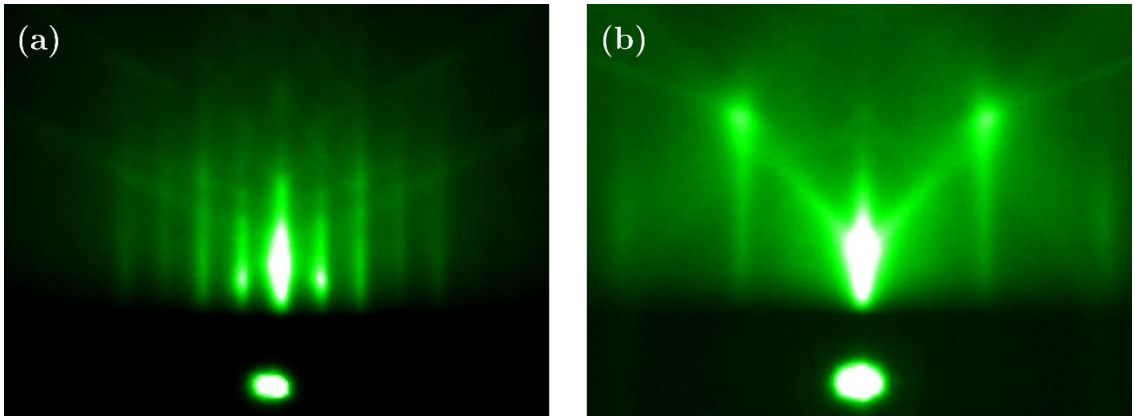


Figure 4.6: RHEED patterns in the (a) [110] and (b) [100] azimuth of Si taken after flashing to 1200 °C, and cooling to 700 °C. The sample was mounted to custom-build tantalum holder and heated directly by IR-laser.

We additionally observed that the RHEED patterns of reconstructed Si surface after flashing exhibited lower quality, which was reflected by either the broad streaks or intensity modulation along the streaks, when tantalum holder was used for the first time or after several days of non-use. The best repeatability was obtained when the experiments were done in series one after the other. Our experience indicated that thorough one or two-days outgassing with a dummy Si sample must be performed within the high vacuum before the newly fabricated holder is sufficiently clean for utilization in high quality Si surface preparation. Hata et al. performed a detailed STM analysis of reconstructed Si surface and claimed that the increase of the vacuum pressure (outgas from the sample holder) during flashing needs to be kept as minimum as possible in order to fabricate a surface with low density of defects [131]. Dependence of the density of defects on vacuum pressure during flashing has also been reported by Ukraintsev and co-workers [133]. Our observations which are based on RHEED experiments showed that the background pressure should not exceed 1×10^{-7} mbar during flashing.

4.1.1.1.1 Carbon contamination behavior on Si(001) surface Thermal budget is one of the most crucial points in modern wafer processing. Cleaning procedure based on flashing to 1200 °C is not viable for industrial applications because of the high temperature involved and limitation to small samples that can be heated and cooled quickly [134]. In addition, high temperature annealing can lead to out-diffusion of dopant boron [135, 136]. The desorption of the native oxide at the temperature of 900 °C would be much more appropriate if the problem related to SiC formation was solved first. By means of XPS examination it was shown that degassing gives rise to significant reduction but not complete elimination of carbon from the surface [114]. Carbon species which are left on the surface could be a source of carbon for SiC formation after further heating. This has led us to hypothesize that organics can be removed from the Si substrate surface using oxygen in PLD chamber (carbon burning). Assmuth reported on successful carbon elimination under appropriate temperature treatment in O_2 ambient [137]. Based on these results different experiments presented in Table 4.2 were conducted in order to verify the hypothesis.

Table 4.2: Experimental conditions for the removal of physisorbed hydrocarbons on Si/SiO_2 by oxygen-bake procedure.

	Step 1	Step 2	Step 3	Step 4
Experiment 1	$p(O_2) = 1\times10^{-5}$ mbar	raise of temperature to 500 °C, waiting for 30 min	12-hour prebaking at 630 °C in vacuum	thermal desorption of oxide at 900 °C in vacuum
Experiment 2	$p(O_2) = 1\times10^{-5}$ mbar	raise of temperature to 600 °C, waiting for 30 min	12-hour prebaking at 630 °C in vacuum	thermal desorption of oxide at 900 °C in vacuum
Experiment 3	$p(O_2) = 1\times10^{-5}$ mbar	raise of temperature to 650 °C, waiting for 30 min	12-hour prebaking at 630 °C in vacuum	thermal desorption of oxide at 900 °C in vacuum
Experiment 4	12-hour prebaking at 630°C in vacuum	cooling to 550 °C	$p(O_2) = 1\times10^{-5}$ mbar, waiting for 30 min	thermal desorption of oxide at 900 °C in vacuum
Experiment 5	$p(O_2) = 1\times10^{-4}$ mbar	raise of temperature to 600 °C, waiting for 30 min	thermal desorption of oxide at 900 °C in vacuum	/
Experiment 6	$p(O_2) = 1\times10^{-4}$ mbar	raise of temperature to 700 °C, waiting for 30 min	thermal desorption of oxide at 900 °C in vacuum	/

In the first three experiments surface was exposed to an O_2 partial pressure of $\sim1\times10^{-5}$ mbar. Then the substrate was heated up to 500 °C, 600 °C and 650 °C in oxygen and kept at these conditions for 30 min in order to burn all organic species that are adsorbed on SiO_2. Afterwards 12-hour prebaking at 630 °C was performed, followed by thermal desorption of native oxide at 900 °C. The effectiveness of cleaning with oxygen was examined by RHEED on a qualitative basis – presence or absence of diffraction spots characteristic for SiC in the RHEED pattern. We were unable to prepare clean Si surface even when temperature of 650 °C (Experiment 3) was used in the carbon burning process. Possible reason could be a recontamination of the substrate from the background gas during the prebaking period. However, no improvement was observed when carbon burning and prebaking processes were switched in experiment 4. In experiments 5 and 6 prebaking was

not implemented at all. Despite higher temperature used in these two experiments, compared to conditions employed by Assmuth [137], RHEED again exhibited SiC transmission pattern superimposed on a (2×1) pattern. This indicates that physisorbed organic species on SiO_2 were either not completely removed from the surface with oxygen bake or they are not the only source of carbon. Carbon could also exist at the Si/SiO_2 interface. Furthermore, it could be buried within the SiO_2 layer where oxygen bake cannot affect it. For better understanding of the problems related to surface carbon contamination, it would be essential to have a good symbiosis of several surface sensitive techniques. In our case, surface carbon contamination was studied indirectly by RHEED after thermal deoxidation. To demonstrate the efficiency of oxygen bake performed at different conditions *in-situ* XPS or AES analysis would be necessary.

So far, carbon contamination was referred to additional diffraction spots observed in [100] direction after thermal deoxidation. However, very weak β-SiC transmission pattern could also be observed in [110] direction when the incident angle of the RHEED beam was very shallow (Figure 4.7a).

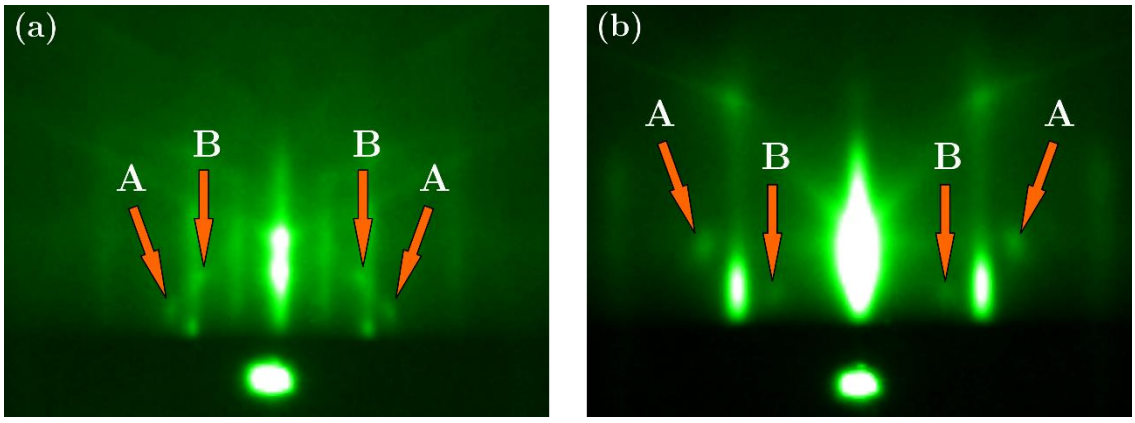


Figure 4.7: RHEED patterns in the (a) [110] and (b) [100] azimuth of Si taken after SiO_2 removal by heating up to 900 °C. The arrows indicate additional diffraction spots due to the epitaxially aligned islands of β-SiC on the Si(001) surface.

Comparison with theoretical transmission electron diffraction patterns was performed in order to show heteroepitaxial relationship of β-SiC islands on Si(001) surface. β-SiC is a cubic form of silicon carbide with unit cell constant of 4.35 Å. It exhibits zincblende crystal structure with $F\bar{4}3m$ space group (No. 216). RHEED patterns were constructed from simulated transmission patterns and primary silicon streaks. Since the Si(001) surface unit cell constants are well known, silicon streaks spacing was used for calibration of distances. Constructed patterns consistent with those experimentally obtained are shown in Figure 4.8.

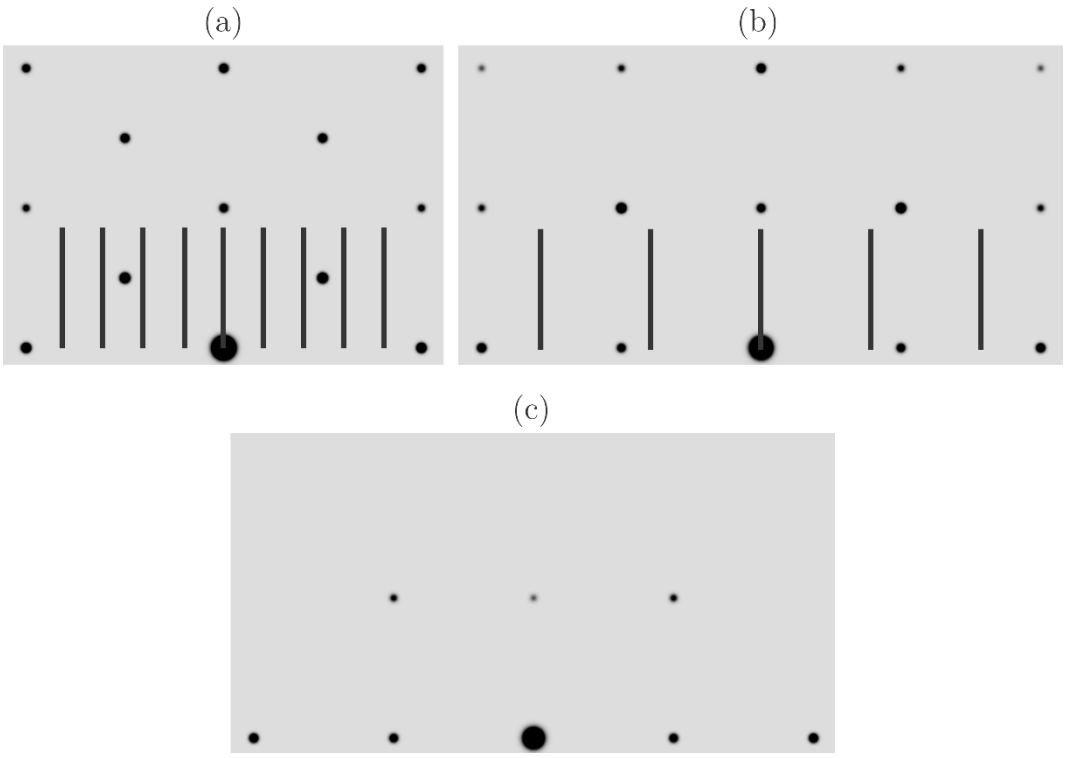


Figure 4.8: Simulated transmission electron diffraction patterns of β-SiC along (a) SiC[110] and (b) SiC[100] with superimposed Si streaks along (a) Si[110] and (b) Si[100]. (c) Simulated diffraction pattern along the SiC[1k0] direction, with k close to 0.

The following heteroepitaxial relationship was concluded:

β-SiC(001)||Si(001) and β-SiC[110]||Si[110]

However, transmission patterns from the Figure 4.8a and b explain diffraction spots positioned to the outside of the primary silicon streaks (arrows A in Figure 4.7) only. Besides the regular diffraction spots of single crystal SiC, additional spots positioned to the inside of the primary silicon streaks are also present in the RHEED patterns (arrows B in Figure 4.7). Both sets of diffraction spots (A and B) arise in the RHEED pattern simultaneously when the thermal deoxidation at moderate temperatures (750-900 °C) is performed and simultaneously disappear from the pattern after flashing at T>1100 °C. This indicates the same origin of both, i.e. SiC. Several authors observed similar RHEED patterns and the additional spots indicated by arrows B were ascribed to twins in SiC [138-140]. Simulated SiC transmission patterns also contain some higher order diffraction spots not visible in experimental patterns. In the study of Becker et al. it is written that SiC spots are mere vestiges of the complete transmission diffraction pattern [127]. According to our understanding, in the RHEED case, electron beam is not penetrating islands exactly along the high-symmetry direction. There is always some inclination angle present between the incident electron beam and the sample surface. Therefore much better agreement with experimentally obtained patterns is achieved with simulations in zone axis close to [100] (Figure 4.8c).

As already mentioned in Section 4.1.1.1., β-SiC–which exists in the form of islands on the Si surface–is removed in few seconds, when temperature higher than 1100 °C is applied. Such a high temperature causes dissociation of SiC and diffusion of carbon into the bulk [141-144]. When the flash-annealed Si surface was cooled down to a temperature of 600 °C

and left in a background gas with a pressure of approximately 1×10^{-8} mbar, significant changes in RHEED pattern were observed. After keeping the sample for 15 min at this temperature, quarter-order streaks emerged in the RHEED pattern and grew in intensity with time (Figure 4.9a). Si(001)-c(4×4) structure was formed with the reciprocal lattice shown in Figure 4.9b.

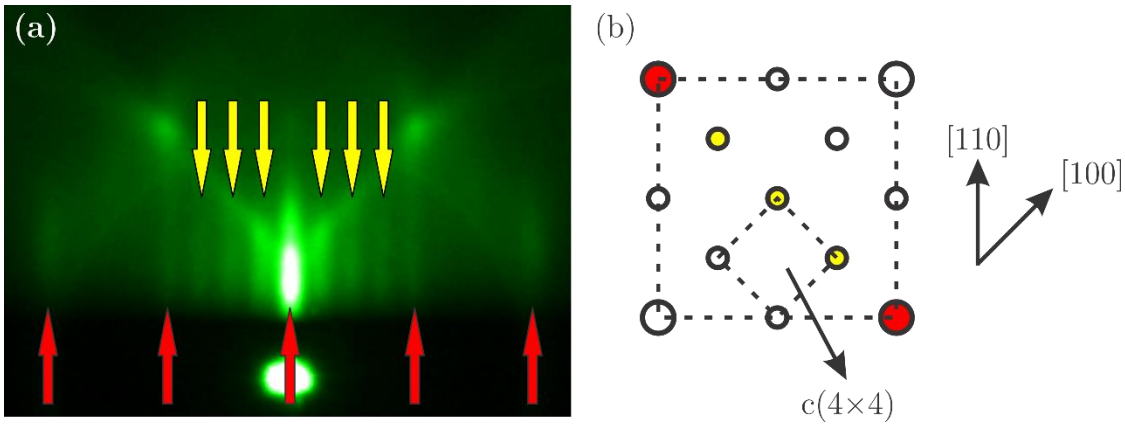


Figure 4.9: (a) RHEED pattern along the [100] azimuth of Si, obtained after flash annealing and keeping the surface at 600 °C for t > 15 min. The arrows pointing up (red) indicate primary silicon streaks (integer-order streaks) and the arrows pointing down (yellow) indicate quarter-order streaks due to the carbon contamination. (b) The c(4 × 4) reciprocal lattice. Larger (red) and smaller (yellow) circles indicate integer- and fractional quarter-order reciprocal lattice rods, respectively.

We additionally observed that reheating the substrate, to a temperature above 730 °C, causes simultaneous disappearance of surface c(4×4) reconstruction and the appearance of the SiC transmission pattern. This is a strong indication that c(4×4) reconstruction is not associated with clean Si surface, as was firstly thought by several research groups [145-148], but with carbon contamination [128, 149-154]. An important question that arises at this stage is whether the c(4×4) structure observed on the Si surface emerges from outdiffusion of carbon from the substrate or from an interaction with organic species from the background gas. Henderson et al. made a computation based on diffusion equations, showing that c(4×4) structure results from the chemical interaction of a carbon-containing adsorbate with the Si surface [155]. The study of the interaction of hydrocarbons with Si(001)(2×1) surface showed that ethylene is adsorbed nondissociatively in the wide temperature range between -196 °C and ~ 327 °C. Heating to 377 °C causes desorption of ~ 40 % of ethylene, while the remainder is decomposed to CH_x and SiH species [156]. However, one should be aware that c(4×4) reconstruction is not induced by ordering of carbon atoms in the top surface atomic layer. SIMS measurements showed that c(4×4) surface structure begins to emerge at carbon concentrations far too low to fill the c(4×4) unit cell with carbon atoms. It was concluded that c(4×4) is in fact a pure Si surface structure, which is formed as a result of stresses caused by carbon atoms in subsurface positions [129]. Many reconstruction models have been proposed, showing common problem of discrepancy between simulated and experimental STM images [145, 146, 148, 152, 157]. Finally, in 2006 He at al. [158] introduced a modified ad-dimer model with one carbon atom per unit cell located in the third subsurface layer (Figure 4.10), which gives the most consistent description of Si(001)-c(4×4) structure on the atomic level.

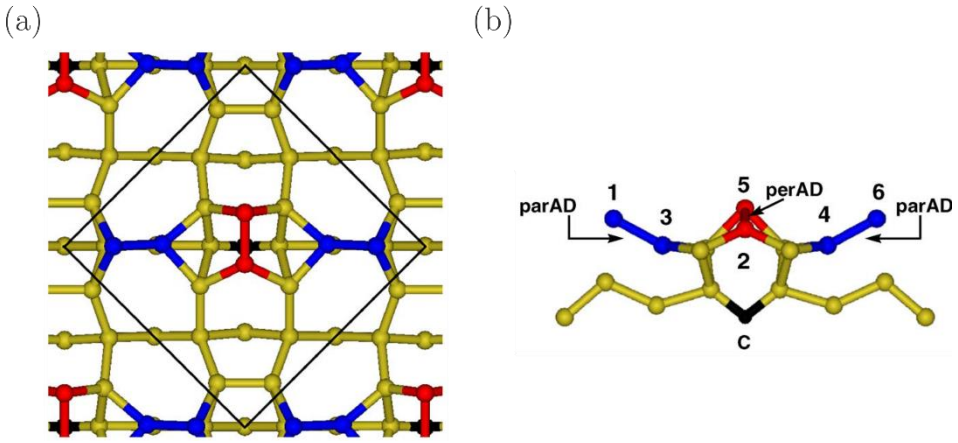


Figure 4.10: Modified ad-dimer model of the Si(001)-c(4×4) reconstructed surface. The unit cell contains one perpendicular dimer in the middle (atoms 2 and 5) and two parallel dimers (atoms 1, 3, 4 and 6). All three dimers are tilted. Carbon atom is positioned below the perpendicular dimer in the third subsurface layer [158].

We additionally determined the stability diagram for the observed surface structures on Si(001), and showed the following: The c(4×4) pattern emerges when a flash-annealed sample is cooled down to a temperature between 580 °C and 730 °C; the β-SiC transmission pattern superimposed on a (2×1) pattern appears after cooling down to a temperature between 730 °C and 1100 °C; whereas the (2×1) pattern is stable below 580 °C and above 1100 °C. If the flash-annealed (carbide free) surface is left in the vacuum at temperatures below 580 °C for a sufficient time, which results in (2×1) pattern, the c(4×4) structure appears with subsequent heating to the temperature between 580 °C and 730 °C, while the β-SiC reappears when substrate is heated above 730 °C. Thus, it is impossible to avoid carbon recontamination of the Si surface after flash annealing. It is within the realms of possibility, however, to improve the vacuum so that the carbon contamination shown by the RHEED, either as the c(4×4) or β-SiC transmission pattern, is significantly delayed. For instance, in UHV of 3×10^{-10} mbar, it takes a few hours to observe carbon contamination with RHEED [159], while in a vacuum of 1×10^{-8} mbar, it takes only around 15 min according to our experience. The exact time, needed for appearance of carbon related features in the RHEED pattern, should depend also on the extent of PLD chamber contamination (hydrocarbons partial pressure). We believe that the use of silver paint should be completely avoided in the PLD experimental work since it is an important source of hydrocarbons in the chamber and therefore does not allow very sensitive surface and interface studies.

4.1.1.2 Strontium-induced deoxidation

In the thermal deoxidation study we showed that at least 900 °C annealing temperature is needed for obtaining sharp and high-intensity diffraction streaks of (2×1) reconstructed Si surface in the RHEED pattern. A significant breakthrough was achieved by Yu et al. [160] who developed a low-temperature procedure that uses Sr or SrO for the removal of SiO_2 from the Si(001) surface. In this procedure, ~1-2 monolayers of Sr [4, 113, 161, 162], or ~3-4 monolayers of SrO [113, 163, 164] is deposited onto the substrate surface at temperature between 500 °C and 700 °C. Then the substrate is heated up to 800°C and maintained at that temperature until an ordered surface structure is observed. In some experiments Sr deposition was conducted at 800 °C [113, 160, 163-167]. However, Sr- or SrO-induced deoxidation was mainly performed using the molecular beam epitaxy technique. There are

also some reports on growing SrO on SiO_2/Si using the atomic layer deposition [168, 169] and PLD [163, 164] techniques. We investigated a deoxidation process based on PLD of elemental strontium which has to the best of our knowledge not yet been reported before. After a 12-hour degassing at 630 °C, the substrate was cooled down to room temperature. The removal of the native oxide was studied by depositing 200 pulses of metallic Sr in a vacuum of ~1×10^{-8} mbar on a Si/SiO_2 substrate at T<100 °C, followed by an annealing stage at 750 °C and 800 °C. During deposition of strontium the fluency, spot size, target-to-substrate distance and repetition rate were kept constant at 1 J/cm^2, 0.14 mm^2, 5.5 cm, and 0.2 Hz, respectively. Deposition of 200 pulses corresponds to ~1.1 ML coverage as determined by means of the surface reconstruction studies presented in the Chapter 4.2.2. RHEED images of the reconstructed Si surface in [110] high-symmetry direction, obtained after the substrate was heated to 750 °C and 800 °C, are shown in Figure 4.11a and b, respectively.

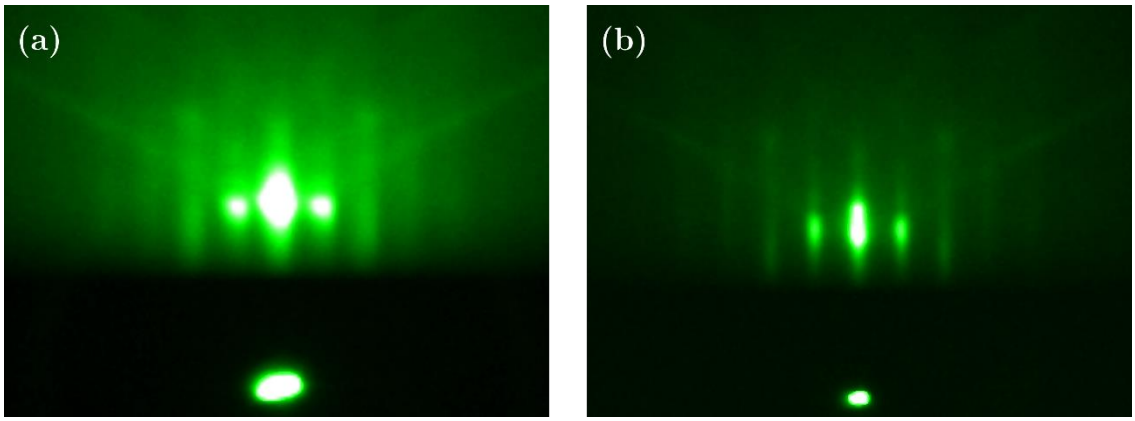


Figure 4.11: RHEED patterns in the [110] azimuth of Si taken after Sr-assisted deoxidation process at (a) 750 °C and (b) 800 °C.

At both temperatures intense 1/2-order streaks were observed, which indicates complete surface reconstruction. For the sample, annealed at 750 °C, however, diffraction streaks appear much broader compared to the sample, annealed at 800 °C. Broader diffraction streaks denote poorer surface order. Besides the advantage of SiO_2 removal at a 100 °C lower temperature compared to the optimum temperature needed for a thermal removal process, there is another advantage of Sr-induced process and is related to the kinetics of SiO_2 removal. In the Sr-induced deoxidation process, performed at 750 °C, the RHEED pattern appeared after ~17 min, while in the thermal deoxidation process, performed at the same temperature, RHEED pattern of much lower quality appeared after 45 min. These findings demonstrate that Sr greatly accelerates oxide removal. Wei et al. [113] investigated the mechanism of removing SiO_2 from the surface using Sr or SrO by means of temperature programmed desorption experiments (TPD). They concluded that the SiO_2 removal is due to the two simultaneous processes: catalyst reaction SiO_2(s) + Sr(or SrO) = SiO(g) + O(g) + Sr(or SrO) on the surface and the reaction SiO_2(s) + Si(s) = 2SiO(g) at the SiO_2/Si interface. After the deoxidation process using 2 ML of Sr they found about 0.25-0.5 ML of Sr remaining on the surface. However, no signal was observed for Sr containing species, i.e. Sr and SrO, in the TPD experiment. Despite this discrepancy, the authors concluded that the reduction of Sr from 2 ML to about 0.25-0.5 ML was caused by thermal desorption. Moreover, the unknown quantity of Sr on the reconstructed Si surface, which is left behind after the SiO_2 is completely removed, is an often encountered problem in the literature [94, 165]. Based on thermodynamic data and our investigation, related to the preparation of a

Sr buffer layer (Chapter 4.2.2), we can propose a more detailed description of the mechanism of removing SiO_2 from the surface using Sr or SrO. Since the SrO has a much greater $-\Delta G^\circ$ than SiO_2 it can be expected that Sr can reduce the SiO_2 to SiO (SrO line lies below the SiO_2 line in the Ellingham diagram). The following reactions might occur under appropriate conditions:

$$Sr(s) + SiO_2(s) = SrO(s) + SiO(g)$$

$$SrO(s) = Sr(s) + O(g)$$

Note that Sr recovers in the proposed reactions, which confirms its catalytic nature. After the complete elimination of SiO_2 layer there should be the same quantity of Sr present on the reconstructed Si surface as initially deposited onto the Si/SiO_2. However, the experiments show that only a partial quantity of initially deposited Sr is left on the surface after the native oxide removal process. To address the problem related to unknown amount of Sr which is left on the surface, we conducted two sets of experiments. In the first set of experiments Sr saturation coverage, which is defined as the thermodynamically stable one [170], was studied at different temperatures by depositing elemental Sr on the reconstructed Si surface. Detailed description of complete experiments is given in Chapter 4.2.3. Here, only the results relevant for Sr-induced deoxidation are presented. We showed that the saturation coverage of Sr on the reconstructed Si(001) surface in the temperature range relevant for the Sr-induced deoxidation (750 °C-800 °C), is 1/6 ML. After the deposition of 1/2 ML of strontium on the reconstructed Si(001) surface at 750 °C it took 5 min for surface reconstruction, characteristic for 1/2 ML coverage, to change into the surface reconstruction, characteristic for 1/6 ML coverage. In the second set of experiments Sr was deposited onto the Si/SiO_2 at room temperature. Then the substrate was heated to 800 °C, where the Sr acted as a catalyst to promote the decomposition of SiO_2. Finally, a Sr-terminated Si(001) surface was obtained after all the Si oxide was removed. We showed that the exact amount of Sr that remains on the surface right after the deoxidation process depends on the amount of deposited Sr and the annealing conditions. The deposition of 100 pulses of Sr (~0.6 ML) onto the substrate surface at room temperature and heating to 800 °C led to less than 1/6 ML Sr coverage. We proved this by the additional deposition of Sr at 750 °C, during which the RHEED pattern – characteristic for 1/6 ML coverage – could be observed. Repeating the same experiment with 200 pulses of Sr (~1.1 ML) showed that more than 1/4 ML of Sr was present on the Si surface, since the RHEED pattern – characteristic for 1/6 ML coverage – did not appear during subsequent Sr deposition this time. However, if we annealed the substrate at 750 °C for a sufficiently long time, before proceeding with additional Sr deposition, we again observed surface reconstruction characteristic for 1/6 ML coverage. The results of these experiments show that Sr desorbs already during the catalytic oxide removal process as well as after SiO_2 is completely removed, until the saturation coverage of 1/6 ML is achieved. Despite the lower temperature, required for SiO_2 removal, the Sr-induced deoxidation approach has proved to be inadequate for SiO_2 layer elimination due to the inevitable problem related to carbon contamination. Namely, all the RHEED patterns exhibited additional diffraction spots, characteristic for β-SiC on Si(001).

4.1.2 Summary

Thermal and Sr-induced deoxidation processes were investigated by RHEED to remove the 2 nm thick amorphous native oxide layer from the Si surface and prepare surface appropriate for further deposition of Sr buffer layer. Among the most important issues affecting the quality of obtained Si surfaces is a selection of proper sample holder. The custom-built tantalum sample holder enabled us to prepare highly-ordered reconstructed Si surface indicated by sharp and intense 1/2-order streaks in the RHEED pattern ([110] azimuth). The failure of such a surface preparation using the resistive-heating sample holder or stainless steel sample plate is related to the strong outgassing during heating, caused by the holder itself and in particular a silver paint used for pasting the substrate to the holder. It was demonstrated that 900 °C and 800 °C are the optimum temperatures for the thermal and Sr-induced deoxidation processes, respectively. The catalytic nature of Sr lowers the optimum temperature of deoxidation for 100 °C and significantly reduces the time needed for complete removal of the SiO_2 layer. In addition, it was shown that after the Sr-induced deoxidation surface is left with $\leq 1/6$ ML Sr coverage. The exact amount of Sr depends on initially deposited quantity of Sr on Si/SiO_2. However, in both processes, thermal and Sr-induced deoxidation, β-SiC islands are formed on the Si(001) surface due to the carbon contamination. The attempt to remove physisorbed organic molecules, responsible for the formation of SiC precipitates, from the SiO_2 surface, by carbon burning process, showed no improvement in achieving carbon-free reconstructed Si surface. Nevertheless, we succeeded in fabricating a clean reconstructed Si surface by flashing the substrate to 1200 °C. Such a high temperature causes dissociation of SiC and diffusion of carbon into the bulk. It was shown that as-obtained Si surface becomes re-contaminated with carbon after a certain period of time, as shown by the RHEED either as the c(4×4) or β-SiC transmission pattern. The recontamination of the surface cannot be completely avoided, however, by improving the vacuum (decreasing the hydrocarbons partial pressure) it can be significantly delayed. This suggests that further deposition of Sr buffer layer should be carried out as quickly as possible after the flash annealing in order to avoid substantial surface recontamination with carbon.

4.2 Formation of a Strontium Buffer Layer on Si(001) [112]

Deposition of $SrTiO_3$ (STO) material directly on the clean reconstructed Si(001) surface leads at best to textured layers [74, 75] due to the high reactivity of silicon, which readily reacts with oxygen during the deposition and in most of the cases forms the amorphous SiO_2 layer that hinders the epitaxial growth. Since the oxygen is an integral element of the STO target, it is inevitable during the deposition process. Furthermore, oxygen background pressure is used for the growth of oxides because the oxygen from the target does not satisfy the stoichiometry of the final film. According to conversation with R. Dittman (Summer School of the SFB 917 'Nanoswitches', March, 2014) oxide layers, deposited by PLD in vacuum (without oxygen background gas), can lack up to 50 % of oxygen. The key issue in the fabrication of epitaxial STO on Si is therefore a control of the oxidation of Si atoms at the interface. An effective way of controlling the reactivity of silicon surface against the oxidation is to form a Sr-based protective (buffer) layer on top of the surface. Several research groups have focused on the preparation of such buffer layer using MBE, ALD or PLD technique. Most of the work has been done using MBE that allows a very precise deposition control at the atomic level. The use of alternative techniques, i.e. ALD and PLD, is rare. Some of the buffer layers prepared using these two techniques are based on crystalline Sr-silicate [163], other on Sr [98] or strontium oxide (SrO) [94, 165] layers of different thicknesses. However, based on a number of MBE studies from the last two decades, Si surface passivated with 1/2 ML of metallic Sr represents the most suitable buffer layer. Furthermore, also the theoretical studies predicted that the optimal coverage of Sr on the Si surface for the epitaxial growth of oxides is 1/2 ML [171]. Silicon surface with this strontium overlayer exhibits a much higher resistance to oxidation compared to the bare silicon surface. Additionally, it provides a structural template in terms of lattice constants that is compatible with the subsequent growth of the STO. Our investigation aimed to explore the possibility of preparing a buffer layer, which is based on 1/2 ML Sr coverage, which has not been investigated with the PLD method yet. Such an aim additionally highlights the question whether the PLD method is capable of such a precise deposition control.

4.2.1 Clean (2×1)+(1×2) reconstructed Si(001) surface [1, 172, 173]

In order to understand the results related to Sr deposition on the clean reconstructed Si(001) surface, some key facts concerning the bare Si(001) surface need to be explained first. It took the researchers over 40 years of intense studies to clarify the atomic structure of Si(001). Such an interest has its roots in CMOS technology that uses exclusively Si(001) wafers. Let us first consider unreconstructed Si(001) 1×1 surface which is the simplest surface from the structure point of view (Figures 4.12a, b). The atoms of the top layer have the same arrangement as in the bulk and are missing two covalent bonds. Each surface Si atom is left with two half-filled sp^3-hybrid orbitals, called also dangling bonds. Atoms are arranged in a square array and the surface unit cell constant is $a_{surface}^{unreconstructed} = \frac{a_{bulk}}{\sqrt{2}} =$ 3.84 Å. The presence of dangling bonds significantly increases the surface energy and leads to the high degree of instability. The surface undergoes the rearrangement (reconstruction) in order to minimize its energy. Strong dimer bonds are formed by pairing of surface Si atoms as shown in Figures 4.12c, d. This dimerization process causes the release of energy due to the formation of a σ bond within each pair of surface Si atoms. All the dimers lie close to perpendicular direction with respect to the bonds between the first and second-layer atoms and prefer to arrange themselves into rows. The surface unit cell doubles along

the dimer direction and the surface becomes (2×1) reconstructed. The pairing of the surface atoms into the dimers reduces the number of dangling-bonds per surface atom to one.

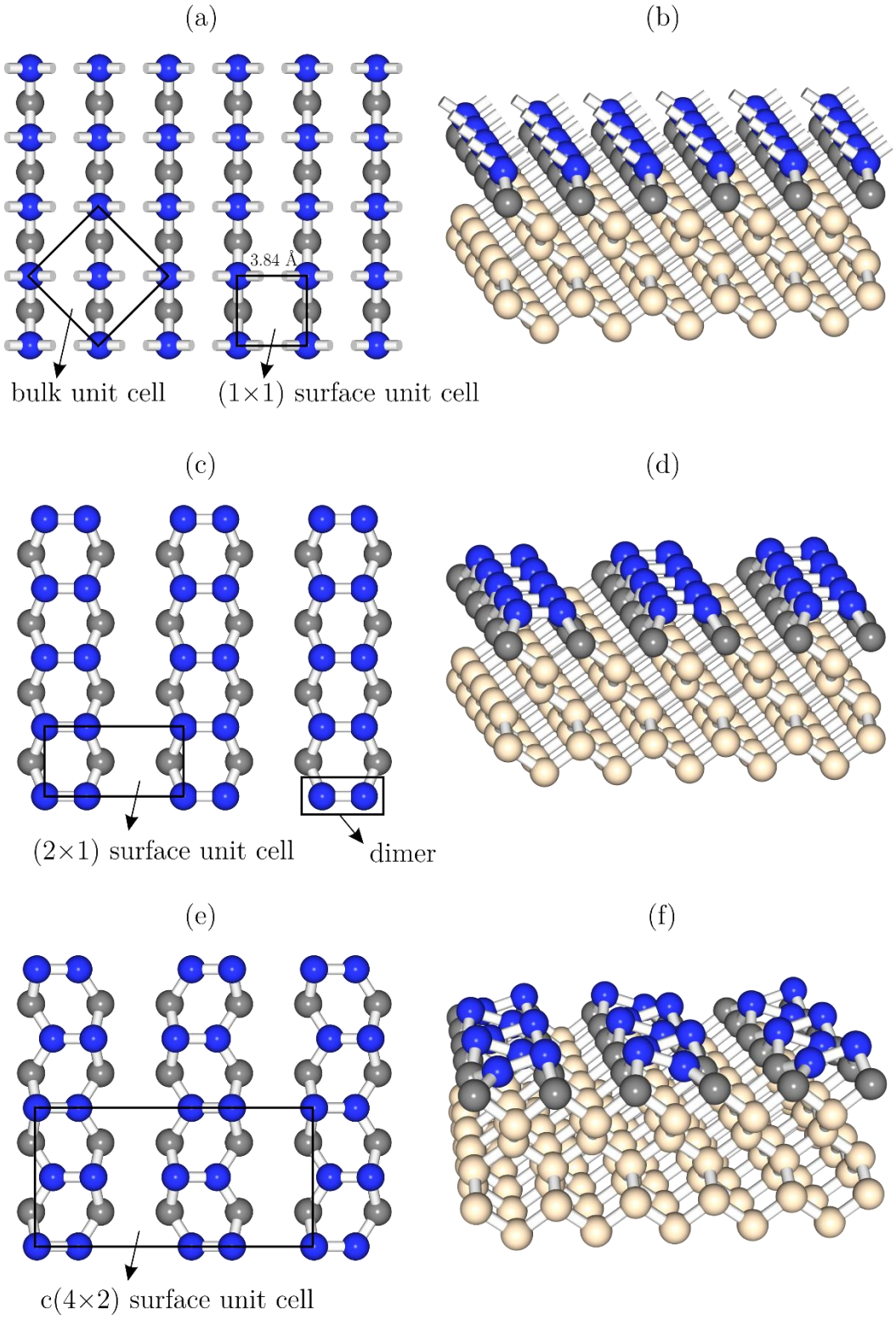


Figure 4.12: Top and side view of an unreconstructed (a, b), (2×1) reconstructed (c, d) and c(4×2) reconstructed (e, f) Si(001) surface.

The energy of the surface is even further reduced by buckling of dimers. The buckling refers to the geometric distortion in which symmetric dimers change to the asymmetric (tilted) form. The buckling direction of the dimers alternates along each row and the buckled rows are out-of-phase with each other which give rise to higher order c(4×2) surface reconstruction (Figures 4.13e, f). However, the buckled dimer model had for a long time not been entirely accepted within the scientific community because the surface diffraction techniques (LEED and RHEED) exhibit the (2×1) surface reconstruction characteristic for the surface with symmetric dimers. Additionally, in STM micrographs the dimers were visible as symmetric ovals [174]. A significant breakthrough was achieved when low-temperature STM studies showed the c(4×2) domains which increase in number by cooling down to 120 K [175]. It was concluded that at room temperature asymmetric dimers rapidly switch their orientation (dimers dynamically flip between two asymmetric configurations), giving rise to a time-averaged (2×1) symmetric appearance. Even after buckling process the surface tends to oxidize as a result of one unpassivated dangling bond per surface Si atom which is left on the surface.

In order to understand RHEED patterns obtained in different high-symmetry directions correctly, one should be aware that no ideally flat Si(001) surface exist in reality. All surfaces have some misorientation which is accommodated by single and double atomic layer steps on the surface. For the miscut angle below 1-2°, steps have monatomic height of 1.35Å. When the miscut increases from 2° to 6°, monatomic steps gradually change to biatomic. For even larger miscuts (>6-8°), steps become almost exclusively biatomic. Wafers used in our experiments were cut with an accuracy of ±0.1° along (001) crystal plane, indicating the presence of monatomic steps with an average distance between steps in the range of thousands Å. Since the tetrahedral bonds rotate for 90° between terraces separated by monatomic steps, the terrace on one side of the step exhibits 2×1 and the adjacent terrace exhibits 1×2 reconstruction. There are two degenerate reconstructed phases present on the surface (Figure 4.13).

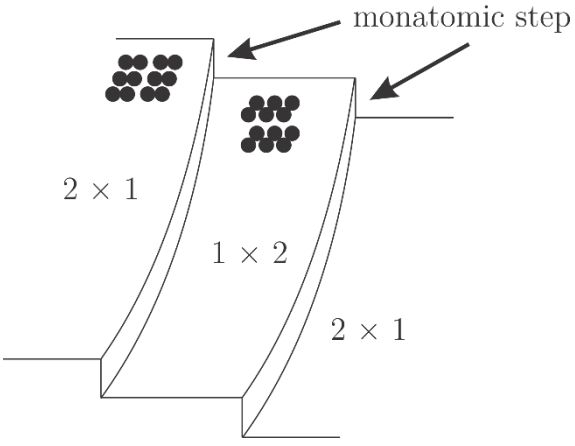


Figure 4.13: A schematic illustration of surface domains on Si(001) surface with single atomic layer steps.

Taking into account the basics of the Si surface we can finally construct the reciprocal lattice and correlate it with experimentally obtained RHEED patterns for the clean reconstructed Si(001) surface. The reciprocal lattice for Si(001) surface is shown in Figure 4.14a. It is presented as a superposition of two reciprocal lattices, one corresponding to (2×1) (Figure 4.14b) and the other one corresponding to (1×2) (Figure 4.14c)

reconstructed phase, due to the mixed surface termination. All the dots in the figure should be considered as reciprocal lattice rods extending into the direction perpendicular to the sheet of this paper as the reciprocal lattice is constructed from the real lattice which is two-dimensional. Larger black dots represent integer-order ((10), (00), ($\bar{1}$0)) reciprocal lattice rods. For the hypothetical unreconstructed surface, reciprocal lattice would consist of these rods only. Due to the surface reconstruction additional fractional-order (half-order) reciprocal lattice rods emerge in the reciprocal space, indicated by smaller red dots. Experimentally obtained RHEED patterns of the reconstructed Si(001) surface after flash-annealing are shown in Figure 4.15. In [110] azimuth only the diffraction streaks from zero Laue circle (L_0) were seen on the RHEED screen. All these streaks, indicated by arrows in Figure 4.15a, result from intersection of reciprocal lattice rods from zero Laue zone with Ewald's sphere. White and black arrows indicate integer- and half-order (1/2×) streaks, respectively. The latter arise from 2× surface reconstruction. When the intensity of incident electron beam was significantly increased, also diffraction spots from intermediate Laue circle ($L_{1/2}$) become visible (Figure 4.15b). Figure 4.15c shows the RHEED pattern along the [100] azimuth of Si. In this direction, diffraction streaks/spots from zero (L_0), intermediate ($L_{1/2}$) and first (L_1) Laue circles are clearly visible. L_0 and L_1 correspond to the intersection of the integer-order reciprocal lattice rods with the Ewald's sphere, while the $L_{1/2}$ corresponds to the intersection of the 1/2-order rods.

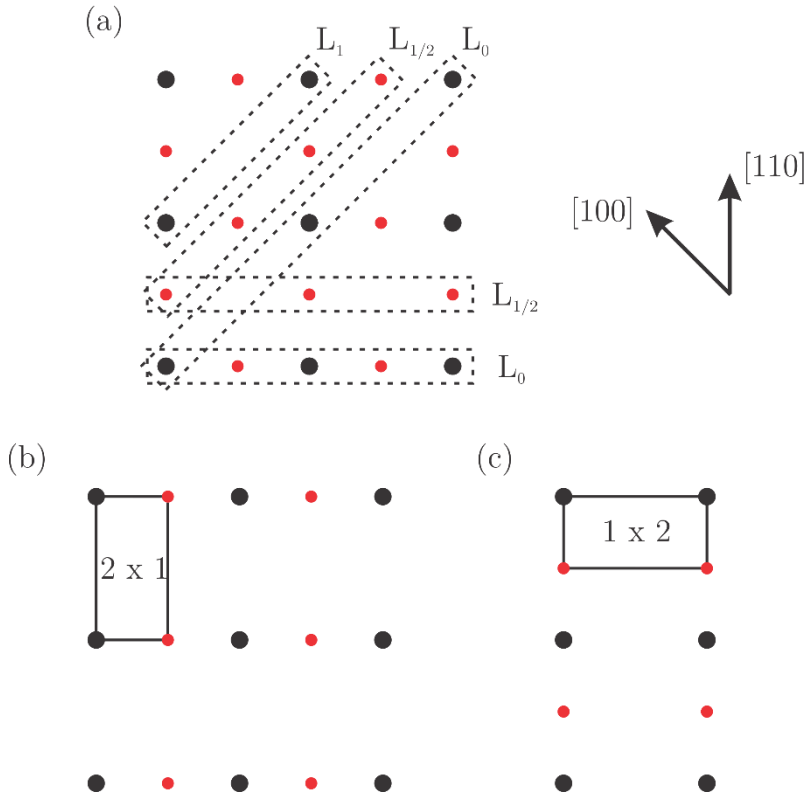
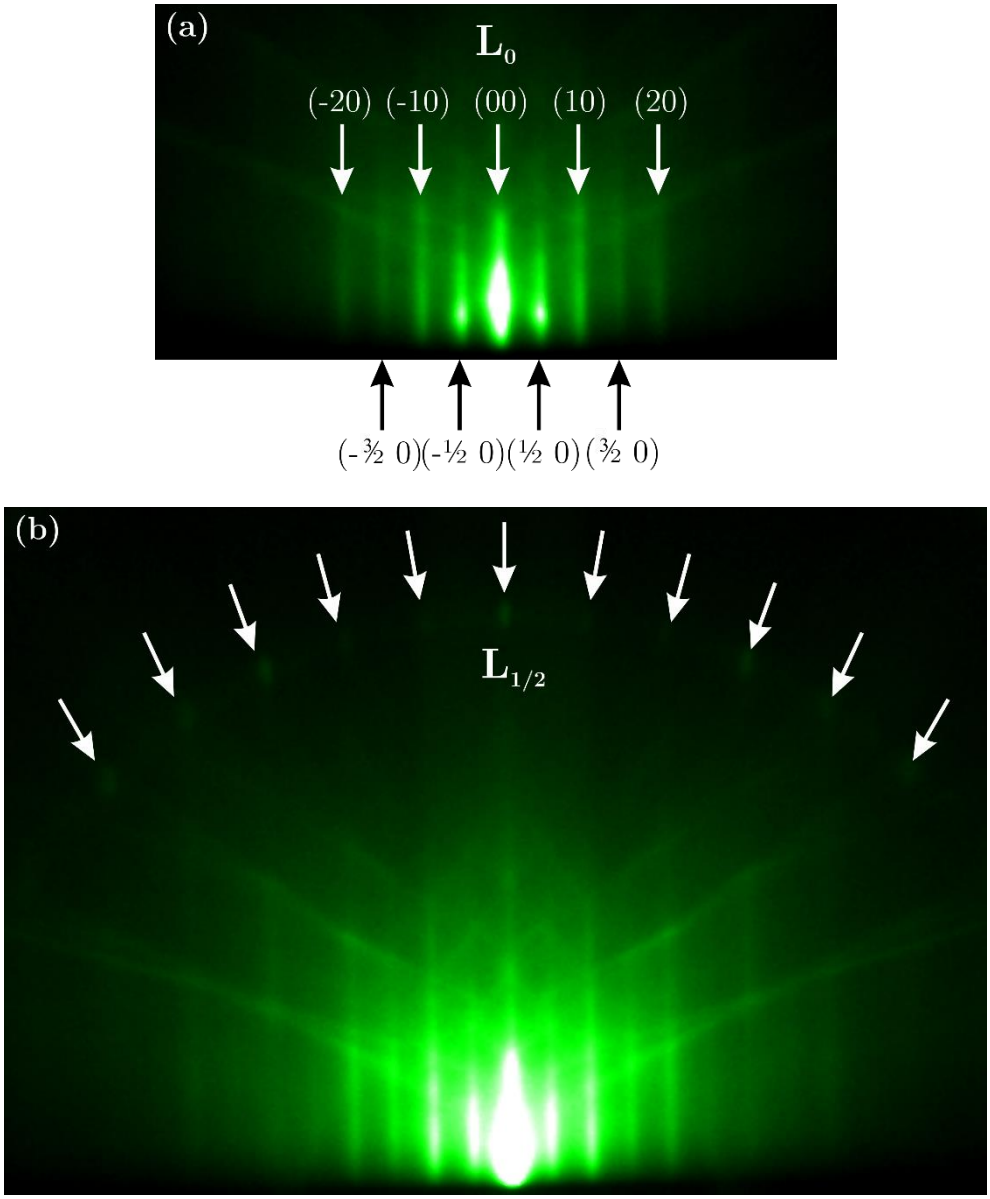


Figure 4.14: Reciprocal lattice for (a) two-domain (2×1)+(1×2), (b) (2×1) and (c) (1×2) reconstructed Si(001) surface. Larger black and smaller red circles indicate integer- and ½-order reciprocal lattice rods, respectively. The row of reciprocal lattice rods within each of the rectangles in (c) represents single Laue zone of rods.


(a)
L0
(-20) (-10) (00) (10) (20)
(-3/2 0)(-1/2 0)(1/2 0)(3/2 0)
(b)
L1/2

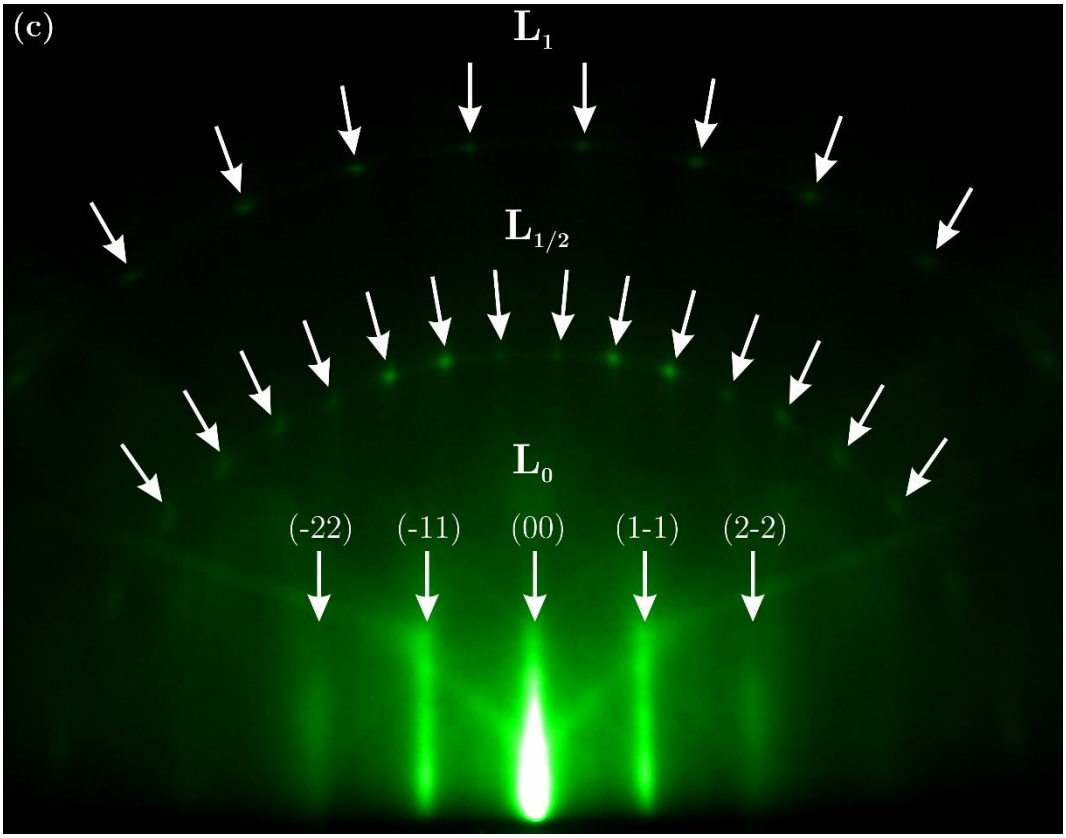


Figure 4.15: RHEED patterns of a (2×1)+(1×2) reconstructed Si(001) surface after flash annealing, in the (a, b) [110] and (b) [100] azimuths. The arrows pointing down (white) and arrows pointing up (black) in (a) indicate integer- and fractional 1/2-order streaks, respectively. (b) Incident beam in the same direction as in (a) but with higher intensity. L_0, $L_{1/2}$ and L_1 in (c) indicate zero, intermediate (due to 2× surface reconstruction) and first Laue circles.

As stated previously, Si(001) surface contains steps. As a result additional periodicity emerges in the reciprocal space, provided that the steps are about equally spaced, giving rise to splitting of diffraction streaks/spots in the RHEED pattern (Figure 4.16a). The splitting can only be seen when the incident electron beam is directed perpendicular to the step edges. Figure 4.16c shows the reciprocal lattice for vicinal surface expressed as a superposition of the reciprocal lattice for the (2×1)+(1×2) reconstructed Si surface (gray vertical lines) and that for a grating of step edges (solid tilted lines). Both, diffraction due to the in-plane lattice constant and diffraction due to the additional periodicity of the step-terrace structure, contribute to the diffracted intensity. In addition a section of two Ewald's spheres is drawn, one for an in-phase and the other one for an out-of-phase condition. Diffraction condition is called in-phase when waves scattered from different terraces interfere constructively. In the case of out-of-phase condition, waves from different terraces differ in phase by half a wavelength and interfere destructively [176]. However, the diffracted intensity is most sensitive for the step-terrace structure on the surface at the out-of-phase condition [177], which results in two strong intersections, shown in Figure 4.16a by arrows.

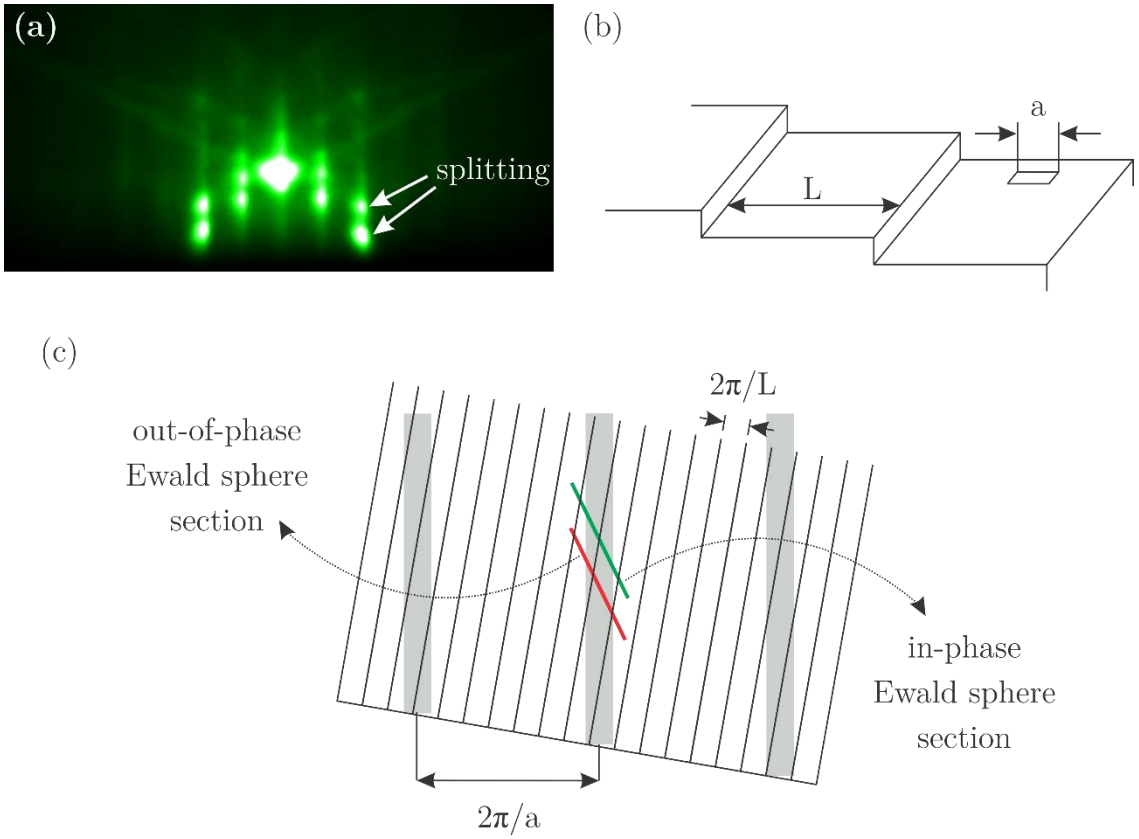


Figure 4.16: (a) Experimentally obtained RHEED pattern with the beam in the [1-10] direction (perpendicular to the step edges). Arrows indicate splitting of the diffraction spots. (b) A schematic model of equally spaced surface steps with a the in-plane lattice parameter and L the terrace width. (c) The reciprocal lattice for a vicinal surface. Out-of-phase (red line) and in-phase (green line) Ewald sphere sections show the condition for diffraction.

4.2.2 Deposition of strontium on Si(001) surface

Strontium (Sr) is known to form different ordered two-dimensional phases (reconstructions) on Si(001) surface at certain sub-monolayer coverages [6, 178-180]. Being able to follow these surface reconstructions, one can prepare exactly half a monolayer Sr coverage on Si – an effective buffer layer. It was our goal, therefore, to find conditions, which would enable us to deposit extremely small quantity of Sr by each laser pulse and observe characteristic surface reconstructions using the RHEED technique. The deposition was performed on (2×1)+(1×2) Si(001) surface using a metallic Sr target and fluency of 1 J/cm^2 at 700 °C in vacuum (~1×10^{-8} mbar). Ablated area size (spot size) proved to be the most critical parameter in the whole deposition process. If the spot size was too large, 3D transmission RHEED pattern formed due to excessive quantity of deposited Sr. For instance, for the spot size of 2.31 mm^2 already a single pulse caused a drastic change of 2D pattern, characteristic for the clean reconstructed Si(001) surface, into a spotty 3D RHEED pattern (Figure 4.17) which presumably originates from Sr islands on the surface. The transmission pattern indicates the presence of Sr islands on the surface. In further experiments we were gradually reducing the spot size using smaller beam masks. We demonstrated that keeping the spot size at 0.14 mm^2 and fluency at 1 J/cm^2 provide the optimum Sr flux for the preparation of sub-monolayer Sr structures on Si(001).

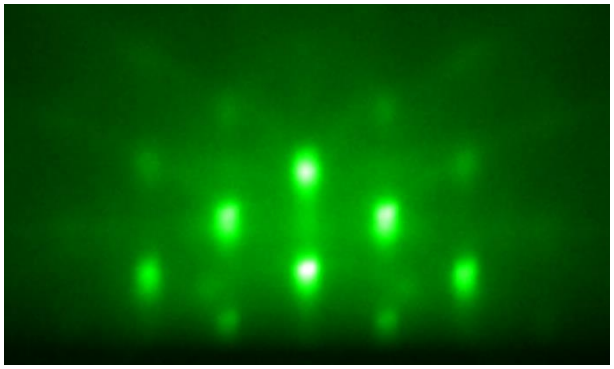


Figure 4.17: Transmission diffraction pattern observed after deposition of one pulse of Sr on reconstructed Si(001) surface at 700 °C in [110] direction. Too large a spot size (2.31 mm^2) caused excessive quantity of deposited Sr.

In Figures 4.18 and Figure 4.19 RHEED data collected at 700 °C during Sr deposition are presented, showing the evolution of the surface structure in the [110] and [100] high-symmetry directions, respectively. The surface evolves from the two-domain (2×1)+(1×2) reconstruction (Figure 4.18(a) and Figure 4.19(a)), exhibited by the bare Si surface, to a two-domain (2×3)+(3×2) structure at 1/6 ML (Figure 4.18(b) and Figure 4.19(b)), which is then replaced by a two-domain (1×2)+(2×1) structure again at 1/4 ML. The final (1×2)+(2×1) pattern was observed to be present up to 1/2 ML Sr coverage (Figure 4.18(c) and Figure 4.19(c)).

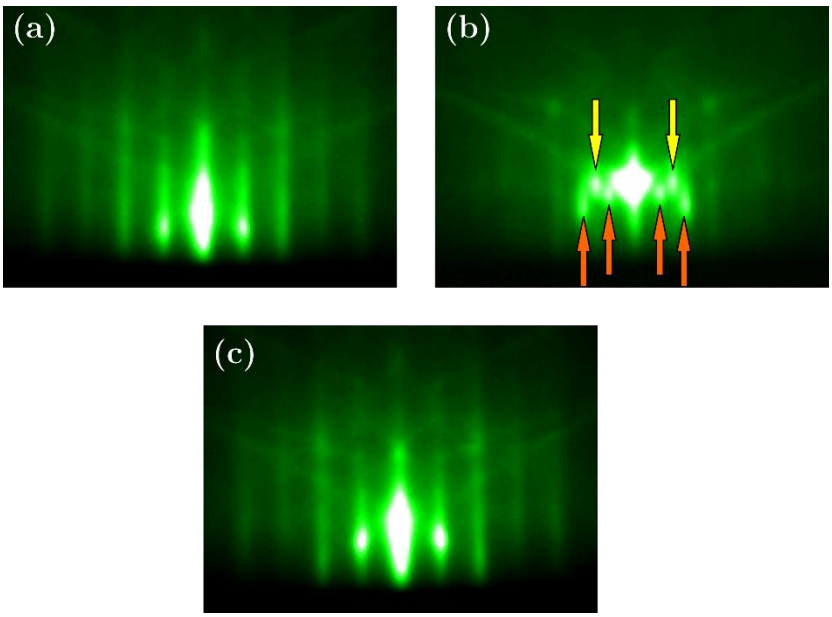


Figure 4.18: RHEED patterns in the [110] azimuth of Si(001) taken at various stages of the Sr deposition. (a) (2×1)+(1×2) reconstructed Si surface at 700 °C after flash annealing. (b) (2×3)+(3×2) reconstructed surface with coverage of 1/6 ML Sr at 700 °C. (c) (1×2)+(2×1) reconstructed surface with coverage of 1/2 ML Sr at 700 °C. The arrows pointing down (yellow) and arrows pointing up (orange) indicate the streaks due to the 2× and 3× reconstructions, respectively.

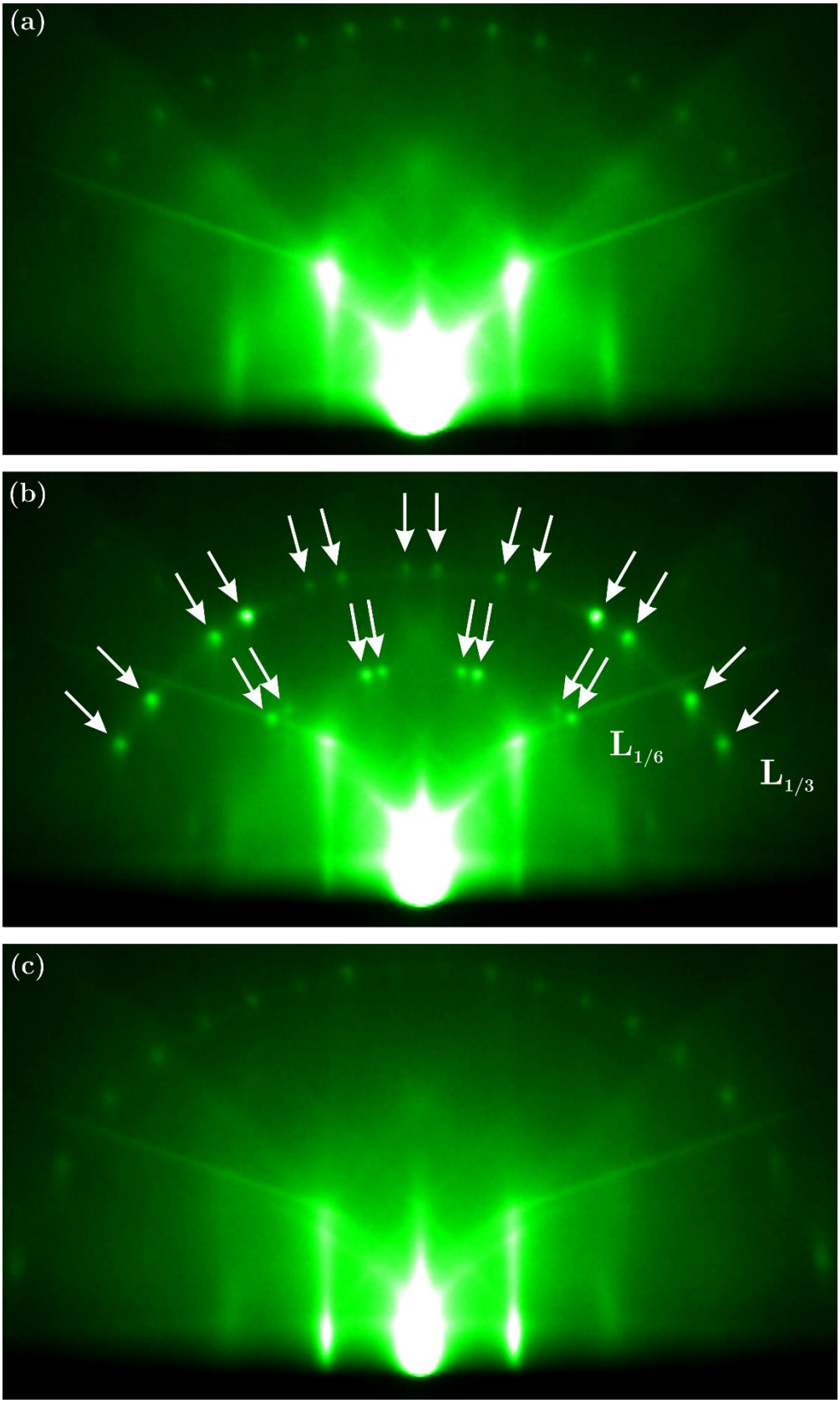


Figure 4.19: RHEED patterns in the [100] azimuth of Si(001) taken at various stages of the Sr deposition. (a) (2×1)+(1×2) reconstructed silicon surface at 700 °C after flash annealing. (b) (2×3)+(3×2) reconstructed surface with coverage of 1/6 ML Sr at 700 °C.

(c) (1×2)+(2×1) reconstructed surface with coverage of 1/2 ML Sr at 700 °C. $L_{1/6}$ and $L_{1/3}$ in (b) indicate intermediate Laue circles due to 3× surface reconstruction.

In the present study the observation of (2×3) surface reconstruction was determined as the key for the preparation of exactly 1/2 ML Sr coverage. Knowing the coverage for (2×3) reconstruction, enabled us to calculate the number of pulses required for the coverage of 1/2 ML. However, different Sr coverages have been reported for the Sr/Si(001) (2×3) structure in the literature [170, 179-183]. More than twenty years of research performed on this surface structure finally led to conclusion, that the (2×3) reconstruction include 1/6 ML Sr atoms [184]. When preparing 1/2 ML coverage, one should not rely on the reappearance of (2×1) RHEED pattern, since the coverage window for (2×1) structure is relatively large, ranging from 1/4 ML to more than 1/2 ML but on the calculated number of pulses based on 1/6 ML coverage.

As the deposition on the bare Si surface is initiated, the intensity of the 1/2-order streaks in the [110] direction gradually decreases with the pulses (Figure 4.20), which is consistent with the increase of the Sr lattice gas (no long-range order) [185] concentration, present on the Si surface from the beginning of the deposition until the occurrence of the (3×2) pattern. After a certain number of laser pulses third-order streaks begin to appear and grow in intensity simultaneously with the 1/2-order streaks, until the maximum is reached, which corresponds to 1/6 ML coverage. As the Sr coverage was further increased, the intensity of both the half- and third-order streaks decreases and the 3×2 structure is extinguished near the 1/4 ML Sr coverage. The 3×2 is replaced by the 1×2 pattern, and the half-order streaks increase again in intensity up to 1/2 ML Sr coverage. Similarly, in [100] direction, two additional intermediate Laue circles $L_{1/6}$ and $L_{1/3}$ arose in the RHEED pattern and reached the maximum intensity at 1/6 ML coverage.

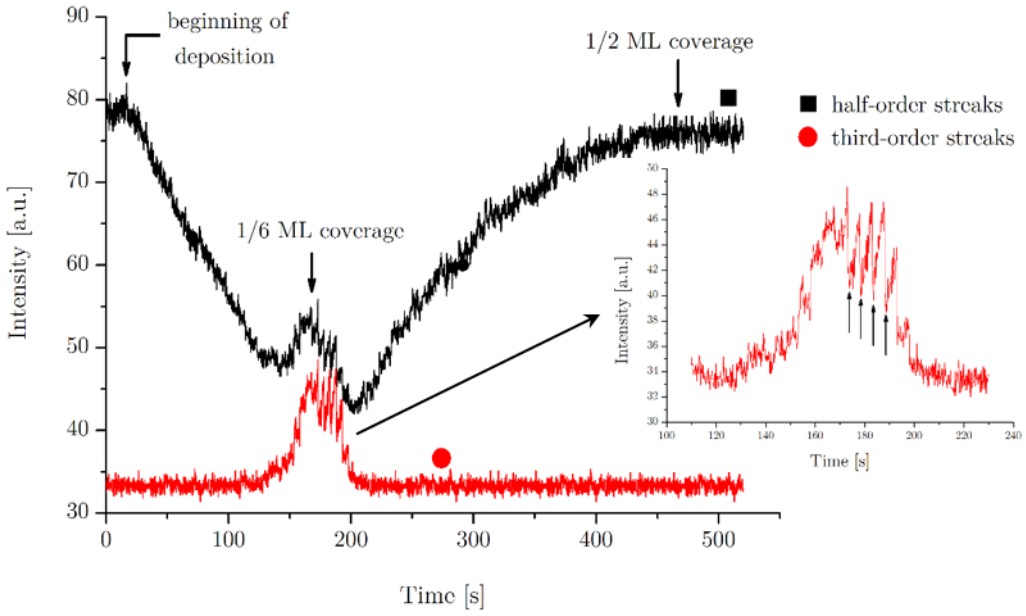


Figure 4.20: RHEED intensity of half- and third-order streaks during Sr deposition. The inset gives enlarged peak which corresponds to 1/6 ML coverage. Arrows pointing up in the inset indicate moments when ablation plume impinges on substrate surface.

Detailed view of the Figure 4.20 reveals specific modulation of the intensity induced by the pulsed nature of the deposition. Broad peak at 1/6 ML coverage consists of several spikes

which give it noisy appearance. Each spike belongs to one pulse. Arrows pointing up in the inset of Figure 4.20 indicate moments when ablation plume impinges on substrate and causes instant surface disorder, which results in drop of intensity. In the time interval between two sequential pulses intensity grows due to the surface ordering until the next ablation plume reaches the surface.

The reciprocal lattice for Sr/Si(001) (2×3)+(3×2) structure is shown in Figure 4.21a. It describes the experimentally obtained RHEED pattern very well and consists of two reciprocal lattices, one corresponding to terraces with (2×3) (Figure 4.21b) and the other one corresponding to terraces with (3×2) (Figure 4.21c) surface structure. Diffraction spots from the $L_{1/2}$ Laue circle in the [100] direction were visible during the entire deposition and exhibited similar behavior in terms of intensity as 1/2-order streaks from the L_0 in the [110] direction.

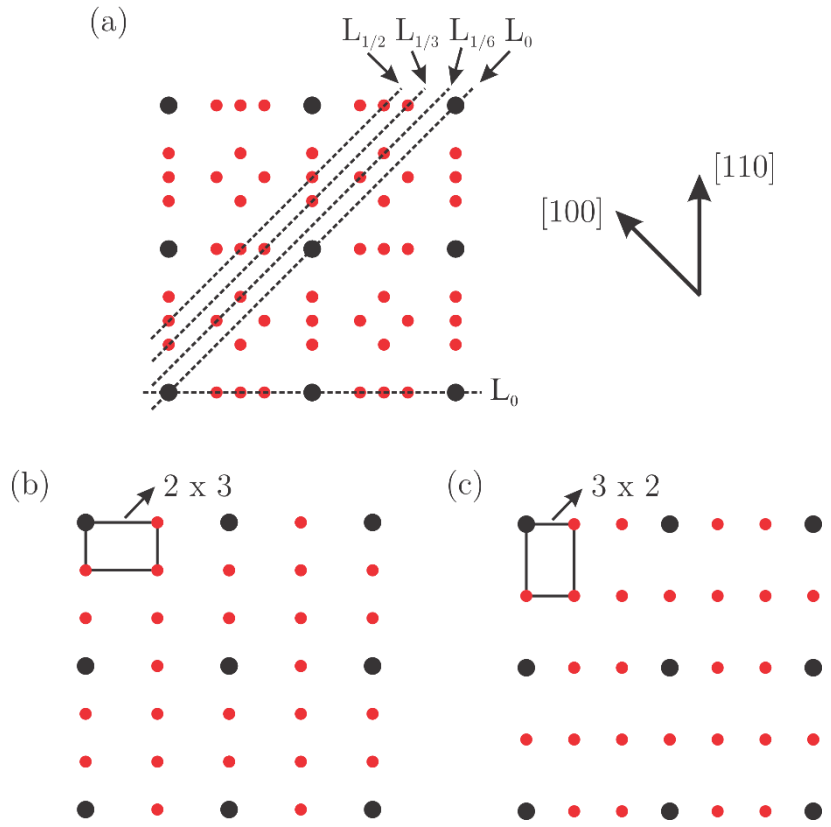


Figure 4.21: Reciprocal lattice for (a) two-domain (2×3)+(3×2), (b) (2×3) and (c) (3×2) reconstructed Sr(1/6 ML)/Si(001) surface. Larger black and smaller red circles indicate integer- and fractional-order reciprocal lattice rods, respectively. The row of reciprocal lattice rods lying on each dashed line in (a) represents one Laue zone of rods.

We should be aware that the dimer pattern of the Si surface (Figure 4.22(a)) changes dynamically when the deposition is conducted at high temperature. The formation of the 3×2 phase at 1/6 ML Sr coverage disrupts the original dimer pattern and forces the motion of 2/3 of the surface Si atoms to step edges (Figure 4.22(b)). This novel atomic structure of Sr/Si(001) (2×3) was introduced by Garrity et al. [173] and Reiner et al. [186] and additionally confirmed just recently by Kuzmin et al. [184] based on first-principles density functional theory (DFT) calculations. After reaching 1/6 ML Sr coverage, the deposition of additional Sr causes the rest of the original surface Si atoms to move to step edges and a (2×1) dimer pattern to form on the now exposed second Si layer. This dimer pattern is

rotated by 90° relative to the original dimers, since an entire monolayer of Si atoms was removed from the surface (Figure 4.22(c)).

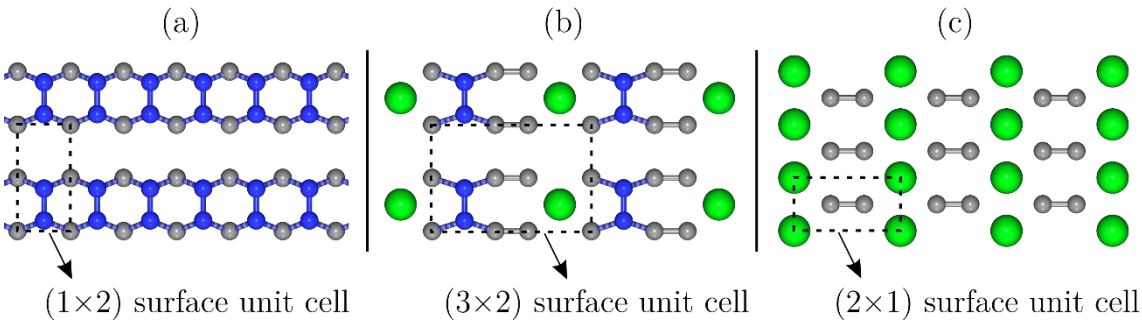


Figure 4.22: Top view of silicon surface at (a) 0 ML (b) 1/6 ML and (c) 1/2 ML Sr coverage. Sr atoms are in green, top layer Si atoms are in blue and second layer Si atoms are in grey.

With RHEED studies on mixed terminated Si(001) wafers, it cannot be established whether the unit-cell orientation changes from 1×2 to 2×1 during the Sr deposition. In fact, both changes of unit cell orientation, from 1×2 to 2×1 on one type of terraces and vice versa on other type of terraces, occur simultaneously. A single transformation from (1×2) to (2×1) can only be observed through RHEED studies of the Sr deposition on single-terminated Si(001) surfaces with a miscut above 4° [186].

Moreover, another procedure for buffer-layer preparation based on the Sr-assisted deoxidation process and the additional deposition of Sr at 700 °C until reaching 1/2 ML coverage was developed. First, 200 pulses of Sr (~1.1 ML) were deposited onto the SiO_2/Si at room temperature. Then the sample was heated to 800 °C which has proved to be the optimum temperature for Sr-catalyzed deoxidation process (see Chapter 4.1.1.2). After the removal of the SiO_2 layer at 800 °C the RHEED pattern exhibited (1×2)+(2×1) reconstruction. Further annealing of the as-prepared surface for several minutes at 800 °C resulted in the appearance of (3×2)+(2×3) RHEED pattern, characteristic for 1/6 ML coverage (see Chapter 4.2.3). Then the temperature was decreased to 700 °C and additional 2/6 ML (60 pulses) Sr was deposited, leading to 1/2 ML Sr coverage in total. Number of pulses required for additional 2/6 ML coverage was derived from separate experiment where Sr deposition was performed on the bare reconstructed Si(001) surface with the aim to determine number of pulses required for the appearance of (3×2)+(2×3) pattern, characteristic for 1/6 ML coverage.

4.2.3 Temperature effect on surface reconstruction

Temperature has a significant impact on surface reconstruction stability. We showed that the buffer layer (1/2 ML Sr coverage) can be prepared also at 750-800 °C, i.e. at 50-100 °C higher temperature compared to the optimum one. However, keeping the buffer layer at 750-800 °C for at least 5 minutes after Sr deposition resulted in the change of the RHEED pattern from the (1×2)+(2×1) to (3×2)+(2×3). This indicates partial desorption of the Sr at 750-800 °C until reaching the saturation coverage at 1/6 ML. In addition, we showed that no strontium is retained on the surface when the buffer layer is heated above 1100 °C. Recovery of the clean Si surface after heating above 1100 °C was demonstrated by the ability to reuse such surface for buffer layer preparation, when exactly the same number of pulses were required for 1/6 and 1/2 ML Sr coverage. We observed that (1×2)+(2×1) reconstruction was stable during the annealing of the buffer layer at T ≤ 700 °C. When the

(3×2)+(2×3) reconstruction, characteristic for 1/6 ML coverage, was prepared at 700-800 °C and gradually cooled to room temperature, the diffraction spots characteristic for 3× surface reconstruction disappeared from the RHEED pattern at ~500 °C. However, heating the surface back up to 700 °C resulted in the re-appearance of the (3×2)+(2×3) RHEED pattern. Fast cooling on the other hand enabled us to preserve the (3×2) surface symmetry way down to room temperature due to the kinetically hindered surface rearrangement. To the best of our knowledge described surface rearrangements induced by temperature change have not been described in the literature yet.

4.2.4 Resistance of Sr(1/2 ML)/Si(001) surface to oxidation

According to the theory, at a Sr coverage of 1/2 ML, all the dangling bonds of the surface dimers are fully occupied. Each Sr atom fully donates two valence electrons to the Si surface, which ensures that every Si dangling bond become passivated, and the reactivity of the surface to oxygen is reduced. In order to confirm this hypothesis and investigate the stability of Sr(1/2 ML)/Si(001) surface phase against oxidation, the surface was exposed to molecular oxygen at several different temperatures (50 °C, 250 °C, 300 °C and 400 °C). A needle valve, which allows a very precise regulation of gas flow, was used for this purpose. The exposure to the oxygen background pressure was performed in steps, indicated by dots in Figure 4.23. At each step the surface was exposed to oxygen for 5 minutes. We started with the pressure of 5×10^{-8} mbar. After 5 minutes the pressure was quickly increased to higher value and this was repeated until intensity of half-order streaks in the RHEED pattern started to decrease. Degradation of the quality of the pattern suggests surface disordering induced by the oxidation. The same set of experiments was performed on the clean reconstructed Si surface prepared by flash-annealing. Figure 4.23 shows a comparison of the reactivity of the two surfaces, indicated by position of black and red line. The red line represents the buffer layer and lies significantly higher than the black line which represents clean reconstructed Si surface. This demonstrates that at elevated temperatures which are important for crystallization of subsequent overgrown STO films, the buffer layer exhibits much higher resistance to oxidation compared to the bare silicon surface.

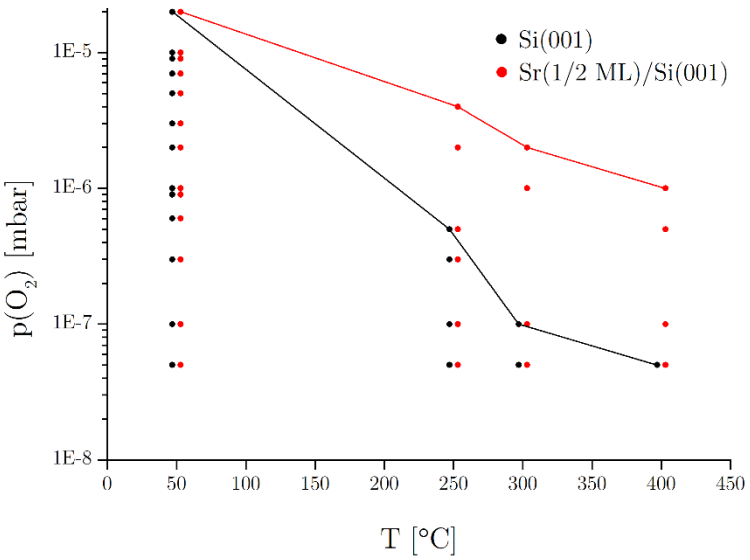


Figure 4.23: Stability of the buffer layer (red line) compared to the bare reconstructed Si surface (black line) at 50 °C, 250 °C, 300 °C and 400 °C in the background gas of oxygen. The lines indicate pressure levels at which the intensity of 1/2-order streaks begins to decrease.

4.2.5 Summary

The formation of ordered Sr sub-monolayer structures on (1×2)+(2×1) Si(001) surface was investigated by PLD using the elemental Sr target. The fabrication conditions which enable the observation of different surface reconstructions during the Sr deposition were determined. *In-situ* RHEED characterization showed (2×1)+(1×2)→(2×3)+(3×2)→(1×2)+(2×1) surface symmetry transition. The observation of (2×3)+(3×2) surface structure, characteristic for 1/6 ML Sr coverage, enabled us to prepare exactly 1/2 ML Sr coverage on Si, which is a prerequisite for the subsequent epitaxial growth of $SrTiO_3$ layer. Two procedures for the buffer layer preparation were developed. The first one is based on flashing the Si substrate to 1200 °C to remove the native oxide layer and subsequent deposition of Sr at 700 °C, while the second one begins with Sr-assisted deoxidation process and the additional deposition of Sr at 700 °C until reaching 1/2 ML coverage. However, the first procedure is more suitable due to the absence of carbon contamination on the surface. We additionally tested the stability of as-prepared buffer layer against oxidation at several different temperatures and showed much higher resistance of Sr(1/2 ML)/Si(001) compared to the bare reconstructed Si surface. Overall, we showed that PLD provides the ability to control formation of different surface reconstructions of Sr on Si(001) on the atomic level, which was previously only explored with the MBE method.

4.3 Growth of $SrTiO_3$ Thin Film on Sr(1/2 ML)/Si(001) Surface

The PLD growth of $SrTiO_3$ (STO) layer on Sr-passivated Si(001) surface can be performed from metallic Sr and Ti, their oxides (SrO and TiO_2) or directly from the STO target. The deposition from the STO target appears to be the most convenient due to several reasons. STO is stable at ambient conditions, making it simple for handling, compared to the elemental Sr and Ti, which readily react with oxygen. The deposition performed from two target materials bring additional complexity in the deposition procedure due to the required *in-situ* target exchange and corresponding fluence changes. In addition, problem related to stoichiometry control is much less pronounced in the case of the single STO target. Kourkoutis et al. showed that a topotactic reaction, which is based on separate deposition of few monolayers (MLs) of SrO and TiO_2 at room temperature in high oxygen partial pressure and subsequent crystallization anneal in vacuum, leads to much more nonuniform surface coverage (STO islands on the surface) compared to the codeposition of Sr and Ti [187]. Therefore, a single-crystal STO target was used as a source of material for deposition in our studies. Since there were only few relevant investigations performed on the PLD growth of STO on Si(001) so far [98-100], an overview of the deposition procedures, which lead to the epitaxial growth, was made on numerous molecular beam epitaxy (MBE) studies, starting with the work of Mori and Ishiwara [188] in 1991, when STO was epitaxially grown on Si for the first time. Among the various procedures used in the literature, we limited ourselves only to those, which include initial preparation of the Sr-buffer layer. Two main MBE strategies for fabricating epitaxial STO thin films on Si are commonly applied. The first strategy is based on deposition of first 2-4 STO MLs on Sr(1/2 ML)/Si(001) at a relatively low O_2 partial pressure in the upper 10^{-8} mbar range and a moderate temperature of ~360 °C. Then the O_2 partial pressure is ramped up to 10^{-6} mbar range for the rest of the growth [61, 189-191]. Kinetically controlled sequential deposition (KCSD) is another approach where the deposition step conducted at low temperature and relatively high O_2 partial pressure is followed by a high temperature and low O_2 partial pressure step [12, 59, 64, 192]. First, 2-3 MLs of amorphous STO are grown at T<300 °C and O_2 partial pressure in 2×10^{-8}-7×10^{-7} mbar range. This amorphous layer is then crystallized in ultrahigh vacuum (UHV) at 500-600 °C. The two-step procedure is repeated until the desired thickness is obtained. In some investigations the first step of KCSD procedure was performed by separate deposition of SrO and TiO_2 (topotactic reaction) [187, 193-196].

Our purpose was to explore the possibility of using the PLD technique for the synthesis of epitaxial STO layer on Si(001) as an alternative manufacturing route to MBE. In the following sections a systematic study of PLD synthesis of STO on Si is presented with particular emphasis placed on the determination of very critical initial deposition parameters. In the last part of this chapter a complete crystallographic characterization of obtained STO layers is given. In addition, the interface structure of STO/Sr(1/2 ML)/Si(001) by means of X-ray photoelectron spectroscopy (XPS) and X-ray reflectivity (XRR) is explained.

4.3.1 Determination of initial deposition conditions

Before the STO deposition was initiated the Si substrate surface was properly prepared. After cleaning with acetone and ethanol, the substrate was introduced into the PLD chamber and outgassed at 630 °C, as described in more details in the Section 3.2.1.3. Then the native oxide layer was desorbed by flashing the substrate to 1200 °C for 1.5 min. After

removal of the native oxide, the substrate temperature was reduced to 700 °C and Sr-buffer layer (1/2 ML coverage) was prepared by the deposition of elemental strontium. The STO layers were deposited at a fluence of 1.3 J/cm^2 and spot size of 0.58 mm^2. Our first STO deposition experiments were performed at T<200°C and different oxygen background pressures in the range from PLD base pressure (8×10^{-9} mbar - 1×10^{-8} mbar) up to 2×10^{-5} mbar, for which the resistance of the buffer layer against oxidation was shown (Section 4.2.3). As-deposited STO layers were amorphous as indicated by high-background intensity on the RHEED screen. The crystallization of the layers was performed by heating in vacuum (~1×10^{-8} mbar). For sufficiently thick layers (>6 ML; 1 ML = 1 unit cell of STO) rings were observed in the RHEED pattern after heating to ~630 °C (Figure 4.24a) which indicates polycrystalline STO layers. During further heating the rings gradually disappeared and streaks with additional spots emerged in the RHEED pattern (Figure 4.24b) at ~890 °C.

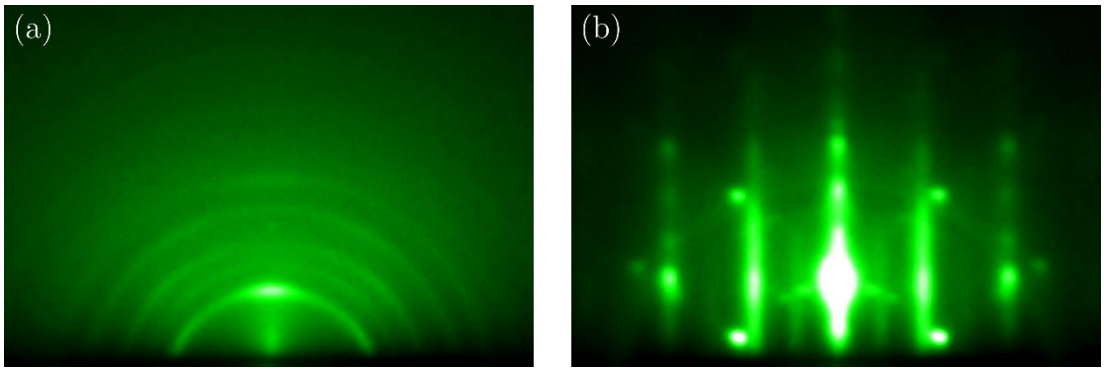


Figure 4.24: RHEED patterns of the STO layer in the [110] azimuth of Si taken after heating to (a) ~630 °C and (b) ~890 °C.

When deposited STO layer was too thin (<6 ML), no long-range order was observed by RHEED up to the temperature of 890 °C, when again the same RHEED pattern as for thicker layers was observed. Polycrystalline instead of epitaxial growth of STO layer at conditions which generally lead to the epitaxial growth by MBE implies the inefficiency of Sr-buffer layer in terms of structural template. As already mentioned in Section 3.2.1.1, high-energetic species from the plasma plume can damage the surface due to collisions that cause interface mixing and cross-contamination between STO layer and substrate. Implantation of ablated ions has been observed for PLD in some cases in literature [197-199]. Further experiments were therefore conducted at much higher background pressure in order to terminate the plume before it reaches the substrate surface. Based on the study of laser ablation plume dynamics, reported by Amoruso et al. [198], we decided for the pressure of 0.1 mbar. Since the buffer layer does not sustain such a high pressure of oxygen, argon gas was used instead.

We investigated the stability of the interface between Si and deposited STO by means of X-ray photoelectron spectroscopy (XPS). Samples of thickness lower than 10 nm were grown in order not to exceed the sampling depth of XPS. Figure 4.25a shows Si2p XPS spectra of samples deposited on the Sr-buffer layer at room temperature in vacuum (~1×10^{-8} mbar, green curve) and at 0.1 mbar Ar (red curve). In the XPS spectrum of vacuum deposited sample two types of chemically bonded Si were found. Beside the peak for elementary Si there exist also a broad peak at higher binding energy which suggests the formation of silicates at the interface region [162, 189]. No such peak was found for the sample prepared in Ar, showing the importance of the background gas in preserving the integrity of the Sr-buffer layer. These preliminary results motivated us for a more detailed

study of the influence of different background pressures of Ar on the interface, presented in section 4.3.1.1, where also results of spectra fitting are presented.

In Figure 4.25a one additional spectrum, indicated by black curve, is shown. It corresponds to the sample for which no buffer layer was prepared prior the STO deposition in vacuum. Only a slight increase of silicate peak intensity can be noticed when compared to the spectrum of the sample with the buffer layer. However, a significant difference between those two samples was noticed in RHEED during the deposition process. We monitored the number of pulses required for complete disappearance of the (1×2)+(2×1) RHEED pattern, characteristic for the Sr-buffer layer as well as the bare Si surface and showed that ~140 pulses were needed when the deposition was performed on the buffer layer, while the pattern of the bare reconstructed Si surface disappeared already after ~55 pulses. Gradual reduction of intensity during the room-temperature deposition is firstly related to the increase of surface coverage with the amorphous STO material, and secondly to the reaction of the surface with the deposited material. Since the contribution of the surface coverage is the same for both samples, the difference in number of pulses can be explained by passivation nature of Sr-buffer layer that slows down the reaction between Si and STO. Nevertheless, XPS spectra in Figure 4.25a show that the presence of Sr-buffer layer does not significantly affect the structure of the final interface when the deposition in vacuum is performed.

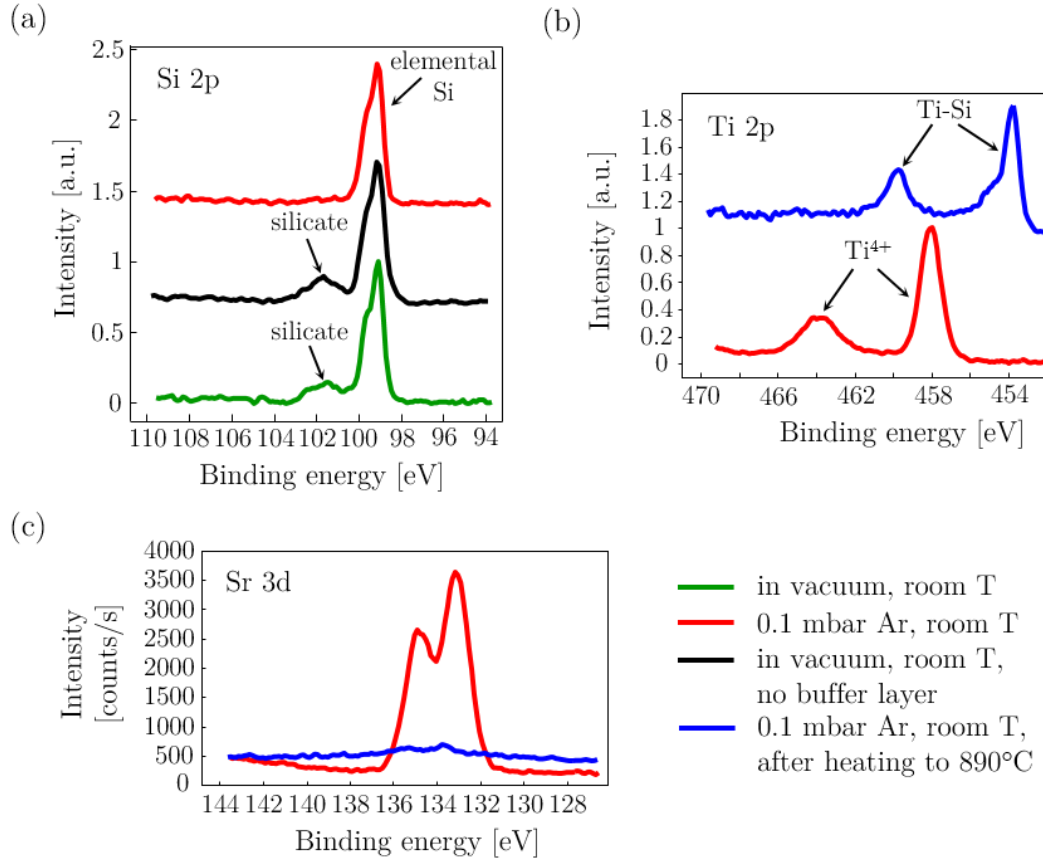


Figure 4.25: (a) Si 2p XPS spectra of STO/Si samples deposited on the Sr buffer layer at room temperature in vacuum (green curve) and at 0.1 mbar Ar pressure (red curve). Black curve represents spectrum of the sample prepared at room temperature in vacuum on the bare reconstructed Si surface (without Sr buffer layer) (b) Ti 2p and (c) Sr 3d XPS spectra acquired after deposition at room temperature and 0.1 mbar Ar pressure (red curve) and after further heating to 890 °C (blue curve).

According to the interface quality of the sample deposited at 0.1 mbar Ar, crystallization of the STO layer in the epitaxial form was expected after heating. Contrary to our expectations we obtained polycrystalline layers after heating to ~660 °C, similarly as already shown for the samples prepared at relatively low O_2 background pressures (Figure 4.24a). We assumed that the deposition in inert atmosphere resulted in strongly oxygen-deficient films which prevented the formation of epitaxial STO phase. This hypothesis is thoroughly discussed in section 4.3.1.3. After further heating to ~890 °C the same RHEED pattern, as the one shown in Figure 4.24b, was obtained. First inspection of the RHEED pattern could lead us to the incorrect conclusion about additional ordering of the STO layer. However, XPS spectra of Ti2p and Sr3d obtained after heating to 890 °C revealed decomposition of the STO layer at such a high temperature. The decomposition process is based on almost complete desorption of Sr containing species and reaction of titanium with the Si. Desorption of Sr is evident from Figure 4.25c, where the comparison of XPS spectra before and after heating to 890 °C is given. Formation of Ti-Si phases can be seen in Figure 4.25b where a large shift of peaks, corresponding to the photoemission from the $Ti2p_{1/2}$ and $Ti2p_{3/2}$, towards lower binding energy can be observed.

In addition, a composition of the layer was calculated from the high-resolution XPS spectra obtained after room-temperature deposition. A large deviation from ideal stoichiometry (Sr/Ti=1) was found, with Sr concentration twice as high as titanium, which is not generally expected for the PLD deposition. Additional investigation of the problem related to non-stoichiometry was therefore needed (see section 4.3.1.2).

4.3.1.1 Optimization of background gas pressure

The interaction dynamics of an expanding ablation plume with a background gas is a rather complex phenomenon. Various authors studied theoretically different effects involved in the process [200-205]. Since only some aspects of this complex phenomenon are revealed by most of these numerical models, the results often refer to specific gas/target systems, and cannot be simply used for the interpretation of results in experiments where other materials and ablation conditions were applied [206].

Our preliminary studies showed that sufficiently high pressure of argon background gas is required during the initial deposition stage in order not to damage the Sr-buffer layer. We demonstrated that the pressure of 0.1 mbar fulfill this requirement. However, not only the propagation of the plasma plume is affected by the background pressure, but also the microstructure of the deposited layer and the deposition rate per laser pulse. For instance, higher pressure can reduce the density of deposited layer and prolong the total deposition time for a given thickness. The determination of optimal pressure is therefore required. For this purpose different samples were prepared by the deposition of 6000 pulses at several different Ar pressures: in vacuum, 0.01, 0.02, 0.03, 0.04, 0.05, 0.1 and 0.15 mbar. Deposition of STO material was performed at room temperature. During each deposition of STO the repetition rate, fluence and spot size were kept constant at 1Hz, 1.5 J/cm^2 and 0.58 mm^2, respectively. The increase of fluence from 1.3 J/cm^2, used in the preliminary studies, to 1.5 J/cm^2, was done in accordance to results from stoichiometry investigation, presented in section 4.3.1.2.

X-ray reflectivity (XRR) proved to be the most convenient technique for characterization of as-deposited thin films. The comparison of reflectivity curves for samples deposited at different argon pressures is shown in Figure 4.26. For all the reflectivity curves the intensity increases within the angular range of $0<\omega<\omega_c$. From theory one would expect the reflectivity intensity to remain constant in this range. However, this is not the case in our experiments because for a given beam width and a very small incident angle, the projection of the incoming beam (A_{beam}) onto the sample surface (A_{sample}) exceeds

the sample size. Therefore, as the incident angle ω is increased during the measurement, A_{beam}/A_{sample} converge to one, causing intensity of reflected beam to increase. At a critical angle ω_c a rapid fall in intensity can be observed. From the position of ω_c, which varies significantly with background pressure (Figure 4.27), density of amorphous STO layers was determined based on fitting (Table 4.3) or calculation using the Equation (3.6). As a reference, reflectivity curve for STO substrate was simulated and is shown in Figure 4.27 as a black curve. Layers with the highest density (~84 % of theoretical density) can be prepared in the pressure range from vacuum up to 0.03 mbar. There was no significant difference in density observed for these samples. As the pressure was further increasing from 0.03 to 0.15 mbar the density was continuously decreasing, reaching 66 % of theoretical value for the pressure of 0.15 mbar.

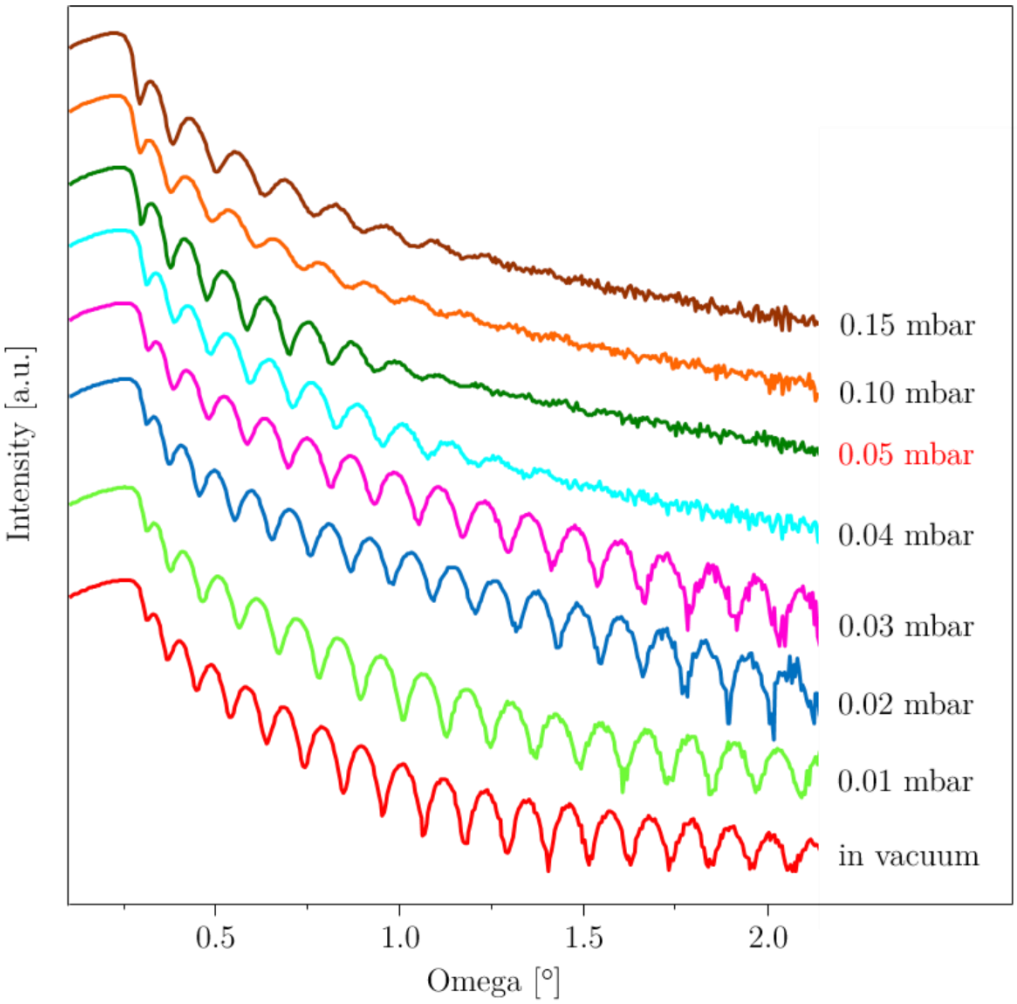


Figure 4.26: Comparison of X-ray reflectivity curves for samples prepared at different Ar background pressures.

The background pressure affects also the thickness of deposited layer. The deposition rate at higher pressures is expected to be lower due to collisional scattering and broadening of the vapor plume.

The thickness of STO layers was determined by Fourier and direct methods, described in more detail in Section 3.2.2.7. Figure 4.28 shows Fourier plot for the sample prepared in vacuum. Three peaks can be observed which correspond to separations of three pairs of interfaces. Peak at 39.4 nm is related to the STO layer, while peak at 2.5 nm corresponds

to interface layer which formed due to reaction between Si and STO. Third peak at 41.9 nm is related to the total thickness. Additional layer at the interface was detected also for the sample prepared at 0.01 mbar Ar pressure, while only one peak was observed in the Fourier plot for all the other samples. This does not necessarily mean that there is no interface layer present for the samples deposited at pressures higher than 0.01 mbar. Under circumstances of a limited dynamical range the reflectivity curve can be misinterpreted by a clean interface. In our case, small sample size significantly reduced the dynamical range which resulted in higher limit for the determination of a thin interface layer. Table 4.3 includes also the results of thickness calculations based on direct method. Several different thicknesses were determined for each sample, depending on which two fringes were selected for calculation. Averaging over more fringes generally leads to more accurate results. By means of both methods it was demonstrated that higher background pressure during the deposition results in lower layer thickness. In addition, a good agreement between the results obtained from both methods was shown.

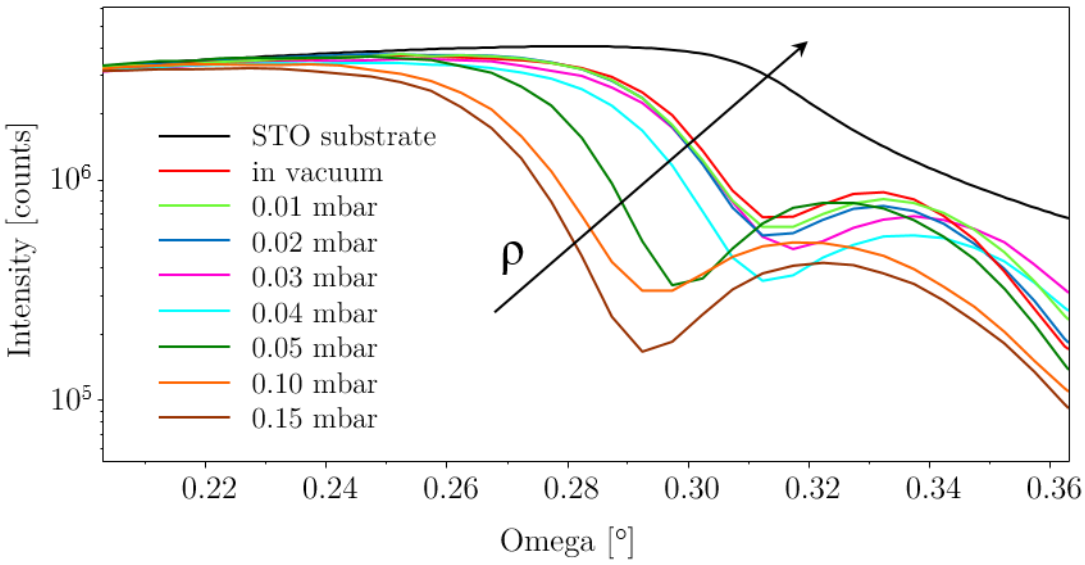


Figure 4.27: Comparison of initial part of X-ray reflectivity curves for samples prepared at different Ar background pressures in terms of critical angle ω_c. Density increases from the left (brown curve) to the right (black curve).

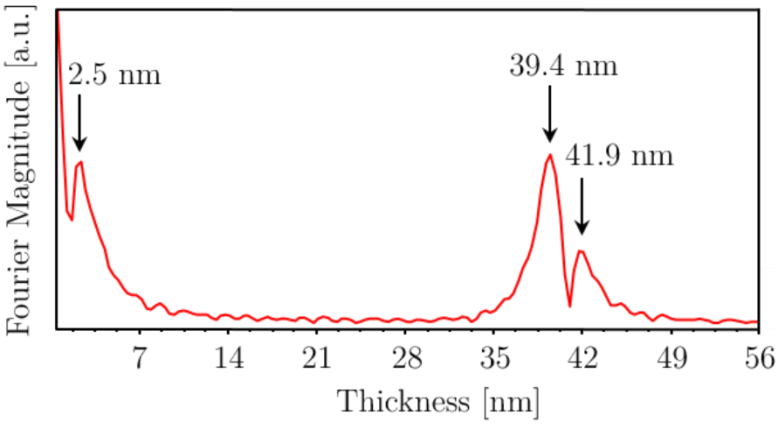


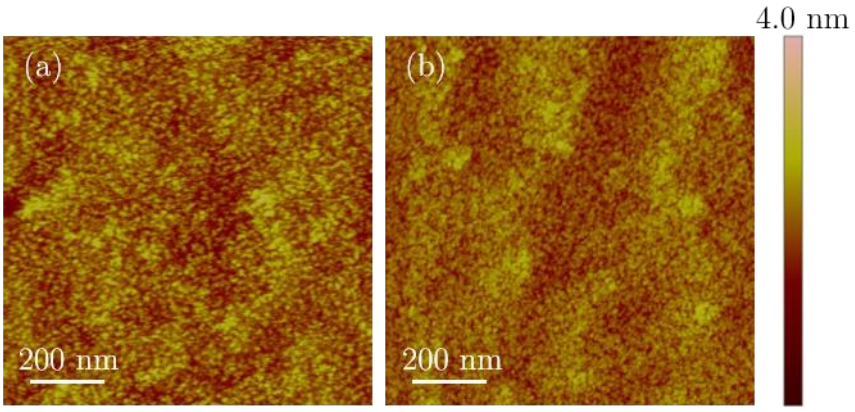
Figure 4.28: Fourier magnitude versus thickness plot for the sample prepared in vacuum ($\sim 1\times10^{-8}$ mbar). Peak positions give thickness information.

Table 4.3: Densities, surface roughnesses, and layer thicknesses of STO/Si samples prepared at different argon background gas pressures.

Argon pressure [mbar]		vac.	0.01	0.02	0.03	0.04	0.05	0.10	0.15
Density [g/cm^3]		4.34	4.26	4.25	4.25	4.09	3.78	3.51	3.39
Surface roughness [nm]		0.31	0.27	n.m.	n.m.	n.m.	0.44	0.46	0.45
Fourier method [nm]	STO layer	39.4	36.6	38.3	37.0	36.2	35.7	33.4	31.5
	Interface layer	2.5	2.3	n.d.	n.d.	n.d.	n.d.	n.d.	n.d.
	Total thickness	41.9	39	38.3	37.0	36.2	35.7	33.4	31.5
Direct method [nm]	1. and 2. fringe	46.6	39.3	38.9	38.4	37.2	36	33.4	32.6
	1. and 3. fringe	43.8	38.4	38.7	38.0	36.7	35.8	33.1	31.9
	1. and 4. fringe	42.8	38.2	38.6	37.7	36.6	35.3	33.2	31.3
	1. and 5. fringe	42.2	38.1	38.3	37.6	36.4	35.3	33.3	30.9
	1. and 6. fringe	41.6	37.6	38.1	37.3	36.3	35.5	33.5	/
	1. and 7. fringe	41.2	37.5	38.1	37.2	36.1	35.5	/	/

* n.d. . . . . not detected, n.m. . . . . not measured

Another very informative feature of reflectivity curve is damping of fringes. Presence of oscillations at high **ω** angles indicates a smooth surface. This is the case for samples prepared in vacuum, 0.01 mbar, 0.02 mbar and 0.03 mbar Ar pressure (Figure 4.26). For the sample deposited at 0.04 mbar the fringes vanished already at 1.45° as a result of significantly higher surface roughness compared to the samples prepared at lower background pressures. Important similarity of reflectivity curves can be observed for the samples prepared at 0.05 mbar, 0.10 mbar and 0.15 mbar pressure. All three curves exhibit oscillations up to the same **ω** angle, indicating constant surface roughness for layers deposited at pressure ≥ 0.05 mbar. This observation was additionally confirmed by atomic force microscopy (AFM) investigation (Figure 4.29). Samples deposited at 0.05 mbar (Figure 4.29c), 0.10 mbar (Figure 4.29d) and 0.15 mbar (Figure 4.29e) exhibit the same root mean square roughness (R_q) of 0.45 nm. On the other hand, significantly lower surface roughness was obtained for the samples deposited in vacuum (R_q=0.31 nm) and 0.01 mbar (R_q=0.27 nm). No AFM micrographs were collected for the samples deposited at 0.02, 0.03 and 0.04 mbar Ar pressure.



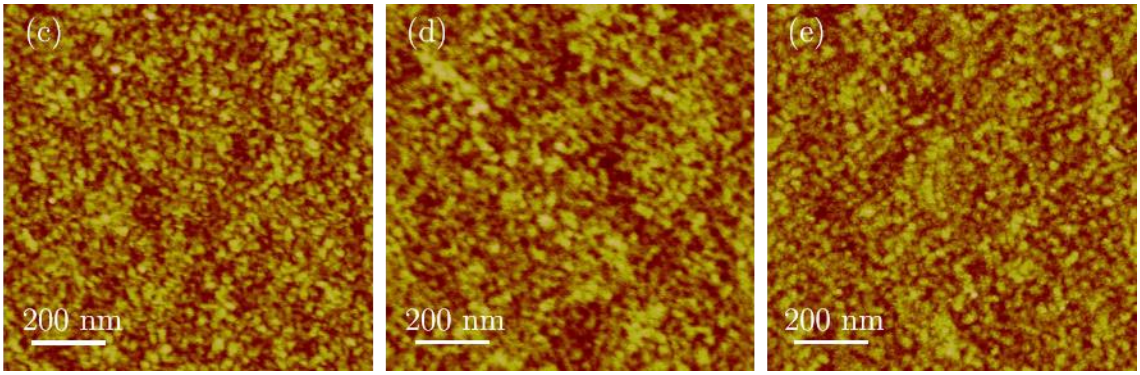


Figure 4.29: AFM images of STO thin films deposited at room temperature and (a) in vacuum, (b) at 0.01 mbar, (c) 0.05 mbar, (d) 0.1 mbar, (e) 0.15 mbar Ar pressure. The lateral scan size is 1×1 μm^2.

The topography was investigated also by scanning electron microscope (SEM). There was no topography contrast observed for the samples deposited in vacuum and 0.01 mbar due to the too small surface roughness, while a very similar microstructures with small cracks on the surface were observed for samples prepared at 0.05, 0.10 and 0.15 mbar (Figure 4.30).

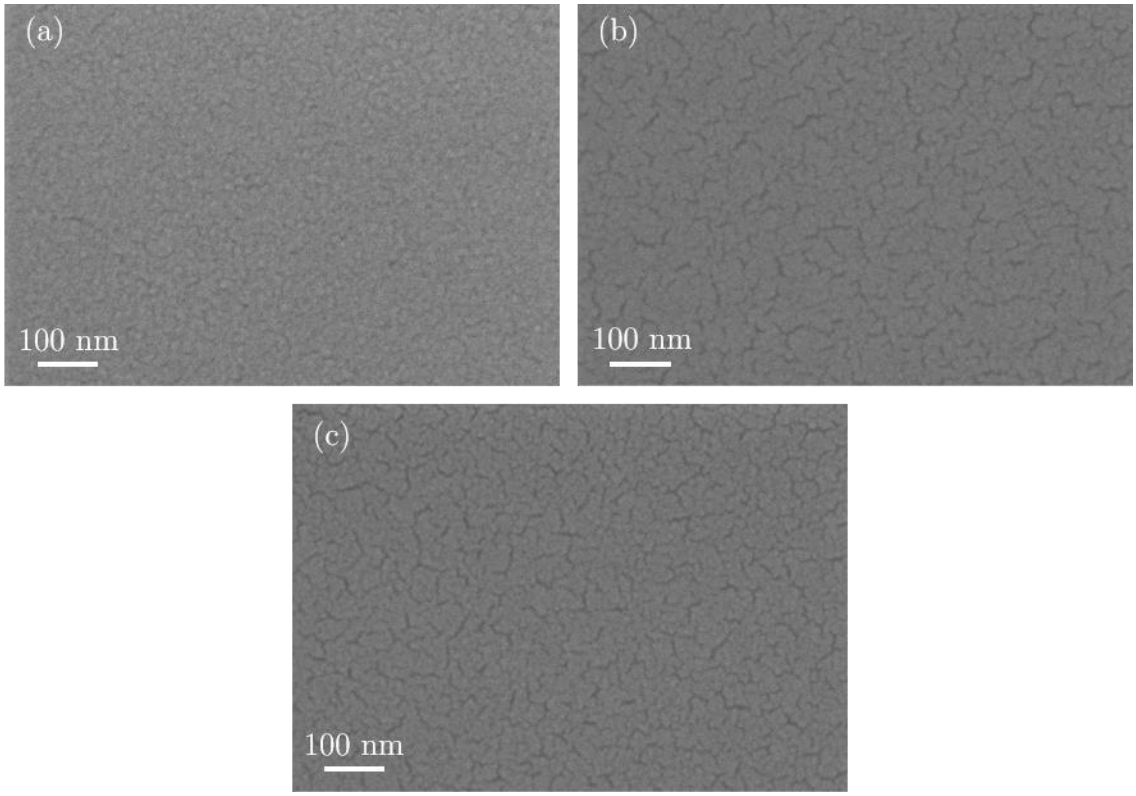


Figure 4.30: SEM images of STO thin films deposited at room temperature and (a) 0.05 mbar, (b) 0.1 mbar, (c) 0.15 mbar Ar pressure.

The influence of the background gas pressure on the surface roughness can be explained in terms of propagation dynamics of the ablation plume. As the pressure is raised the plume impacts the substrate at a progressively smaller velocity due to the interaction of the plasma species with the background gas. When the species reach the substrate surface their

kinetic energy is converted into surface diffusion energy which affects the final surface roughness. Another important property of the plume is its transition towards a diffusion-like propagation. This transition is related to plume stopping that occurs at progressively earlier times and shorter distances from the target surface by increasing the background pressure. Thus, constant surface roughness for the samples deposited at pressures ≥ 0.05 mbar can be explained by plume stopping which occurs at distance lower than target to substrate spacing. In this pressure range species arrive to the substrate surface by the diffusion and simply condense on it without further diffusion along the surface. Furthermore, no damage is expected to be caused to the Sr buffer layer by the species from the plume for such a high pressures. This was additionally confirmed by means of XPS studies. In order to be able to observe the interface region separate samples with STO thickness of 4.5 nm were prepared at the same conditions. The number of pulses required for 4.5 nm thick STO layers was obtained from the thickness analysis of reflectivity curves presented above. Figure 4.31a shows a series of detailed scans for different samples in the Si 2p region with all the spectra aligned for the Si 2p signal from the non-treated substrate (black curve on top).

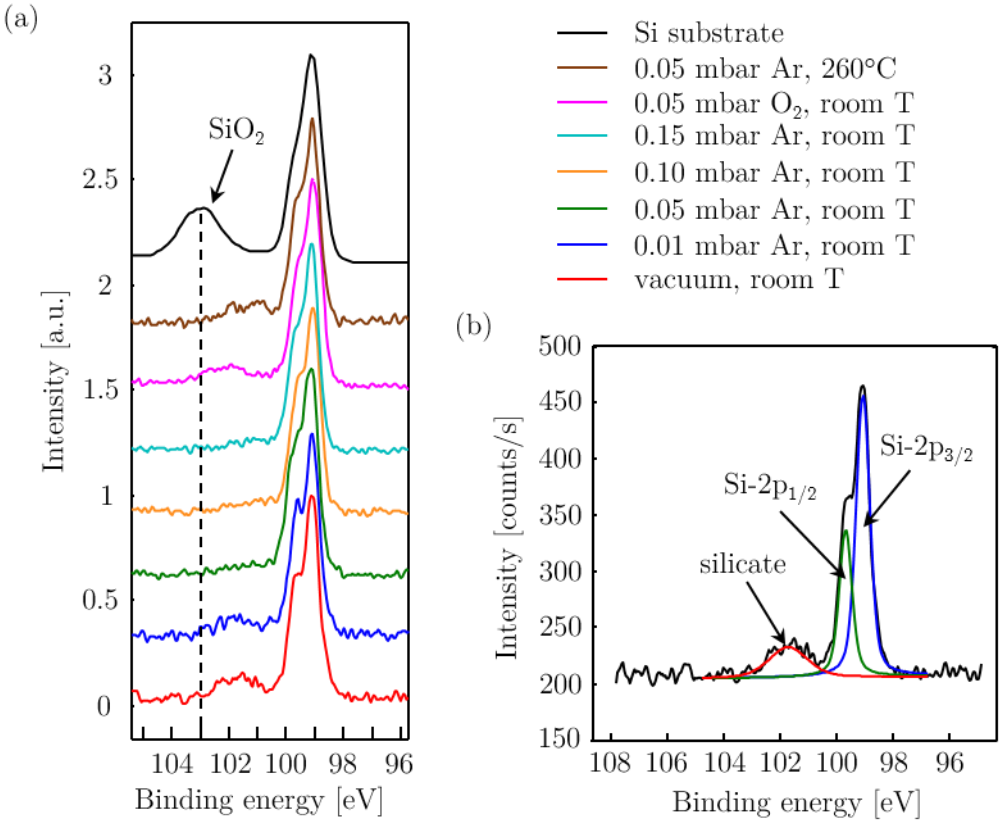


Figure 4.31: Si 2p XPS spectra from a 4.5 nm STO/Si samples prepared under experimental conditions which differ in background gas type (Ar and O_2), background gas pressure (vacuum-0.15 mbar) and substrate temperature (room T and 260 °C). (b) Si 2p XPS spectrum of the sample deposited in vacuum. The Si 2p can be well fitted by Si-$2p_{1/2}$ and $2p_{3/2}$ core levels and by silicate peak.

In XPS spectra of the samples prepared in vacuum and at 0.01 mbar two types of chemically bonded Si were found. Beside the elementary Si presented by a doublet Si-$2p_{1/2}$ and Si-$2p_{3/2}$, there exists also a broad peak at higher binding energy (Figure 4.31b). From the comparison with the spectrum for Si substrate covered with the native oxide layer it

is clear that this additional peak is not related to SiO_2. Based on the literature it can be explained by silicate phase which in our case forms due to the interface mixing and reaction of high-energetic species from the plasma plume with the Si substrate. Samples deposited at 0.05, 0.10 and 0.15 mbar Ar pressures exhibit the same XPS spectra where beside the elementary Si no other types of chemically bonded Si were observed, indicating the stable interface between the STO and Si. In summary, on the basis of XRR and XPS studies it was shown that the initial deposition of STO should be performed at pressure ≥ 0.05 mbar in order to ensure diffusion-like arrival of species to the substrate surface and consequently avoid formation of silicate at the interface. Furthermore, the pressure of 0.05 mbar seems to be the most suitable in terms of layer density and deposition rate when compared to higher pressures.

Using the optimal pressure for the deposition, two additional experiments were done. In the first experiment the influence of temperature on interface stability was studied. We showed that the deposition at 260 °C already results in thin silicate layer formation at the interface (brown curve). These results define also the optimal deposition temperature which should be close to room temperature. In the second experiment, oxygen was used instead of argon. Deposition in oxygen would considerably simplify the whole synthesis process since no further consideration about oxidation was necessary. However, also the oxygen atmosphere did not allow preparation of the clean STO/Si interface (pink curve) which is in accordance with instability of the Sr buffer layer at such high oxygen pressure.

4.3.1.2 Optimization of laser fluence

Our preliminary XPS studies showed twice as much strontium (Sr) as titanium (Ti) in the deposited STO layers. Considering the fact that the PLD is the most widely used method for the growth of complex oxides, in particular due to the generally excepted assumption of proper stoichiometry transfer from the target to the thin film, this large deviation from ideal N(Sr)/N(Ti)=1 stoichiometry surprised us even more. However, Dam et al. and Ohnishi et al. demonstrated that for PLD-grown films, the variation in stoichiometry can be achieved by varying the laser fluence [109, 207-209]. In addition, it was shown that stoichiometry is changing also with target-to-substrate distance when keeping the fluence constant [210].

To assure the right composition of initially deposited STO layer at room temperature and 0.05 mbar Ar pressure, a set of samples at several different fluencies was prepared and analyzed *ex-situ* by XPS. Figure 4.32a shows variation of ratio of the Sr to Ti with the laser fluence. A large excess of Sr compared to Ti can be noticed for all the samples. As a reference, composition of the STO substrate was measured in order to check reliability of the method. Obtained value of N(Sr)/N(Ti)=1.13 indicates slight overestimation of Sr content compared to Ti but still resembles the actual composition which should also apply to the results presented in Figure 4.32a. However, XPS is surface sensitive technique which results may not reflect the composition of the whole STO layer. To verify this hypothesis deep profiling by ion sputtering was performed on the sample prepared at 1.5 J/cm^2 in order to access the STO material also at larger depths. From the depth profile in Figure 4.33 it is evident that both, Sr and Ti atomic concentrations vary with sputtering time (sample depth), indicating inhomogeneous distribution of elements in the STO layer. Since the composition was calculated using a simplified model of a homogeneous matrix, this introduce an additional error in the concentration profile which should therefore be viewed on the relative scale only. In addition, preferential sputtering can also significantly affect the final concentration profile. The highest difference between concentrations of both elements can be observed at surface region. With depth, the strontium concentration

slightly decreases, while the Ti concentration increases. Such an inhomogeneity of Sr and Ti is not problematic if the overall content of Sr in the STO layer is equal to Ti due to complete homogenization of the layer during the crystallization step at higher temperature. Since the overall content of both metals cannot be derived from XPS investigation, inductively coupled plasma mass spectrometry (ICP-MS) and Rutherford backscattered spectroscopy (RBS) were used for that purpose. ICP-MS proved to be less appropriate due to the difficulties encountered during sample preparation (solubility problem). RBS analysis which results are presented in Figure 4.32b revealed that the overall composition of STO layers is much closer to the ideal one compared to the surface composition. Regardless of fluence used all the samples still exhibit larger atomic concentration of Sr than Ti. This can be explained by preferential scattering of light plume species, e.g., Ti in STO, during their flight towards the substrate. The plume species can undergo several collisions, both with the background gas molecules/atoms and among themselves. In any scattering event, the lighter species diffuses to larger angles, resulting in higher concentration of heavier species (Sr for STO) along the direction normal to the substrate. In order to confirm the above described impact of the background gas on stoichiometry additional set of samples was prepared in vacuum where no scattering with the background gas is present. All the vacuum-deposited samples exhibit stoichiometry very close to the ideal one. The maximum difference between Sr and Ti atomic concentrations was encountered for the fluence of 1 J/cm^2 (51.1 % Sr and 48.9 % Ti). Interpretation of observed variation of the STO thin film stoichiometry with the laser fluence is rather difficult and presumably results from an intricate combination between plume-background gas interaction (e.g. preferential scattering) and incongruent ablation of the STO target [210, 211]. In the case of vacuum-deposited samples also impact of re-sputtering on the film stoichiometry should be taken into account due to high kinetic energy of the plume species reaching the substrate [199]. Overall, we showed that the fluence of 1.5 J/cm^2 results in the most stoichiometric STO layers (51.4 % Sr and 48.6 % Ti) for the deposition performed at room temperature and 0.05 mbar Ar pressure.

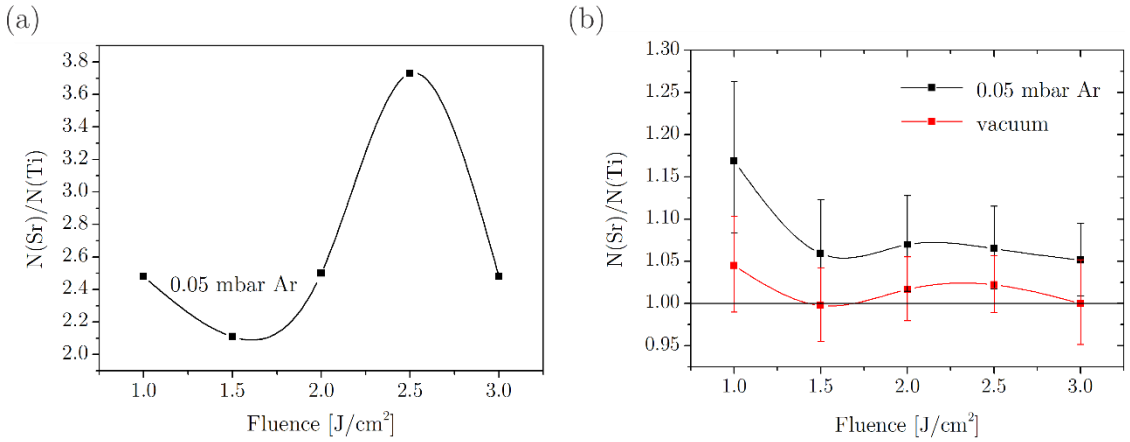


Figure 4.32: Sr/Ti atomic ratio in STO films deposited at different fluencies determined by (a) XPS and (b) RBS.

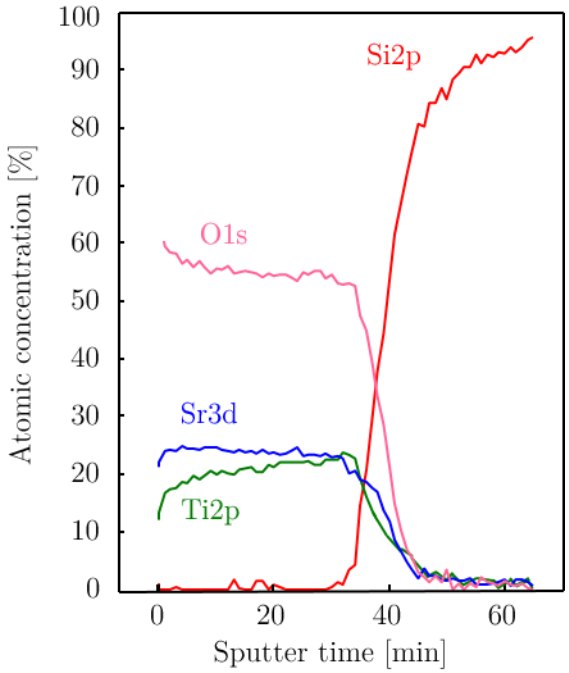


Figure 4.33: XPS depth profiles obtained on the sample deposited at room temperature, 0.05 mbar Ar pressure and 1.5 J/cm^2.

4.3.1.3 Oxidation of strontium and titanium

The most common way to deposit oxide films by PLD is to use an excess oxidant environment. The excess of oxygen helps to ensure that the grown film will be fully oxidized. However, this cannot be the case for STO deposition on Si where the prepared Sr buffer layer sustains oxygen pressure not higher than ~1×10^{-5} mbar. Introduction of oxidant into the system is therefore one of the most important and delicate steps in the transition from silicon to STO. Since strontium (Sr) and titanium (Ti) have very different electronegativities, it is also expected for them to have different oxidation behaviors. Sr becomes fully oxidized much more easily than Ti [55, 212] because of its smaller electronegativity. As a result, the threshold for oxidation of titanium represents an important process parameter. This threshold relates to the absolute minimum pressure where one can completely oxidize the metal and depends on deposition temperature as well as arrival rate of Ti. For a Ti metal flux of about one monolayer per minute, this pressure was experimentally found to be around 1.3-2.7$\times10^{-6}$ mbar [213, 214]. In addition, it was shown that the presence of Sr promotes Ti oxidation by providing a different transition state that has a lower reaction barrier for Ti oxidation [212]. Consequently, growth of STO can be conducted at even lower oxygen pressure than 1.3×10^{-6} mbar. Despite the resistivity of the buffer layer against oxidation at the pressures required for complete oxidation of Ti and Sr, we showed that at least 0.05 mbar pressure is needed during the initial deposition of STO in order to completely avoid the reaction at the interface due to the collisions of high-energetic species from the plasma plume with the Si substrate. Such a high pressure allowed us to work in inert atmosphere of Ar only. Regardless of the presence of oxygen in the STO target, we assumed that the deposition in Ar leads to oxygen deficient films which could prevent STO to crystallize in an epitaxial and highly crystalline manner. In order to determine the extent of Ti oxidation in STO films deposited at room temperature and 0.05 mbar Ar pressure, XPS depth profiling by ion sputtering was performed. Figure 4.34 shows a stack of Ti2p XPS spectra obtained at different depths during XPS depth profiling.

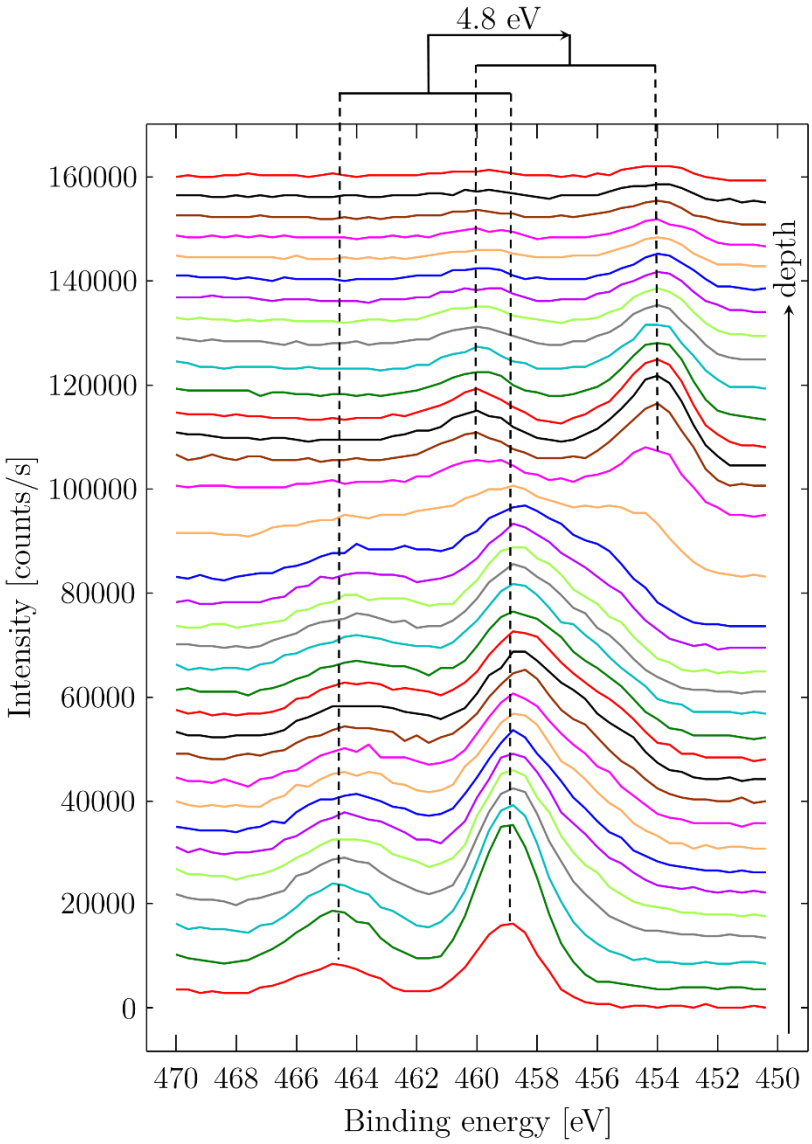


Figure 4.34: Ti 2p XPS spectra obtained at different depths during XPS depth profiling of the STO layer deposited at room temperature and 0.05 mbar Ar pressure. Left and right peaks in each of the spectrum correspond to the photoemission from the Ti $2p_{1/2}$ and Ti $2p_{3/2}$ energy levels, respectively.

Two peaks which correspond to the photoemission from the Ti $2p_{3/2}$ and Ti $2p_{1/2}$ energy levels can be observed in all the spectra. The second feature from Figure 4.34 is a shift of both peaks for 4.8 eV to lower binding energies in the XPS spectra obtained deeper in the sample (closer to the Si substrate). The Ti $2p_{3/2}$ binding energies of ~459.0 eV and 454.2 eV are characteristic for TiO_2 and metallic Ti, respectively. This indicates that in the upper part of STO layer Ti is oxidized while in the interior part it is metallic. Presence of TiO_2 can be explained by the exposure of the sample to air during transfer from the PLD to XPS UHV chamber. In order to limit the exposure to the shortest possible time, the sample was first transferred from the PLD chamber to the glove-box. In inert atmosphere of the glove-box sample was inserted into special gas-tight sample holder and transferred to the XPS laboratory. Interaction with air occurred for less than 30 s just prior the insertion of the sample into the XPS UHV chamber. Another feasible reason for the presence of TiO_2

could be oxidation caused by oxygen from the STO target. However, presence of metallic Ti deeper in the sample is a clear indication of strongly oxygen deficient film and we believe it reflects Ti oxidation state throughout the whole STO layer after PLD deposition in argon. Based on these results it can be concluded that the initial deposition of STO should be done in sections. We first need to grow amorphous STO with the right stoichiometry at room temperature and 0.05 mbar Ar pressure, preventing the formation of silicate at the interface. Then we evacuate the argon and perform oxidation at oxygen partial pressure sufficiently high to fully oxidize titanium as a second step. For complete oxidation of titanium across the whole thickness, deposited STO layer from the first step should not be too thick. These two steps are then repeated until the optimal thickness for the crystallization at higher temperature is achieved.

4.3.2 Final deposition of $SrTiO_3$

Final and most important goal was to grow epitaxial STO layer on Si(001). In order to succeed in this very challenging task all the knowledge gained from investigation performed so far was combined and used in this final step. First, clean (free of carbon) reconstructed Si(001) surface was prepared by flashing the substrate to 1200 °C for 1.5 min. In the next step 1/2 ML of Sr was deposited on clean Si(001) at 700 °C to form the Sr-buffer layer with (1×2)+(2×1) reconstruction. The substrate temperature was then reduced to room temperature where deposition of STO seed layer was initiated. The deposition procedure for the seed layer was derived from detailed studies of initial deposition conditions and is as follows. First, ~1 ML of amorphous STO layer with the right stoichiometry (fluence=1.5 J/cm^2) was grown at room temperature and 0.05 mbar Ar pressure, preventing the formation of silicate at the interface. The number of pulses required for 1 ML was determined from XRR measurement. Then, the Ar was removed from the growth chamber and oxygen was introduced to a partial pressure of 1.1×10^{-7} mbar for 5 min in order to oxidize Ti and Sr. Deposition of the second and third ML of STO was performed at the same conditions as the first one. The only difference was in the oxidation step which was conducted at slightly higher oxygen pressure of 9.3×10^{-7} mbar. After the oxidation of the last (third) ML of STO oxygen was removed from the growth chamber and the 3 MLs thick seed layer was slowly heated up in vacuum (~1×10^{-8} mbar) to the temperature in the range from 517 °C to 636 °C for 15 min to crystallize it. We continued with the growth of the STO seed layer. Again, 3 MLs thick STO layer was deposited at room temperature and 0.05 mbar Ar pressure in parts of 1 ML with intermediate 5 min long oxidation periods at 9.3×10^{-7} mbar. The deposition step was followed by crystallization step as already described for the first 3 MLs. These two steps were then repeated until achieving the desired seed layer thickness. In experiments described later in this chapter either 9 (3×3 MLs) or 15 MLs (5×3 MLs) thick STO seed layer was prepared. Normally, to grow crystalline oxides, one needs both a high temperature and sufficiently high oxygen pressure. But because simultaneous use of those two conditions led to oxidation of the silicon, we had to separate them in time. Once the crystalline STO seed layer was formed in this way, additional STO was deposited on top of it in much faster growth regime. This subsequent STO was deposited at temperature in the range from 517 °C to 636 °C and 1.3×10^{-6} mbar oxygen pressure. The amount of oxygen pressure was selected according to investigation done by Heyd et al. [213]. They showed that the minimum pressure for complete oxidation of Ti at growth speed of about one ML per minute amounts to around 1.3-2.7×10^{-6} mbar. In total 7366 pulses were deposited during the subsequent STO growth with the repetition rate of 1 Hz. For the sake of clarity schematic drawing of complete fabrication procedure is shown in Figure 4.35.

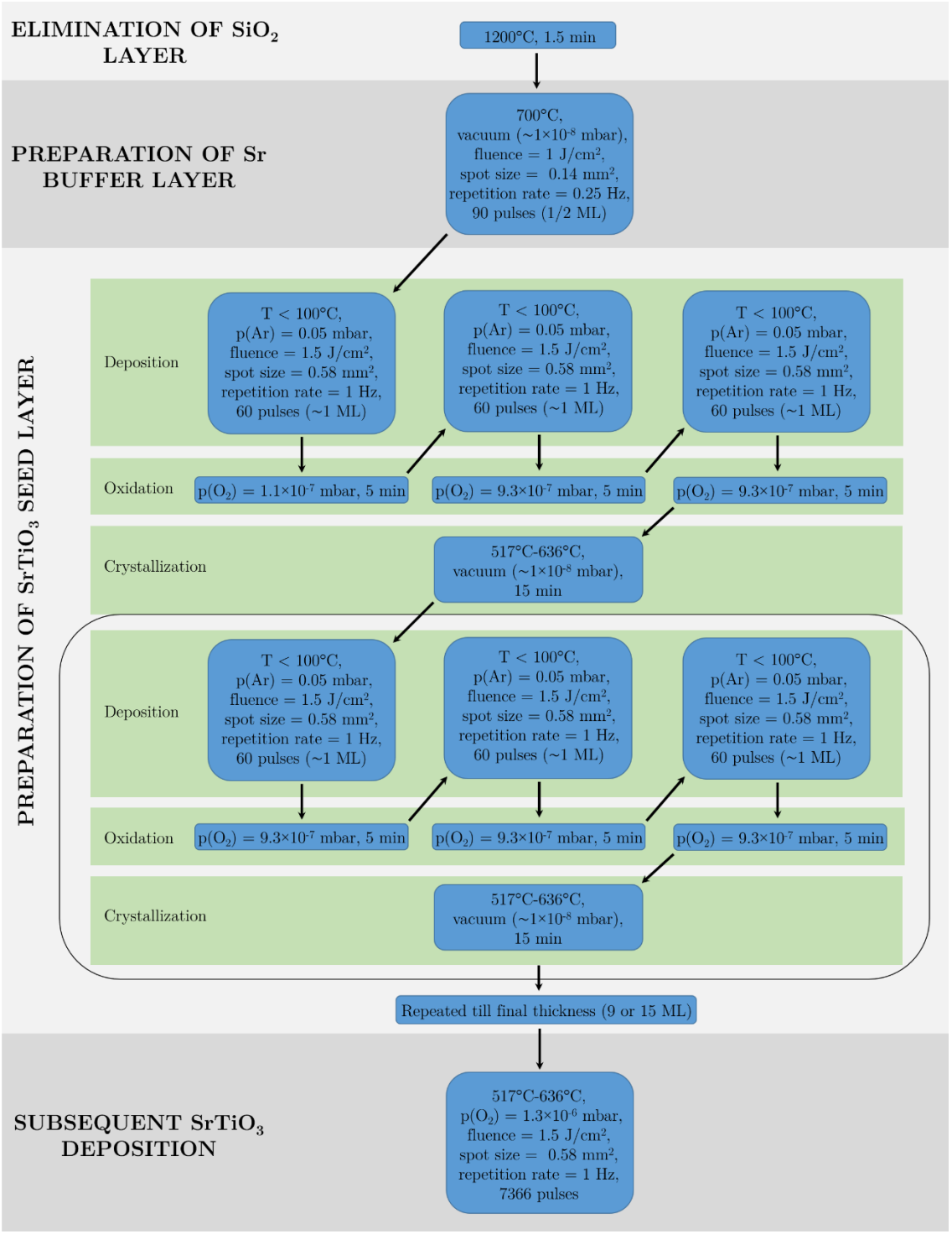


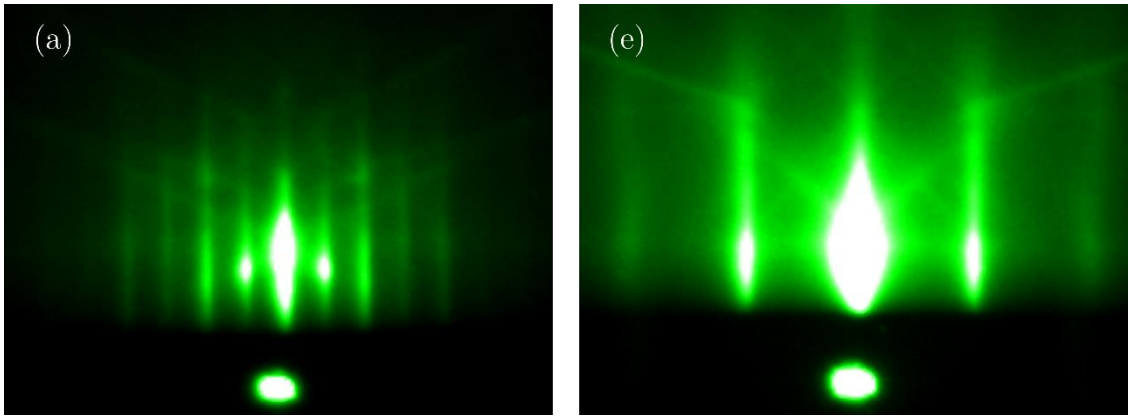
Figure 4.35: Complete experimental procedure for the preparation of STO layers on Si(001).

We found that the quality of final STO layer is significantly influenced by the crystallization temperature, thickness of the STO seed layer as well as the temperature of the subsequent STO deposition. All the experiments that will be discussed below are summarized in Table 4.4.

Table 4.4: Summary of experiments conducted under different experimental conditions

	STO seed layer		Subsequent STO deposition
	Thickness [ML]	Crystallization temperature [°C]	Deposition temperature [°C]
Experiment 1	9	636	636
Experiment 2	9	577	636
Experiment 3	9	517	636
Experiment 4	9	577	577
Experiment 5	9	546	546
Experiment 6	15	546	546
Experiment 7	15	517	517

Figure 4.36 shows RHEED patterns in [110] and [100] high-symmetry directions of Sr-buffered Si obtained before the deposition of the STO seed layer (Figure 4.36a, e) and after the deposition of 1 ML (Figure 4.36b, f), 2 MLs (Figure 4.36c, g) and 3 MLs (Figure 4.36d, h) of STO at room temperature. Deposition was initiated on (1×2)+(2×1) reconstructed surface characteristic for the Sr-buffer layer. After the deposition of 1 ML the intensity of integer and half-order streaks greatly decreased as a result of surface coverage with amorphous STO material which does not exhibit any diffraction. Their faint visibility can be explained either by incomplete surface coverage or penetration depth (more accurately information depth) of electron beam which is somewhere in the range from 5 to 20 Å, depending on material and incidence angle. After the deposition of 2 MLs the only visible feature was the central spot, while after 3 MLs only high background could be observed.



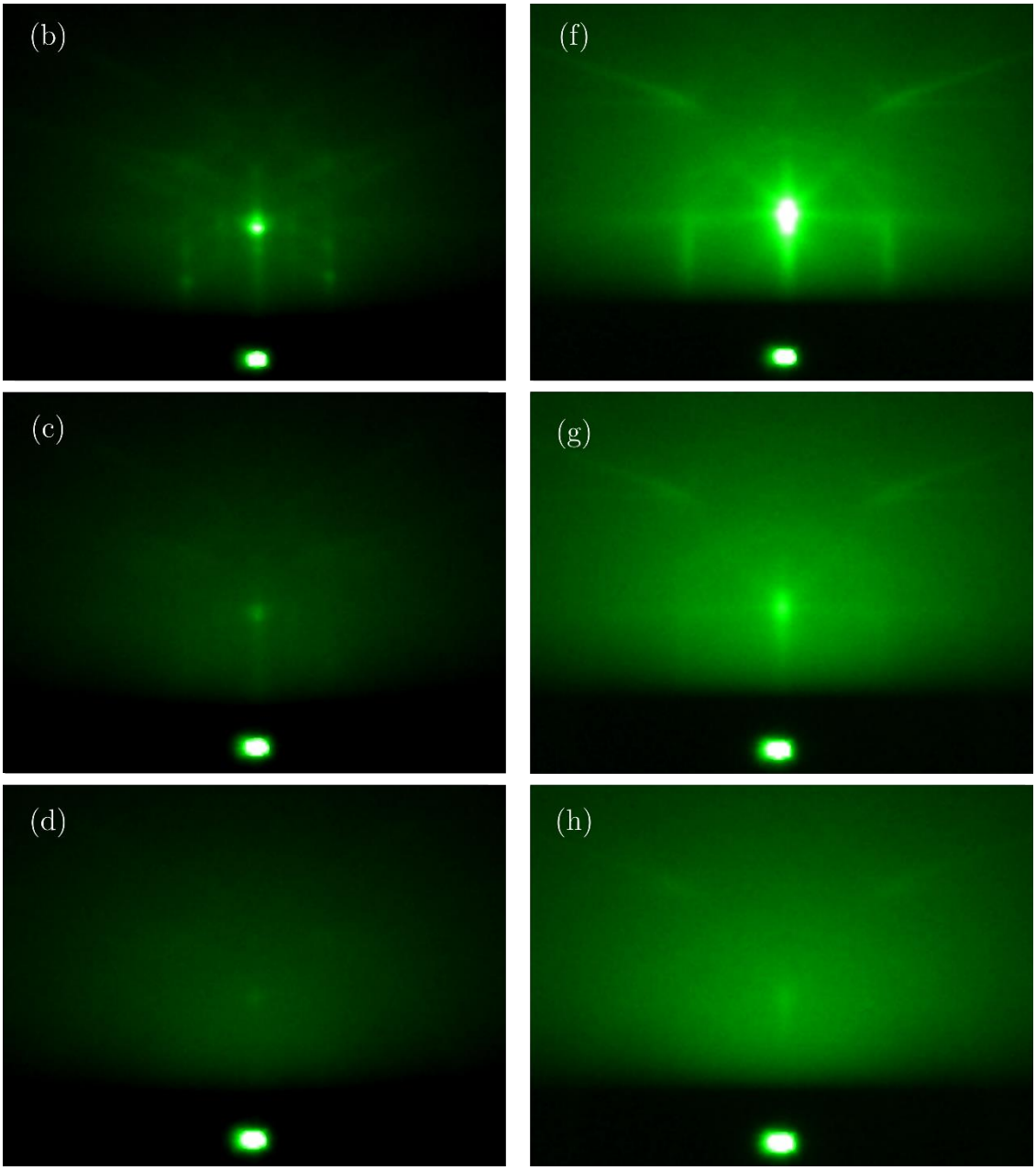


Figure 4.36: RHEED patterns in the [110] (a-d) and [100] (e-h) azimuth of Sr-buffered Si taken before the deposition of the STO seed layer (a, e) and after the deposition of 1 ML (b, f), 2 MLs (c, g) and 3 MLs (d, h) of STO at room temperature.

In Experiment 1 this 3 MLs thick STO layer was heated to 636 °C. At this temperature very weak streaks emerged in the RHEED pattern after few minutes and this was our first indication of the epitaxial growth (Figure 4.37a). The crystallization of next 3 MLs thick amorphous STO layer at 636 °C resulted in significantly improved intensity of the diffraction streaks (Figure 4.37b). This is related to larger total thickness which amounts to 6 MLs after the second crystallization step. Figure 4.37c shows RHEED pattern of 9 MLs thick crystalline STO seed layer with even higher intensity of diffraction streaks. Similarly, streaks were also observed in [110] azimuth of STO, as shown in Figure 4.37d which represents RHEED pattern of 6 MLs thick STO layer after the crystallization. However, in addition to streaks corresponding to epitaxially grown STO layer with only one in-plane

and one out-of-plane orientation, some quasi-spots were observed at small tilt angle, indicated with white arrows. These quasi-spots reveal that the epitaxial growth is not perfect and are presumably related to some additional crystallographic orientations of the STO seed layer. Subsequent deposition of 7366 pulses at 636 °C resulted in RHEED patterns presented in Figure 4.37e, f. Besides the streaks a lot of spots can be observed in both azimuths, showing the growth is far from being epitaxial.

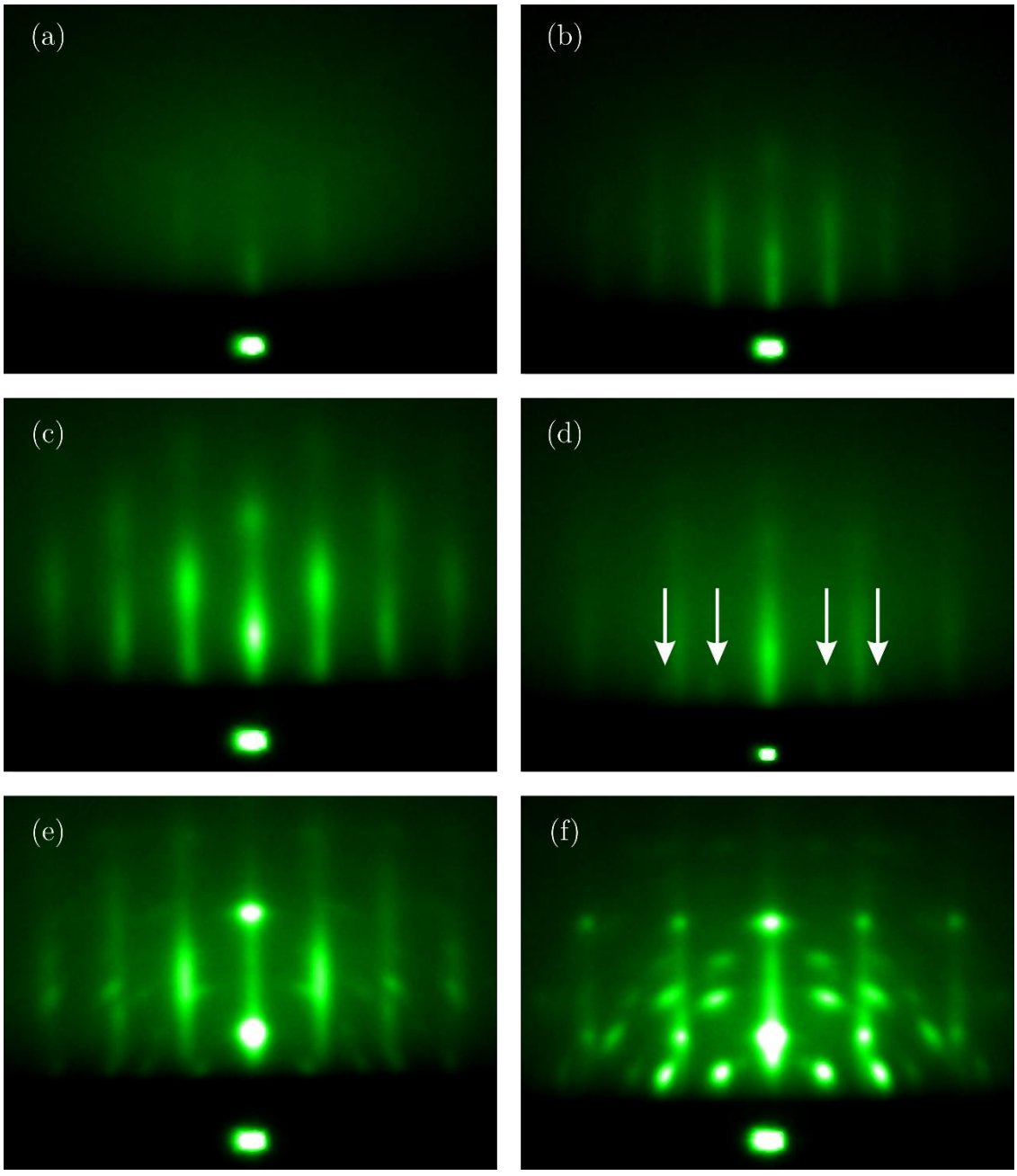


Figure 4.37: Experiment 1 - RHEED patterns in the [100] azimuth of STO taken after (a) first (3 MLs), (b) second (6 MLs) and (c) third (9 MLs) crystallization step at 636°C. (d) RHEED pattern in the [110] azimuth of STO taken after second (6 MLs) crystallization step. White arrows indicate additional quasi-spots. RHEED patterns in the (e) [100] and (f) [110] azimuth of STO taken after subsequent deposition of 7366 pulses at 636 °C.

XRD analysis of the STO film from the Experiment 1 shows strong (001) and (002) peaks and much weaker (111) and (011) peaks of STO in addition to Si substrate peaks, indicating highly textured nature of the layer (red curve in Figure 4.38). In order to make (111) and (011) peaks in the diffractogram visible y-axis is presented in logarithmic scale. We believe the subsequent growth of STO at 636 °C was not successful due to the poorly prepared seed layer as indicated by additional spots in the RHEED pattern (Figure 4.37d), and is a consequence of too high crystallization temperature.

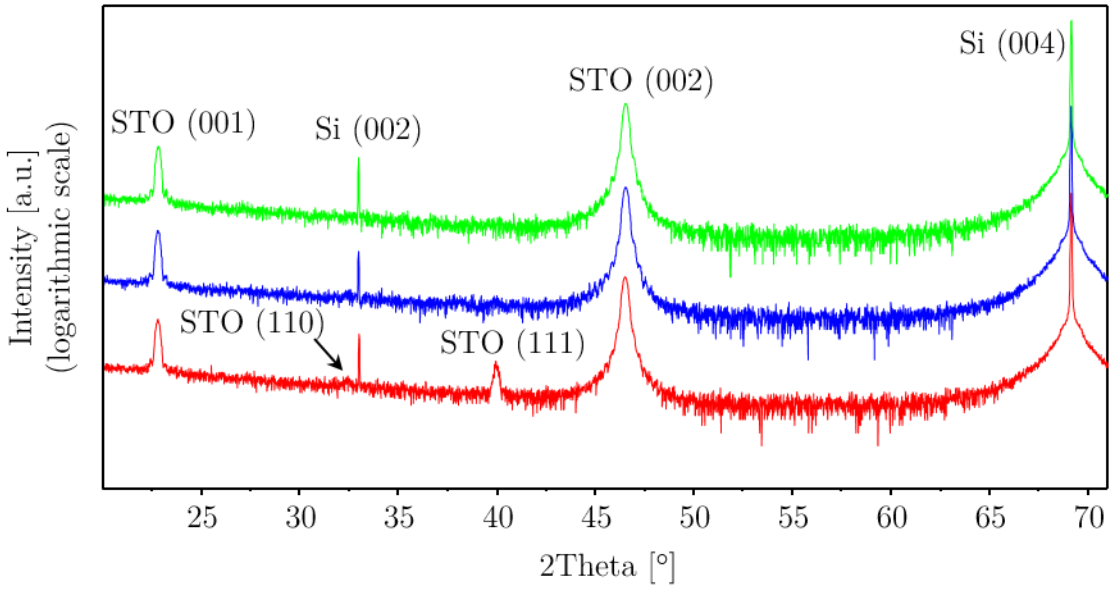


Figure 4.38: XRD 2Theta/Theta scans of STO/Si samples prepared in Experiment 1 (red curve), Experiment 2 (blue curve) and Experiment 3 (green curve).

Therefore, in Experiment 2 the crystallization temperature of the STO seed layer was decreased to 577 °C while the temperature of the subsequent STO deposition was kept the same as in the Experiment 1. Firstly, diffraction streaks of lower intensity were observed after first (3 MLs), second (6 MLs) and third (9 MLs) crystallization step (Figure 4.39a, b, c) compared to the Experiment 1 and secondly, no additional quasi-spots emerged in [110] azimuth (Figure 4.39d). Higher quality of the STO seed layer also resulted in less textured structure of the final STO film (after subsequent deposition) (Figure 4.39e, f).

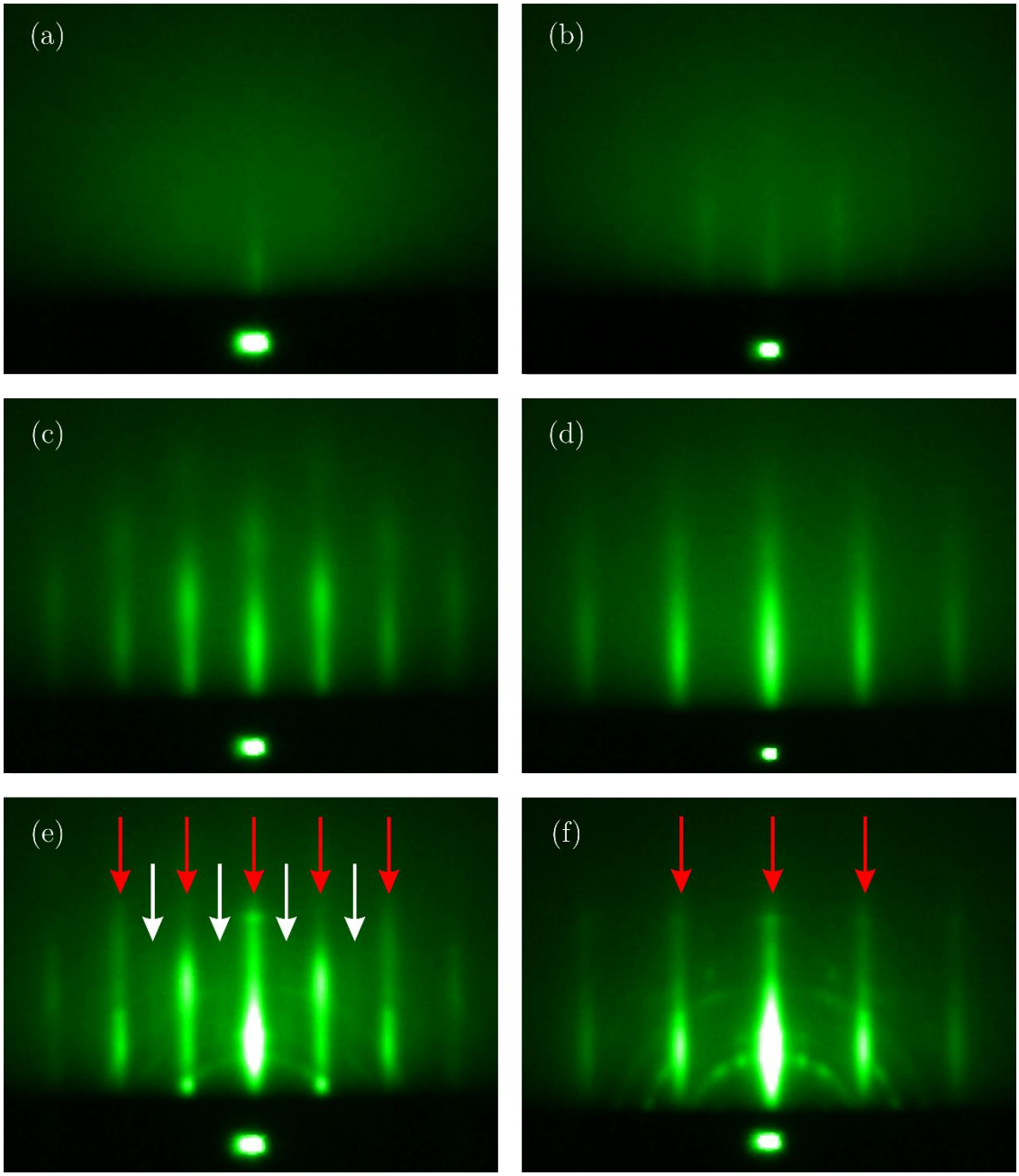


Figure 4.39: Experiment 2 - RHEED patterns in the [100] azimuth of STO taken after (a) first (3 MLs), (b) second (6 MLs) and (c) third (9 MLs) crystallization step at 577 °C. (d) RHEED pattern in the [110] azimuth of STO taken after second (6 MLs) crystallization step. RHEED patterns in the (e) [100] and (f) [110] azimuth of STO taken after subsequent deposition of 7366 pulses at 636 °C.

This was additionally confirmed by XRD where only a slight increase of intensity was observed at 2Theta positions characteristic for (111) and (110) STO peaks (blue curve in Figure 4.38). Epitaxial STO layers with the right stoichiometry exhibit a (1×1) surface reconstruction which results in streaks, indicated by red arrows in Figure 4.39e, f. However, we observed additional streaks along the [100] azimuth which arise from 2× surface reconstruction. These additional streaks, indicated by white arrows, have very low intensity and are characteristic for Ti rich surface [4, 12, 161]. They were also observed in final RHEED patterns of all the following experiments, showing that the subsequent deposition

results in slightly Ti-rich films. Thus, in this special case of $SrTiO_3$ real-time RHEED enables precise in-situ analysis of the stoichiometry.

In Experiment 3 even lower crystallization temperature of 517 °C was applied. This time streaks in RHEED patterns firstly appeared during the second crystallization step (Figure 4.40b). In addition to streaks one very faint ring can be observed close to the direct beam in the RHEED patterns in both azimuths of the final STO layer (Figure 4.40e, f). Besides, some distinct spots lying on Laue circles, are present in [110] direction. However, a significant improvement of those two patterns compared to the patterns from the Experiment 2 can be noticed.

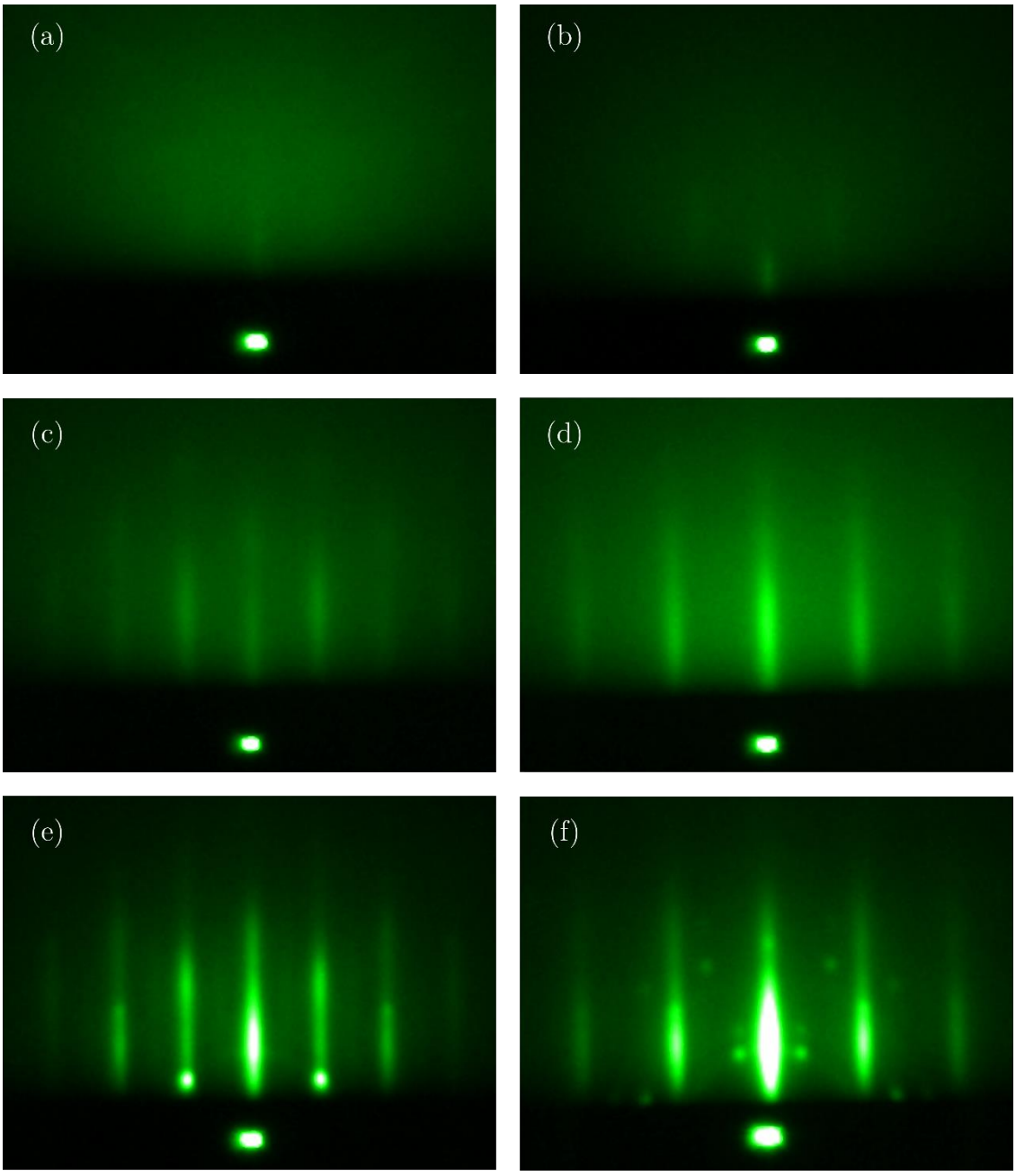


Figure 4.40: Experiment 3 - RHEED patterns in the [100] azimuth of STO taken after (a) first (3 MLs), (b) second (6 MLs) and (c) third (9 MLs) crystallization step at 517 °C. (d) RHEED pattern in the [110] azimuth of STO taken after second crystallization step.

RHEED patterns in the (e) [100] and (f) [110] azimuth of STO taken after subsequent deposition of 7366 pulses at 636 °C.

In the diffractogram of 2Theta/Theta scan only (00l) reflections are present, indicating single (001) out-of-plane orientation (green curve in Figure 4.38).

In experiments 4 and 5 another two combinations of crystallization and subsequent deposition temperatures were applied. Crystallization of the STO seed layer was conducted at 577 °C and 546 °C in Experiments 4 and 5, respectively. According to the RHEED patterns the STO seed layer from both of the experiments is completely epitaxial. The subsequent deposition at 577 °C (Experiment 4, Figure 4.41a, b) and 546 °C (Experiment 5, Figure 4.41c, d) resulted in RHEED patterns very similar to those from experiments 2 and 3, respectively. Since in the Experiments 4 and 2 STO seed layer was prepared under the same experimental conditions, it can be concluded that the decrease of subsequent deposition temperature from 636 °C to 577 °C does not result in any significant improvement in quality of the final STO layer. From the comparison of Experiments 5 and 3 it can be additionally concluded that the crystallization of the STO seed layer in the temperature range from 517 °C to 546 °C and subsequent deposition performed in the temperature range of 546-636 °C result in same RHEED patterns of the final STO layers. Thus, the improvement achieved in the Experiment 5 compared to Experiment 4 can almost exclusively be ascribed to lower crystallization temperature of the STO seed layer. Based on the experiments so far described the crystallization temperature of the STO seed layer should not be higher than 546 °C.

Since there was no improvement expected to be provoked by even further lowering of the temperature, we increased the thickness of the STO seed layer from 9 to 15 MLs (Experiment 6). It could be the case that 9 MLs thick STO seed layer does not provide sufficient barrier between subsequently deposited STO material and Si/STO(seed layer) interface. Besides, due to the non-uniform surface coverage some areas can be poorly covered and therefore very sensitive in the interaction with high energetic species from the plasma plume during the subsequent deposition. Preparation of thicker STO seed layer proved to be advantageous because the final RHEED pattern in [110] direction exhibited less spots (Figure 4.41f), the intensity of remaining spots slightly decreased compared to the Experiment 5 and no rings could be encountered anymore.

In Experiment 7 the temperature of the crystallization and subsequent deposition was decreased to 517 °C, maintaining the thickness of the STO seed layer at 15 MLs. Under these conditions the intensity of spots in [110] direction was the lowest among all the samples (Figure 4.41h). Since this was the most promising sample in terms of RHEED results, a detailed crystallographic characterization of the layer was performed. However, before proceeding with XRD results, we would like to discuss possible reasons for emergence of these additional diffraction spots in [110] direction. Yu et al. claimed that when the Sr and Ti flux imbalance is not corrected during the co-deposition (MBE growth), secondary phases of either SrO (Sr flux is slightly higher than Ti flux) or TiO_2 (Ti flux is slightly higher than Sr flux) forms in the film and on the surface, causing spotty features to appear in between the major RHEED streaks [161]. Since the subsequent deposition in our case leads to slightly Ti-rich films, there could exist some TiO_2 precipitates in the STO films. However, according to the study performed by Suzuki et al. precipitates of the TiO_2 phase were observed for strongly Sr-deficient films only [215]. In addition, TiO_2 precipitates were found to be amorphous and therefore cannot explain appearance of diffraction spots in the RHEED. Another explanation could be that these spots arise from crystallites with crystallographic orientation different from majority of the STO film.

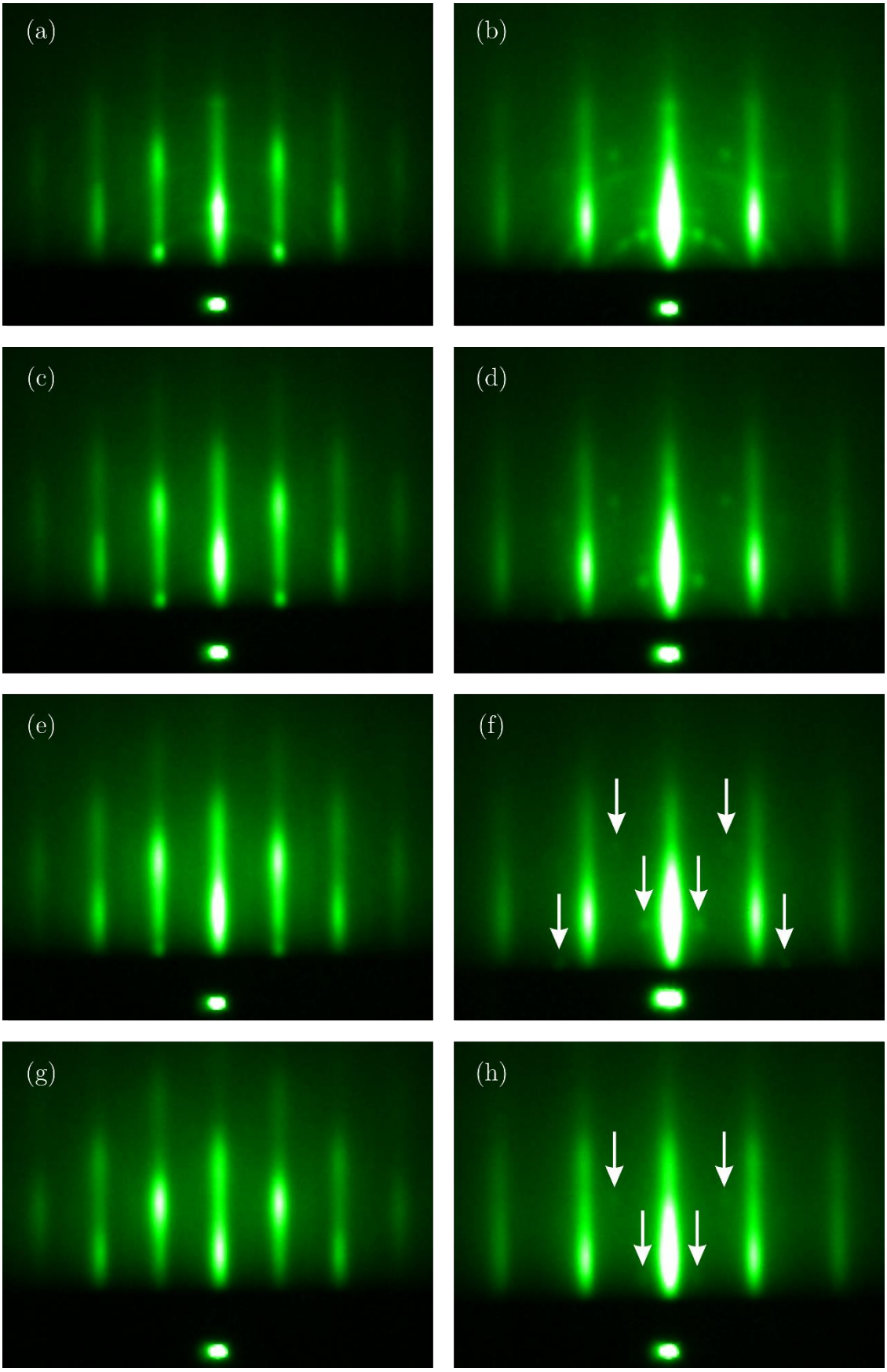

(a)
(b)
(c)
(d)
(e)
(f)
(g)
(h)

Figure 4.41: RHEED patterns in the [100] (a, c, e, g) and [110] (b, d, f, h) azimuth of Si taken after subsequent deposition of STO in Experiment 4 (a, b), Experiment 5 (c, d), Experiment 6 (e, f) and Experiment 7 (g, h). White arrows indicate additional spots which most likely arise from small portion of crystallites with other crystallographic orientation than the majority of the STO film.

Figure 4.42 shows the XRD 2Theta/Theta scan of the sample. All the peaks present in the diffractogram can be described with Si and STO phases, indicating single-phase film. In addition, only STO (00l) reflections were observed, showing the film out-of-plane relationship as STO(001)||Si(001).

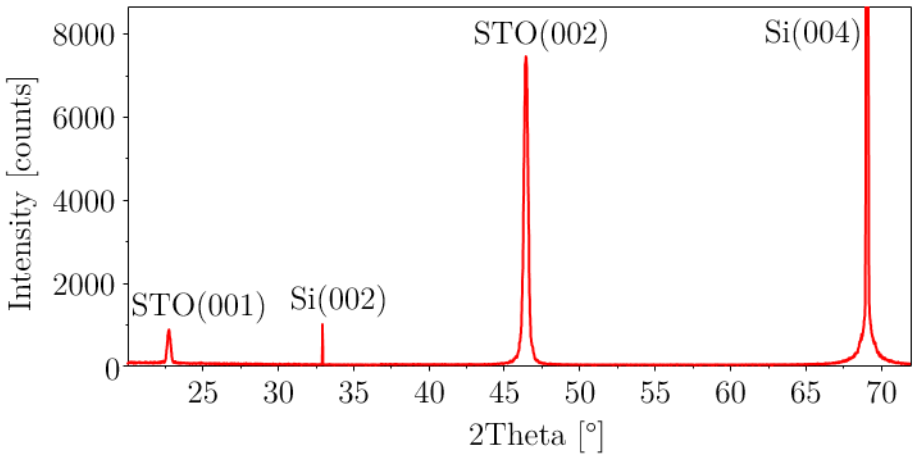


Figure 4.42: XRD 2Theta/Theta scan of STO/Si sample prepared in Experiment 7.

In order to determine the epitaxial relation of STO layer and the substrate, an azimuthal or Phi (ϕ) scan was performed. The measurement was done on {011} and {022} family of asymmetric (off-normal) crystallographic planes for STO and Si, respectively (Figure 4.43a). Since the reciprocal lattice points of both families of crystallographic planes lie within the inaccessible region which correspond to areas where either the incident beam or the diffracted beam lies below the surface of the sample, the sample was rotated through specific angle about Chi axis before the measurement was initiated in order to enable access to the selected family of planes. The results from the ϕ scan are shown in Figure 4.43b. Silicon substrate exhibits four peaks which are 90° apart from each other indicating its four-fold symmetry. Similarly, there are four peaks with the same spacing between them present in the ϕ scan of the STO layer which reveal only one in-plane orientation of the film. These peaks are shifted for 45° relative to substrate peaks, showing the in-plane epitaxial relationship of STO[110] || Si[100] which is consistent with results in the literature where also the epitaxial growth of STO on Si was achieved [216, 217]. Thus, STO unit cell is rotated 45° with respect to the conventional cubic cell of Si as shown in Figure 4.43c. The reason for STO in-plane rotation arises from much better agreement of STO unit cell parameter with 1×1 surface Si cell than conventional cell. The lattice constant of a 1×1 surface cell is 3.84 Å, which is very close to 3.905 Å of cubic STO and results in 1.66 % lattice mismatch only.

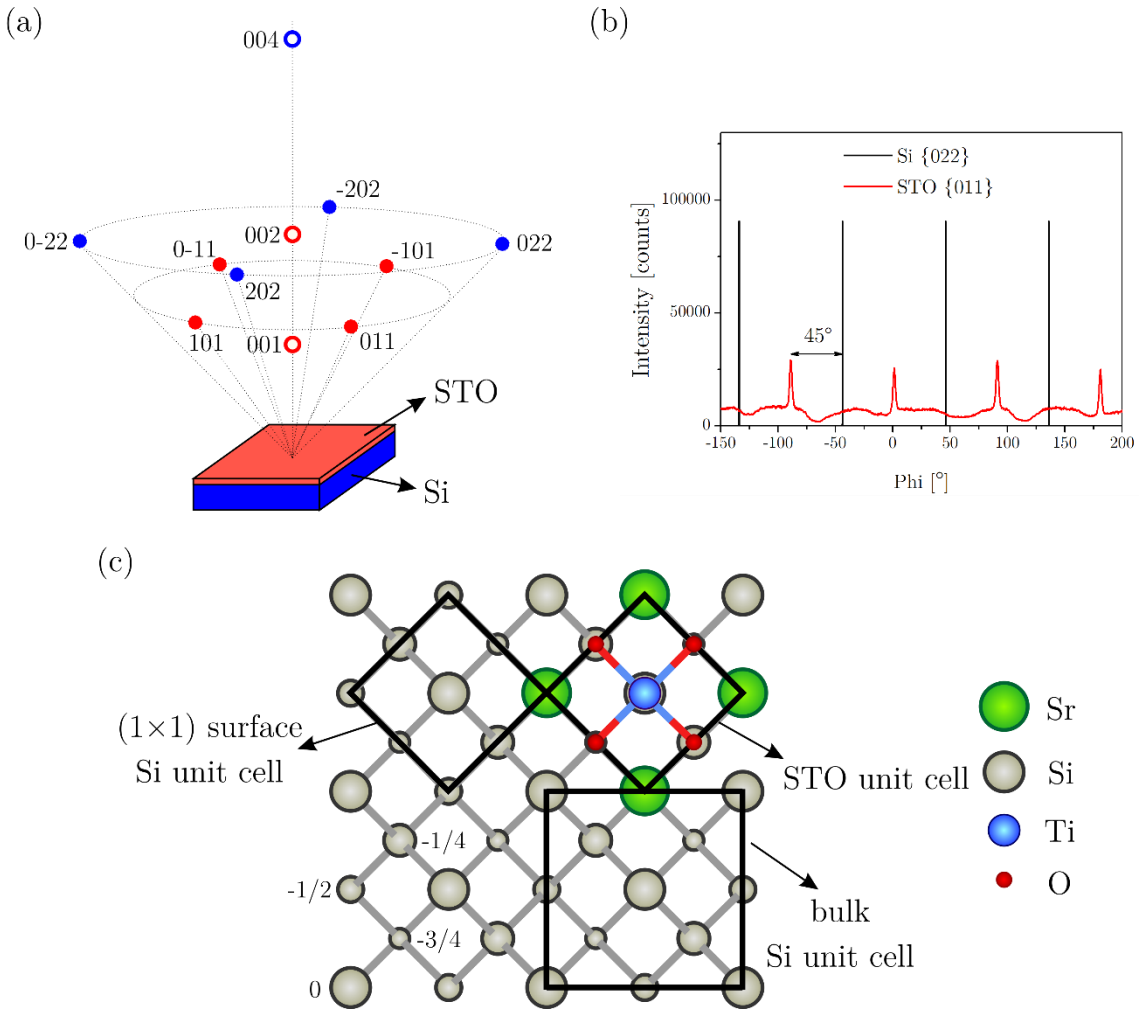


Figure 4.43: (a) Family of asymmetric reciprocal lattice points for STO (filled red circles) and Si (filled blue circles), measured during the Phi-scan. (b) X-ray diffraction measurements demonstrating the epitaxial relationship between STO and Si. The ϕ positions of the {011} and {022} peaks of the thin film and substrate, respectively, indicate the rotation of the STO unit cell by 45° with respect to the bulk Si cubic cell. (c) Epitaxial matching of STO and Si (001). The numbers refer to the vertical position of Si atoms with respect to the surface (set at zero), in the units of Si lattice constant.

Such an in-plane epitaxial relationship is evident also from the RHEED zone axis (Figure 4.41g,h). However, few additional spots with low intensity in [110] direction may imply that some small volume fraction of the STO layer does not obey epitaxial relationship determined by XRD. These crystallites with other orientation were not revealed by ϕ-scan either due to their small quantity (they were below the limit of detection) or insensitivity of the measurement (diffraction condition cannot be fulfilled for these crystallites). Latter case would be plausible if the out-of-plane orientation of these crystallites were different from (001). Absence of additional peaks in 2Theta/Theta scan can in this case be explained again by being below the limit of detection for selected measurement parameters. Nevertheless, we showed that the STO layer is fully epitaxial when the deposition is performed at room temperature and crystallized in vacuum at the temperature in the range from 517 °C to 577 °C since for the as-prepared layers only streaks were observed in RHEED patterns along both azimuths.

X-ray diffraction reciprocal space maps (RSMs) were recorded around (002) and (-103) reflections in order to obtain unit cell parameters and evaluate the mosaicity and lateral correlation of the STO layer (Figure 4.44a, b).

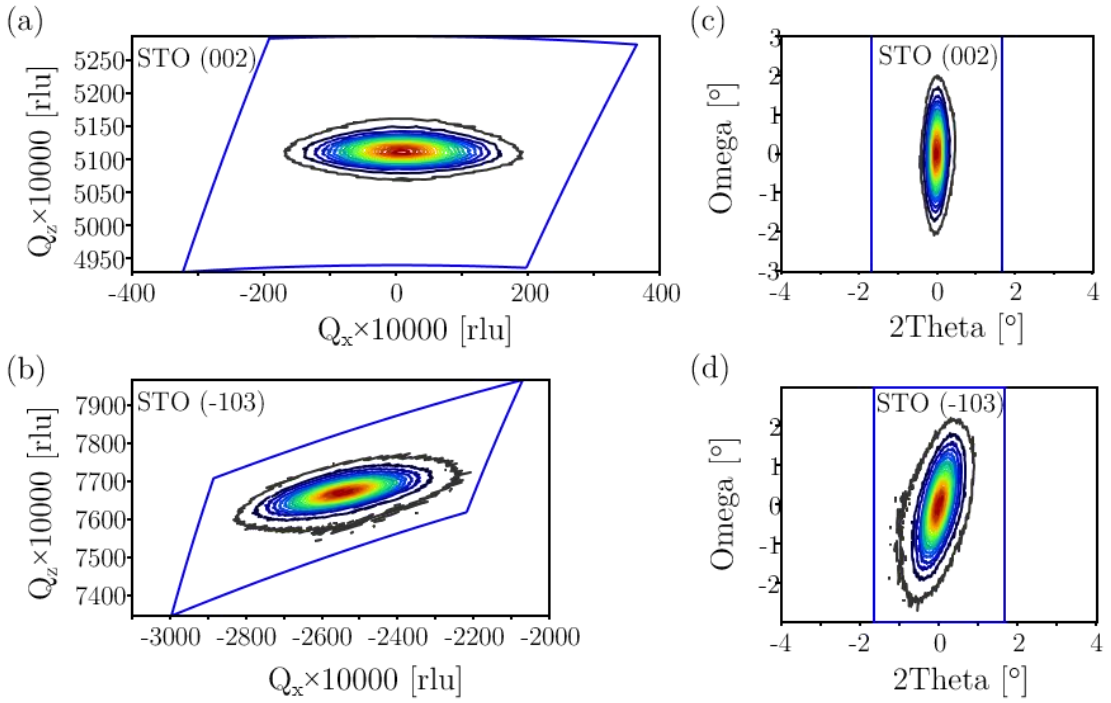


Figure 4.44: STO reciprocal space maps around (a) symmetric (002) reflection and (b) asymmetric (-103) reflection, plotted in reciprocal lattice units. (c, d) The same two reciprocal lattice points, plotted in relative angles in degrees with zero at the center of each of the scan axes.

Measurement of two reciprocal lattice spots (one symmetric and one asymmetric) instead of a single asymmetric one was performed due to the crystallographic tilt (offcut) which is common in epitaxial layers and represents tilt in the layer lattice with respect to the surface (Figure 4.45). This tilt can arise if the substrate is offcut and if there are dislocations at the layer/substrate interface.

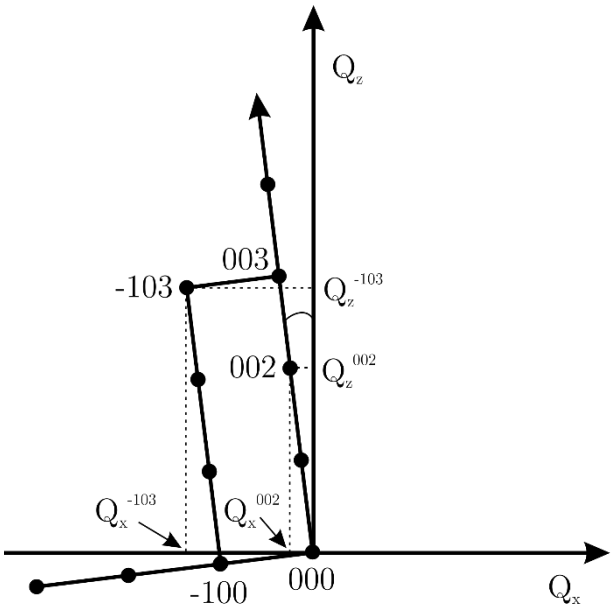


Figure 4.45: Illustration of how lattice parameters can be obtained from measurement of two reciprocal lattice spots where there is a layer tilt.

The coordinates of the center (Q_x, Q_z) of both reciprocal lattice spots were determined by Epitaxy software (PANalytical B. V., The Netherlands, Version 4.3a). Then the unit cell parameters were calculated using the equations (4.1) and (4.2).

$$d_{001} = \frac{1}{Q^{001}} = [(Q_z^{001})^2 + (Q_x^{001})^2]^{-\frac{1}{2}} = \left[\left(\frac{1}{2}Q_z^{002}\right)^2 + \left(\frac{1}{2}Q_x^{002}\right)^2\right]^{-\frac{1}{2}} \tag{4.1}$$

$$d_{-100} = \frac{1}{Q^{-100}} = \left[\left(\frac{3 \times Q_z^{002}}{2} - Q_z^{-103}\right)^2 + \left(Q_x^{-103} - \frac{3 \times Q_x^{002}}{2}\right)^2\right]^{-\frac{1}{2}} \tag{4.2}$$

It was found that in-plane (a=b) and out-of-plane (c) STO lattice parameters are 3.913±0.006 Å and 3.911±0.001 Å, respectively. The accuracy of the measurement was estimated by taking into account the precision by which the coordinates of the reciprocal lattice spot maxima were determined. This precision is significantly limited by relatively large full width at half maximum (FWHM) of the STO reflections. It is clear that the STO unit cell is larger than that of STO bulk single crystal (3.905 Å). There are two possible reasons for unit cell expansion, nonstoichiometry in STO thin film and strain. The strain can arise from lattice mismatch or thermal expansion mismatch between STO and Si. The lattice mismatch gives rise to compressive strain of 1.66 % when STO layer is coherently epitaxial. In this state the layer is in total registry with the substrate across the layer/substrate interface and is called also fully or commensurately strained. In our case, the contribution of the strain induced by the lattice mismatch can be completely excluded because the STO layer thickness (~46 nm) is far above the critical thickness of STO on Si which was experimentally found to be approximately 2 nm (5 MLs) [12, 192]. Above the critical thickness STO begins to relax, while the first 5 MLs maintain their registry with the Si substrate. Warusawithana et al. demonstrated that as the film thickness increases,

the relative integrated intensity of sharp peak, corresponding to coherently strained STO, decreases while that of a broad peak, corresponding to relaxed STO, increases. Such behavior clearly shows the transition from mostly commensurate STO to mostly relaxed STO as the film thickness is increased. After approximately 25 MLs (~10 nm) of STO the only observable feature in RSM is broad peak representing completely relaxed STO layer [12].

Therefore, in our case the strain originates exclusively from thermal expansion mismatch. The thermal expansion coefficient of Si is $\alpha_{Si}=2.6\times10^{-6}$ K^{-1} while the one of STO is $\alpha_{STO}=8.8\times10^{-6}$ K^{-1} [218]. In other words at the growth temperature a semiconductor is slightly larger than what it is at room temperature, while the oxide is significantly larger, and thus one can expect large in-plane tensile strain to develop in the film upon cooling. At the growth temperature of 517 °C the bulk unit-cell parameter of STO is given by:

$$a_{bulk\ STO}^{517°C} = a_{bulk\ STO}^{20°C}[1 + \alpha_{STO}(517 - 20)] = 3.922\ \text{Å} \tag{4.3}$$

For the bulk unit-cell parameter of STO at room temperature ($a_{bulk\ STO}^{20°C}$) value of 3.905 Å was taken. Equation (4.3) also gives the lattice parameter of the STO layer grown on Si at 517 °C for the completely relaxed STO layer. When the temperature is ramped from the growth temperature down to the ambient temperature (23 °C) after growth, the lattice parameters of both Si and STO are reduced. The contraction for the Si substrate is driven by α_{Si} while in the case of freestanding STO layer is driven by α_{STO}. However, in the case of STO thin film on Si the thickness of the STO layer is negligible as compared to the one of the substrate which results in the contraction of the in-plane lattice parameter of the oxide layer driven by the thermal coefficient of Si. The in-plane STO lattice parameter at ambient temperature can therefore be calculated by Eq. (4.4).

$$a_{STO}^{23°C} = a_{STO}^{517°C}[1 + \alpha_{Si}(23 - 517)] = 3.917\ \text{Å} \tag{4.4}$$

This value is larger than the bulk lattice parameter of the STO and is close to the value of the in-plane lattice parameter derived from XRD measurement (a=3.913±0.006 Å). With regard to the accuracy of the measurement, calculated value can be considered as being equal to the experimentally obtained one. However, the values are indeed not expected to be completely the same due to the slight nonstoichiometry of STO thin films, revealed by a faint 2× reconstruction in RHEED along the [100] azimuth of STO, which also affects the unit cell parameters. Similarly, also the experimentally obtained out-of-plane lattice parameter c=3.911±0.001 Å should be considered as a convolution of two contributions, one coming from slight deviation of composition and another one coming from strain induced by thermal expansion mismatch. According to the size of the in-plane lattice parameter, the out-of-plane parameter c is expected be smaller than 3.905 Å. However, the measurement showed an increase in c parameter which can be related to the nonstoichiometry observed by several research groups [10, 11, 210].

Characteristics of STO thin layer are provided not only by the position of the reciprocal lattice points but also by their shape which depend upon sample dimensions and perfection. Broadening of reciprocal lattice point along omega-2theta direction (FWHM of peak in 2Theta/Theta scan) can be related to small thickness of the layer, variation in d-spacing with depth or wavelength broadening if incident beam is not monochromatic. For comparison of different epitaxially grown films in quality, broadening in omega direction is much more important. It gives us information about mosaic spread, lateral incoherence and broadening due to sample curvature which is a result of incident beam having a range of angles of incidence. In order to imagine these two directions of broadening more easily,

both reciprocal lattice points are plotted not only in reciprocal lattice units (Figure 4.44a, b) but also in degrees (Figure 4.44c, d).

In our case, the STO layer exhibits mosaicity of 1.088° and lateral correlation length of 27 Å as calculated by Epitaxy software. Mosaic spread is related to the range of microscopic tilt in the sample, which may arise either because of a fine mosaic structure giving a variation in the tilt of the reflecting plane for different mosaic grains or it may be a result of »rippled« reflecting planes due to the presence of a uniform dislocation density. It is important to note that a layer that contains mosaic blocks is still considered to be a single crystal, but the blocks may differ slightly in their sizes and orientations. On the other hand, lateral correlation length gives an indication of the lateral uniformity of the layer. If the layer is perfectly smooth and of uniform thickness in all directions parallel to the interface then the lateral width of the diffraction peak will depend only on the coherence width of the incident beam. In most real cases the layer has some lateral irregularities which give rise to peak broadening. An average value of the separation of these lateral irregularities is referred to as the lateral correlation length. Since the contributions of both parameters, mosaicity and lateral correlation length, to the broadening in omega direction can only be separated when the layer peak is recorded using an asymmetric reflection, (-103) reflection of STO was used for calculation. For symmetric (002) reflection both parameters lie in the same direction, i.e. parallel to surface, and therefore cannot be distinguished. Nevertheless, FWHM along the omega axis of (002) reflection is the most commonly used parameter to compare the structural perfection of samples. Figure 4.46 shows an overview of achieved crystallinities for STO on Si(001) by several different research groups. Unfortunately, there are numerous publications where no omega-rocking curve or RSM around STO(002) is given, making their layers impossible to compare in terms of crystal quality. STO layer from the Experiment 7 exhibits FWHM of 1.68° and is shown in Figure 4.46 by red square.

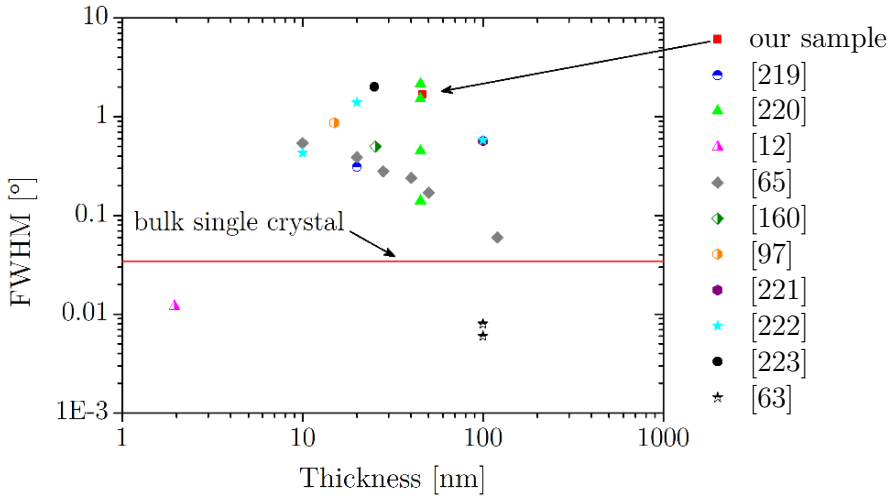


Figure 4.46: Crystallinity of our STO layer (Experiment 7) compared to the layers fabricated by MBE from other research groups.

Since the layer thickness can have a large influence on its crystallinity, one should be careful when comparing FWHM values for different samples. The most appropriate way is to compare samples with equal or very similar thicknesses. The best crystallinity achieved so far was reported in Ref. [63]. They succeeded in fabricating 100 nm thick STO films on Si(001) with FWHM=0.006° as obtained from out-of-plane (002) STO omega-rocking

curve. Very high crystallinity (FWHM=0.012°) was achieved also by Warusawithana et al. in Ref. [12] for coherently strained STO layer with thickness of only 2 nm (5 MLs). In both cases films were prepared by MBE and exhibit much lower FWHM than STO bulk single crystal (0.035°). We tried to improve the crystallinity of the STO layer by annealing at 650 °C and 1.3×10^{-6} mbar oxygen pressure for 30 min after deposition. It was expected for the post-annealing to decrease the concentration of defects in the STO layer. The FWHM extracted from the RSM (not shown here) improved from 1.68° to 1.55°. However, in 2Theta/Theta scan one additional peak at 30.80° 2Theta was observed with very low intensity (Figure 4.47). This peak does not correspond to the STO phase and is most likely related to a secondary phase as a result of interfacial reaction between STO and Si during the post-annealing step.

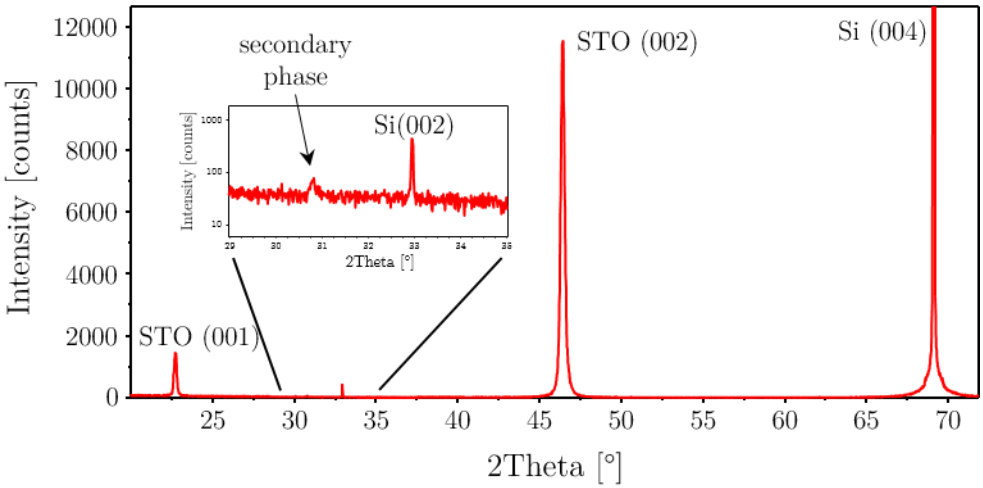


Figure 4.47: XRD 2Theta/Theta scan of STO/Si sample prepared in Experiment 7 with additional post-annealing performed at 650 °C and 1.3×10^{-6} mbar oxygen pressure for 30 min. In the inset 29-35° 2Theta range is plotted in logarithmic scale in order to make additional peak, corresponding to the secondary phase, visible.

In order to improve the crystal quality of pulsed-laser deposited STO layers further optimization of deposition parameters is needed, in particular those related to subsequent STO deposition which lead to the formation of unwanted additional diffraction spots in RHEED.
The AFM image of the STO surface (unannealed sample from the Experiment 7) is shown in Figure 4.48, where relatively smooth surface morphology is observed. The measured RMS surface roughness is only 2.7 Å.

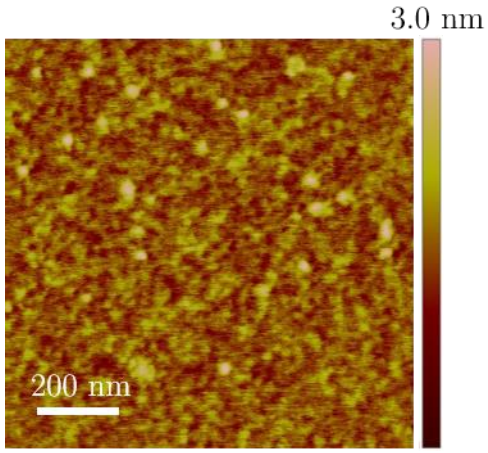


Figure 4.48: AFM height image of STO thin film prepared in Experiment 7 (unannealed). The lateral scan size is 1×1 μm^2.

4.3.3 Interface structure of epitaxial $SrTiO_3$ thin film on silicon

X-ray reflectivity measurement of the sample prepared in Experiment 7 revealed some details about the STO/Si interface. In addition to equally spaced fringes indicated by arrows (Figure 4.49) one very broad fringe centered at around 1.75° in omega can be observed. This additional fringe implies that there is some very thin layer present at the interface between STO and Si. Very thin layers give rise to a very low frequency fringe in the reflectivity scan. The thickness of the interface layer is ~2.3 nm according to the Fourier plot, shown in the inset of Figure 4.49.

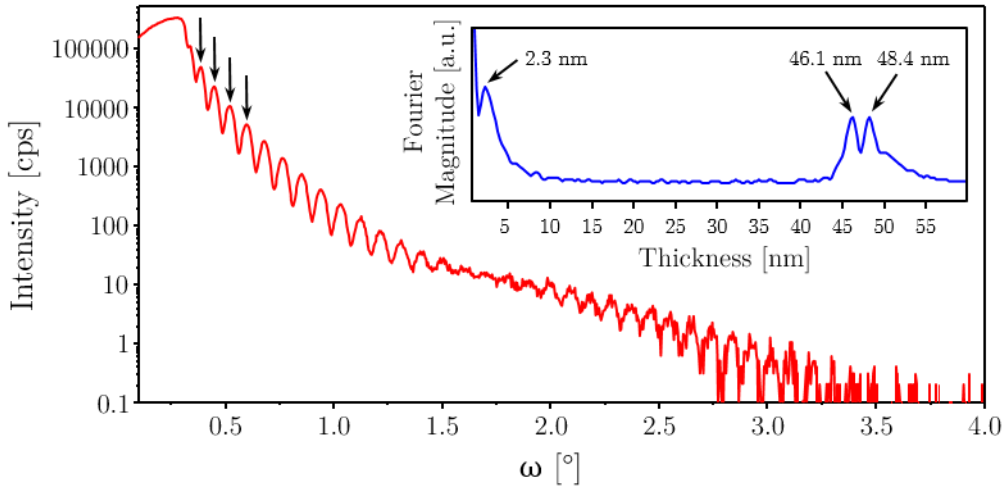


Figure 4.49: X-ray reflectivity curve for the sample prepared in Experiment 7 (red curve) with Fourier magnitude versus thickness plot in the inset.

Our RHEED results indicate that the formation of interface layer, which is according to the literature expected to be amorphous [224], occurred during the subsequent growth of the STO at 517 °C since the 6 MLs thick amorphous STO seed layer deposited at room temperature is fully crystalline after the crystallization step at 517 °C. We tried to confirm this by measuring the XPS Si 2p spectrum of the STO seed layer with thickness of only ~12 MLs (4.7 nm) in order to be able to detect the Si 2p signal (Figure 4.50). We found that the interface layer formation is in fact initiated already during the crystallization steps

of the STO seed layer, as shown by the broad peak centered at 2.6 eV higher binding energy compared to the elementary Si-$2p_{3/2}$ peak (red curve). Such an energy difference is characteristic for silicates.

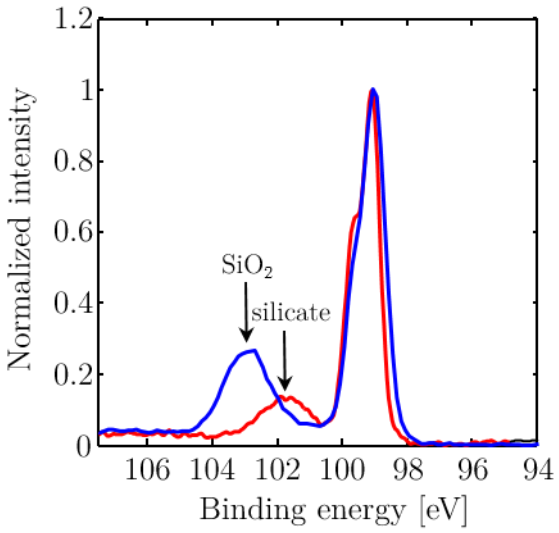


Figure 4.50: XPS Si 2p spectrum measured on Si substrate covered with the native SiO_2 layer (blue curve) and on a sample containing ~4.7 nm thick STO seed layer deposited at room temperature and crystallized at 517 °C (red curve).

There was no SiO_2 phase found in addition to silicate as demonstrated from the comparison with XPS spectrum of Si substrate covered with native SiO_2 layer (blue curve). We attribute the formation of the interface layer to the instability of the Si/STO interface. Since the crystallization of the STO seed layer was performed in vacuum, it is though that growth of the interface layer occurs at the expense of oxygen from the STO film [225]. However, it is expected that only a small fraction of the final silicate interface layer was formed during the crystallization steps of the STO seed layer and that most of it was formed during the subsequent deposition when high temperature and relatively high oxygen partial pressure were applied simultaneously.

4.3.4 Summary

Growth of $SrTiO_3$ on (1×2)+(2×1) reconstructed Sr(1/2 ML)/Si(001) surface was investigated with the aim to prepare epitaxial layer with high crystallinity. Detailed study of initial deposition parameters in terms of background gas pressure, deposition temperature, fluence, and oxidation peculiarities proved to be extremely important. It was demonstrated that the growth is fully epitaxial when the STO is deposited at room temperature and 0.05 mbar Ar pressure with intermediate oxidation periods and crystallized in vacuum at the temperature in the range from 517 °C to 546 °C. However, such the deposition procedure is relatively slow and therefore appropriate for preparation of first few nanometers of STO only. It results in very thin amorphous silicate layer at the interface between Si and STO. The subsequent deposition was performed in much faster regime when both, high-temperature and high-oxygen partial pressure, were applied simultaneously. XRD examination of the final STO layer revealed exclusively STO(001)||Si(001) out-of-plane and STO[110]||Si[100] in-plane orientations, as derived from 2Theta/Theta and Phi scans, respectively. On the other hand, besides the streaks characteristic for the epitaxial STO layer, few well defined additional spots with low intensity emerged in the RHEED pattern along the [110] azimuth of STO during the subsequent deposition at 517 °C. These additional spots could arise from the presence of small portion of crystallites having different crystallographic orientation than majority of the STO film and suggest that further optimization of subsequent deposition parameters is needed. The STO layer exhibits crystallinity of 1.68°, as derived from FWHM of (002) reflection along omega axis which is similar to some of MBE deposited films. Nevertheless, further improvement of crystallinity is required in order to achieve bulk single crystal quality.

Conclusions

This work highlights the possibility of using the pulsed-laser deposition (PLD) technique for the epitaxial growth of $SrTiO_3$ (STO) layer on Si(001) surface as an alternative manufacturing route to molecular beam epitaxy (MBE). The achieved epitaxial integration of these two materials required several tasks to be accomplished first.

Initially, studies were focused on elimination of the native SiO_2 layer and carbon contamination from the Si substrate surface with the aim to prepare atomically clean (2×1)+(1×2) reconstructed Si(001) surface. Removal of 2 nm thick amorphous SiO_2 layer was investigated *in-situ* by RHEED, using thermal and Sr-induced deoxidation processes. It was shown that resistive-heating sample holder as well as stainless steel sample plate, which are both commonly used sample holders in the PLD chambers, do not allow preparation of clean and ordered Si surface. This is primarily related to the strong outgassing during heating, caused by the holder itself and in particular a silver paint used for pasting the substrate to the holder. In order to avoid the use of silver paint, sample holder with special clamping mechanism was designed and fabricated out of refractory metal tantalum. The sample was heated by the IR-laser from the back side. Such a holder enabled preparation of reconstructed Si surface in wide temperature range from 750 °C to 1200 °C. A large influence of the temperature on the kinetics of SiO_2 layer elimination was demonstrated. In addition, with increasing temperature of the thermal deoxidation from 750 °C to 900 °C, both, the intensity and sharpness of the 1/2-order streaks increase, indicating an improvement in the surface order. It was shown in terms of RHEED pattern quality that 900 °C is the optimal temperature for the thermal deoxidation process. However, at this temperature besides the streaks corresponding to (2×1)+(1×2) reconstructed Si(001) surface some faint and broad diffraction spots positioned to the outside of the primary silicon streaks were observed in both, [100] and [110] azimuths. These additional diffraction spots are related to epitaxially aligned β-SiC islands on the surface with twin boundaries present within the SiC structure. The attempt to remove physisorbed organic molecules, responsible for the formation of SiC precipitates, from the SiO_2 surface, by carbon burning process, showed no improvement in achieving carbon-free reconstructed Si surface. This indicates that organic species were either not completely removed from the SiO_2 surface or they are buried within the SiO_2 layer where oxygen bake cannot affect them. Nevertheless, we succeeded in fabricating a clean (carbon free) reconstructed Si surface by flashing the substrate to 1200 °C for ~1.5 min. Such a high temperature causes dissociation of β-SiC and diffusion of carbon into the bulk. Several interesting surface phenomena were observed after cooling the flash-annealed Si(001) surface: The c(4×4) pattern emerges when a flash-annealed sample is cooled down to a temperature between 580 °C and 730 °C; the β-SiC transmission pattern superimposed on (2×1)+(1×2) pattern appears after cooling down to a temperature between 730 °C and

1100 °C, whereas solely the (2×1)+(1×2) pattern is stable below 580 °C and above 1100 °C. It was additionally observed that re-heating of the c(4×4) reconstructed surface to a temperature above 730 °C results in simultaneous disappearance of surface c(4×4) reconstruction and the appearance of the SiC transmission pattern. Based on the obtained results it was concluded that c(4×4) reconstruction is associated with carbon contamination as well. It is not induced by ordering of carbon atoms in the top surface atomic layer but is in fact a pure Si surface structure, which is formed as a result of stresses caused by carbon atoms in subsurface positions. In summary, we demonstrated that in a vacuum of 1×10^{-8} mbar it takes around 15 min for surface to become re-contaminated with carbon to an extent that can be observed with RHEED either as the c(4×4) or β-SiC transmission pattern. Carbon contamination is always present and cannot be avoided completely. It is within the realms of possibility, however, to improve the vacuum so that the carbon re-contamination is significantly delayed. Furthermore, the extent of PLD chamber contamination determined by the hydrocarbons partial pressure should be decreased to a minimum level. This concerns in particular the use of silver paint which is an important source of hydrocarbons in the PLD chamber.

In addition to the thermal also Sr-induced deoxidation process was developed. It is based on deposition of 1-2 ML of elemental Sr on SiO_2/Si at room temperature and heating to 800 °C, where the Sr acts as a catalyst to promote the decomposition of SiO_2. The catalytic nature of Sr lowers the optimal temperature of deoxidation for 100 °C (from 900 °C to 800 °C) compared to the thermal deoxidation process and significantly reduces the time needed for complete removal of the SiO_2 layer. Moreover, an efficient way of quantifying the amount of Sr which is left on the Si surface after complete SiO_2 removal was developed. Despite the lower temperature, required for SiO_2 removal, the Sr-induced deoxidation approach proved to be inadequate due to the formation of β-SiC islands on the Si surface during heating to 800 °C.

The next challenge was related to the preparation of an effective buffer (protective) layer on top of the (2×1)+(1×2) reconstructed Si(001) surface using the PLD method in order to decrease the reactivity of the Si surface to oxidation. This buffer layer is based on 1/2 ML metallic Sr coverage and is a prerequisite for the successful epitaxial growth of STO layer. It was shown that by proper selection of deposition parameters PLD is capable to control the deposition with sub-monolayer precision. Keeping the spot size at 0.14 mm^2 and fluency at 1 J/cm^2 provide the optimum Sr atom flux for the preparation of sub-monolayer Sr structures on Si(001). During the deposition of Sr at 700 °C *in-situ* analysis using RHEED showed surface structure evolution from two-domain (2×1)+(1×2) reconstruction, exhibited by the bare Si surface, to a (2×3)+(3×2) structure at 1/6 ML, which is then replaced by a (1×2)+(2×1) structure again at 1/4 ML. The final (1×2)+(2×1) structure is observed to be stable up to 1/2 ML Sr coverage. The observation of (2×3)+(3×2) surface reconstruction was determined as the key for the preparation of exactly 1/2 ML Sr on Si. Knowing the coverage for (2×3)+(3×2) reconstruction, enabled us to calculate the number of pulses required for the coverage of 1/2 ML. RHEED patterns of all the observed surface reconstructions were further correlated with corresponding reciprocal lattices and real surface atomic structures reported in the literature. Two procedures for the buffer layer preparation were developed. The first one is based on flashing the Si substrate to 1200 °C to remove the native oxide layer and subsequent deposition of Sr at 700 °C, while the second one begins with Sr-assisted deoxidation process and the additional deposition of Sr at 700 °C until reaching 1/2 ML coverage. However, the first procedure is more suitable due to the absence of carbon contamination on the surface. It was found that there exists a saturation coverage of Sr on Si(001) surface which is temperature dependent. As a result the buffer layer (1/2 ML Sr coverage) was observed to be stable up to 700 °C. Keeping the buffer layer at 750-800 °C leads to partial desorption

of Sr until reaching the saturation coverage at 1/6 ML, while no Sr retains on the surface above 1100 °C. In addition, resistance of the Sr buffer layer to oxidation was tested at several different temperatures. It was shown that Sr(1/2 ML)/Si(001) exhibits much higher resistance compared to the bare Si surface as a consequence of fully occupied Si surface dangling bonds with electrons donated by Sr atoms.

Successful fabrication of the Sr buffer layer enabled the final and most important part of the whole investigation to be initiated, i.e. the attempt to grow epitaxial STO layer on Sr(1/2 ML)/Si(001) surface using the PLD technique. Initial deposition proved to be the most critical part of the whole deposition process since integrity of the Sr-buffer layer can easily be disrupted by high energetic species from the laser plume if the deposition of the first few monolayers is performed at too low background pressure. By means of XRR and XPS studies it was demonstrated that the initial deposition of STO should be performed at room temperature and pressure $\geq$ 0.05 mbar in order to ensure diffusion-like arrival of species to the substrate surface and consequently avoid the formation of silicate at the interface. Considering also the impact of the background gas pressure on layer density and deposition rate, 0.05 mbar was determined as the optimal pressure. In addition, we addressed the issues related to nonstoichiometry encountered by XPS and showed that Sr and Ti atomic concentrations vary with sample depth indicating inhomogeneous distribution of elements in the STO layer deposited by PLD at room temperature. However, RBS analysis revealed that the overall composition of STO layers is much closer to the ideal one compared to the surface composition and that the fluence of 1.5 J/cm^2 results in the most stoichiometric STO layers (1 % Sr enriched) for the deposition performed at room temperature and 0.05 mbar Ar pressure. XPS depth profiling by ion sputtering revealed metallic Ti in the as-deposited STO layer indicating insufficient oxidation by the oxygen from the STO target and suggesting that in-between the room temperature deposition and crystallization steps, complete oxidation of Ti at sufficiently high background pressure of oxygen should be performed.

Such a detailed study of initial deposition parameters in terms of background gas pressure, deposition temperature, fluence and oxidation peculiarities proved to be advantageous since it was shown that the PLD growth of STO layer is fully epitaxial when the deposition is performed at room temperature and crystallized in vacuum at the temperature in the range from 517 °C to 546 °C. Using this procedure one can grow epitaxial STO layer of any thickness. However, the slowness and complexity of the process confines its use only to the first few monolayers which are referred to as STO seed layer. The subsequent deposition was performed in a much faster continuous manner at high temperature and 1.3×10^{-6} mbar oxygen pressure. During the subsequent deposition at 517 °C, besides the streaks characteristic for the epitaxial STO layer, a few well defined additional spots emerged in the RHEED pattern along the [110] azimuth of STO which presumably arise from crystallites with crystallographic orientation different from the majority of the STO films. From the 2Theta/Theta and Phi scans only one out-of plane (STO(001)||Si(001)) and one in-plane (STO[110]||Si[100]) orientations were shown, without any evidence of the existence of crystallites with other orientations which could be explained by a small quantity of these crystallites, being below the limit of detection for selected measurement parameters.

The lattice parameter values extracted from RSMs are a=b=3.913±0.006 Å and c=3.911±0.001 Å, indicating larger STO unit cell compared to the bulk single crystal unit cell. It was shown that the expanded unit cell dimensions result from two contributions, one coming from the strain induced by thermal expansion mismatch between STO and Si, and another one coming from nonstoichiometry of the final STO layer which was found to be slightly Ti enriched. The FWHM of the (002) reflection is 1.68°. During post-deposition

annealing in oxygen, the FWHM decreased to 1.55°. Nevertheless, further improvement of crystallinity is required in order to achieve bulk single-crystal quality.

Furthermore, interface structure of epitaxial STO thin film on Si was investigated by means of XRR and XPS. It was found that ~2.3 nm thick silicate layer exists at the interface between STO and Si. This interface layer formation is initiated already during the crystallization steps of the STO seed layer due to the oxygen diffusion from the STO layer. However, most of the interface layer is expected to be formed during the subsequent deposition when both, high temperature and oxygen partial pressure, were applied simultaneously.

Overall, these findings represent large and very promising step towards the growth of high-quality epitaxial STO layer on Si(001) with the PLD method, needed for the integration of different functional oxides with the Si platform.

References

[1] J. Dabrowski and H. J. Müssig, *Silicon Surfaces and Formation of Interfaces: Basic Science in the Industrial World*. Singapore: World Scientific, 2000.

[2] A. A. Demkov and A. B. Posadas, "Other Epitaxial Oxides on Semiconductors," in *Integration of Functional Oxides with Semiconductors*, A. A. Demkov and A. B. Posadas, Eds., ed Austin, TX, 2014, pp. 205-208.

[3] J. Ramdani, R. Droopad, Z. Yu, J. A. Curless, C. D. Overgaard, J. Finder, K. Eisenbeiser, J. A. Hallmark, W. J. Ooms, V. Kaushik, P. Alluri, and S. Pietambaram, "Interface characterization of high-quality $SrTiO_3$ thin films on Si(100) substrates grown by molecular beam epitaxy," *Applied Surface Science,* vol. 159, pp. 127-133, Jun 2000.

[4] R. Droopad, Z. Yu, H. Li, Y. Liang, C. Overgaard, A. Demkov, X. Zhang, K. Moore, K. Eisenbeiser, M. Hu, J. Curless, and J. Finder, "Development of integrated heterostructures on silicon by MBE," *Journal of Crystal Growth,* vol. 251, pp. 638-644, 2003.

[5] J. Robertson, "High dielectric constant oxides," *European Physical Journal-Applied Physics,* vol. 28, pp. 265-291, Dec 2004.

[6] R. A. McKee, F. J. Walker, and M. F. Chisholm, "Crystalline oxides on silicon: The first five monolayers," *Physical Review Letters,* vol. 81, pp. 3014-3017, Oct 1998.

[7] S. A. Chambers, Y. Liang, Z. Yu, R. Droopad, and J. Ramdani, "Band offset and structure of $SrTiO_3$/Si(001) heterojunctions," *Journal of Vacuum Science & Technology a-Vacuum Surfaces and Films,* vol. 19, pp. 934-939, May-Jun 2001.

[8] C. J. Forst, C. R. Ashman, K. Schwarz, and P. E. Blochl, "The interface between silicon and a high-k oxide," *Nature,* vol. 427, pp. 53-56, Jan 2004.

[9] J. Junquera, M. Zimmer, P. Ordejon, and P. Ghosez, "First-principles calculation of the band offset at $BaO/BaTiO_3$ and $SrO/SrTiO_3$ interfaces," *Physical Review B,* vol. 67, p. 12, Apr 2003.

[10] D. J. Keeble, S. Wicklein, R. Dittmann, L. Ravelli, R. A. Mackie, and W. Egger, "Identification of A- and B-Site Cation Vacancy Defects in Perovskite Oxide Thin Films," *Physical Review Letters,* vol. 105, p. 4, Nov 2010.

[11] D. J. Keeble, S. Wicklein, L. Jin, C. L. Jia, W. Egger, and R. Dittmann, "Nonstoichiometry accommodation in $SrTiO_3$ thin films studied by positron annihilation and electron microscopy," *Physical Review B,* vol. 87, p. 11, May 2013.

[12] M. P. Warusawithana, C. Cen, C. R. Sleasman, J. C. Woicik, Y. L. Li, L. F. Kourkoutis, J. A. Klug, H. Li, P. Ryan, L. P. Wang, M. Bedzyk, D. A. Muller, L. Q. Chen, J. Levy, and D. G. Schlom, "A ferroelectric oxide made directly on silicon," *Science,* vol. 324, pp. 367-370, Apr 2009.

[13] M. Suzuki, "Review on future ferroelectric nonvolatile memory: FeRAM : From the point of view of epitaxial oxide thin films," *Journal of the Ceramic Society of Japan,* vol. 103, pp. 1099-1111, Nov 1995.

[14] P. Vettiger and G. Binnig, "The nanodrive project," *Scientific American,* vol. 288, pp. 46-53, Jan 2003.

[15] Y. R. Wu and J. Singh, "Polar heterostructure for multifunction devices: Theoretical studies," *Ieee Transactions on Electron Devices,* vol. 52, pp. 284-293, Feb 2005.

[16] K. Zhao, Y. H. Huang, Q. L. Zhou, K. J. Jin, H. B. Lu, M. He, B. L. Cheng, Y. L. Zhou, Z. H. Chen, and G. Z. Yang, "Ultraviolet photovoltage characteristics of SrTiO3- δ /Si heterojunction," *Applied Physics Letters,* vol. 86, p. 3, May 2005.

[17] D. G. Schlom, L. Q. Chen, X. Q. Pan, A. Schmehl, and M. A. Zurbuchen, "A thin film approach to engineering functionality into oxides," *Journal of the American Ceramic Society,* vol. 91, pp. 2429-2454, Aug 2008.

[18] A. A. Demkov and A. B. Posadas, "Integration of Functional Oxides on $SrTiO_3$/Si Pseudo-Substrates," in *Integration of Functional Oxides with Semiconductors*, A. A. Demkov and A. B. Posadas, Eds., ed Austin, TX, 2014, pp. 159-198.

[19] S. H. Baek and C. B. Eom, "Epitaxial integration of perovskite-based multifunctional oxides on silicon," *Acta Materialia,* vol. 61, pp. 2734-2750, May 2013.

[20] A. Lin, X. Hong, V. Wood, A. A. Verevkin, C. H. Ahn, R. A. McKee, F. J. Walker, and E. D. Specht, "Epitaxial growth of $Pb(Zr_{0.2}Ti_{0.8})O_3$ on Si and its nanoscale piezoelectric properties," *Applied Physics Letters,* vol. 78, pp. 2034-2036, Apr 2001.

[21] D. M. Kim, C. B. Eom, V. Nagarajan, J. Ouyang, R. Ramesh, V. Vaithyanathan, and D. G. Schlom, "Thickness dependence of structural and piezoelectric properties of epitaxial $Pb(Zr_{0.52}Ti_{0.48})O_3$ films on Si and $SrTiO_3$ substrates," *Applied Physics Letters,* vol. 88, p. 3, Apr 2006.

[22] G. Niu, S. Yin, G. Saint-Girons, B. Gautier, P. Lecoeur, V. Pillard, G. Hollinger, and B. Vilquin, "Epitaxy of $BaTiO_3$ thin film on Si(001) using a $SrTiO_3$ buffer layer for non-volatile memory application," *Microelectronic Engineering,* vol. 88, pp. 1232-1235, Jul 2011.

[23] C. Dubourdieu, J. Bruley, T. M. Arruda, A. Posadas, J. Jordan-Sweet, M. M. Frank, E. Cartier, D. J. Frank, S. V. Kalinin, A. A. Demkov, and V. Narayanan, "Switching of ferroelectric polarization in epitaxial $BaTiO_3$ films on silicon without a conducting bottom electrode," *Nature Nanotechnology,* vol. 8, pp. 748-754, Oct 2013.

[24] S. Abel, T. Stoferle, C. Marchiori, C. Rossel, M. D. Rossell, R. Erni, D. Caimi, M. Sousa, A. Chelnokov, B. J. Offrein, and J. Fompeyrine, "A strong electro-optically active lead-free ferroelectric integrated on silicon," *Nature Communications,* vol. 4, p. 6, Apr 2013.

[25] B. Oregan and M. Gratzel, "A low-cost, high-efficiency solar cell based on dye-sensitized colloidal TiO_2 films," *Nature,* vol. 353, pp. 737-740, Oct 1991.

[26] A. Fujishima, X. T. Zhang, and D. A. Tryk, "TiO_2 photocatalysis and related surface phenomena," *Surface Science Reports,* vol. 63, pp. 515-582, Dec 2008.

[27] X. B. Chen, S. H. Shen, L. J. Guo, and S. S. Mao, "Semiconductor-based photocatalytic hydrogen generation," *Chemical Reviews,* vol. 110, pp. 6503-6570, Nov 2010.

[28] N. S. Lewis and D. G. Nocera, "Powering the planet: Chemical challenges in solar energy utilization," *Proceedings of the National Academy of Sciences of the United States of America,* vol. 103, pp. 15729-15735, Oct 2006.

[29] H. G. Yang, C. H. Sun, S. Z. Qiao, J. Zou, G. Liu, S. C. Smith, H. M. Cheng, and G. Q. Lu, "Anatase TiO_2 single crystals with a large percentage of reactive facets," *Nature,* vol. 453, pp. 638-U4, May 2008.

[30] S. A. Chambers, C. M. Wang, S. Thevuthasan, T. Droubay, D. E. McCready, A. S. Lea, V. Shutthanandan, and C. F. Windisch, "Epitaxial growth and properties of MBE-grown ferromagnetic Co-doped TiO_2 anatase films on $SrTiO_3$(001) and $LaAlO_3$(001)," *Thin Solid Films,* vol. 418, pp. 197-210, Oct 2002.

[31] T. Kanki, R. W. Li, Y. Naitoh, H. Tanaka, T. Matsumoto, and T. Kawai, "Nanoscale observation of room-temperature ferromagnetism on ultrathin (La,Ba)MnO_3 films," *Applied Physics Letters,* vol. 83, pp. 1184-1186, Aug 2003.

[32] A. K. Pradhan, J. B. Dadson, D. Hunter, K. Zhang, S. Mohanty, E. M. Jackson, B. Lasley-Hunter, K. Lord, T. M. Williams, R. R. Rakhimov, J. Zhang, D. J. Sellmyer, K. Inaba, T. Hasegawa, S. Mathews, B. Joseph, B. R. Sekhar, U. N. Roy, Y. Cui, and A. Burger, "Ferromagnetic properties of epitaxial manganite films on $SrTiO_3$/Si heterostructures," *Journal of Applied Physics,* vol. 100, p. 5, Aug 2006.

[33] D. Fuchs, E. Arac, C. Pinta, S. Schuppler, R. Schneider, and H. V. von Lohneysen, "Tuning the magnetic properties of $LaCoO_3$ thin films by epitaxial strain," *Physical Review B,* vol. 77, p. 8, Jan 2008.

[34] A. Posadas, M. Berg, H. Seo, A. de Lozanne, A. A. Demkov, D. J. Smith, A. P. Kirk, D. Zhernokletov, and R. M. Wallace, "Epitaxial integration of ferromagnetic correlated oxide $LaCoO_3$ with Si (100)," *Applied Physics Letters,* vol. 98, p. 3, Jan 2011.

[35] S. Datta and B. Das, "Electronic analog of the electro-optic modulator," *Applied Physics Letters,* vol. 56, pp. 665-667, Feb 1990.

[36] A. B. Posadas, C. Mitra, C. W. Lin, A. Dhamdhere, D. J. Smith, M. Tsoi, and A. A. Demkov, "Oxygen vacancy-mediated room-temperature ferromagnetism in insulating cobalt-substituted $SrTiO_3$ epitaxially integrated with silicon," *Physical Review B,* vol. 87, p. 9, Apr 2013.

[37] S. E. Park and T. R. Shrout, "Characteristics of relaxor-based piezoelectric single crystals for ultrasonic transducers," *IEEE Transactions on Ultrasonics Ferroelectrics and Frequency Control,* vol. 44, pp. 1140-1147, Sep 1997.

[38] S. E. Park and T. R. Shrout, "Ultrahigh strain and piezoelectric behavior in relaxor based ferroelectric single crystals," *Journal of Applied Physics,* vol. 82, pp. 1804-1811, Aug 1997.

[39] S. H. Baek, J. Park, D. M. Kim, V. A. Aksyuk, R. R. Das, S. D. Bu, D. A. Felker, J. Lettieri, V. Vaithyanathan, S. S. N. Bharadwaja, N. Bassiri-Gharb, Y. B. Chen, H. P. Sun, C. M. Folkman, H. W. Jang, D. J. Kreft, S. K. Streiffer, R. Ramesh, X. Q. Pan, S. Trolier-McKinstry, D. G. Schlom, M. S. Rzchowski, R. H. Blick, and C.

B. Eom, "Giant Piezoelectricity on Si for Hyperactive MEMS," *Science,* vol. 334, pp. 958-961, Nov 2011.

[40] D. Lebeugle, D. Colson, A. Forget, and M. Viret, "Very large spontaneous electric polarization in $BiFeO_3$ single crystals at room temperature and its evolution under cycling fields," *Applied Physics Letters,* vol. 91, p. 3, Jul 2007.

[41] J. Wang, H. Zheng, Z. Ma, S. Prasertchoung, M. Wuttig, R. Droopad, J. Yu, K. Eisenbeiser, and R. Ramesh, "Epitaxial $BiFeO_3$ thin films on Si," *Applied Physics Letters,* vol. 85, pp. 2574-2576, Sep 2004.

[42] L. W. Martin, Y. H. Chu, Q. Zhan, R. Ramesh, S. J. Han, S. X. Wang, M. Warusawithana, and D. G. Schlom, "Room temperature exchange bias and spin valves based on $BiFeO_3/SrRuO_3/SrTiO_3/Si$ (001) heterostructures," *Applied Physics Letters,* vol. 91, p. 3, Oct 2007.

[43] H. W. Jang, S. H. Baek, D. Ortiz, C. M. Folkman, C. B. Eom, Y. H. Chu, P. Shafer, R. Ramesh, V. Vaithyanathan, and D. G. Schlom, "Epitaxial (001) $BiFeO_3$ membranes with substantially reduced fatigue and leakage," *Applied Physics Letters,* vol. 92, p. 3, Feb 2008.

[44] R. P. Laughlin, D. A. Currie, R. Contreras-Guererro, A. Dedigama, W. Priyantha, R. Droopad, N. Theodoropoulou, P. Gao, and X. Q. Pan, "Magnetic and structural properties of $BiFeO_3$ thin films grown epitaxially on $SrTiO_3$/Si substrates," *Journal of Applied Physics,* vol. 113, p. 3, May 2013.

[45] S. G. Lim, S. Kriventsov, T. N. Jackson, J. H. Haeni, D. G. Schlom, A. M. Balbashov, R. Uecker, P. Reiche, J. L. Freeouf, and G. Lucovsky, "Dielectric functions and optical bandgaps of high-K dielectrics for metal-oxide-semiconductor field-effect transistors by far ultraviolet spectroscopic ellipsometry," *Journal of Applied Physics,* vol. 91, pp. 4500-4505, Apr 2002.

[46] J. Robertson, "High dielectric constant gate oxides for metal oxide Si transistors," *Reports on Progress in Physics,* vol. 69, pp. 327-396, Feb 2006.

[47] Y. Y. Mi, Z. Yu, S. J. Wang, P. C. Lim, Y. L. Foo, A. C. H. Huan, and C. K. Ong, "Epitaxial $LaAlO_3$ thin film on silicon: Structure and electronic properties," *Applied Physics Letters,* vol. 90, p. 3, Apr 2007.

[48] J. W. Reiner, A. Posadas, M. Wang, T. P. Ma, and C. H. Ahn, "Growth and structural properties of crystalline $LaAlO_3$ on Si(001)," *Microelectronic Engineering,* vol. 85, pp. 36-38, Jan 2008.

[49] T. Q. Ngo, A. Posadas, M. D. McDaniel, D. A. Ferrer, J. Bruley, C. Breslin, A. A. Demkov, and J. G. Ekerdt, "Epitaxial growth of $LaAlO_3$ on $SrTiO_3$-buffered Si (001) substrates by atomic layer deposition," *Journal of Crystal Growth,* vol. 363, pp. 150-157, Jan 2013.

[50] A. Ohtomo and H. Y. Hwang, "A high-mobility electron gas at the $LaAlO_3/SrTiO_3$ heterointerface," *Nature,* vol. 427, pp. 423-426, Jan 2004.

[51] Y. W. Xie, Y. Hikita, C. Bell, and H. Y. Hwang, "Control of electronic conduction at an oxide heterointerface using surface polar adsorbates," *Nature Communications,* vol. 2, p. 5, Oct 2011.

[52] P. Irvin, Y. J. Ma, D. F. Bogorin, C. Cen, C. W. Bark, C. M. Folkman, C. B. Eom, and J. Levy, "Rewritable nanoscale oxide photodetector," *Nature Photonics,* vol. 4, pp. 849-852, Dec 2010.

[53] J. W. Park, D. F. Bogorin, C. Cen, D. A. Felker, Y. Zhang, C. T. Nelson, C. W. Bark, C. M. Folkman, X. Q. Pan, M. S. Rzchowski, J. Levy, and C. B. Eom, "Creation of a two-dimensional electron gas at an oxide interface on silicon," *Nature Communications,* vol. 1, p. 6, Oct 2010.

[54] T. Tambo, T. Nakamura, K. Maeda, H. Ueba, and C. Tatsuyama, "Molecular beam epitaxy of $SrTiO_3$ films on Si(100)-2x1 with SrO buffer layer," *Japanese Journal of Applied Physics Part 1-Regular Papers Short Notes & Review Papers,* vol. 37, pp. 4454-4459, Aug 1998.

[55] J. Lettieri, J. H. Haeni, and D. G. Schlom, "Critical issues in the heteroepitaxial growth of alkaline-earth oxides on silicon," *Journal of Vacuum Science & Technology a-Vacuum Surfaces and Films,* vol. 20, pp. 1332-1340, Jul-Aug 2002.

[56] G. J. Norga, C. Marchiori, A. Guiller, J. P. Locquet, C. Rossel, H. Siegwart, D. Caimi, J. Fompeyrine, and T. Conard, "Phase of reflection high-energy electron diffraction oscillations during (Ba,Sr)O epitaxy on Si(100): A marker of Sr barrier integrity," *Applied Physics Letters,* vol. 87, p. 3, Dec 2005.

[57] G. J. Norga, C. Marchiori, C. Rossel, A. Guiller, J. P. Locquet, H. Siegwart, D. Caimi, J. Fompeyrine, J. W. Seo, and C. Dieker, "Solid phase epitaxy of $SrTiO_3$ on (Ba,Sr)O/Si(100): The relationship between oxygen stoichiometry and interface stability," *Journal of Applied Physics,* vol. 99, p. 7, Apr 2006.

[58] K. Eisenbeiser, J. M. Finder, Z. Yu, J. Ramdani, J. A. Curless, J. A. Hallmark, R. Droopad, W. J. Ooms, L. Salem, S. Bradshaw, and C. D. Overgaard, "Field effect transistors with $SrTiO_3$ gate dielectric on Si," *Applied Physics Letters,* vol. 76, pp. 1324-1326, Mar 2000.

[59] H. Li, X. Hu, Y. Wei, Z. Yu, X. Zhang, R. Droopad, A. A. Demkov, J. Edwards, K. Moore, W. Ooms, J. Kulik, and P. Fejes, "Two-dimensional growth of high-quality strontium titanate thin films on Si," *Journal of Applied Physics,* vol. 93, pp. 4521-4525, Apr 2003.

[60] G. Delhaye, C. Merckling, M. El-Kazzi, G. Saint-Girons, M. Gendry, Y. Robach, G. Hollinger, L. Largeau, and G. Patriarche, "Structural properties of epitaxial $SrTiO_3$ thin films grown by molecular beam epitaxy on Si(001)," *Journal of Applied Physics,* vol. 100, p. 5, Dec 2006.

[61] G. Niu, G. Saint-Girons, B. Vilquin, G. Delhaye, J. L. Maurice, C. Botella, Y. Robach, and G. Hollinger, "Molecular beam epitaxy of $SrTiO_3$ on Si (001): Early stages of the growth and strain relaxation," *Applied Physics Letters,* vol. 95, p. 3, Aug 2009.

[62] M. Choi, A. Posadas, R. Dargis, C. K. Shih, A. A. Demkov, D. H. Triyoso, N. D. Theodore, C. Dubourdieu, J. Bruley, and J. Jordan-Sweet, "Strain relaxation in single crystal $SrTiO_3$ grown on Si (001) by molecular beam epitaxy," *Journal of Applied Physics,* vol. 111, p. 6, Mar 2012.

[63] J. W. Park, S. H. Baek, C. W. Bark, M. D. Biegalski, and C. B. Eom, "Quasi-single-crystal (001) $SrTiO_3$ templates on Si," *Applied Physics Letters,* vol. 95, p. 3, Aug 2009.

[64] X. Gu, D. Lubyshev, J. Batzel, J. M. Fastenau, W. K. Liu, R. Pelzel, J. F. Magana, Q. Ma, L. P. Wang, P. Zhang, and V. R. Rao, "Commercial molecular beam epitaxy production of high quality $SrTiO_3$ on large diameter Si substrates," *Journal of Vacuum Science & Technology B,* vol. 27, pp. 1195-1199, May 2009.

[65] X. Gu, D. Lubyshev, J. Batzel, J. M. Fastenau, W. K. Liu, R. Pelzel, J. F. Magana, Q. Ma, and V. R. Rao, "Growth, characterization, and uniformity analysis of 200 mm wafer-scale $SrTiO_3$/Si," *Journal of Vacuum Science & Technology B,* vol. 28, p. 5, May 2010.

[66] B. Jalan, R. Engel-Herbert, N. J. Wright, and S. Stemmer, "Growth of high-quality $SrTiO_3$ films using a hybrid molecular beam epitaxy approach," *Journal of Vacuum Science & Technology A,* vol. 27, pp. 461-464, May 2009.

[67] C. D. Theis and D. G. Schlom, "Cheap and stable titanium source for use in oxide molecular beam epitaxy systems," *Journal of Vacuum Science & Technology a-Vacuum Surfaces and Films,* vol. 14, pp. 2677-2679, Jul-Aug 1996.

[68] S. A. Chambers, "Epitaxial growth and properties of thin film oxides," *Surface Science Reports,* vol. 39, pp. 105-180, 2000.

[69] M. Naito, H. Yamamoto, and H. Sato, "Reflection high-energy electron diffraction and atomic force microscopy studies on homoepitaxial growth of $SrTiO_3$(001)," *Physica C,* vol. 305, pp. 233-250, Sep 1998.

[70] A. A. Demkov and A. B. Posadas, "Crystalline Functional Oxide Growth Methods," in *Integration of Functional Oxides with Semiconductors*, A. A. Demkov and A. B. Posadas, Eds., ed, 2014, pp. 64-66.

[71] T. Y. Kometani and W. Wiegmann, "Measurement of Ga and Al in a molecular-beam epitaxy chamber by atomic-absorption spectrometry (AAS)," *Journal of Vacuum Science & Technology,* vol. 12, pp. 933-936, 1975.

[72] D. H. A. Blank, M. Dekkers, and G. Rijnders, "Pulsed laser deposition in Twente: from research tool towards industrial deposition," *Journal of Physics D: Applied Physics,* vol. 47, p. 034006, 2014.

[73] D. W. Oh, J. Ravichandran, C. W. Liang, W. Siemons, B. Jalan, C. M. Brooks, M. Huijben, D. G. Schlom, S. Stemmer, L. W. Martin, A. Majumdar, R. Ramesh, and D. G. Cahill, "Thermal conductivity as a metric for the crystalline quality of $SrTiO_3$ epitaxial layers," *Applied Physics Letters,* vol. 98, p. 3, May 2011.

[74] F. Sanchez, M. Varela, X. Queralt, R. Aguiar, and J. L. Morenza, "Preparation of $SrTiO_3$ thin films on Si(100) substrates by laser ablation: Application as buffer layer for $YBa_2Cu_3O_7$ films," *Applied Physics Letters,* vol. 61, pp. 2228-2230, Nov 1992.

[75] O. Nakagawara, M. Kobayashi, Y. Yoshino, Y. Katayama, H. Tabata, and T. Kawai, "Effects of buffer layers in epitaxial growth of $SrTiO_3$ thin film on Si(100)," *Journal of Applied Physics,* vol. 78, pp. 7226-7230, Dec 1995.

[76] J. H. Hao, J. Gao, Z. Wang, and D. P. Yu, "Interface structure and phase of epitaxial $SrTiO_3$ (110) thin films grown directly on silicon," *Applied Physics Letters,* vol. 87, p. 3, Sep 2005.

[77] J. H. Hao, J. Gao, and H. K. Wong, "Laser molecular beam epitaxy growth and properties of $SrTiO_3$ thin films for microelectronic applications," *Thin Solid Films,* vol. 515, pp. 559-562, Oct 2006.

[78] J. H. Hao, J. Gao, and H. K. Wong, "$SrTiO_3$(110) thin films grown directly on different oriented silicon substrates," *Applied Physics a-Materials Science & Processing,* vol. 81, pp. 1233-1236, Nov 2005.

[79] F. Sanchez, R. Aguiar, V. Trtik, C. Guerrero, C. Ferrater, and M. Varela, "Epitaxial growth of $SrTiO_3$ (00h), (0hh), and (hhh) thin films on buffered Si(001)," *Journal of Materials Research,* vol. 13, pp. 1422-1425, Jun 1998.

[80] M. B. Lee, M. Kawasaki, M. Yoshimoto, and H. Koinuma, "Pulsed laser deposition of epitaxial ferroelectric $Pb(Zr,Ti)O_3$ films on Si(100) substrate," *Japanese Journal of Applied Physics Part 2-Letters,* vol. 35, pp. L574-L576, May 1996.

[81] A. K. Sharma, J. Narayan, C. Jin, A. Kvit, S. Chattopadhyay, and C. Lee, "Integration of $Pb(Zr_{0.52}Ti_{0.48})O_3$ epilayers with Si by domain epitaxy," *Applied Physics Letters,* vol. 76, pp. 1458-1460, Mar 2000.

[82] M. B. Lee and H. Koinuma, "Structural and dielectric properties of epitaxial $SrTiO_3$ films grown on Si(100) substrate with TiN buffer layer," *Journal of Applied Physics,* vol. 81, pp. 2358-2362, Mar 1997.

[83] R. D. Vispute, J. Narayan, K. Dovidenko, K. Jagannadham, N. Parikh, A. Suvkhanov, and J. D. Budai, "Heteroepitaxial structures of $SrTiO_3$/TiN on Si(100) by in situ pulsed laser deposition," *Journal of Applied Physics,* vol. 80, pp. 6720-6724, Dec 1996.

[84] E. M. Kim, J. Y. Cho, J. H. Moon, W. J. Lee, H. S. Kim, and J. H. Kim, "Effects of deposition temperature on the crystallinity of $Ba_{0.5}Sr_{0.5}TiO_3$ epitaxial thin films integrated on Si substrates by pulsed laser deposition method," *Ceramics International,* vol. 34, pp. 1017-1021, May 2008.

[85] M. B. Lee, M. Kawasaki, M. Yoshimoto, and H. Koinuma, "Heteroepitaxial growth of $BaTiO_3$ films on Si by pulsed laser deposition," *Applied Physics Letters,* vol. 66, pp. 1331-1333, Mar 1995.

[86] R. A. Araujo, J. Yoon, X. H. Zhang, and H. Y. Wang, "Cubic TaN diffusion barrier for Cu interconnects using an ultra-thin TiN seed layer," *Thin Solid Films,* vol. 516, pp. 5103-5106, Jun 2008.

[87] J. Narayan, P. Tiwari, X. Chen, J. Singh, R. Chowdhury, and T. Zheleva, "Epitaxial growth of TiN films on (100) silicon substrates by laser physical vapor deposition," *Applied Physics Letters,* vol. 61, pp. 1290-1292, Sep 1992.

[88] W. B. Wu, K. H. Wong, and C. L. Choy, "Epitaxial growth of $SrTiO_3$ films with different orientations on TiN buffered Si(001) by pulsed laser deposition," *Thin Solid Films,* vol. 360, pp. 103-106, Feb 2000.

[89] R. Chowdhury, R. D. Vispute, K. Jagannadham, and J. Narayan, "Characteristics of titanium nitride films grown by pulsed laser deposition," *Journal of Materials Research,* vol. 11, pp. 1458-1469, Jun 1996.

[90] B. R. Kim, T. U. Kim, W. J. Lee, J. H. Moon, B. T. Lee, H. S. Kim, and J. H. Kim, "Effects of periodicity and oxygen partial pressure on the crystallinity and dielectric property of artificial $SrTiO_3/BaTiO_3$ superlattices integrated on Si substrates by pulsed laser deposition method," *Thin Solid Films,* vol. 515, pp. 6438-6441, Jun 2007.

[91] T. U. Kim, B. R. Kim, W. J. Lee, J. H. Moon, B. T. Lee, and J. H. Kim, "Integration of artificial $SrTiO_3/BaTiO_3$ superlattices on Si substrates using a TiN buffer layer by pulsed laser deposition method," *Journal of Crystal Growth,* vol. 289, pp. 540-546, Apr 2006.

[92] M. B. Lee, M. Kawasaki, M. Yoshimoto, M. Kumagai, and H. Koinuma, "Epitaxial growth of highly crystalline and conductive nitride films by pulsed laser deposition," *Japanese Journal of Applied Physics Part 1-Regular Papers Short Notes & Review Papers,* vol. 33, pp. 6308-6311, Nov 1994.

[93] K. H. Wong and Y. S. Leung, "Heteroepitaxial growth of $La_{0.7}Ca_{0.3}MnO_3/SrTiO_3/TiN/Si$ by pulsed laser deposition," *Thin Solid Films,* vol. 354, pp. 55-58, Oct 1999.

[94] M. Spreitzer, R. Egoavil, J. Verbeeck, D. H. A. Blank, and G. Rijnders, "Pulsed laser deposition of $SrTiO_3$ on a H-terminated Si substrate," *Journal of Materials Chemistry C,* vol. 1, pp. 5216-5222, 2013.

[95] T. Yamada, N. Wakiya, K. Shinozaki, and N. Mizutani, "Epitaxial growth of $SrTiO_3$ films on CeO_2/yttria-stabilized zirconia/Si(001) with TiO_2 atomic layer by pulsed-laser deposition," *Applied Physics Letters,* vol. 83, pp. 4815-4817, Dec 2003.

[96] D. H. Kim, L. Bi, N. M. Aimon, P. Jiang, G. F. Dionne, and C. A. Ross, "Combinatorial pulsed laser deposition of Fe, Cr, Mn, and Ni-substituted $SrTiO_3$ films on Si substrates," *Acs Combinatorial Science,* vol. 14, pp. 179-190, Mar 2012.

[97] H. Z. Guo, Y. H. Huang, K. J. Jin, Q. L. Zhou, H. B. Lu, L. F. Liu, Y. L. Zhou, B. L. Cheng, and Z. H. Chen, "Temperature effect on carrier transport characteristics in $SrTiO_{3-\delta}$ /Si p-n heterojunction," *Applied Physics Letters,* vol. 86, p. 3, Mar 2005.

[98] X. Y. Zhou, J. Miao, J. Y. Dai, H. L. W. Chan, C. L. Choy, Y. Wang, and Q. Li, "Epitaxial growth of $SrTiO_3$ thin film on Si by laser molecular beam epitaxy," *Applied Physics Letters,* vol. 90, Jan 1 2007.

[99] X. Y. Zhou, J. Miao, X. B. Lu, P. F. Lee, J. Y. Dai, H. L. W. Chan, C. L. Choy, and Y. Wang, "Influence of processing conditions on the structure of strontium titanate thin films grown on SI by laser MBE," *Integrated Ferroelectrics,* vol. 86, pp. 109-116, 2006.

[100] H. Ji, X. Y. Zhou, W. Wang, Y. R. Li, and Y. Wang, "Interface characterization of $SrTiO_3$/Sr/Si heterostructure through X-ray reflectivity," *Journal of Physics: Conference Series,* vol. 152, p. 012001, 2009.

[101] S. Migita and S. Sakai, "Epitaxial structure $SrTiO_3 < 011 >$ on Si $< 001 >$," *Journal of Applied Physics,* vol. 89, pp. 5421-5424, May 2001.

[102] S. J. Wang and C. K. Ong, "Epitaxial Y-stabilized ZrO_2 films on silicon: Dynamic growth process and interface structure," *Applied Physics Letters,* vol. 80, pp. 2541-2543, Apr 2002.

[103] M. Kondo, K. Maruyama, and K. Kurihara, "Epitaxial ferroelectric thin films on silicon substrates for future electronic devices," *Fujitsu Scientific & Technical Journal,* vol. 38, pp. 46-53, 2002.

[104] Y. Li, X. Yao, and K. Tanabe, "Improved surface morphology of $NdBa_2Cu_3O_{7-\delta}$ films grown by pulsed laser deposition using a large single crystal target," *Physica C: Superconductivity,* vol. 304, pp. 239-244, 1998.

[105] G. Hass and J. B. Ramsey, "Vacuum deposition of dielectric and semiconductor films by a CO_2 Laser," *Applied Optics,* vol. 8, pp. 1115-1118, 1969.

[106] H. M. Smith and A. F. Turner, "Vacuum deposited thin films using a ruby laser," *Applied Optics,* vol. 4, pp. 147-148, 1965.

[107] J. G. Bednorz and K. A. Müller, "Possible high-Tc superconductivity in the Ba—La—Cu—O system," *Zeitschrift für Physik B Condensed Matter,* vol. 64, pp. 189-193, 1986.

[108] Y. Yamagata, A. Sharma, J. Narayan, R. M. Mayo, J. W. Newman, and K. Ebihara, "Optical emission study of ablation plasma plume in the preparation of diamond-like carbon films by KrF excimer laser," *Journal of Applied Physics,* vol. 86, pp. 4154-4159, 1999.

[109] T. Ohnishi, H. Koinuma, and M. Lippmaa, "Pulsed laser deposition of oxide thin films," *Applied Surface Science,* vol. 252, pp. 2466-2471, 2006.

[110] A. Howie, *Surface and Interface Characterization by Electron Optical Methods.* New York and London: Plenum Press, 1988.

[111] I. Hernández-Calderón and H. Höchst, "New method for the analysis of reflection high-energy electron diffraction: α-Sn(001) and InSb(001) surfaces," *Physical Review B,* vol. 27, pp. 4961-4965, 1983.

[112] D. Klement, M. Spreitzer, and D. Suvorov, "Formation of a strontium buffer layer on Si(001) by pulsed-laser deposition through the Sr/Si(001)(2 x 3) surface reconstruction," *Applied Physics Letters,* vol. 106, p. 5, Feb 2015.

[113] Y. Wei, X. Hu, Y. Liang, D. C. Jordan, B. Craigo, R. Droopad, Z. Yu, A. Demkov, J. L. Edwards, and W. J. Ooms, "Mechanism of cleaning Si(100) surface using Sr or SrO for the growth of crystalline $SrTiO_3$ films," *Journal of Vacuum Science & Technology B,* vol. 20, pp. 1402-1405, 2002.

[114] O. Senftleben, H. Baumgärtner, and I. Eisele, "Cleaning of silicon surfaces for nanotechnology," *Materials Science Forum,* vol. 573-574, pp. 77-117, 2008.

[115] W. Kern and D. A. Puotinen, "Cleaning solutions based on hydrogen peroxide for use in silicon semiconductor technology," *RCA review,* vol. 31, p. 187, 1970.

[116] G. W. Trucks, K. Raghavachari, G. S. Higashi, and Y. J. Chabal, "Mechanism of HF etching of silicon surfaces: A theoretical understanding of hydrogen passivation," *Physical Review Letters,* vol. 65, pp. 504-507, Jul 1990.

[117] T. Takahagi, I. Nagai, A. Ishitani, H. Kuroda, and Y. Nagasawa, "The formation of hydrogen passivated silicon single-crystal surfaces using ultraviolet cleaning and HF etching," *Journal of Applied Physics,* vol. 64, pp. 3516-3521, Oct 1 1988.

[118] Y. J. Chabal, G. S. Higashi, K. Raghavachari, and V. A. Burrows, "Infrared spectroscopy of Si(111) and Si(100) surfaces after HF treatment: Hydrogen

termination and surface morphology," *Journal of Vacuum Science & Technology a-Vacuum Surfaces and Films,* vol. 7, pp. 2104-2109, May-Jun 1989.

[119] X. Zhang, E. Garfunkel, Y. J. Chabal, S. B. Christman, and E. E. Chaban, "Stability of HF-etched Si(100) surfaces in oxygen ambient," *Applied Physics Letters,* vol. 79, pp. 4051-4053, Dec 10 2001.

[120] C. C. Cheng, P. A. Taylor, R. M. Wallace, H. Gutleben, L. Clemen, M. L. Colaianni, P. J. Chen, W. H. Weinberg, W. J. Choyke, and J. T. Yates Jr, "Hydrocarbon surface chemistry on Si(100)," *Thin Solid Films,* vol. 225, pp. 196-202, 1993.

[121] J. J. Lander and J. Morrison, "Low voltage electron diffraction study of the oxidation and reduction of silicon," *Journal of Applied Physics,* vol. 33, p. 2089, 1962.

[122] N. Miyata, H. Watanabe, and M. Ichikawa, "Thermal decomposition of an ultrathin Si oxide layer around a Si(001)-(2 x 1) window," *Physical Review Letters,* vol. 84, pp. 1043-1046, Jan 2000.

[123] R. Tromp, G. W. Rubloff, P. Balk, F. K. LeGoues, and E. J. van Loenen, "High-temperature SiO_2 decomposition at the SiO_2/Si interface," *Physical Review Letters,* vol. 55, pp. 2332-2335, 1985.

[124] M. Liehr, J. E. Lewis, and G. W. Rubloff, "Kinetics of high-temperature thermal decomposition of SiO_2 on Si(100)," *Journal of Vacuum Science & Technology A,* vol. 5, pp. 1559-1562, 1987.

[125] Y. K. Sun, D. J. Bonser, and T. Engel, "Spatial inhomogeneity and void-growth kinetics in the decomposition of ultrathin oxide overlayers on Si(100)," *Physical Review B,* vol. 43, pp. 14309-14312, Jun 1991.

[126] Y. Wei, R. M. Wallace, and A. C. Seabaugh, "Void formation on ultrathin thermal silicon oxide films on the Si(100) surface," *Applied Physics Letters,* vol. 69, pp. 1270-1272, Aug 1996.

[127] J. P. Becker, R. G. Long, and J. E. Mahan, "Reflection high-energy electron diffraction patterns of carbide-contaminated silicon surfaces," *Journal of Vacuum Science & Technology a-Vacuum Surfaces and Films,* vol. 12, pp. 174-178, Jan-Feb 1994.

[128] K. Miki, K. Sakamoto, and T. Sakamoto, "Is the c(4×4) reconstruction of Si(001) associated with presence of carbon?," *Applied Physics Letters,* vol. 71, p. 3266, 1997.

[129] K. Miki, K. Sakamoto, and T. Sakamoto, "Surface preparation of Si substrates for epitaxial growth," *Surface science,* vol. 406, pp. 312-327, 1998.

[130] V. A. Ukraintsev, Z. Dohnálek, and J. T. Yates, "Electronic characterization of defect sites on Si(001)-(2×1) by STM," *Surface science,* vol. 388, p. 132, 1997.

[131] K. Hata, T. Kimura, S. Ozawa, and H. Shigekawa, "How to fabricate a defect free Si(001) surface," *Journal of Vacuum Science & Technology A,* vol. 18, pp. 1933-1936, 2000.

[132] O. Senftleben, T. Stimpel-Lindner, I. Eisele, and H. Baumgärtner, "Epitaxial silicon overgrowth of C_{60} on the Si(001)-(2×1) surface," *Surface science,* vol. 602, pp. 493-498, 2008.

[133] V. A. Ukraintsev and J. T. Yates, "The role of nickel in Si(001) roughening," *Surface science,* vol. 346, pp. 31-39, Feb 1996.

[134] G. D. Wilk, Y. Wei, H. Edwards, and R. M. Wallace, "In situ Si flux cleaning technique for producing atomically flat Si(100) surfaces at low temperature," *Applied Physics Letters,* vol. 70, pp. 2288-2290, Apr 1997.

[135] T. C. Shen, C. Wang, J. W. Lyding, and J. R. Tucker, "STM study of surface reconstructions of Si(111):B," *Physical Review B,* vol. 50, pp. 7453-7460, 1994.

[136] R. Hull, *Properties of crystalline silicon.* London: INSPEC, the Institution of Electrical Engineers, 1999.

[137] A. Assmuth, "Cleaning methods for silicon surfaces," presented at the 3rd FORNEL Workshop on Nanoelectronics, Erlangen, 2007.

[138] T. Miyazawa, S. Yoshida, S. Misawa, S. Gonda, and I. Ohdomari, "Molecular and ion beam epitaxy of 3C-SiC," *Applied Physics Letters,* vol. 45, pp. 380-382, 1984.

[139] T. Hatayama, Y. Tarui, T. Yoshinobu, T. Fuyuki, and H. Matsunami, "Controlled carbonization of Si(001) surface using hydrocarbon radicals in ultrahigh vacuum," *Journal of Crystal Growth,* vol. 136, pp. 333-337, 1994.

[140] Y. S. Wang, J. M. Li, L. Y. Lin, and F. F. Zhang, "The growth of SiC on Si substrates with C_2H_4 and Si_2H_6," *Applied Surface Science,* vol. 148, pp. 189-195, 1999.

[141] A. Ishizaka and Y. Shiraki, "Low temperature surface cleaning of silicon and its application to silicon MBE," *Journal of the electrochemical society,* vol. 133, p. 666, 1986.

[142] R. E. Thomas, M. J. Mantini, R. A. Rudder, D. P. Malta, S. V. Hattangady, and R. J. Markunas, "Carbon and oxygen removal from silicon (100) surfaces by remote plasma cleaning techniques," *Journal of Vacuum Science & Technology A,* vol. 10, pp. 817-822, 1992.

[143] T. Nakahata, K. Yamamoto, J. Tanimura, T. Inagaki, T. Furukawa, S. Maruno, Y. Tokuda, A. Miyamoto, S. Satoh, and H. Kiyama, "Low thermal budget surface cleaning after dry etching for selective silicon epitaxial growth," *Journal of Crystal Growth,* vol. 226, pp. 443-450, 2001.

[144] Y. Shiraki, "Epitaxial growth techniques: Molecular beam epitaxy," *Silicon Epitaxy,* vol. 72, pp. 151-183, 2001.

[145] H. Wang, R. Lin, and X. Wang, "Structural model of Si(100)-c(4×4)," *Physical Review B,* vol. 36, pp. 7712-7714, 1987.

[146] K. Kato, T. Ide, T. Nishimori, and T. Ichinokawa, "Formation and atomic configuration of Si(100)c(4 × 4) structure," *Surface science,* vol. 207, pp. 177-185, 1988.

[147] W. K. Liu, S. M. Mokler, N. Ohtani, C. Roberts, and B. A. Joyce, "A RHEED study of the surface reconstructions of Si(001) during gas source MBE using disilane," *Surface science,* vol. 264, pp. 301-311, 1992.

[148] R. I. G. Uhrberg, J. E. Northrup, D. K. Biegelsen, R. D. Bringans, and L. E. Swartz, "Atomic structure of the metastable c(4X4) reconstruction of Si(100)," *Physical Review B,* vol. 46, pp. 10251-10256, 1992.

[149] R. Butz and H. Lüth, "The surface morphology of Si (100) after carbon deposition," *Surface science,* vol. 411, pp. 61-69, 1998.

[150] R. Butz and H. Lüth, "The influence of carbon on the surface morphology of Si(100) and on subsequent Ge island formation," *Thin Solid Films,* vol. 336, pp. 69-72, 1998.

[151] M. L. Shek, "Observations regarding a c(4x4) C-Si(100) surface," *Surface science,* vol. 414, pp. 353-362, 1998.

[152] O. Leifeld, D. Grützmacher, B. Müller, K. Kern, E. Kaxiras, and P. C. Kelires, "Dimer pairing on the C-Alloyed Si(001) surface," *Physical Review Letters,* vol. 82, pp. 972-975, 1999.

[153] M. Stoffel, L. Simon, J. L. Bischoff, D. Aubel, and L. Kubler, "MBE Si regrowth on carbon-induced Si(001)-c(4x4) reconstructions studied by RHEED," *Thin Solid Films,* vol. 380, pp. 259-262, 2000.

[154] J. Y. Maeng and S. Kim, "Scanning tunneling microscopy study on c(4 x 4) structure of Si(100)," *Surface science,* vol. 482-485, p. 1445, 2001.

[155] R. C. Henderson, R. B. Marcus, and W. J. Polito, "Carbide contamination of silicon surfaces," *Journal of Applied Physics,* vol. 42, pp. 1208-1215, 1971.

[156] J. Yoshinobu, H. Tsuda, M. Onchi, and M. Nishijima, "The adsorbed states of ethylene on Si(100)c(4×2), Si(100)(2×1), and vicinal Si(100) 9º: Electron energy loss spectroscopy and low-energy electron diffraction studies.," *Journal of Chemical Physics,* vol. 87, pp. 7332-7340, Dec 1987.

[157] K. C. Pandey, "Reconstruction of the Si(100)-2x1 Surface," in *Proceedings of the 17th International Conference on the Physics of Semiconductors*, J. D. Chadi and W. A. Harrison, Eds., ed San Francisco, California, 1984.

[158] J. He, G. V. Hansson, and R. I. G. Uhrberg, "Atomic structure of the carbon induced Si(001)-c(4×4) surface," *Applied Surface Science,* vol. 252, pp. 5284-5287, 2006.

[159] H. Nörenberg and G. A. D. Briggs, "Influence of carbon on the formation of the Si(001) c(4×4) surface reconstruction," *Surface science,* vol. 433–435, pp. 397-400, 1999.

[160] Z. Yu, J. Ramdani, J. A. Curless, C. D. Overgaard, J. M. Finder, R. Droopad, K. W. Eisenbeiser, J. A. Hallmark, W. J. Ooms, and V. S. Kaushik, "Epitaxial oxide thin films on Si(001)," *Journal of Vacuum Science & Technology B,* vol. 18, pp. 2139-2145, 2000.

[161] Z. Yu, Y. Liang, C. Overgaard, X. Hu, J. Curless, H. Li, Y. Wei, B. Craigo, D. Jordan, R. Droopad, J. Finder, K. Eisenbeiser, D. Marshall, K. Moore, J. Kulik, and P. Fejes, "Advances in heteroepitaxy of oxides on silicon," *Thin Solid Films,* vol. 462–463, pp. 51-56, 2004.

[162] G. Delhaye, M. El Kazzi, M. Gendry, G. Hollinger, and Y. Robach, "Hetero-epitaxy of $SrTiO_3$ on Si and control of the interface," *Thin Solid Films,* vol. 515, pp. 6332-6336, 2007.

[163] A. Imanaka, T. Sasaki, Y. Hotta, and S. Satoh, "Fabrication of Sr silicate buffer layer on Si(100) substrate by pulsed laser deposition using a SrO target," *Journal of Vacuum Science & Technology A,* vol. 32, p. 051501, 2014.

[164] Z. Jovanović, M. Spreitzer, J. Kovač, D. Klement, and D. Suvorov, "Silicon surface deoxidation using strontium oxide deposited with the pulsed laser deposition technique," *ACS Applied Materials & Interfaces,* vol. 6, pp. 18205-18214, 10/22 2014.

[165] M. N. K. Bhuiyan, A. Matsuda, T. Yasumura, T. Tambo, and C. Tatsuyama, "Study of epitaxial $SrTiO_3$ (STO) thin films grown on Si(0 0 1)–2 × 1 substrates by molecular beam epitaxy," *Applied Surface Science,* vol. 216, pp. 590-595, 2003.

[166] N. K. Bhuiyan, K. H., T. T., and T. C., "Solid-phase epitaxial growth of $SrTiO_3$ thin films on Si(001) substrates at low temperature," *Japanese journal of applied physics,* vol. 43, p. 7879, 2004.

[167] M. N. K. Bhuiyan, H. Kimura, T. Tambo, and C. Tatsuyama, "Two-step growth of $SrTiO_3$ films on Sr-modulated Si(001) substrates," *Journal of materials science: materials in electronics* vol. 16, p. 225, 2005.

[168] B. G. Willis and A. Mathew, "Growth of ordered SrO layers on Si(100) using metal-organic surface reactions," *Journal of Vacuum Science & Technology A,* vol. 26, pp. 83-89, Jan-Feb 2008.

[169] C. B. Zhang, L. Wielunski, and B. G. Willis, "Formation of strontium template on Si(100) by atomic layer deposition," *Applied Surface Science,* vol. 257, pp. 4826-4830, 2011.

[170] A. Herrera-Gomez, F. S. Aguirre-Tostado, Y. Sun, P. Pianetta, Z. Yu, D. Marshall, R. Droopad, and W. E. Spicer, "Photoemission from the Sr/Si(001) interface," *Journal of Applied Physics,* vol. 90, pp. 6070-6072, Dec 2001.

[171] C. R. Ashman, C. J. Forst, K. Schwarz, and P. E. Blochl, "First-principles calculations of strontium on Si(001)," *Physical Review B,* vol. 69, p. 13, Feb 2004.

[172] A. Ramstad, G. Brocks, and P. J. Kelly, "Theoretical study of the Si(100) surface reconstruction," *Physical Review B,* vol. 51, pp. 14504-14523, May 1995.

[173] K. Garrity and S. Ismail-Beigi, "Phase diagram of Sr on Si(001): A first-principles study," *Physical Review B,* vol. 80, Aug 2009.

[174] R. M. Tromp, R. J. Hamers, and J. E. Demuth, "Si(001) dimer structure observed with scanning tunneling microscopy," *Physical Review Letters,* vol. 55, pp. 1303-1306, 1985.

[175] R. A. Wolkow, "Direct observation of an increase in buckled dimers on Si(001) at low temperature," *Physical Review Letters,* vol. 68, pp. 2636-2639, Apr 1992.

[176] A. Ichimiya and P. I. Cohen, *Reflection high energy electron diffraction.* United Kingdom: Cambridge University Press, 2004.

[177] R. Eason, *Pulsed laser deposition of thin films: Applications-led growth of functional materials.* Ney Jersey: John Wiley & Sons, Inc., Hoboken, 2006.

[178] W. C. Fan, N. J. Wu, and A. Ignatiev, "Observation of ordered structures of Sr on the Si(100) surface," *Physical Review B,* vol. 42, pp. 1254-1257, Jul 1990.

[179] R. Z. Bakhtizin, J. Kishimoto, T. Hashizume, and T. Sakurai, "Scanning tunneling microscopy of Sr adsorption on the Si(100)-2x1 surface," *Journal of Vacuum Science & Technology B,* vol. 14, pp. 1000-1004, Mar-Apr 1996.

[180] R. Z. Bakhtizin, J. Kishimoto, T. Hashizume, and T. Sakurai, "STM study of Sr adsorption on Si(100) surface," *Applied Surface Science,* vol. 94-5, pp. 478-484, Mar 1996.

[181] D. M. Goodner, D. L. Marasco, A. A. Escuadro, L. Cao, B. P. Tinkham, and M. J. Bedzyk, "X-ray standing wave study of the Sr/Si(001)-(2 x 3) surface," *Surface science,* vol. 547, pp. 19-26, Dec 2003.

[182] W. H. Du, B. Wang, L. Xu, Z. P. Hu, X. F. Cui, B. C. Pan, J. L. Yang, and J. G. Hou, "Identifying atomic geometry and electronic structure of (2 x 3)-Sr/Si(100) surface and its initial oxidation," *Journal of Chemical Physics,* vol. 129, p. 7, Oct 2008.

[183] M. Choi, A. B. Posadas, H. Seo, R. C. Hatch, and A. A. Demkov, "Charge transfer in Sr Zintl template on Si(001)," *Applied Physics Letters,* vol. 102, p. 4, Jan 2013.

[184] M. Kuzmin, M. P. J. Punkkinen, P. Laukkanen, J. J. K. Lang, J. Dahl, L. Vitos, and K. Kokko, "Atomic-level understanding of interfaces in the synthesis of crystalline oxides on semiconductors: Sr- and Ba/Si(100) (2×3) reconstructions," *Journal of Physical Chemistry C,* vol. 118, pp. 1894-1902, Jan 2014.

[185] K. F. Garrity, M. R. Padmore, Y. Segal, J. W. Reiner, F. J. Walker, C. H. Ahn, and S. Ismail-Beigi, "Phase transition of Sr on Si (001): First principles prediction and experiment," *Surface science,* vol. 604, pp. 857-861, May 2010.

[186] J. W. Reiner, K. F. Garrity, F. J. Walker, S. Ismail-Beigi, and C. H. Ahn, "Role of strontium in oxide epitaxy on silicon (001)," *Physical Review Letters,* vol. 101, p. 4, Sep 2008.

[187] L. F. Kourkoutis, C. S. Hellberg, V. Vaithyanathan, H. Li, M. K. Parker, K. E. Andersen, D. G. Schlom, and D. A. Muller, "Imaging the phase separation in atomically thin buried $SrTiO_3$ layers by electron channeling," *Physical Review Letters,* vol. 100, p. 4, Jan 2008.

[188] H. Mori and H. Ishiwara, "Epitaxial growth of $SrTiO_3$ films on Si(100) substrates using a focused electron beam evaporation method," *Japanese Journal of Applied Physics Part 2-Letters,* vol. 30, pp. L1415-L1417, Aug 1991.

[189] X. M. Hu, H. Li, Y. Liang, Y. Wei, Z. Yu, D. Marshall, J. Edwards, R. Droopad, X. Zhang, A. A. Demkov, K. Moore, and J. Kulik, "The interface of epitaxial $SrTiO_3$ on silicon: in situ and ex situ studies," *Applied Physics Letters,* vol. 82, pp. 203-205, Jan 2003.

[190] G. Niu, W. W. Peng, G. Saint-Girons, J. Penuelas, P. Roy, J. B. Brubach, J. L. Maurice, G. Hollinger, and B. Vilquin, "Direct epitaxial growth of $SrTiO_3$ on Si (001): Interface, crystallization and IR evidence of phase transition," *Thin Solid Films,* vol. 519, pp. 5722-5725, Jun 2011.

[191] G. Niu, J. Penuelas, L. Largeau, B. Vilquin, J. L. Maurice, C. Botella, G. Hollinger, and G. Saint-Girons, "Evidence for the formation of two phases during the growth of $SrTiO_3$ on silicon," *Physical Review B,* vol. 83, p. 9, Feb 2011.

[192] J. C. Woicik, H. Li, P. Zschack, E. Karapetrova, P. Ryan, C. R. Ashman, and C. S. Hellberg, "Anomalous lattice expansion of coherently strained $SrTiO_3$ thin films grown on Si(001) by kinetically controlled sequential deposition," *Physical Review B,* vol. 73, p. 5, Jan 2006.

[193] D. M. Schaadt, E. T. Yu, V. Vaithyanathan, and D. G. Schlom, "Nanoscale current transport in epitaxial $SrTiO_3$ on n(+)-Si investigated with conductive atomic force microscopy," *Journal of Vacuum Science & Technology B,* vol. 22, pp. 2030-2034, Jul-Aug 2004.

[194] J. Q. He, C. L. Jia, V. Vaithyanathan, D. G. Schlom, J. Schubert, A. Gerber, H. H. Kolhstedt, and R. H. Wang, "Interfacial reaction in the growth of epitaxial $SrTiO_3$ thin films on (001) Si substrates," *Journal of Applied Physics,* vol. 97, p. 6, May 2005.

[195] L. V. Goncharova, D. G. Starodub, E. Garfunkel, T. Gustafsson, V. Vaithyanathan, J. Lettieri, and D. G. Schlom, "Interface structure and thermal stability of epitaxial $SrTiO_3$ thin films on Si(001)," *Journal of Applied Physics,* vol. 100, p. 6, Jul 2006.

[196] S. B. Mi, C. L. Jia, V. Vaithyanathan, L. Houben, J. Schubert, D. G. Schlom, and K. Urban, "Atomic structure of the interface between $SrTiO_3$ thin films and Si(001) substrates," *Applied Physics Letters,* vol. 93, p. 3, Sep 2008.

[197] S. Fahler, S. Kahl, M. Weisheit, K. Sturm, and H. U. Krebs, "The interface of laser deposited Cu/Ag multilayers: evidence of the 'subsurface growth mode' during pulsed laser deposition," *Applied Surface Science,* vol. 154, pp. 419-423, Feb 2000.

[198] J. P. Barnes, A. K. Petford-Long, A. Suarez-Garcia, and R. Serna, "Evidence for shallow implantation during the growth of bismuth nanocrystals by pulsed laser deposition," *Journal of Applied Physics,* vol. 93, pp. 6396-6398, May 2003.

[199] J. Schou, "Physical aspects of the pulsed laser deposition technique: The stoichiometric transfer of material from target to film," *Applied Surface Science,* vol. 255, pp. 5191-5198, Mar 2009.

[200] R. F. Wood, K. R. Chen, J. N. Leboeuf, A. A. Puretzky, and D. B. Geohegan, "Dynamics of plume propagation and splitting during pulsed-laser ablation," *Physical Review Letters,* vol. 79, pp. 1571-1574, Aug 1997.

[201] A. V. Bulgakov and N. M. Bulgakova, "Gas-dynamic effects of the interaction between a pulsed laser-ablation plume and the ambient gas: analogy with an underexpanded jet," *Journal of Physics D-Applied Physics,* vol. 31, pp. 693-703, Mar 1998.

[202] N. Arnold, J. Gruber, and J. Heitz, "Spherical expansion of the vapor plume into ambient gas: an analytical model," *Applied Physics a-Materials Science & Processing,* vol. 69, pp. S87-S93, Dec 1999.

[203] F. Garrelie, C. Champeaux, and A. Catherinot, "Expansion dynamics of the plasma plume created by laser ablation in a background gas," *Applied Physics a-Materials Science & Processing,* vol. 69, pp. S55-S58, Dec 1999.

[204] T. E. Itina, J. Hermann, P. Delaporte, and M. Sentis, "Laser-generated plasma plume expansion: Combined continuous-microscopic modeling," *Physical Review E,* vol. 66, p. 12, Dec 2002.

[205] S. Amoruso, J. Schou, and J. G. Lunney, "Multiple-scattering effects in laser ablation plume propagation in gases," *Europhysics Letters,* vol. 76, pp. 436-442, Nov 2006.

[206] A. Sambri, S. Amoruso, X. Wang, F. M. Granozio, and R. Bruzzese, "Plume propagation dynamics of complex oxides in oxygen," *Journal of Applied Physics,* vol. 104, p. 8, Sep 2008.

[207] B. Dam, J. H. Rector, J. Johansson, J. Huijbregtse, and D. G. De Groot, "Mechanism of incongruent ablation of $SrTiO_3$," *Journal of Applied Physics,* vol. 83, pp. 3386-3389, Mar 1998.

[208] T. Ohnishi, M. Lippmaa, T. Yamamoto, S. Meguro, and H. Koinuma, "Improved stoichiometry and misfit control in perovskite thin film formation at a critical fluence by pulsed laser deposition," *Applied Physics Letters,* vol. 87, p. 3, Dec 2005.

[209] T. Ohnishi, K. Shibuya, T. Yamamoto, and M. Lippmaa, "Defects and transport in complex oxide thin films," *Journal of Applied Physics,* vol. 103, p. 6, May 2008.

[210] S. Wicklein, A. Sambri, S. Amoruso, X. Wang, R. Bruzzese, A. Koehl, and R. Dittmann, "Pulsed laser ablation of complex oxides: The role of congruent ablation and preferential scattering for the film stoichiometry," *Applied Physics Letters,* vol. 101, p. 5, Sep 2012.

[211] T. E. Itina, W. Marine, and M. Autric, "Monte Carlo simulation of pulsed laser ablation from two-component target into diluted ambient gas," *Journal of Applied Physics,* vol. 82, pp. 3536-3542, Oct 1997.

[212] Y. Liang, Y. Wei, X. M. Hu, Z. Yu, R. Droopad, H. Li, and K. Moore, "Heteroepitaxy of $SrTiO_3$ on vicinal Si(001): Growth and kinetic effects," *Journal of Applied Physics,* vol. 96, pp. 3413-3416, Sep 2004.

[213] J. Heyd, G. E. Scuseria, and M. Ernzerhof, "Hybrid functionals based on a screened Coulomb potential " *Journal of Chemical Physics,* vol. 124, p. 1, Jun 2006.

[214] A. A. Demkov and A. B. Posadas, "Critical Issues in Oxide-Semiconductor Heteroepitaxy," in *Integration of Functional Oxides with Semiconductors*, A. A. Demkov and A. B. Posadas, Eds., ed Austin, TX, 2014, p. 33.

[215] T. Suzuki, Y. Nishi, and M. Fujimoto, "Defect structure in homoepitaxial non-stoichiometric strontium titanate thin films," *Philosophical Magazine a-Physics of Condensed Matter Structure Defects and Mechanical Properties,* vol. 80, pp. 621-637, Mar 2000.

[216] Y. Wang, C. Ganpule, B. T. Liu, H. Li, K. Mori, B. Hill, M. Wuttig, R. Ramesh, J. Finder, Z. Yu, R. Droopad, and K. Eisenbeiser, "Epitaxial ferroelectric Pb(Zr, Ti)O_3 thin films on Si using $SrTiO_3$ template layers," *Applied Physics Letters,* vol. 80, pp. 97-99, Jan 2002.

[217] G. Y. Yang, J. M. Finder, J. Wang, Z. L. Wang, Z. Yu, J. Ramdani, R. Droopad, K. W. Eisenbeiser, and R. Ramesh, "Study of microstructure in $SrTiO_3$/Si by high-resolution transmission electron microscopy," *Journal of Materials Research,* vol. 17, pp. 204-213, Jan 2002.

[218] K. Munakata and A. Okazaki, "Ultra-high-angle double-crystal X-ray diffractometry (U-HADOX) for determining a change in the lattice spacing: experiment," *Acta Crystallographica Section A,* vol. 60, pp. 33-39, Jan 2004.

[219] L. Mechin, C. Adamo, S. Wu, B. Guillet, S. Lebargy, C. Fur, J. M. Routoure, S. Mercone, M. Belmeguenai, and D. G. Schlom, "Epitaxial $La_{0.7}Sr_{0.3}MnO_3$ thin films grown on $SrTiO_3$ buffered silicon substrates by reactive molecular-beam epitaxy,"

Physica Status Solidi a-Applications and Materials Science, vol. 209, pp. 1090-1095, Jun 2012.

[220] G. Niu, B. Vilquin, J. Penuelas, C. Botella, G. Hollinger, and G. Saint-Girons, "Heteroepitaxy of $SrTiO_3$ thin films on Si (001) using different growth strategies: Toward substratelike quality," *Journal of Vacuum Science & Technology B,* vol. 29, p. 5, Jul 2011.

[221] T. Bauer, S. Gsell, M. Schreck, J. Goldfuss, J. Lettieri, D. G. Schlom, and B. Stritzker, "Growth of epitaxial diamond on silicon via iridium/$SrTiO_3$ buffer layers," *Diamond and Related Materials,* vol. 14, pp. 314-317, Mar-Jul 2005.

[222] S. Gsell, M. Fischer, R. Brescia, M. Schreck, P. Huber, F. Bayer, B. Stritzker, and D. G. Schlom, "Reduction of mosaic spread using iridium interlayers: A route to improved oxide heteroepitaxy on silicon," *Applied Physics Letters,* vol. 91, p. 3, Aug 2007.

[223] G. Panomsuwan, O. Takai, and N. Saito, "Enhanced memory window of Au/$BaTiO_3$/$SrTiO_3$/Si(001) MFIS structure with high c-axis orientation for non-volatile memory applications," *Applied Physics a-Materials Science & Processing,* vol. 108, pp. 337-342, Aug 2012.

[224] G. J. Yong, R. M. Kolagani, S. Adhikari, W. Vanderlinde, Y. Liang, K. Muramatsu, and S. Friedrich, "Thermal stability of $SrTiO_3$/SiO_2/Si interfaces at intermediate oxygen pressures," *Journal of Applied Physics,* vol. 108, p. 8, Aug 2010.

[225] V. Shutthanandan, S. Thevuthasan, Y. Liang, E. M. Adams, Z. Yu, and R. Droopad, "Direct observation of atomic disordering at the $SrTiO_3$/Si interface due to oxygen diffusion," *Applied Physics Letters,* vol. 80, pp. 1803-1805, Mar 2002.

Bibliography

Publications Related to the Thesis

Journal Articles

D. Klement, M. Spreitzer and D. Suvorov, "Formation of a strontium buffer layer on Si(001) by pulsed-laser deposition through the Sr/Si(001)(2 x 3) surface reconstruction," *Applied Physics Letters,* vol. 106, no. 7, pp. 071602-1-071602-5, 2015.

Z. Jovanović, M. Spreitzer, J. Kovač, D. Klement and D. Suvorov, "Silicon surface deoxidation using strontium oxide deposited with the pulsed laser deposition technique," *ACS Applied Materials and Interfaces,* vol. 6, no. 20, pp. 18205-18214, 2014.

Published scientific conference contribution abstract (invited lecture)

M. Spreitzer, D. Klement and D. Suvorov, "Interfacing oxides with silicon using pulsed laser deposition," in *E-MRS 2014 Fall Meeting and Exhibit*, Boston, Massachusetts: Materials Research Society, 2014.

M. Spreitzer, Z. Jovanović, D. Klement and D. Suvorov, "Pulsed laser deposition of epitaxial SrO on Si substrate," in *E-MRS 2013 Spring Meeting*, Strasbourg, France: European Materials Research Society, 2013.

D. Klement, M. Spreitzer, A. Meden and D. Suvorov, " Synthesis peculiarities of microwave $Ag(Ta_xNb_{(1-x)})O_3$ ceramics," in *Book of abstracts of the 7th International Conference on Microwave Materials and Their Applications*, Taiwan, 2012.

Published scientific conference contribution abstract

D. Klement, M. Spreitzer and D. Suvorov, "Synthesis of epitaxial $SrTiO_3$ thin film on Si(001) surface covered with 1/2 ML of Sr using pulsed-laser deposition," in *E-MRS 2015 Spring Meeting*, Lille, France: European Materials Research Society, 2015.

D. Klement, M. Spreitzer and D. Suvorov, "Epitaxial growth of a $SrTiO_3$ thin layer on a Si(001) surface buffered with 1/2 ML Sr using the pulsed-laser-deposition technique," in *Program and abstract book of the 9th Young researchers' day*, Ljubljana, Slovenia: Jožef Stefan Institute, 2015.

D. Klement, M. Spreitzer and D. Suvorov, "First steps towards the growth of single-crystal $SrTiO_3$ on Si(001) by pulsed-laser deposition: Formation of a strontium buffer layer," in *Science and Applications of Thin Films*, Çeşme, Izmir, Turkey, 2014.

D. Klement, M. Spreitzer and D. Suvorov, "Structural and dielectric characteristics of $AgNb_{0.5}Ta_{0.5}O_3$ single-phase vs. composite ceramics," in *Program and abstract book of the 8th Young researchers' day*, Ljubljana, Slovenia: Jožef Stefan Institute, 2014.

M. Spreitzer, Z. Jovanović, D. Klement, J. Kovač and D. Suvorov, " Interfacing oxides with Si substrates," in *Programme and book of abstracts of the 21st International Scientific Meeting on Vacuum Science and Technologies*, Zagreb, Croatia: Croatian Vacuum Society, 2014.

D. Klement, M. Spreitzer and D. Suvorov, "Reflection high-energy electron diffraction of a Si crystal surface: kinematical simulations vs. experimentally obtained patterns," in *Program and abstract book of the 7th Young Researchers' Day*, Ljubljana, Slovenia: Jožef Stefan Institute, 2013.

D. Klement, M. Spreitzer, A. Meden and D. Suvorov, "Influence of synthesis conditions on the structural and electrical properties of the $Ag(Ta_xNb_{(1-x)})O_3$ ceramics," in *Program and book of abstracts of the 19th Conference on Materials and Technology*, Portorož, Slovenia: Institute of Metals and Technology, 2011.

Other Publications

Journal Articles

D. Klement, M. Spreitzer and D. Suvorov, "Suppressed temperature dependence of the resonant frequency of a $AgNb_{0.5}Ta_{0.5}O_3$ composite vs. single-phase ceramics," *Journal of the European Ceramic Society,* vol. 34, no. 6, pp. 1537-1545, 2014.

M. M. Kržmanc, D. Klement, B. Jančar and D. Suvorov, " Hydrothermal conditions for the formation of tetragonal $BaTiO_3$ particles from potassium titanate and barium salt," *Ceramics International,* doi: 10.1016/j.ceramint.2015.08.085.